POLYMER WAVEGUIDE AMPLIFIERS

Marcin Ziarko

Corpus Christi College

Department of Engineering

University of Cambridge

This dissertation is submitted for the degree of Doctor of Philosophy

October 2019

To my parents

DECLARATION

This dissertation is the result of my own work and includes nothing which is the outcome of work done in collaboration except as declared in the Preface and specified in the text.

It is not substantially the same as any that I have submitted, or, is being concurrently submitted for a degree or diploma or other qualification at the University of Cambridge or any other University or similar institution except as declared in the Preface and specified in the text. I further state that no substantial part of my dissertation has already been submitted, or, is being concurrently submitted for any such degree, diploma or other qualification at the University of Cambridge or any other University or similar institution except as declared in the Preface and specified in the text.

In accordance with the Department of Engineering guidelines, this thesis is does not exceed 65,000 words, and it contains less than 150 figures.

Marcin Ziarko

Cambridge, October 2019

ACKNOWLEDGEMENTS

First and foremost I would like to thank my supervisors Prof. Ian White and Prof. Richard Penty. Their guidance and support were invaluable during my PhD study. Their advice and knowledge led me through the process and enabled me to gain an understanding of the subject as well as a wider perspective.

I also wish to thank all my colleagues from the Centre for Photonic Systems (CPS) group for sharing their time and expertise with me. In particular, I would like to thank Dr Nikos Bamiedakis for patiently sharing his knowledge about polymer fabrication processes, waveguide simulations and experimental procedures; Adrian Wonfor for support on laboratory- and computer-related activities; Victoria Barrett for help with all the daily organisational challenges as well as Illana Toledano and Eric Lowe for the inspirational coffee breaks. They have all made my time in CAPE an enlightening and enjoyable experience.

I would also like to acknowledge close collaborators from the Seamatics project, especially Dr Eric Kumi-Barimah, Dr Billy Richards and Sri Rahayu for the provision of the samples used in this work. I would also like to thank Dow Corning Corporation for providing polymer materials employed in this thesis.

I wish to express my gratitude to EPSRC for the funding they provided me with through Integrated Photonic and Electronic Systems CDT as well as Corpus Christi College for financial support in the form of a travel grant that enabled me to attend an international conference.

I would also like to thank to all the rowers, coxes and coaches that I have spent countless early mornings over my years in Cambridge. During the time at CCCBC I have developed many great friendships as well as learnt the importance of teamwork, persistence and responsibility required to succeed.

Finally, I want to express my gratitude to Laura for her support and encouragement during the ups and downs of the PhD journey while experiencing the same odyssey herself. Thank you for always being there for me and sharing the exploration of probably all the Milton Keynes roundabouts. Last but not least, special thanks to my parents and sisters for their love and support throughout my study that made it all possible.

ABSTRACT

Polymer-based optical waveguides are a promising technology for integrating optical links onto standard printed circuit boards as they enable cost-effective manufacturing and assembly as well as offer high bandwidth. The motivation for this work is to address the lack of amplifying components the currently demonstrated polymer interconnects, which limits the complexity, functionality and reach of these systems. This dissertation studies combination of rare-earth-doped material with polymer platform to create compact erbium-doped waveguide amplifiers (EDWAs) for board-level interconnect applications.

Siloxane polymer materials developed by Dow Corning are used as they have shown the necessary optical, mechanical and thermal properties required for EDWA designs (such as the ability to withstand temperatures in excess of 350 °C). The feasibility of two approaches for integrating Er-doped materials into siloxane polymer layers is investigated, namely: (i) ultrafast laser plasma implantation (ULPI) and (ii) solution-based dispersion of Er-doped nanoparticles (NP). Er-doped thin films are prepared with these two methods and their properties investigated. The maximum dopant concentrations and lifetimes are determined to be 16.3, 4.4 and 1.5×10^{20} cm^{-3} and 12.1, 4.2 and 5.7 ms for ULPI into silica glass, ULPI into polymer and the dispersion of erbium NPs in a polymer matrix, respectively.

An EDWA numerical modelling framework is developed to optimise the erbium-ytterbium ratio to maximise the device gain while accounting for various potential integration methods and waveguide design parameters. Using a channel geometry based on the measured optical properties of Er-doped glass, an internal gain of 9.6 dB/cm is predicted at the optimal Er:Yb ratio of $9.0{:}7.3 \times 10^{20}$ cm^{-3} when pumped at an optical power of 200 mW. A hybrid, polymer-glass strip-loaded design is proposed to combine the highly doped glass layer with the polymer material. While a slightly lower gain of 7.4 dB/cm is projected in the re-optimised design under the same operating conditions, it benefits from a simpler fabrication procedure.

An experimental study of devices prepared through the direct Er integration into polymer waveguides enables a comparison with developed theoretical models. A good agreement between measured and modelled results show that a practical amplifier operation with erbium concentration of 1.5×10^{20} cm^{-3} is prevented by the dopant NP clustering and the potential gain limited by the absence of ytterbium co-doping. The excess scattering loss of 9.3 dB/cm could not be further reduced only with the proposed additional ultrasonication and filtering fabrication steps indicating alternative approaches such as core-shell structures are required.

LIST OF PUBLICATIONS

Journal Papers

1. E. Kumi-Barimah, **M. Ziarko**, N. Bamiedakis, I.H. White, R.V. Penty and G. Jose "Erbium-doped glass nanoparticle embedded polymer thin films using femtosecond pulsed laser deposition" , Optical Materials Express, Vol. 8, Issue 7, pp. 1997-2007, 2018.

Under Review

1. E. Kumi-Barimah, S. Rahayu, **M. Ziarko**, N. Bamiedakis, I.H. White, R.V. Penty, G. Kale and G. Jose "Photoluminescent Erbium doped Nanaoparticle-Polymer Composite Thin Films for Optical Waveguide Amplifier", Optical Materials Express, submitted July 2019.

International Conferences

1. **M. Ziarko**, N. Bamiedakis, E. Kumi-Barimah, G. Jose, R. V. Penty, and I. H. White "Erbium-doped polymer waveguide amplifiers for board-level optical interconnects", International Conference on Transparent Optical Networks (ICTON), Angers, France, July 2019 [Invited, 10.1109/ICTON.2019.8840529].
2. E. Kumi-Barimah, S. Rahayu, **M. Ziarko**, N. Bamiedakis, I.H. White, R.V. Penty, G. Kale and G. Jose "Erbium doped Nanoparticle-Polymer Composite Thin Films for Integrated Photonics", Conference on Lasers and Electro-Optics (CLEO Europe), Munich, Germany, June 2019 [OSA Technical Digest, paper ck_11_1].
3. **M. Ziarko**, N. Bamiedakis, E. Kumi-Barimah, G. Jose, R. V. Penty, and I. H. White "Erbium-doped polymer waveguide amplifiers for PCB-integrated optical links", Photonics West OPTO, San Francisco, USA, March 2019 [Proc. SPIE 10924, Optical Interconnects XIX, 1092403].
4. E. Kumi-Barimah, **M. Ziarko**, N. Bamiedakis, I.H. White, R.V. Penty and G. Jose "Femtosecond-Pulsed Laser Deposition of Erbium-Doped Glass Nanoparticles in Polymer Layers for Hybrid Optical Waveguide Amplifiers", AVS International Symposium and Exhibition, Long Beach, USA, October 2018.
5. **M. Ziarko**, N. Bamiedakis, E. Kumi-Barimah, G. Jose, R.V. Penty and I.H. White "Hybrid polymer-based Er-doped waveguide amplifiers", Semiconductor and Integrated OptoElectronics (SIOE), Cardiff, UK, April 2018.

CONTENTS

LIST OF FIGURES

LIST OF TABLES

NOMENCLATURE

ALD	atomic layer deposition
ASE	amplified spontaneous emission
B2B	back-to-back
CO	central office
CUC	cooperative upconversion
CW	continuous wave
dB	decibel
dBm	decibel power ratio (referenced to a milliwatt)
DBR	distributed Bragg reflector
DFB	distributed feedback
EDFA	erbium-doped fibre amplifier
EDPWA	erbium-doped polymer waveguide amplifier
EDTS	erbium-doped tellurite-modified silica
EDWA	erbium-doped waveguide amplifier
EGC	erbium-gadolium co-doped ceria
EM	energy migration
Er	erbium
ESA	excited state absorption
ETU	energy transfer upconversion
FBG	fibre Bragg grating
FR4	flame retardant 4
FWHM	full width at half maximum
GSA	ground state absorption
HRTEM	high resolution transmission electron microscopy
HUC	homogenous upconversion
ICP	inductively coupled plasma
IR	infrared
LAP	Leeds alginate process
LIDAR	light detection and ranging
MIMIC	micromoulding in capillaries
MM	multi-mode
NA	numerical aperture
NC	nanocrystal

NIR	near-infrared
NOA	Norland optical adhesive
NP	nanoparticle
NRZ	non-return-to-zero
OLED	organic light emitting diode
OLT	optical line termination
ONU	optical network unit
OSA	optical spectrum analyser
PCB	printed circuit board
PDMS	polydimethylsiloxane
PIC	photonic integrated circuit
PIQ	pair induced quenching
PL	photoluminescence
PLC	planar lightwave circuit
PLD	plasma laser deposition
PMMA	poly(methyl methacrylate)
POF	plastic optical fibre
PON	passive optical network
POSS	polyhedral oligometric silsesquioxane
RE	rare earth
RI	refractive index
RIE	reactive ion etching
RMS	root mean square
RMSE	root mean square error
RPM	rotation per minute
SAL	sodium alginate solution
SEM	scanning electron microscopy
SM	single mode
SOI	silicon-on-insulator
TDM	time division multiplexing
TE	transverse electric
TIR	total internal reflection
TM	transverse magnetic
TZN	zinc-sodium tellurite
ULPI	ultrafast laser plasma implantation

UV	ultra-violet
VCSEL	vertical-cavity surface-emitting laser
WDM	wavelength division multiplexing
WG	waveguide
Yb	ytterbium

1 INTRODUCTION

In this chapter a short introduction to the topic of optical technologies is given with a focus on integrated systems based on polymer materials. The qualities of the polymer platform in terms of mechanical, thermal and optical properties are discussed and compared with alternative technologies. Numerous polymer-based systems and components have been demonstrated over the years showing a range of potential applications in different fields. However, the majority of the reported systems have been non-amplifying which limits the potential of polymer-based solutions. Therefore, key potential techniques for achieving gain in polymer materials are discussed. The three types of the gain mechanics in the platform, namely rare-earth (RE) doping, use of conjugated polymers and laser dyes are examined, and previously reported experimental results are reviewed.

Polymer-based optical systems with active components have a number of potential applications in fields such as communications and optical sensing. The most important characteristics and requirements for practical applications are discussed. These design specifications are then compared with research that has been done so far in developing such devices not only employing polymers, but also in other material systems.

Finally, an overview of the aims and the work of this thesis is given. The focus has been placed on developing an extensive modelling framework as well as experimental study of two-dimensional waveguide amplifiers that are based on rare-earth-doped material for polymer-based integrated optics.

1.1 Polymer-based optical systems

The last four decades have witnessed great changes in communication systems. The exponential growth in computer processing speed and data volume has resulted in ever-increasing requirement for transmission capacity. This has been initially addressed through the use of optical transmission systems in long-haul telecommunication networks [1]. These systems have grown at an equally rapid pace, becoming more sophisticated through the addition of new functionalities such as signal multiplexing, processing and routing. A basic system consisting of a light source, a detector and a transmission medium has been enhanced over time. The performance has been improved by complementing the basic components with more advanced such as multiplexers, amplifiers and switches [2].

Initially adding new advanced optical functionality to the network required the use of bulk optics elements such as lenses. This has sometimes proven problematic due to misalignment sensitivity, handling difficulties and instability. The limited scalability and

handling difficulties can be avoided in a system integration, which combines many functionalities on a single element.

The idea of integrated optics was initially developed in 1969 at Bell Labs to describe a system composing of a single planar layer that includes a number of photonic components [3]. Photonic integrated circuits (PICs) highly resemble their electrical counterparts, where numerous components are compactly placed next to one another and connected together via waveguides. Photonic integration is a very broad topic with extensive research being currently undertaken. As a result, detailed investigation of the field is not done here, but a good overview of theory and implementations can be found in the literature [4]-[6].

Waveguides are a key component of almost any photonic system. They are especially important in case of integrated photonic devices such as optical circuits [7], where due to the small size of the system's elements, good quality transmission lines are key components required to send light signals between different parts of the circuit. One of the main reasons for the increasing interest in the optical transmission for board-level interconnects is the much higher bandwidth it offers compared with traditional electrical connections [8],[9]. However, currently this benefit comes with a disadvantage of relatively high cost of fabrication [10],[11].

Even though data transmission has been the main motivation behind the development of optical waveguide systems, there are a number of other research areas and potential applications for such designs. A compact and planar layout is advantageous in any complex system as it provides increased efficiency required by a number of fields such as biochemical analysis [12],[13].

Optical fibre networks for long-haul telecommunication systems have been based on silica glass. Therefore, there has been much research in integrating new functionality on this platform as well as other types of glass [14]. The work in this PhD dissertation however focuses on using polymer as a material of choice for photonic integration. This choice offers a possibility of fabricating optical components that have the increased communication bandwidth advantage of glass, but come at a comparatively lower cost [15],[16]. While this is not crucial for long-haul optical communications due to component cost being a small part of the whole project, it is a key requirement for short distance, compact systems. Polymer-based optical fibres are already used in many automotive and short-haul communications applications [17]. However, there is an

increasing need to develop integrated components such as waveguides, splitters or modulators for inter- and intra-chip applications.

In contrast to inorganic systems that require expensive and time-consuming fabrication techniques such as reactive ion etching or sputtering [18], polymers components can be easily produced and patterned using spin-coating, embossing or direct laser writing [19]. In addition to the ease of deposition, a thin film can be produced on a wide range of substrates (glass, silicon, FR4) that are both rigid and flexible. All of the above properties make polymers an attractive alternative to inorganic semiconductors for short-transmission-distance applications.

The mixture of the above advantages combined with the fact that polymer structure can be modified in order to adjust or improve its properties to address a specific need has made it a popular material for a number of systems [20],[21]. What is more, many polymers can exhibit high thermo-optic and electro-optic coefficients which has led to the development of high-speed and low-voltage modulators and switches [22],[23]. Both of these components are crucial as they add necessary functionality for a practical integrated optics system.

The main physical problem with many polymer materials is their intrinsically high loss at second and third communication windows corresponding to 1310 nm and 1550 nm, respectively. This mid-IR (infrared) wavelengths absorption loss results from the overtones of the fundamental molecular vibrations [24] and an additional scattering loss can be introduced through thermally-induced crystallisation. While the latter can be minimised through careful processing during fabrication, the former requires more careful material engineering. Methods such as deuteration and halogenation (removal of hydrogen atoms from the polymer molecule in order to eliminate highly absorbing C-H bond) have been developed in order to reduce losses to acceptable levels [25]. As a result, an increasing number of commercially available organic materials offers low losses reaching 0.1 dB/cm at both 1.31 μm and 1.55 μm [26]. Even though some inorganic materials such as glasses still offer a better performance, these are generally low enough for most short-distance, integrated applications [27].

Furthermore, a prolonged exposure to the UV radiation may result in breaking of the polymer chains that eventually leads to deterioration of the optical properties. Even though the visible yellowing and embrittlement has a detrimental effect on the material performance, a number of system stabilisers has been used to minimise these effects [28].

1.2 Applications of Active Polymer-based Optical Devices

Optical amplifiers are currently widely employed for a number of applications. One of the most common examples is in long-haul optical communication systems where they have replaced signal repeaters in order to increase the transmission lengths without a need for electro-optical conversion. In such systems various types of amplifiers can be used as booster amplifiers at the transmitter end, in-line amplifiers and pre-amplifiers at the receiver end of a link [29]. Another important application is in high-power systems, where power in range of hundreds of watts is required. These include not only material processing, but often specialised scientific setups such as atom trapping [30] or gravitational wave antennas [31].

Miniaturisation of such devices explored in this work has opened a new group of potential applications related to PICs, sometimes also referred to as to planar lightwave circuits (PLCs). The need for simple, low-cost fabrication sources and amplifiers for high-end scalable systems makes organic solid-state devices a great candidate. Their potential to integrate active components with existing functionalities on the same chip leading to reduced size, increased performance, portability and reliability is considered one of the key factors for the success of this technology [32]. Possible applications of such compact devices range from optical interconnects to next generation passive optical networks and optical sensing.

1.2.1 Backplane and Chip-to-chip Interconnections

Optical interconnect technologies have gained much research interest for short-reach communication links in high-performance computing systems such as data centres and supercomputers. The reason behind that is the currently observed trend of rapidly increasing internet traffic, particularly within data centres. Figure 1-1 shows a recent report by Cisco estimating the compound annual growth rate of data centre traffic to be 25% and the trend is expected to continue in the near future putting strain on the current infrastructure.

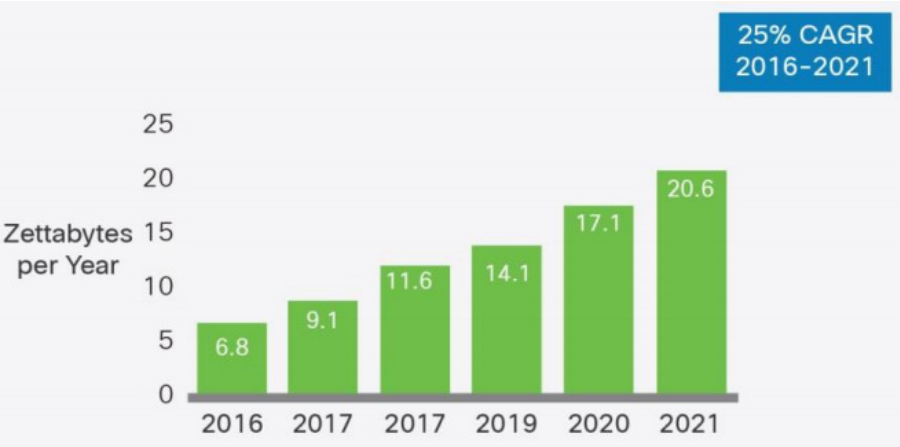

Figure 1-1: Predicted growth of the global inter- and intra-data centre IP traffic flow from 2019 to 2021 based on the actual data (2016-2018) [33]

Currently used board-to-board and chip-to-chip copper interconnects have reached their physical limits and replacing them with optical system promises to overcome the resulting transmission bottleneck [34]. The main arguments supporting the use of optics in such environments are related to the performance advantages they offer over conventional electrical solutions. The benefits of optical links include lower power consumption, higher bandwidth and increased density required to meet the predicted need for 780 Tb/s with a 50 fJ/bit energy budget of future 310 mm^2 chips [35].

One of the leading candidates for the implementation of board-level optical interconnects, that are compatible with electrical printed circuit boards (PCBs), are polymer waveguides [36],[37]. A number of successful system demonstrators based on various types of polymer materials and implementing different optical bus architectures have been reported in the past [38]–[40]. What is more, high-speed data transmission over polymer multimode waveguides has been achieved using 850 nm low-cost vertical-cavity surface-emitting lasers (VCSELs), with record values of 40 Gb/s and 56 Gb/s demonstrated over 1-m-long link using non-return-to-zero (NRZ) and 4-level pulse amplitude modulation (PAM-4) respectively [41].

There is currently a great interest in migrating this multimode technology from the first communications window (around 850 nm) to longer telecommunications' wavelengths (1310 nm and 1550 nm) and single mode waveguides. The main driver behind this trend is to enable a direct interface of board-level polymer waveguides with the emerging high-performance Si photonics chips and PICs based on III-V materials as suggested by IBM technology roadmap as shown in Figure 1-2.

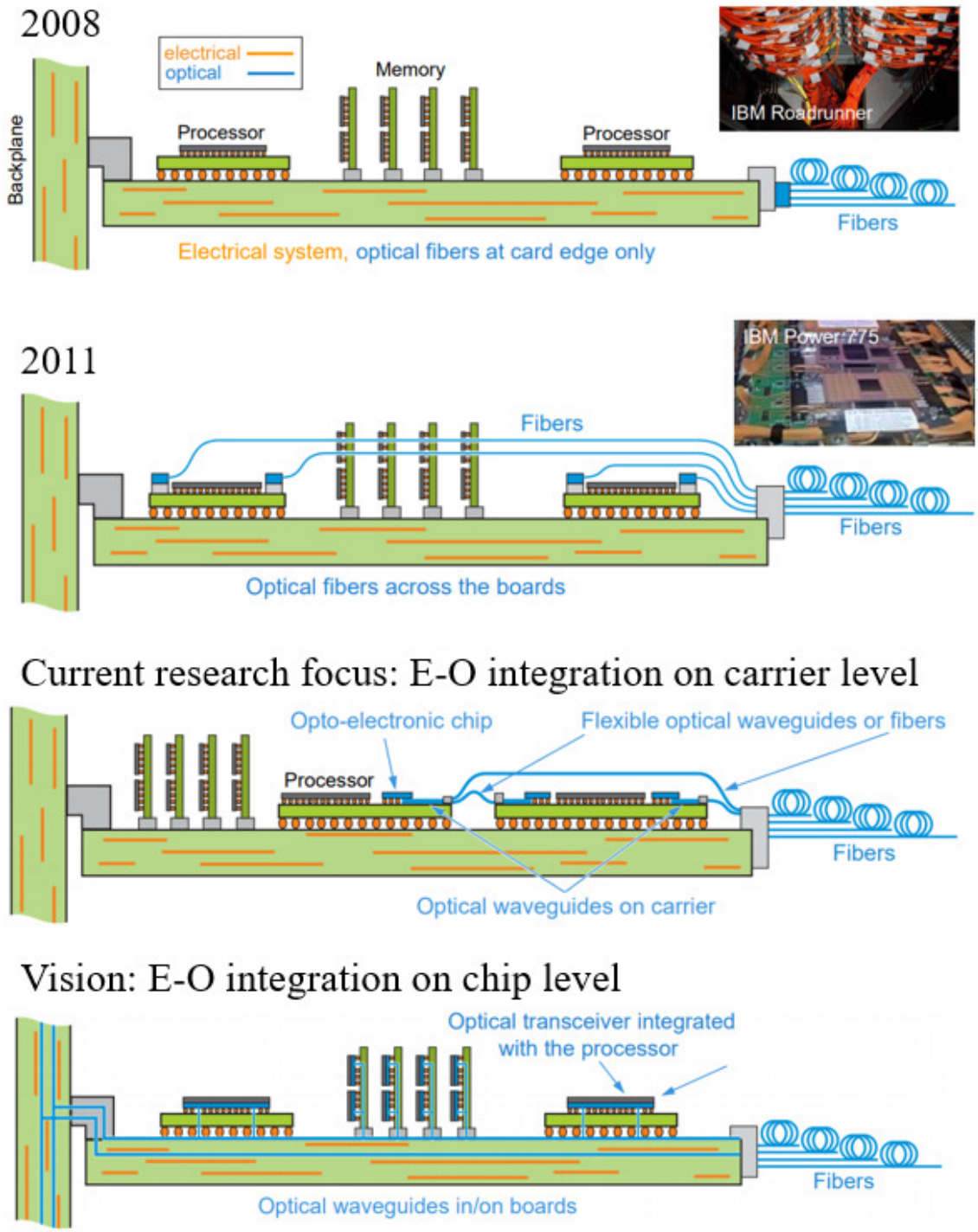

Figure 1-2: Electro-optical interconnect development roadmap [42]

Despite the great progress made, there is still a number of challenges before a fully integrated elecro-optical chip-level backplane can be fabricated. One of such problems, addressed in this work, is the fact that all currently implemented polymer-based optical backplanes have been non-amplifying. This not only imposes a limit on the length of the on-board links as well as on the number of components that can be interconnected via, for example, splitters in a bus architecture.

In the past, this limitation has been addressed through employing optoelectronic 3R regenerators [43]. However, this solution requires multiple signal conversions that could be more efficiently addressed by an all-optical device. As a result, there is great interest in developing optical amplifiers suitable for integration onto PCBs [44]. Although various materials and doping approaches have been studied and some encouraging results have been reported in recent years [45]–[47], high-gain, power-efficient and PCB-compatible EDWAs are still to be demonstrated.

1.2.2 Next Generation PONs

Access networks cover the final part, sometimes referred as the 'last mile', of a telecommunications infrastructure connecting individual customers to the service provider's central offices (COs). A passive optical network is an approach that promises to provide end customers high-capacity traffic in a cost-efficient way. Even though the underlying standards and technologies have evolved over time, the common property is the absence of active components between an optical line termination (OLT) and optical network unit (ONU) [48].

Increasing demand for bandwidth has been satisfied by a continuous evolution of the technical standards through inclusion of solutions such as time division multiplexing (TDM) and wavelength division multiplexing (WDM) [49]. Most of current research is carried out on next generation PONs (NG-PON) promising downstream speeds of 10 Gb/s and eventually 40 Gb/s (NG-PON2) and more in the near future [50].

As the demand for bandwidth in access networks is expected to keep rising, future standards are being put forward to satisfy the demand for a more scalable solution that can serve a large enough number of subscribers to make it economically viable. The most recent development has been a super-PON proposal put forward by Google that opened a discussion for the IEEE 802.3 task group [51]. The proposed architecture, shown in Figure 1-3 (a), offers cost effective network design capable of reaching up to 1024 customers within 50 km radius.

One of the key components in the CO is the optical amplifier used as both preamps and boosters to compensate for not only the distance to the nodes, but also the high splitting loss to reach all the nodes. The proposed wavelength allocation depicted in Figure 1-3 (b) assumes usage of 1530-1600 nm window which is compatible with the erbium-based amplifiers. Therefore, there is an emerging need for a future high-volume integrated

solution, possibly employing EDWAs instead of discrete components, to bring the unit cost down allowing for a mass market delivery.

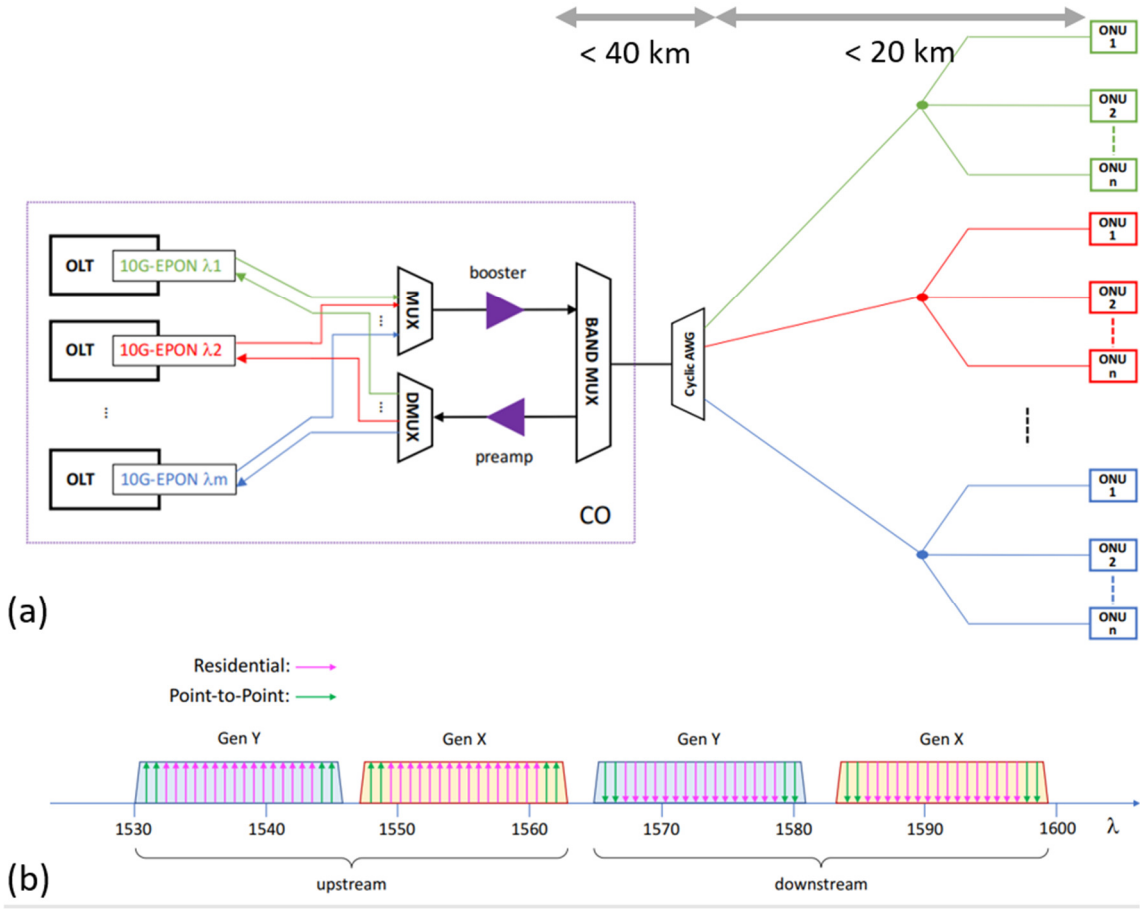

Figure 1-3: Super PON (a) suggested architecture,
b) potential wavelength allocation [from [51]]

1.2.3 Sensing

Another emerging area of application for a polymer waveguide platform is to use an integrated device as a sensor. The concept of a miniaturised lab-on-chip has been developed to analyse a number of biological or chemical substances [52]. The characterisation of samples is performed through testing optical properties using a small polymer device, where optical waveguides are placed in proximity of microfluidic channels. Polymer has been successfully deployed in this application as it offers ease of fabrication of all the necessary structures for a full system through various patterning techniques as well as chemical stability required for reliable results [53],[54]. These sensors can be used to detect certain substances, such as ammonia [55], or used to detect other environmental factors, for example, temperature changes [56] as shown in Figure 1-4.

Even though optical amplifiers are generally not required for such small, few-centimetre-squared devices, light sources can be useful in such systems. This has been demonstrated in the past that a sensor platform benefits from the presence of an active rare-earth doped microring structure as it boosts the sensitivity and increases the limit of detection for cancer biomarkers by an order of magnitude [57].

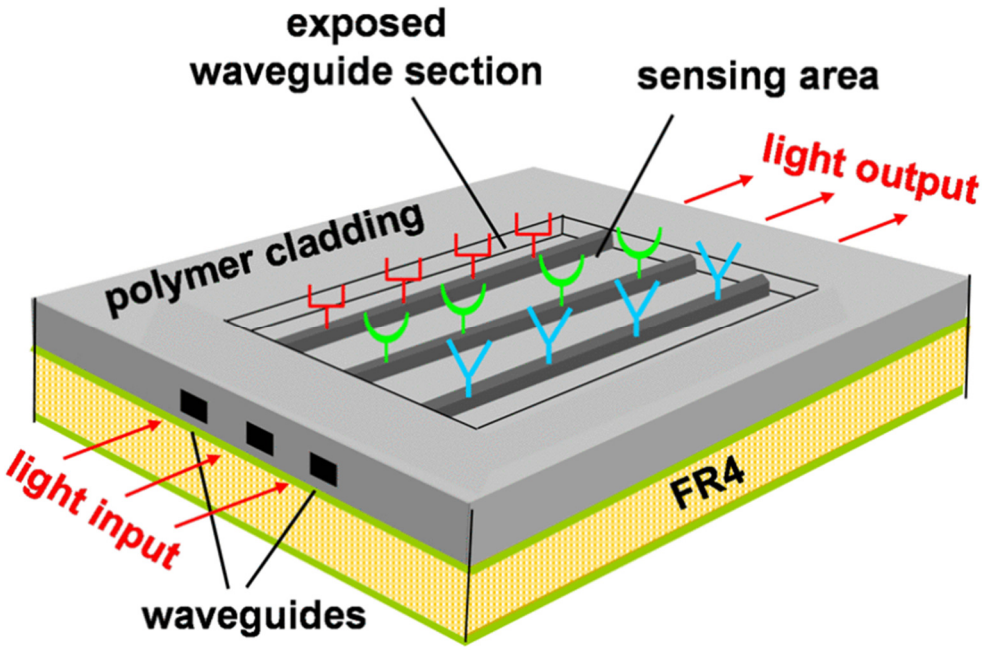

Figure 1-4: Polymer-based sensor used to measure ammonia concentration through exposed waveguides [55]

Another emerging application for erbium-doped integrated devices in sensing has been the use of both amplifiers and sources for light detection and ranging (LiDAR) systems [58]. Wavelengths around 1550 nm offer an advantage in such systems due to not being perceivable by human eye and relatively higher 'eye-safe' power levels that are needed in order to extend the device range. What is more, erbium-based planar amplifiers have been considered for satellite-based CO_2 and CH_4 mapping systems due to suitable absorption features of these greenhouse gasses around 1570 nm [59].

1.2.4 Infrared Upconverters

Over the past few years, there has been intensive research in using various materials as hosts for rare-earth doped infrared-to-visible light upconverters. These offer a range of applications, but the primary focus is for colour displays. In contrast to the previously mentioned applications for RE-doped systems, where the upconversion process is seen as a shortcoming and the design effort is focused on minimising the phenomena, in this case the process is desirable.

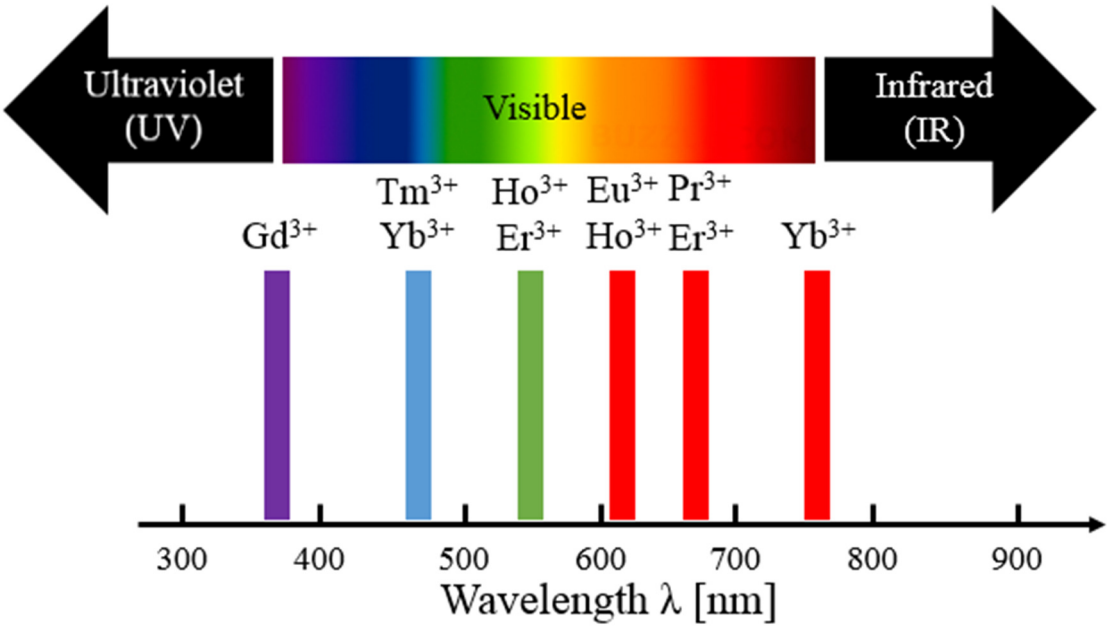

Figure 1-5: Visible light upconversion emission from rare-earth materials

One of the key driving factors has been the demonstration that various lanthanides have energy transitions that cover wavelengths across the visible spectrum as shown in Figure 1-5. Initially, various excitation frequencies have been used for different elements, however, such systems are not suitable for practical applications. In order to overcome this problem, rare-earth doped materials are co-doped with ytterbium. This acts as an effective sensitizer due to its very high absorption cross-section combined with efficient energy-transfer mechanism between Yb and neighbouring acceptor ions [60]. This principle has been demonstrated to work well for thulium, praseodymium, erbium, holmium, europium and gadolinium under 980 nm excitation wavelength [61]. The final step towards a practical design has been combining different RE ions in order to produce a white light source. This has been successfully achieved by a number of systems, for example by using a combination of Tm-Ho-Yb to generate almost perfect colour light for RGB devices as defined by CIE chromaticity diagram [62].

Upconversion is still an inefficient process, but considerable interest resulted in finding a number of suitable host materials that enhance this phenomena. Most of the research in this area has focused on various glasses and optimising their structure to enhance the upconverters efficiency. This has been shown for systems based not only on tellurite, fluorolead germinate, fluorophosphates or lithium borate but also on other materials including crystals and polymers [63],[64].

1.3 Active Components in Polymer Systems

Most of the polymer systems demonstrated so far only include a combination of non-amplifying components such as waveguides, splitters and modulators. While this may be sufficient for certain applications, there is an increasing need for adding active (amplifying) components into the photonic integrated circuits as explained in the previous section. These would not only improve the existing designs by increasing the link lengths and scalability, but also add new functionalities.

As already stated, this work focuses on developing an integrated polymer amplifier that combines compact size with relatively low-cost fabrication. An active region in polymer, required for not only an amplifier but also for an optical source, can be realised by either introducing optically active dopants into the polymer or by using special type of polymer with behaviour similar to that of semiconductors. Based on the above distinction, there are three major candidates for implementation of optical amplifiers in polymers: dye-doped, conjugated polymer and rare-earth ion doped.

1.3.1 Dye-doped Polymer

Lasing action in dye material was first observed in 1960s [65],[66] with a great number of new dyes developed since [67]. Dyes are complex organic molecules that have many sub-states that naturally form a four-level laser system. This allows them to absorb and emit light over a relatively broad range of wavelengths. The two spectra are separated due to the presence of sub-states leading to absorption of higher energy photons followed by a fast, non-radiative relaxation inside the energy level and finally a light emission as shown in Figure 1-6. This means that dyes with a large Stokes shift have a clearly separated absorption and emission wavelengths.

Dyes can be used in a number of both organic and inorganic hosts. The former type makes the fabrication process easier [69] leading to successful doping of a variety polymer host materials over a range of emission wavelengths [70],[71]. Most of the reported dye-doping attempts show visible light spontaneous or stimulated emission between 400 and 600 nm [72],[73] including a combination of multiple materials to generate a white light emitter [74]. There has been increasing interest in near-infrared (NIR) dyes mainly for biological imaging with emission wavelengths greater than 1000 nm [75].

Most of the work on dye-doped polymers has been focused on creating organic lasers using resonator structures such as planar cavities, gratings, rings or discs [76],[77].

However, in the process of creating working dye-doped based devices, a number of problems have been encountered including low radiation damage threshold, photobleaching, short device lifetimes and difficulties with continuous wave (CW) operation [78]. These problems have been addressed by improving dye and polymer formulation [79],[80] or quenching triplet states that absorbed energy [81].

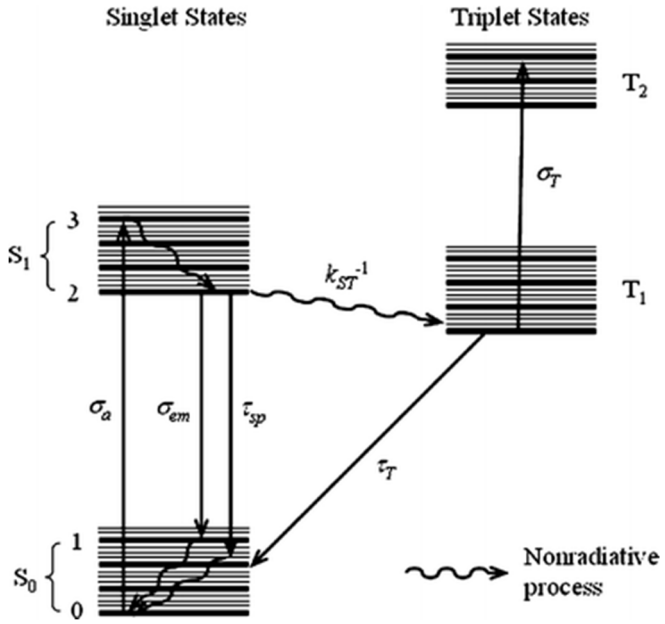

Figure 1-6: Typical energy levels of a dye molecule showing transitions lifetimes and emission/absorption cross-sections [68]

Semi CW lasing through a dye jet replenishment has been demonstrated since the 1970s in liquid solutions [82], but the same approach is not possible in a solid-state system. There have been successful attempts of non-CW (sometimes referred to as quasi-CW) amplifiers and lasers both in plastic optical fibres (POFs) [83], [84] as well as in integrated systems [85],[86]. Although there have been no reports of devices working in the telecom C-band, lasing has been reported in the near-infrared. Gain coefficients of 11 cm^{-1} at 1270 nm [87] and 14 cm^{-1} at 970 nm [88] were achieved under low optical pumping duties. The improvements in the device efficiency have been realised through a reduction of the triplet state exciton accumulation via triplet conversion [89] and a decrease of the lasing threshold under 1 $\mu J/cm^2$ [67].

1.3.2 Conjugated Polymer

Ordinarily a polymer is an insulator, but there exists a group of organic materials that conduct electricity. They are made of conjugated molecule chains, where atoms form a sequence of alternating single and double covalent bonds. The overlapping orbitals lead

to a band structure similar to the one seen in semiconductors [90]. These types of polymer are particularly attractive due to the fact that they eliminate the need for an external optical pump source. This in turn would enable fabrication of thin, flexible lasers that can be made at low cost.

Organic materials with electroluminescent properties are widely used in organic light emitting diodes (OLEDs), but there has been a number of challenges to combine them with an efficient resonator structure capable of creating a directly-pumped laser [91].

As in dye-doped materials, most of the demonstrated systems operate in the visible light emission range, as creating conjugated chains that are long enough to emit IR has proven difficult.

Amplified spontaneous emission (ASE) phenomena in this type of material has been achieved from both solid state and liquid form polymers. This was demonstrated with assistance of not only top, but also edge pulsed optical pumping with gain exceeding 70 cm^{-1} in the visible spectrum [92],[93]. These materials are therefore a good potential candidate for optical amplifiers and initially have been demonstrated in liquid polymer [94] and later in waveguide structures [95].

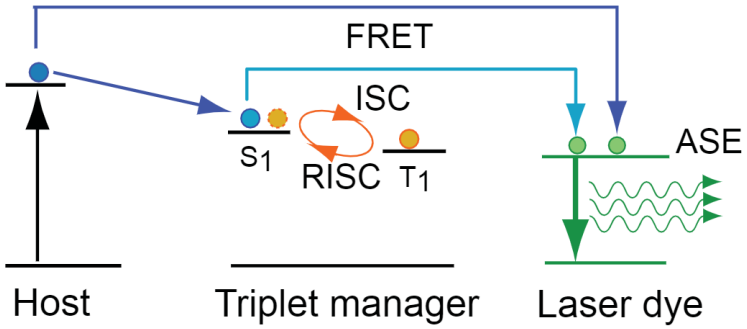

Figure 1-7: Energy transfer cascade in polymer system combining conducting host with a dye and triplet manager [96]

The promise of conjugated polymer-based amplifiers lies in electrical pumping that cannot be achieved with other polymer amplifiers. There have been attempts at achieving such a device, but a number of problems are preventing the creation of a reliable and practical prototype. The difficulty with attaching electrical contacts that usually leads to gain quenching has been addressed by adjusting device geometry [97].

The problems aforementioned for the dye-doped polymers are also present in conjugated polymer systems. The practical applications are limited by the triplet state absorption and operational lifetimes of approximately 2×10^7 pulses before the output drops by 50%

[98],[99]. These are particularly relevant as there have been attempts in combining conducting polymer hosts with dye molecules as well as triplet state managers in order to create a more complex system combining benefits of multiple materials as shown in Figure 1-7.

Finally, there has been also been increasing research interest to combine OLEDs with rare-earth-ion dopants. As a result of this investigation, early reports show a potential for electroluminescence in IR wavelength range albeit with very low external quantum efficiencies under 0.1 % [100] -[102].

1.3.3 Rare-earth-doped Polymer

The two previously mentioned types of polymer amplifiers are in most cases optically active under 1 μm which means that they do not cover the second and third communications windows (around 1300 nm and 1550 nm respectively) [103]. An alternative approach is to use RE ions, which are a group of 17 elements that differ in terms of their optical properties, as dopant in active region. These have a multi-level energy band structure with various trivalent RE having energy transitions corresponding to different emission wavelengths. In many cases the multiple different radiative and non-radiative decay paths are possible depending on factors such as wavelength of the absorbed photon supplied to the system through optical pumping.

The most widely used element from the RE group is erbium (Er), as its emission spectra coincides with third communication window. This led to creation of erbium doped fibre amplifiers (EDFA) used in long distance communication that are optically pumped to achieve stimulated emission at wavelengths between 1530 and 1580 nm. More detailed information on progress in Er-doped integrated optics is given in Section 1.4 as the use of this material is the topic of this thesis.

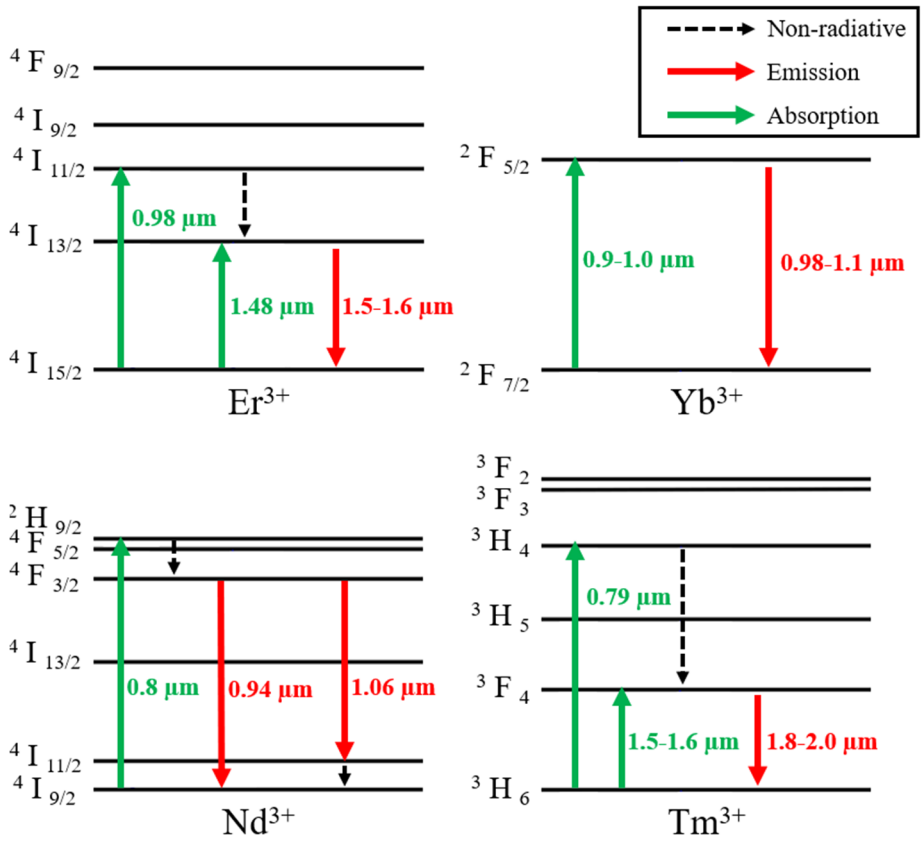

Figure 1-8: Simplified energy diagram for Er, Yb, Nd and Tm

Even though most research on RE-doped systems has focused on Er, there has been interest in other trivalent ions due to a wide range of emission wavelengths they offer. Other commonly used elements are ytterbium (Yb), neodymium (Nd) and thulium (Tm). They all offer the potential for amplifier devices at a range of IR wavelengths between 940 nm and 2 µm as shown in Figure 1-8.

These materials, as well as other rare-earths, have been widely used as active laser media in optical fibre based amplifiers and lasers, as well as in solid state devices such as Nd:YAG for many years [104],[105]. More recently, with the emergence of plastic optical fibres (POFs), attempts have been made to dope them with rare-earths, such as europium, to achieve stimulated emission [106]. However, most of the reported attempts have focused on devices working in the visible range [107]-[109]. This in turn has led to an investigation of polymer as potential host for waveguide amplifiers to take full advantage of the ease of fabrication of polymer waveguides combined with the potential for high gain devices [110],[111].

The main difficulty preventing the demonstration of a fully successful compact device has been due to poor solubility of rare-earth ions, not only in polymer matrix, but also in most widely used glasses [112]. The resulting formation of clusters highly limits the

achievable gain per unit length of the device. This issue has been confronted by trying different combinations of host and active materials that reduces the ligand formation and resulting emission quenching. It is the potential for low pumping energy required, combined with absence of the exciton annihilation processes observed in dye-doped polymer devices, that allows CW operation without thermally damaging the polymer structure.

The intensive research in optimising the host-dopant dynamics has resulted in a number of encouraging results. Lasing or amplification has been reported for a number of rare-earth doped polymers covering a range of wavelengths. Some notable examples in IR include neodymium-doped 6FDA capable of lasing and 1.4 dB/cm amplification at 1060 nm [113],[114]. Furthermore, a number of demonstrations for visible light amplification has been reported. Europium-doped Norland optical adhesive (NOA) has produced strong red emission and a gain of 17.4 dB/cm at 612 nm under CW pumping with 60 mW at 337 nm [115]. Furthermore, a 5-mm-long poly(methyl methacrylate) (PMMA) waveguide doped with terbium has been shown to generate strong green light and an estimated gain of up to 10.8 dB/cm at 545 nm under 488 nm pumping [116].

All the above attempts have demonstrated the potential for combining polymer hosts with active RE-based dopants to create practical devices. The range of available materials allows light emission at a range of wavelengths with different applications. However, the most intensive research, including this work, has been carried out in combining polymer hosts with erbium ions which enable creation of integrated components that are compatible with currently used telecommunications networks.

1.4 Erbium-doped Polymer Waveguide Amplifiers (EDWAs)

Erbium-doped optical amplifiers have been intensively researched since the 1990s due to the fact that their emission spectra around 1550 nm matches low loss region in glass fibre. This has led to rapid improvements in their designs leading to a better performance [117]. Optimisation in terms of dopant-concentration, pump power [118] and adding sensitizing elements [119] to increase efficiency have allowed erbium-doped fibre amplifiers (EDFAs) to replace regenerator units and dominate long haul transmission systems [120].

As the technology matured for long-distance applications, new possible applications emerged with device miniaturisation. Small size systems have been previously dominated by semiconductor materials due to more efficient electrical pumping and larger transition cross-sections leading to higher gain per unit length [121]. Recent developments in

enhancing optical gain in compact devices have shown evidence that rare-earth-ion-doped dielectric waveguide amplifiers and lasers can be competitive for integrated photonic applications [122].

The main reason that practical EDWAs have not been demonstrated so far is due to the fact that high-enough dopant concentrations have not been achieved without triggering detrimental quenching mechanisms in the material. In case of EDFAs that are widely employed to overcome losses in long haul telecommunications systems, high gain without saturation effects is obtained by optimising amplifier pump power, dopant level and fibre length [123]. Since the transmission distance is usually measured in hundreds of kilometres, the EDFA can be as long as tens of meters, which in turn leads to required dopant concentrations in range of 10^{18} cm^{-3} [124].

In case of waveguide amplifiers for integrated photonics based on silicon chips, there is much less freedom when designing a device. A practical size is limited to a few centimetres with the pump power being also capped due to possibility of thermally damaging the device. As a result, much higher Erbium concentrations are needed to achieve a practical amplifier. The exact concentration needed is still affected by waveguide dimensions, pump power and device efficiency, but is expected to be in range of 10^{21} cm^{-3} or even higher [125],[126].

In addition to increasing the concentration of erbium in the waveguide, it is necessary to increase the absorption efficiency of the pump signal. This is usually achieved by co-doping the host material with other materials, sensitizers such as ytterbium [127]. This is a popular technique used to compensate for relatively low absorption cross-section of erbium compared to that of ytterbium. The two elements combine well because Yb absorbs light at 980 nm and efficiently transfers it to neighbouring Er ions to be later emitted around 1550 nm. Figure 1-9 shows a demonstration in aluminium oxide, where almost seven-fold increase of emission intensity for a co-doped waveguide under the same pumping conditions has been achieved.

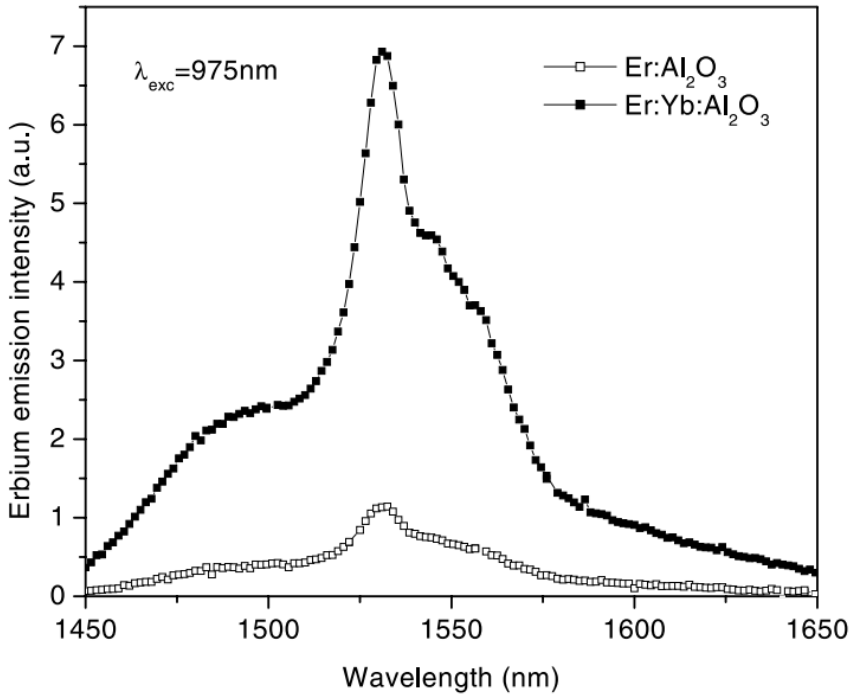

Figure 1-9: Emission intensity of erbium and erbium-ytterbium doped material [128]

A much more detailed description of the theory behind erbium-based systems is given in Chapter 2. Not only the mechanisms governing the performance will be explained, but also key design factors discussed. This is followed by overview of the current state-of-the-art designs in both polymer hosts as well as other materials such as glasses.

1.5 Thesis Aims and Outline

The aim of this thesis is to explore the potential behind a new fabrication process – ultrafast laser plasma implantation (ULPI) to create high gain erbium-doped amplifiers. This doping method has been recently demonstrated to achieve a very high Er concentration of 1.63×10^{21} cm^{-3} in silica while maintaining a long metastable lifetime required for practical devices [129]. The underlying potential of the reported results is researched with the help of a model developed to quantify effects of various performance factors. Based on measured parameters, performance of a standard channel waveguide geometry is investigated to assess material suitability for formation of optical amplifier with gain of 10 dB/cm. This dissertation continues with a novel process of a dopant ratio optimisation in order to maximise the potential EDWA gain.

Furthermore, the focus is placed on possible integration methods of the ULPI with the polymer platform. The work in this thesis assess if, by adjusting implantation process

parameters, Er-doped thin films of comparable quality can be formed. A study sets to identify the most suitable materials and viable approaches to doping the polymer either directly or through compatible hybrid waveguide architectures proposed in this thesis. This dissertation assesses not only the implementation feasibility but also the performance of designed and modelled devices. The issue of minimising impact of the alternative waveguide geometries on the amplifier performance is addressed and quantified through the dopant profile optimisation.

This dissertation describes the work performed on understanding the performance factors, design and characterisation of the erbium-doped systems. The reminder of this document is structured as follows:

Chapter 2 describes the operation principles and factors affecting the performance of the EDWA. It discusses the processes that diminish the achievable gain in highly doped, miniaturised systems. The effect of these concentration quenching mechanisms leading to the upconversion is debated and a number of methods to counteract them is presented. The chapter ends with a presentation of the current state-of-the-art devices based on a number of a different host materials.

Chapter 3 presents the design considerations that have to be accounted for in the polymer-based waveguide amplifier. It discusses the waveguiding theory and simulations undertaken in order to establish single mode operation conditions in various device architectures. It then presents a multi-level rate equations model required for a simulation of the gain dynamics in EDWAs. The impact of various parameters such as ion concentration, length of the device, pump power, upconversion and co-doping is described quantitatively. These theoretical predictions are then used to propose alternative device geometries for further studies.

Chapter 4 introduces in detail the fabrication techniques and steps required for implementation of the designed polymer-based devices. The siloxane polymer features are developed using a prepared mask and characterised in terms of loss. Ultrafast laser plasma implantation and nanoparticle dispersion methods of erbium doping are described and employed to prepare Er thin films. The qualitative and quantitative characterisation results of the obtained layers, such as spectroscopy and erbium lifetime measurements, are presented and compared between various samples. These findings are then used to identify most promising approaches for an amplifier feasibility study.

Chapter 5 discusses the process used to design hybrid glass-polymer devices using channel and strip-loaded geometries. The procedure to estimate key simulation parameters from material properties is presented with the obtained values then used in more detailed amplifier studies. The implementation of strip-loaded devices is chosen due to their predicted performance and relative ease of fabrication. The process of the polymer ridge deposition on glass is optimised and the prepared samples experimentally assessed for their potential to form EDWAs.

Chapter 6 describes the nanoparticle dispersion process employed to create Er-doped polymer devices. The obtained waveguides are visually inspected to optimise the fabrication recipe and characterised in terms of their transmission across the C-band. The experimental results are fitted to a loss model used to extract and analyse the underlying device properties. The EDWA model introduced in the third chapter is then used to verify the experimental results and determine the device potential. Finally, the performance is compared with the alternative state-of-the-art NP-doped polymer systems.

Chapter 7 presents the main conclusions drawn from the results obtained in this thesis and suggestions regarding the future work. All of the key findings from the amplifier modelling and feasibility studies on different EDWA approaches are summarised. The limitations addressable through a further development based on other existing technologies as well as simulation work are discussed.

1.6 Summary

In this chapter a brief introduction of polymer-based integrated optical systems is given. The key advantages of polymer materials, such as high processability and favourable mechanical, thermal and optical properties are discussed. This is followed by a description of previously demonstrated components and their applications in a wide range of fields. However, the performance and scalability of current systems is constrained by a lack of integrated amplifying elements. Therefore, a number of potential techniques of introducing gain into polymer systems to overcome this limitation is presented. Methods of using rare earth doping, conjugated polymers and laser dyes are introduced and the current progress in these fields is summarised.

Potential applications of polymer-based systems with amplifying capabilities, such as optical interconnects or sensors, are presented. Practical design requirements in each case are discussed and compared with the latest research achievements.

Finally, an outline and aims of the work included in the following chapters in this thesis are summarised. The focus is placed on exploring the potential behind promising fabrication processes as well as developing a detailed modelling framework to optimise device performance. The key aspects and findings presented in each section are briefly explained with short description of the most relevant findings.

1.7 References

[1] J. M. Senior, *Optical Fiber Communications Principles and Practice*, 3rd ed. Prentice Hall, 2009.

[2] T. E. Stern, G. Ellinas, and K. Bala, *Multiwavelength Optical Networks Architectures, Design, and Control*. Cambridge University Press, 2009.

[3] S. E. Miller, "Integrated Optics: An Introduction," *Bell Syst. Tech. J.*, vol. 48, no. 7, pp. 2059–2069, 1969.

[4] R. Hunsperger, *Integrated Optics: Theory and Technology*, 6th ed. New York: Springer-Verlag, 2009.

[5] C. R. Doerr, "Silicon photonic integration in telecommunications," *Front. Phys.*, vol. 3, no. August, pp. 1–16, 2015.

[6] A. Hosseini *et al.*, "System-on-Chip Photonic Integrated Circuits," *IEEE J. Sel. Top. Quantum Electron.*, vol. 24, no. 1, pp. 1–20, 2017.

[7] L. Vivien and L. Pavesi, *Handbook in Silicon Photonics*, First. Boca Raton: CRC Press, 2013.

[8] C. Cole, B. Huebner, and J. E. Johnson, "Photonic integration for high-volume, low-cost applications," *IEEE Commun. Mag.*, vol. 47, no. 3, pp. S16–S22, 2009.

[9] D. A. B. Miller, "Optical interconnects to electronic chips," *Appl. Opt.*, vol. 49, no. 25, pp. 59–70, 2010.

[10] T. Barwicz *et al.*, "A novel approach to photonic packaging leveraging existing high-throughput microelectronic facilities," *IEEE J. Sel. Top. Quantum Electron.*, vol. 22, no. 6, pp. 455–466, 2016.

[11] D. Liang and J. E. Bowers, "Photonic integration: Si or InP substrates?," *Electron. Lett.*, vol. 45, no. 12, p. 578, 2009.

[12] G. T. Roman and R. T. Kennedy, "Fully integrated microfluidic separations

systems for biochemical analysis," *J. Chromatogr. A*, vol. 1168, no. 1–2, pp. 170–188, 2007.

[13] L. Guo, J. Feng, Z. Fang, J. Xu, and X. Lu, "Application of microfluidic 'lab-on-a-chip' for the detection of mycotoxins in foods," *Trends Food Sci. Technol.*, vol. 46, no. 2, pp. 252–263, 2015.

[14] R. Decorby and M. Irannejad, "Glasses for Photonic Integration," in *Springer Handbook of Electronic and Photonic Materials*, Springer, 2017, pp. 1059–1080.

[15] I. Papakonstantinou, D. R. Selviah, R. C. A. Pitwon, and D. Milward, "Low-cost, precision, self-alignment technique for coupling laser and photodiode arrays to polymer waveguide arrays on multilayer PCBs," *IEEE Trans. Adv. Packag.*, vol. 31, no. 3, pp. 502–511, 2008.

[16] N. Bamiedakis, A. Hashim, J. Beals, R. V. Penty, and I. H. White, "Low-cost PCB-integrated 10 GB/s optical transceiver built with a novel integration method," *IEEE Trans. Components Packag. Manuf. Technol.*, vol. 3, no. 4, pp. 592–600, 2013.

[17] G. Stepniak, M. Schüppert, and C.-A. Bunge, "Polymer-optical fibres for data transmission," in *Polymer Optical Fibres*, Woodhead Publishing, 2017, pp. 217–310.

[18] L. Eldada and L. W. Shacklette, "Advances in polymer integrated optics," *IEEE J. Sel. Top. Quantum Electron.*, vol. 6, no. 1, pp. 54–68, 2000.

[19] B. W. Swatowski *et al.*, "Flexible, stable, and easily processable optical silicones for low loss polymer waveguides," in *Proc. SPIE 8622, Organic Photonic Materials and Devices XV*, 2013.

[20] J. Wang *et al.*, "Polymer PLC as an Optical Integration Bench," *2011 Opt. Fiber Commun. Conf. Expo. Natl. Fiber Opt. Eng. Conf.*, p. OWM1, 2013.

[21] J. Wang *et al.*, "Polymer-based photonic toolbox: passive components, hybrid integration and polarisation control," *IET Optoelectron.*, vol. 5, no. 5, pp. 226–232, 2011.

[22] Z. Pan *et al.*, "High-Speed Modulator Based on Electro-Optic Polymer Infiltrated Subwavelength Grating Waveguide Ring Resonator," *Laser Photonics Rev.*, vol. 12, no. 6, pp. 10–15, 2018.

[23] A. M. Al-Hetar, A. B. Mohammad, A. S. M. Supa'At, and Z. A. Shamsan, "MMI-MZI polymer thermo-optic switch with a high refractive index contrast," *J. Light.*

Technol., vol. 29, no. 2, pp. 171–178, 2011.

[24] A. Skumanich and C. R. Moylan, "The vibrational overtone spectrum of a thin polymer film," *Chem. Phys. Lett.*, vol. 174, no. 2, pp. 139–144, 1990.

[25] R. Yoshimura, M. Hikita, S. Tomaru, and S. Imamura, "Low-loss polymeric optical waveguides fabricated with deuterated polyfluoromethacrylate," *J. Light. Technol.*, vol. 16, no. 6, pp. 1030–1036, 1998.

[26] H. Ma, A. K. Y. Jen, and L. R. Dalton, "Polymer-based optical waveguides: Materials, processing, and devices," *Adv. Mater.*, vol. 14, no. 19, pp. 1339–1365, 2002.

[27] M. Johnck, L. Muller, A. Neyer, and J. W. Hofstraat, "Copolymers of halogenated acrylates and methacrylates for the application in optical telecommunication : optical properties , thermal analysis and determination of unsaturation by quantitative FT-Raman and FT-IR spectroscopy," *Eur. Polym. J.*, vol. 36, pp. 1251–1264, 2000.

[28] E. Yousif and R. Haddad, "Photodegradation and photostabilization of polymers , especially polystyrene : review," pp. 1–32, 2013.

[29] A. Lucero, J.-X. Cai, and D. G. Foursa, "Long-Haul Raman/ROPA-Assisted EDFA Systems," in *OFC 2009*, 2009, pp. 1–3.

[30] J. Ding, B. Samson, and P. Ahmadi, "High-power fiber amplifiers enable leading-edge scientific applications," 2011. [Online]. Available: http://tinyurl.com/poweramplifier. [Accessed: 01-Jan-2016].

[31] C. Greverie, A. Brillet, C. N. Man, W. Chaibi, J. P. Coulon, and K. Feliksik, "High power fiber amplifier for Advanced Virgo," in *Conference on Lasers and Electro-Optics*, 2010.

[32] C. Grivas, "Optically pumped planar waveguide lasers: Part II: Gain media, laser systems, and applications," *Prog. Quantum Electron.*, vol. 45–46, pp. 3–160, 2016.

[33] I. Cisco Systems, "Cisco Global Cloud Index: Forecast and Methodology, 2016–2021," *White Pap.*, p. 46, 2018.

[34] A. Alduino and M. Paniccia, "Interconnects: Wiring electronics with light," *Nat. Photonics*, vol. 1, pp. 153–155, 2007.

[35] D. Miller, "Device Requirements for Optical Interconnects to Silicon Chips," *Proc.*

IEEE, vol. 97, no. 7, pp. 1166–1185, Jul. 2009.

[36] N. Bamiedakis, A. Hashim, J. Beals, R. V. Penty, and I. H. White, "Low-cost PCB-integrated 10-Gb/s optical transceiver built with a novel integration method," *IEEE Trans. Components, Packag. Manuf. Technol.*, vol. 3, no. 4, pp. 592–600, 2013.

[37] H. J. Yan, M. Immonen, L. X. Zhu, T. Rapala-Virtanen, P. Chen, and J. Wu, "Development of electro-optical PCBs with embedded waveguides for data center and high performance computing applications," *Opt. Interconnects XIV*, vol. 8991, no. March 2014, p. 899113, 2014.

[38] F. Horst *et al.*, "Polymer waveguides for electro-optical integration in data centers and high-performance computers," *Opt. Express*, vol. 23, no. 4, p. 4736, 2015.

[39] J. Beals, J. V. DeGroot, N. Bamiedakis, I. H. White, T. V. Clapp, and R. V. Penty, "Cost-Effective Multimode Polymer Waveguides for High-Speed On-Board Optical Interconnects," *IEEE J. Quantum Electron.*, vol. 45, no. 4, pp. 415–424, 2009.

[40] F. E. Doany *et al.*, "160 Gb/s Bidirectional Polymer-Waveguide Board-Level Optical Interconnects Using CMOS-Based Transceivers," *IEEE Trans. Adv. Packag.*, vol. 32, no. 2, pp. 345–359, 2009.

[41] N. Bamiedakis *et al.*, "56 Gb/s PAM-4 Data Transmission Over a 1 m Long Multimode Polymer Interconnect," *2015 Conf. Lasers Electro-Optics*, vol. 1, p. STu4F.5, 2015.

[42] B. J. Offrein *et al.*, "Optical Interconnects for Computing Systems and the Need for Integration," in *Frontiers in Optics 2015*, 2015, p. FW4B.1.

[43] N. Bamiedakis, A. Hashim, R. V. Penty, and I. H. White, "A 40 Gb/s optical bus for optical backplane interconnections," *J. Light. Technol.*, vol. 32, no. 8, pp. 1526–1537, 2014.

[44] J. D. B. Bradley *et al.*, "170 Gbit/s transmission in an erbium-doped waveguide amplifier on silicon," *Opt. Express*, vol. 17, no. 24, pp. 22201–22208, 2009.

[45] K. Vu, S. Farahani, and S. Madden, "980nm pumped erbium doped tellurium oxide planar rib waveguide laser and amplifier with gain in S, C and L band," *Opt. Express*, vol. 23, no. 2, p. 747, 2015.

[46] D. Brüske, S. Suntsov, C. E. Rüter, and D. Kip, "Efficient ridge waveguide amplifiers and lasers in Er-doped lithium niobate by optical grade dicing and three-

side Er and Ti in-diffusion," *Opt. Express*, vol. 25, no. 23, p. 29374, 2017.

[47] F. Ay, M. Pollnau, D. Geskus, K. Wörhoff, J. D. B. Bradley, and L. Agazzi, "Gain bandwidth of 80 nm and 2 dB/cm peak gain in Al_2O_3:Er^{3+} optical amplifiers on silicon," *J. Opt. Soc. Am. B*, vol. 27, no. 2, p. 187, 2010.

[48] S. Weinstein, Y. Luo, and T. Wang, *The Comsoc Guide to Passive Optical Networks*. 2012.

[49] S. Bindhaiq *et al.*, "Recent development on time and wavelength-division multiplexed passive optical network (TWDM-PON) for next-generation passive optical network stage 2 (NG-PON2)," *Opt. Switch. Netw.*, vol. 15, pp. 53–66, 2015.

[50] J. I. Kani *et al.*, "Next-generation PON-part I: Technology roadmap and general requirements," *IEEE Commun. Mag.*, vol. 47, no. 11, pp. 43–49, 2009.

[51] C. De Santi, L. Du, C. Lam, and J. Jiang, "Super-PON: Scale Fully Passive Optical Access Networks to Longer Reaches and to a Significantly Higher Number of Subscribers," 2018.

[52] K. B. Mogensten, J. El-Alli, A. Wolff, and J. P. Kutter, "Integration of polymer waveguides for optical detection in microfabricated chemical analysis systems," *Appl. Opt.*, vol. 42, no. 19, pp. 4072–4079, 2003.

[53] A. R. Leeds, E. R. Van Keuren, M. E. Durst, T. W. Schneider, J. F. Currie, and M. Paranjape, "Integration of microfluidic and microoptical elements using a single-mask photolithographic step," *Sensors Actuators, A Phys.*, vol. 115, no. 2–3 SPEC. ISS., pp. 571–580, 2004.

[54] D. Psaltis, S. R. Quake, and C. Yang, "Developing optofluidic technology through the fusion of microfluidics and optics," *Nature*, vol. 442, no. 7101, pp. 381–386, 2006.

[55] N. Bamiedakis, T. Hutter, R. V. Penty, I. H. White, and S. R. Elliott, "PCB-integrated optical waveguide sensors: An ammonia gas sensor," *J. Light. Technol.*, vol. 31, no. 10, pp. 1628–1635, 2013.

[56] M. C. LeMieux *et al.*, "Polymeric Nanolayers as Actuators for Ultrasensitive Themal Bimorphs," *Nano Lett.*, vol. 6, no. 4, pp. 730–734, 2006.

[57] S. M. García-Blanco, C. I. van Emmerik, J. Mu, M. de Goede, M. Dijkstra, and L. Chang, "On-chip amplifiers and lasers on the Al_2O_3 integrated photonics platform," in *Silicon Photonics XIV*, 2019, p. 10.

[58] E. S. Hosseini *et al.*, "CMOS-compatible 75 mW erbium-doped distributed feedback laser," *Opt. Lett.*, vol. 39, no. 11, pp. 3106–3109, 2014.

[59] J. I. Mackenzie *et al.*, "Er:YGG planar waveguides grown by pulsed laser deposition for LIDAR applications," in *Proc. SPIE 10082, Solid Lasers XXVI: Technology and Devices*, 2017, vol. 10082, p. 100820A.

[60] A. S. Gouveia-Neto, E. B. Da Costa, L. A. Bueno, and S. J. L. Ribeiro, "Red, green, and blue upconversion luminescence in ytterbium-sensitized praseodymium-doped lead-cadmium-germanate glass," *Opt. Mater. (Amst).*, vol. 26, no. 3, pp. 271–274, 2004.

[61] V. A. G. Rivera, F. A. Ferri, L. A. O. Nunes, and E. Marega, "White light generation via up-conversion and blue tone in $Er^{3+}/Tm^{3+}/Yb^{3+}$-doped zinc-tellurite glasses," *Opt. Mater. (Amst).*, vol. 67, pp. 25–31, 2017.

[62] A. S. Gouveia-Neto, L. A. Bueno, R. F. Do Nascimento, E. A. Da Silva, E. B. Da Costa, and V. B. Do Nascimento, "White light generation by frequency upconversion in Tm^{3+}-Ho^{3+}-Yb^{3+}-codoped fluorolead germanate glass," *Appl. Phys. Lett.*, vol. 91, no. 9, pp. 1–4, 2007.

[63] G. Krieke, A. Sarakovskis, and M. Springis, "Upconversion luminescence of a transparent glass ceramics with hexagonal $Na(Gd,Lu)F_4$ nanocrystals," *J. Alloys Compd.*, vol. 694, pp. 952–958, 2017.

[64] A. Escudero *et al.*, "Rare earth based nanostructured materials: synthesis, functionalization, properties and bioimaging and biosensing applications," *Nanophotonics*, vol. 6, no. 5, pp. 881–921, 2017.

[65] P. P. Sorokin and J. R. Lankard, "Stimulated Emission Observed from an Organic Dye, Chloro-aluminum Phthalocyanine," *IBM J. Res. Dev.*, vol. 10, no. 2, pp. 162–163, 1966.

[66] F. P. Schafer, W. Schmidt, and J. Volze, "Organic Dye Solution Laser," *Appl. Phys. Lett.*, vol. 9, no. 8, pp. 306–309, 1966.

[67] A. J. C. Kuehne and M. C. Gather, "Organic Lasers: Recent Developments on Materials, Device Geometries, and Fabrication Techniques," *Chem. Rev.*, vol. 116, no. 21, pp. 12823–12864, 2016.

[68] Z. Li and D. Psaltis, "Optofluidic dye lasers," *Microfluid. Nanafluidics*, vol. 4, no. 1, pp. 145–158, 2008.

[69] M. Casalboni, F. De Matteis, V. Merlo, P. Prosposito, and R. Russo, "1.3 μm light amplification in dye-doped hybrid sol-gel channel waveguides," *Appl. Phys. Lett.*, vol. 83, no. 3, pp. 416–418, 2003.

[70] E. K. Keshmarzi, R. N. Tait, and P. Berini, "Near infrared amplified spontaneous emission in a dye-doped polymeric waveguide for active plasmonic applications," *Opt. Express*, vol. 22, no. 10, pp. 12452–12460, 2014.

[71] W. Lu, B. Zhong, and D. Ma, "Amplified spontaneous emission and gain from optically pumped films of dye-doped polymers," *Appl. Opt.*, vol. 43, no. 26, pp. 5074–5078, 2004.

[72] E. M. Calzado, P. G. Boj, and M. A. Díaz-García, "Optimization of the laser properties of polymer films doped with N,N'-bis(3-methylphenyl)-N,N'-diphenylbenzidine," *Materials (Basel).*, vol. 2, no. 3, pp. 1288–1304, 2009.

[73] V. Navarro-Fuster *et al.*, "Amplified Spontaneous Emission in Pentathienoacene Dioxides by Direct Optical Pump and by Energy Transfer: Correlation with Photophysical Parameters," *Adv. Opt. Mater.*, vol. 1, no. 8, pp. 588–599, 2013.

[74] M. Enculescu, A. Evanghelidis, and I. Enculescu, "White-light emission of dye-doped polymer submicronic fibers produced by electrospinning," *Polymers (Basel).*, vol. 10, no. 7, 2018.

[75] R. Fukushima, M. Kamimura, K. Soga, S. Takahiro, Y. Hashimoto, and M. Yoshida, "Over-1000 nm near-infrared fluorescent biodegradable polymer nanoparticles for deep tissue in vivo imaging in the second biological window," *Polym. J.*, vol. 49, no. 12, pp. 799–803, 2017.

[76] M. C. Gather and S. H. Yun, "Bio-optimized energy transfer in densely packed fluorescent protein enables near-maximal luminescence and solid-state lasers," *Nat. Commun.*, vol. 5, pp. 1–8, 2014.

[77] V. Bulović, V. G. Kozlov, V. B. Khalfin, and S. R. Forrest, "Transform-limited, narrow-linewidth lasing action in organic semiconductor microcavities," *Science (80-.).*, vol. 279, no. 5350, pp. 553–555, 1998.

[78] M. Lehnhardt, T. Riedl, T. Weimann, and W. Kowalsky, "Impact of triplet absorption and triplet-singlet annihilation on the dynamics of optically pumped organic solid-state lasers," *Phys. Rev. B - Condens. Matter Mater. Phys.*, vol. 81, no. 16, pp. 1–5, 2010.

[79] T. Rabe *et al.*, "Quasi-continuous-wave operation of an organic thin-film distributed feedback laser," *Appl. Phys. Lett.*, vol. 89, no. 8, pp. 10–13, 2006.

[80] M. Lehnhardt, T. Riedl, U. Scherf, T. Rabe, and W. Kowalsky, "Spectrally separated optical gain and triplet absorption: Towards continuous wave lasing in organic thin film lasers," *Org. Electron. physics, Mater. Appl.*, vol. 12, no. 8, pp. 1346–1351, 2011.

[81] S. Kéna-Cohen *et al.*, "Plasmonic sinks for the selective removal of long-lived states," *ACS Nano*, vol. 5, no. 12, pp. 9958–9965, 2011.

[82] O. G. Peterson, S. A. Tuccio, and B. B. Snavely, "CW operation of an organic dye solution laser," *Appl. Phys. Lett.*, vol. 17, no. 6, pp. 245–247, 1970.

[83] A. Tagaya, Y. Koike, T. Kinoshita, E. Nihei, T. Yamamoto, and K. Sasaki, "Polymer optical fiber amplifier," *Appl. Phys. Lett.*, vol. 63, no. 7, pp. 883–884, 1993.

[84] S. Lam and M. J. Damzen, "Characterisation of solid-state dyes and their use as tunable laser amplifiers," *Appl. Phys. B*, vol. 77, no. 6, pp. 577–584, 2003.

[85] Y. Zhang and S. R. Forrest, "Existence of continuous-wave threshold for organic semiconductor lasers," *Phys. Rev. B - Condens. Matter Mater. Phys.*, vol. 84, no. 24, pp. 1–4, 2011.

[86] A. S. D. Sandanayaka *et al.*, "Quasi-Continuous-Wave Organic Thin-Film Distributed Feedback Laser," *Adv. Opt. Mater.*, vol. 4, no. 6, pp. 834–839, 2016.

[87] M. Casalboni, F. De Matteis, V. Merlo, P. Prosposito, R. Russo, and S. Schutzmann, "1.3 μm light amplification in dye-doped hybrid sol-gel channel waveguides," *Appl. Phys. Lett.*, vol. 83, no. 3, pp. 416–418, 2003.

[88] S. Yuyama, T. Nakajima, K. Yamashita, and K. Oe, "Solid state organic laser emission at 970 nm from dye-doped fluorinated-polyimide planar waveguides," *Appl. Phys. Lett.*, vol. 93, no. 2, pp. 91–94, 2008.

[89] A. E. Nikolaenko, M. Cass, F. Bourcet, D. Mohamad, and M. Roberts, "Thermally Activated Delayed Fluorescence in Polymers : A New Route toward Highly Effi cient Solution Processable OLEDs," pp. 7236–7240, 2015.

[90] R. H. Friend *et al.*, "Electroluminescence in conjugated polymers," *Nature*, vol. 397, pp. 121–128, 1999.

[91] D. Kabra, H. J. Snaith, R. H. Friend, B. Wenger, and M. H. Song, "Optically-Pumped Lasing in Hybrid Organic-Inorganic Light-Emitting Diodes," *Adv. Funct. Mater.*, vol. 19, no. 13, pp. 2130–2136, 2009.

[92] R. Xia, G. Heliotis, Y. Hou, and D. D. C. Bradley, "Fluorene-based conjugated polymer optical gain media," *Org. Electron.*, vol. 4, no. 2–3, pp. 165–177, 2003.

[93] F. Hide, M. A. Diaz-Garcia, B. J. Schwartz, M. R. Andersson, Q. Pei, and A. J. Heeger, "Semiconducting Polymers: A New Class of Solid-State Laser Materials," *Science (80-.).*, vol. 273, no. 5283, pp. 1833–1836, 1996.

[94] J. R. Lawrence, G. A. Turnbull, and I. D. W. Samuel, "Broadband optical amplifier based on a conjugated polymer," *Appl. Phys. Lett.*, vol. 30, no. 17, pp. 3036–3038, 2002.

[95] N. Liu, A. Rusackas, N. A. Montgomery, I. D. Samuel, and G. A. Turnbull, "Semiconducting polymer waveguides for endfired ultra-fast optical amplifiers," *Opt. Express*, vol. 17, no. 24, pp. 21452–21548, 2009.

[96] H. Nakanotani, T. Furukawa, and C. Adachi, "Light Amplification in an Organic Solid-State Film with the Aid of Triplet-to-Singlet Upconversion," *Adv. Opt. Mater.*, vol. 3, no. 10, pp. 1381–1388, 2015.

[97] M. Reufer *et al.*, "Low-threshold polymeric distributed feedback lasers with metallic contacts," *Appl. Phys. Lett.*, vol. 84, no. 17, pp. 3262–3264, 2004.

[98] M. D. McGhee and A. J. Heeger, "Semiconducting (Conjugated) Polymers as Materials for Solid-State Lasers," *Adv. Mater.*, vol. 12, no. 22, pp. 1655–1668, 2000.

[99] G. Heliotis, R. Xia, D. D. C. Bradley, G. A. Turnbull, and I. D. W. Samuel, "Two-dimensional distributed feedback lasers using a broadband, red polyfluorene gain medium," *J. Appl. Phys.*, vol. 96, no. 12, pp. 6959–6965, 2004.

[100] J.-M. Nunzi *et al.*, "Enhanced near-infrared electroluminescence from a neodymium complex in organic light-emitting diodes with a solution-processed exciplex host," *Appl. Phys. Lett.*, vol. 114, no. 3, p. 033301, 2019.

[101] K. Jinnai, R. Kabe, and C. Adachi, "A near-infrared organic light-emitting diode based on an Yb(III) complex synthesized by vacuum co-deposition," *Chem. Commun.*, vol. 53, no. 39, pp. 5457–5460, 2017.

[102] H. Wei, G. Yu, Z. Zhao, Z. Liu, Z. Bian, and C. Huang, "Constructing lanthanide

[Nd(iii), Er(iii) and Yb(iii)] complexes using a tridentate N,N,O-ligand for near-infrared organic light-emitting diodes," *Dalt. Trans.*, vol. 42, no. 24, pp. 8951–8960, 2013.

[103] C. Grivas and M. Pollnau, "Organic solid-state integrated amplifiers and lasers," *Laser Photonics Rev.*, vol. 6, no. 4, pp. 419–462, 2012.

[104] M. Digonnet, *Rare-Earth-Doped Fiber Lasers and Amplifiers*. New York: Marcel Dekker, Inc., 2001.

[105] S. Tanabe, "Rare-earth-doped glasses for fiber amplifiers in broadband telecommunication," *Comptes Rendus Chim.*, vol. 5, no. 12, pp. 815–824, 2002.

[106] Y. Luo *et al.*, "Energy transfer in a ternary system composed of $Tb(DBM)_3Phen$, $Eu(DBM)_3Phen$, and poly(N-vinylcarbazole)," *J. Mater. Res.*, vol. 24, no. 10, pp. 3023–3031, 2009.

[107] H. Liang *et al.*, "Optical amplification of Eu(DBM)3Phen-doped polymer optical fiber," *Opt. Lett.*, vol. 29, no. 5, pp. 477–479, 2004.

[108] J. Arrue *et al.*, "Gain in europium-chelate-doped polymer-optical-fiber amplifiers," *J. Opt. Soc. Am. B-Optical Phys.*, vol. 35, no. 11, pp. 2770–2779, 2018.

[109] P. Miluski, M. Kochanowicz, J. Zmojda, and D. Dorosz, "Properties of Eu^{3+} doped poly(methyl methacrylate) optical fiber," *Opt. Eng.*, vol. 56, no. 2, p. 027106, 2017.

[110] C. Koeppen, S. Yamada, G. Jiang, A. F. Garito, and L. R. Dalton, "Rare-earth organic complexes for amplification in polymer optical fibers and waveguides," *J. Opt. Soc. Am.*, vol. 14, no. 1, pp. 155–162, 1997.

[111] L. H. Slooff *et al.*, "Rare-earth doped polymers for planar optical amplifiers," *J. Appl. Phys.*, vol. 91, no. 7, pp. 3955–3980, 2002.

[112] F. Auzel and P. Goldner, "Towards rare-earth clustering control in doped glasses," *Opt. Mater. (Amst).*, vol. 16, no. 1–2, pp. 93–103, 2001.

[113] J. Yang, M. Pollnau, K. Wörhoff, R. M. de Ridder, E. H. Bernhardi, and J. D. B. Bradley, "Rare-earth-ion Doped Waveguide Amplifiers and Lasers in Alumina and Polymers," p. FWD1, 2013.

[114] J. Yang, M. B. J. Diemeer, C. Grivas, G. Sengo, A. Driessen, and M. Pollnau, "Steady-state lasing in a solid polymer," *Laser Phys. Lett.*, vol. 7, no. 9, pp. 650–

656, 2010.

[115] K. C. Tsang, C.-Y. Wong, and E. Y. B. Pun, "High-gain optical amplification in Eu^{3+}-doped polymer," *Opt. Lett.*, vol. 35, no. 4, p. 520, 2010.

[116] K. Yamashita *et al.*, "Amplification properties of Tb(III) green emission in polymeric waveguide doped with Tb–Al nanocluster," *J. Lumin.*, vol. 129, no. 5, pp. 526–530, 2009.

[117] M. Digonnet, *Rare-Earth-Doped Fiber Lasers and Amplifiers*, Second. New York: CRC Press, 2001.

[118] C. Jiang and Q. Zeng, "Optimization of erbium-doped waveguide amplifier," *Opt. Laser Technol.*, vol. 36, no. 2, pp. 167–171, 2004.

[119] J. Nilsson, P. Scheer, and B. Jakorzynska, "Modelling and Optimization of Short Yb^{3+}-Sensitized Er^{3+}-Doped Fiber Amplifiers," *IEEE Photonics Technol. Lett.*, vol. 6, no. 3, pp. 383–385, 1994.

[120] R. Ramaswami, K. Sivarajan, and G. Sasaki, *Optical Networks: A Practical Perspective*. Boston: Elsevier, 2010.

[121] M. Pollnau, "Rare-Earth-Ion-Doped Channel Waveguide Lasers on Silicon," *IEEE J. Sel. Top. Quantum Electron.*, vol. 21, no. 1, 2015.

[122] C. Grivas, "Optically pumped planar waveguide lasers, Part I: Fundamentals and fabrication techniques," *Prog. Quantum Electron.*, vol. 35, no. 6, pp. 159–239, 2011.

[123] R. Papannareddy, *Lightwave Communication Systems: A practical Perspective*, First. Mumbai: Penram International Publishing, 2004.

[124] P. Myslinski, D. Nguyen, and J. Chrostowski, "Effects of Concentration on the Performance of Erbium-Doped Fiber Amplifiers," *J. Light. Technol.*, vol. 15, no. 1, pp. 112–120, 1997.

[125] A. Malek, M. Aly, and K. El-Shennawy, "Erbium Doped Waveguide Amplifier Gain for Different Erbium Concentration Profiles: Effect of Chip Area and Pump Power," in *Proc. of ICCTA*, 2007.

[126] V. Prajzler, I. Huttel, O. Lyutakov, J. Oswald, V. Machovic, and V. Jarabek, "Optical Properties of PMMA Doped With Erbium(III)and Ytterbium(III) Complexes," *Polym. Eng. Sci.*, vol. 49, no. 9, pp. 1814–1817, 2009.

[127] A. Polman and F. C. J. M. van Veggel, "Broadband sensitizers for erbium-doped planar optical amplifiers: review," *J. Opt. Soc. Am. B*, vol. 21, no. 5, p. 871, 2004.

[128] C. Strohhofer and A. Polman, "Absorption and emission spectroscopy in Er^{3+}–Yb^{3+} doped aluminum oxide waveguides," *Opt. Mater. (Amst).*, vol. 21, no. 4, pp. 705–712, 2003.

[129] J. Chandrappan *et al.*, "Doping silica beyond limits with laser plasma for active photonic materials," *Opt. Mater. Express*, vol. 5, no. 12, p. 2849, 2015.

2 Review and Theoretical Analysis of Erbium Doped Waveguide Amplifiers

Efficient optical amplifiers and sources are indispensable components of any communications system. The widespread use of EDFAs in long-haul telecommunications systems has been enabled by the broad gain spectrum coinciding with the low-dispersion and low-loss region of optical. Substantial research effort has combined these advantages with the benefits of multi-component integration on a miniaturised chip. Despite the maturity of fibre-based amplifiers and systems, fabrication of practical EDWAs still remains a challenge.

The required increase in the gain per unit length resulting from the scaling of the existing erbium-based systems has exposed a number of problematic processes that have previously played an insignificant role in an amplifier's performance. A wide range of materials and designs have been put forward in order to overcome these engineering issues.

In this chapter, the material and design factors affecting performance of the EDWAs are discussed. Particular focus is placed on understanding the physical processes that reduce the achievable gain in miniaturised systems and how they can be mitigated. This is followed by consideration of techniques and methods, such as sensitisation, used to optimise the device performance. Furthermore, an analysis of optical waveguide theory to produce an effective amplifier structure is employed with particular consideration of the losses and overlap between the guided modes and active region. Finally, a review of current state-of-the art EDWAs is presented comparing various integration platforms and performance levels reported to date.

2.1 Properties and factors affecting EDWA performance

The amplifier performance is highly dependent on the spectroscopic properties of erbium ions. This not only includes possible radiative and non-radiative energy transitions, but also emission and absorption cross-sections, energy level lifetimes and upconversion mechanisms. A functional amplifier can be designed only when all the relevant factors are considered. In contrast to an EDFA, a three-level system approximation is no longer valid for high-dopant-density systems since certain undesirable processes emerge and need to be accounted for in EDWAs as outlined in this section.

2.1.1 Erbium energy levels and transitions

Rare earth ions usually have a trivalent oxidation state and atomic-like energy structure in most of the host materials. When erbium is assimilated into a solid, weakly-bound

electrons are removed, leaving a partially filled 4f shell protected by a larger radius 5s and 5p orbitals. This shielding of the inner shell results in the position of the energy levels being barely affected by the host material [1]. The localised electronic environment allows for various distinct energy transitions possible within the 4f-shell with each of the degenerate levels being Stark-split into a manifold.

The lowest seven energy levels of an erbium ion, from $^4I_{15/2}$ ground to $^4F_{7/2}$ state using Russell-Sanders notation are shown in Figure 2-1. The diagram also includes typical Er^{3+} lifetimes of these states in oxide glasses, which are later used as a benchmark for polymer systems, as well as for the most relevant radiative and non-radiative energy transitions.

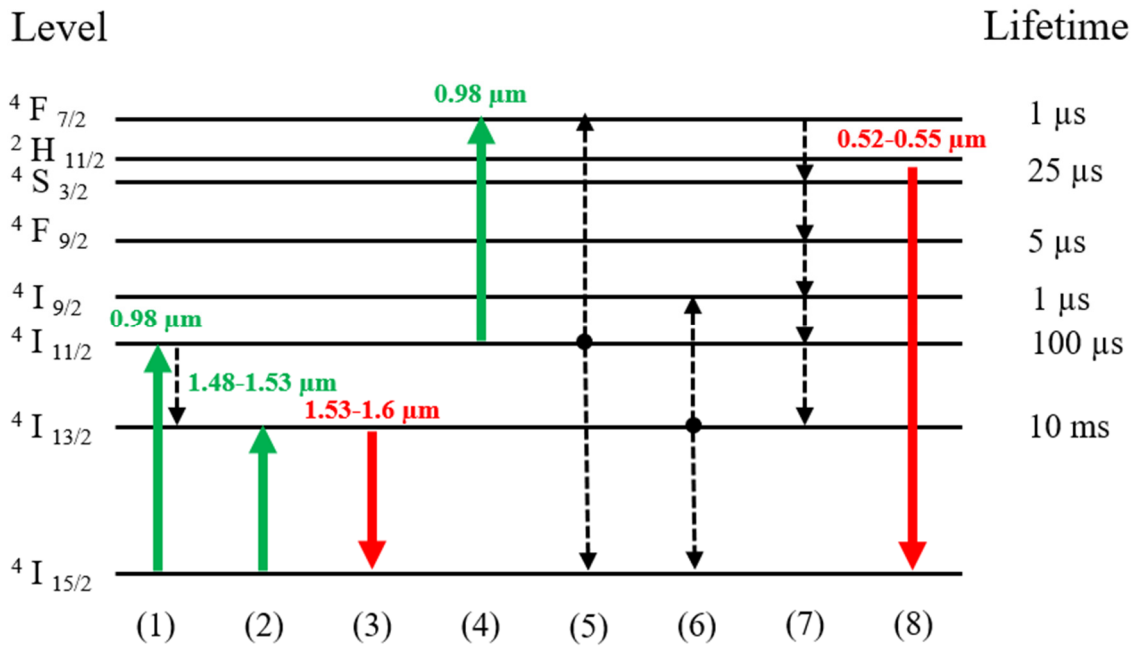

Figure 2-1: Er^{3+} energy diagram schematic with relevant transitions and typical lifetimes. Green lines show photon absorption, red emission and black non-radiative transitions.

Erbium-based amplifiers and lasers are used at wavelengths of around 1.5-1.6 µm. In order for this to be possible, the Er ions are excited from the ground $^4I_{15/2}$ to higher levels, eventually resulting in population inversion of the system. Typically pump wavelengths of either approximately 980 nm (1) or 1480 nm (2) are used leading to ground state absorption (GSA) and transitions to levels $^4I_{11/2}$ or $^4I_{13/2}$, respectively. The former is then followed by a rapid non-radiative decay $^4I_{13/2}$ to the level through multiphonon relaxation [2]. The relatively long lifetime of the level $^4I_{13/2}$ leads to the accumulation of excited ions that are available for amplification. A passing signal photon of wavelength around 1530 nm can induce a stimulated emission in the $^4I_{13/2} \rightarrow {}^4I_{15/2}$ transition (3). This transition

is also possible without an incoming signal leading to a spontaneous emission. In a similar way to the 1480 nm pump light absorption, a signal light can also be reabsorbed by an unexcited erbium ion through the $^4I_{15/2} \rightarrow {}^4I_{13/2}$ transition (2).

In addition to the absorption and emission processes occurring in the lowest three energy levels, there are a number of undesirable transitions that can occur in densely doped systems. There is a possibility for an already excited Er ion to absorb a second 980 nm photon leading to a $^4I_{11/2} \rightarrow {}^4F_{7/2}$ transition (4) referred to as excited state absorption (ESA) [3]. This is a disadvantageous phenomenon for device performance as it results in increased pump absorption while decreasing its efficiency. The processes (5) and (6) depict energy transfer upconversion (ETU). These two transitions require interaction between two neighbouring ions where one of them acts as a donor and passes the energy to the acceptor. As a result, the donor is de-excited back to the ground state $^4I_{15/2}$ while the acceptor is promoted to either $^4F_{7/2}$ (5) or $^4I_{9/2}$ (6). In both cases the upconversion process is detrimental to the device operation as it reduces the number of ions available for stimulated emission [4].

In the case of an ion excited above the $^4I_{11/2}$ level, a number of non-radiative transitions are required for the ion to revert back to the useful $^4I_{13/2}$ state (7). These transitions release energy in the form of phonons and are generally relatively fast leading to the Er ion eventually returning to the radiative emission level. However, there is also a probability of spontaneous emission taking place, which is inversely proportional to the lifetime of a given manifold. In addition to already described $^4I_{13/2} \rightarrow {}^4I_{15/2}$ transfer, the transition from $^2H_{11/2}$ and $^4S_{3/2}$ to the ground state is also shown (8) as it leads to characteristic green light emitted by highly doped devices [5].

2.1.2 Emission and absorption cross-sections

The typical photon absorption and emission transitions described in the previous section are linked to a given cross section. The absorption cross-section ($\boldsymbol{\sigma_a}$) describes the probability of an unexcited ion being promoted to a higher energy level through the absorption of either the pump or signal light. On the other hand, the emission cross-section ($\boldsymbol{\sigma_e}$) determines the likelihood of an erbium ion emitting a photon. These quantities depend on the system's host material and are usually quoted in units of cm^2 and typical values for most materials are in the 10^{-21} order of magnitude [6]. The absorption cross-section can be calculated by measuring the loss in light intensity travelling through a given medium and using the Beer-Lambert formula.

$$\sigma_a(\lambda) = \frac{\alpha(\lambda)}{N} \tag{2.1}$$

where $\alpha(\lambda)$ is the absorption at a given wavelength (cm^{-1}) and N is the total ion concentration (cm^{-3}). In an ideal 'loss-less' case, where no other loss mechanisms are present, or all the other loss mechanisms have been accounted for and subtracted from the total, the absorption can be determined using the formula below.

$$\alpha(\lambda) = {-ln\left(\frac{I(\lambda)}{I_0(\lambda)}\right)}\Big/{L} \tag{2.2}$$

where I and I_0 are the light intensity measured after length L and incident on the sample, respectively. The emission cross-section can be estimated from the emission spectrum using the Füchtbauer-Ladenburg method [7] which states that:

$$\sigma_e(\lambda) = \frac{\lambda_{e,peak}^4 I_e(\lambda)}{8\pi c n^2 \tau \int I_e(\lambda) d\lambda} \tag{2.3}$$

Here, $\lambda_{e,peak}$ is the wavelength at the emission peak, τ is the lifetime of the metastable level, n is the refractive index of the material, c is the velocity of light and $I_e(\lambda)$ is the fluorescence spectrum. Furthermore, the theory developed by McCumber [8] enabled a straightforward procedure to determine the link between the two cross-sections, and this theory has since been confirmed experimentally for many Er-doped systems [9].

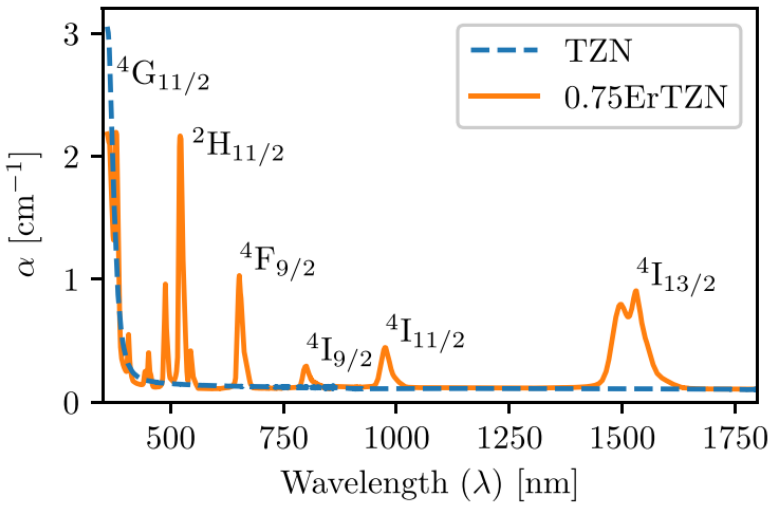

Figure 2-2: Absorption spectra of Er-doped TZN glass showing selected intra-ion transitions [10]

The absorption and emission spectra of an erbium-doped system have a number of peaks corresponding to the energies of different electronic transitions occurring inside the ion. An example based on zinc-sodium tellurite (TZN) glass can be found in Figure 2-2 where

certain energy levels can be observed as absorbance peaks and, therefore, as wavelengths of the increased absorption cross-section.

In a simple system, where both the populations of ground (N_1) and excited (N_2) states as well as the corresponding cross-sections are known, the internal gain is given by:

$$G_{dB}(\lambda) = 10\, log_{10}(\sigma_e(\lambda)N_2 - \sigma_a(\lambda)N_1)L \tag{2.4}$$

The above relationship highlights the importance of high cross-sections, particularly of the $^4I_{13/2}$ level, needed for effective amplification. While this formula can be used to estimate the gain potential in a given system, a more complex model is required that takes into account other transitions, such as upconversion.

2.1.3 Lifetime

Every energy level has a certain lifetime associated with it. This time constant indicates the decay rate from that level in the absence of the stimulated emission. In an ideal case, with no detrimental energy transfer processes present, the luminescent decay in time is represented by a single exponential curve. However, in a host material with defects, several pathways exist for population decay, which can be divided into radiative and non-radiative such as vibrations of the host material. The decay probability per unit time, which is inversely proportional to the lifetime, is a sum of the individual probabilities of those transition channels and the total lifetime of a given energy level is given by:

$$\frac{1}{\tau_i} = \frac{1}{\tau_{r,i}} + \frac{1}{\tau_{nr,i}} \tag{2.5}$$

where τ_i is the total, $\tau_{r,i}$ radiative and $\tau_{nr,i}$ non-radiative lifetime of a given energy level respectively. Using this fact, the rate of spontaneous emission from an energy level in an Er-doped system is given by the number of ions divided by the total lifetime.

Non-radiative decay between two states takes place via an energy transfer to the host material through the generation of a number of phonons. This multiphonon relaxation has a total energy equal to that of the difference between the two levels and its probability is inversely proportional to the number of phonons required to cover this gap. Even though the phonon energy varies between different host materials affecting higher energy levels in erbium ion, the lifetime of the $^4I_{13/2}$ state remains relatively long due to the large number required for the $^4I_{13/2} \rightarrow {}^4I_{15/2}$ transition [11].

The long lifetime of the second level allows for a build-up of population inversion in the system required for gain in Er-based systems. In the most common host materials used

for EDWAs, luminescent lifetimes of approximately 10 ms have been demonstrated, including 8.1 ms in phosphate glass [12], 8 ms in Al_2O_3 [13] and 14 ms in TZN [14]. However, the lifetime depends not only on the material but also on the erbium ion density and accompanying energy transfers between ions.

2.1.4 Ion Concentration

The main difference between the EDFA and the EDWA is the scale of the device. While a typical fibre amplifier is metres to tens of metres long [15], miniaturised waveguide-based systems require it to be in the range of a few centimetres long. In a fibre-based device, a typical Er concentration is set to around 10^{18} cm^{-3} [16] as increasing beyond that point results in reduced efficiency of the device [17]. However, to achieve a similar net gain in the EDWA device, a much higher Erbium concentration is required.

Doping a host material with a great number of ions results in reduced spacing between introduced dopants. This leads to solubility issues when dopant ions start to cluster together as well as undesirable interactions such as energy exchanges between ions [18]–[20]. The outcome of these processes is reduced efficiency and, therefore, diminished gain of the amplifier device. In an ideal scenario, with no inter-ion interactions as shown in the simplified Equation (2.4), a better gain in a compact device could be achieved through increasing the Er concentration and the number of inverted erbium ions in the system.

Table 2-1: Reported erbium concentrations for various host materials

Host material	**Er concentration [$\times 10^{20}$ cm^{-3}]**	**Reference**
Aluminium oxide (Al_2O_3)	0.27-4.2	[21]
Phosphate glass	5.3	[22]
Tellurite glass (TZN) in silica	16.3	[23]
Soda-lime silicate glass	0.6-1.2	[24]
Fluorazirconate glass (ZBLAN)	0.4-14	[25]
Potassium double tungstate ($KY(WO_4)_2$)	6.36	[26]
Lithium niobate ($LiNbO_3$)	2.0	[27]
$NaYF_4$ nanocrystals in SU-8 polymer	2.8	[28]

However, with this proving difficult in a silica glass a number of alternative host materials with improved solubility have been explored. Some of the highest reported values to date are listed in Table 2-1 showing attempts at using different systems as well as glass modifiers such as aluminium or phosphate in order to reach higher Er concentrations. Even with the improved materials with reduced quenching used in these highly doped systems, undesirable energy transfers are still present and need to be taken into account when designing an amplifier.

2.1.5 Energy Transfers

Since EDWAs require very high dopant concentrations to achieve high gain over short propagation distances, they need to overcome gain quenching. The processes responsible for the deterioration of the device efficiency through energy transfer can be divided into a number of categories. The three most common quenching mechanisms encountered in erbium-doped systems are: energy transfer upconversion (ETU), excited state absorption (ESA) and energy migration (EM) as shown in Figure 2-3.

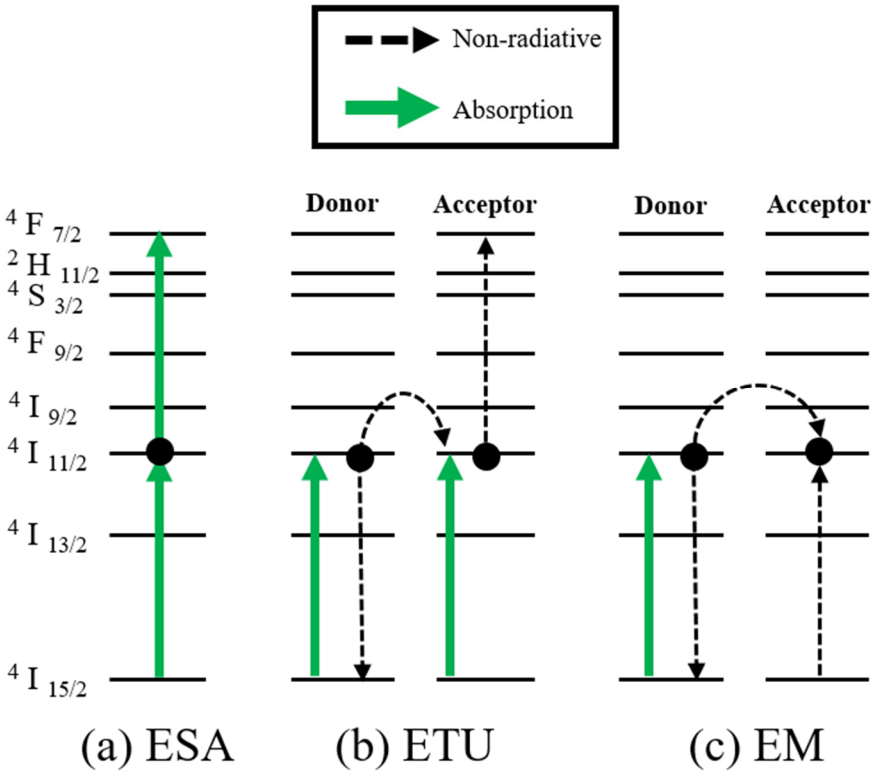

Figure 2-3: Selected erbium energy transfer processes based on 980 nm pumping

2.1.5.1 Energy Transfer Upconversion

The most common energy transfer process limiting the performance of high concentration rare-earth-doped devices is ETU [29]. This process, also referred to as co-operative

upconversion (CUC), takes place when two neighbouring ions that are already in the excited state interact with one another. In this scenario one ion, the donor, transfers energy non-radiatively to the second, the acceptor. Therefore, the first ion becomes de-excited and moves back to the ground state while the second is promoted to a higher energy level. In Figure 2-3 (b) the process is depicted for one of the possible pathways where the acceptor ion is promoted to the $^4F_{7/2}$ state as a result of 980 nm pumping. However, the same process applies to a 1480 nm excitation with the difference that the acceptor ion is excited from level $^4I_{13/2}$ to $^4I_{9/2}$. Once an erbium element is exited to a higher energy level it undergoes a number of multi-phonon transitions back to the metastable level $^4I_{13/2}$ or occasionally emits spontaneously from one of the higher energy levels as explained in section 2.1.1.

There have been extensive studies of the underlying structural factors leading to CUC inside of the host material [30]–[32]. In general, two underlying phenomena contributing to upconversion process have been identified as shown in Figure 2-4. Homogenous upconversion (HUC) is the result of the high concentrations reducing the spacing between erbium ions that in turn enables energy transfer between neighbouring ions. This process occurs even in a system where the dopant ions are separated by more than their diameter. However, when the distance becomes smaller, leading to the formation of clusters, the dopant distribution is no longer uniform. In this case, usually pairs of erbium ions interact with one another resulting in pair induced quenching (PIQ). While the first process occurs even at relatively lower Er concentrations, the latter becomes dominant at high concentrations [33].

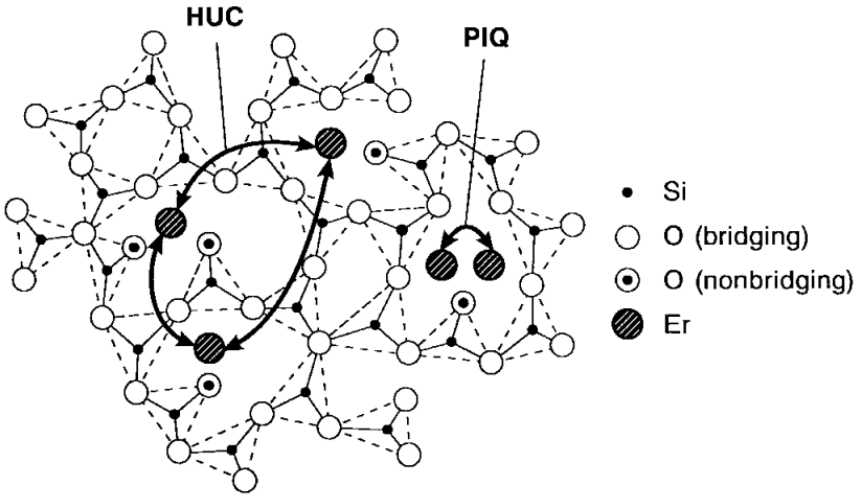

Figure 2-4: Two dimensional model of Er-doped silica glass structure with illustrated HUC and PIQ processes [34]

The ETU process in EDWAs has a significant impact on performance as it de-populates the $^4I_{13/2}$ level, thus reducing the population inversion of the system. In addition, this can also result in significant heat dissipation in the host material due to multiphonon relaxations taking place when an Er ion is undergoing non-radiative transitions [35].

Table 2-2: ETU coefficient measured in various Er-doped materials

Host material	Er concentration [$\times 10^{20}$ cm^{-3}]	ETU coefficient [$\times 10^{-18}$ cm^{3}s^{-1}]	Reference
Aluminium oxide	0.27-4.22	0.7-7.8	[36]
Phosphate glass	2.0-4.0	0.8-1.1	[37]
Soda-lime silicate glass	1.4	3.2 ± 0.8	[24]
Tellurite glass	3.4	2.74	[38]
Fluorazirconate glass (ZBLAN)	2-14	13-67	[25]
$LiYF_4$ crystals	6.9	17	[25]

The energy transfer upconversion limits the maximum concentration of the dopant ions that can be efficiently introduced to the host material. Once the optimum point is exceeded, the CUC process reduces the gain of the device due to concentration quenching [39], [40]. This behaviour can be modelled through the introduction of a material-dependent upconversion rate which is proportional to the square of the population density of the energy level on which it occurs [41]. The ETU coefficient varies depending on the material and some experimentally derived values for level $^4I_{13/2}$ and corresponding Er concentrations are shown in Table 2-2.

2.1.5.2 Excited State Absorption

The process of excited state absorption shown in Figure 2-3 (a) does not involve an energy transfer between different ions, but it is involved in upconversion and leads to efficiency reduction of the EDWA. In this case, a single Er ion that has previously been excited to $^4I_{11/2}$ level absorbs a second pump photon resulting in a second transition to $^4F_{7/2}$ state. As with ETU, this can also occur through a $^4I_{15/2} \rightarrow {}^4I_{13/2} \rightarrow {}^4I_{9/2}$ double absorption of a 1480 nm light. In these two most common scenarios a single ion absorbs two photons; however, multistep processes leading to even higher excited state absorptions are also possible [42].

Similar to transfer upconversion, the ion then undergoes multiple non-radiative decays back to the metastable level or is emitted as a high energy photon in the visible spectrum. In either case, the outcome is a reduced population available for amplification at the $^4I_{13/2}$ level and the reduced efficiency of the system due to energy loss.

Even though ESA has been shown to have less impact at the typical pumping wavelengths of 980/1480 nm than at shorter wavelengths such as 800 nm [43], its contribution to upconversion cannot be ignored. It becomes more problematic in materials with longer lifetimes at higher energy levels as it leads to population increases in these states. Furthermore, in miniaturised systems such as EDWAs, where higher pumping densities are required, this mechanism has been shown to cause a signal loss [44].

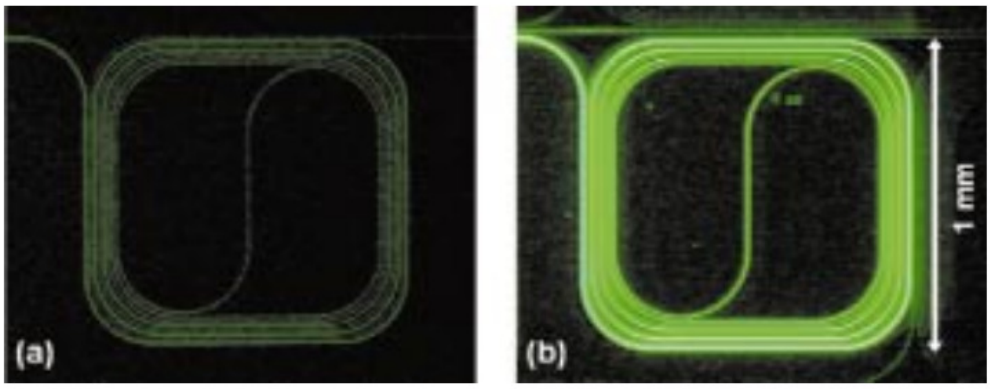

Figure 2-5: Al_2O_3 EDWAs with similar Er-content fabricated using (a) ion implantation and (b) co-sputtering and operated under same conditions [39]

The upconversion arising in the erbium system due to both energy transfer and excited state absorption is dependent on many factors such as lifetimes, cross-sections and phonon energies of the host. This process is dependent on the material, but also on the fabrication technique employed. Figure 2-5 shows aluminium oxide devices with either 0.28% Er ion implanted into Al_2O_3 or 0.31% Er co-sputtered with Al_2O_3. When operated under exactly the same conditions, a co-sputtered device was shown to emit much stronger green light while having a lower gain at 1530 nm [39]. This difference was attributed to a more homogenous erbium distribution leading to a reduced upconversion.

It is worth noting that in compact EDWAs that have high dopant concentrations and are pumped at high energy densities, some degree of upconversion and accompanying green light emission is expected. In the most common communications applications, the effort is placed on minimising the 530-570 nm emission as this reduces the device efficiency, but as described in Chapter 1 there is also an interest in maximising clustering for infrared-to-visible upconverters.

2.1.5.3 Energy Migration

The process depicted in Figure 2-3 (c) shows energy migration where an excited ion (donor) transfers energy to a neighbouring ion that is in the ground state (acceptor). As a result, the donor becomes de-excited back to the ground state while the acceptor is promoted to the state previously occupied by the first ion. Even though the population of the $^4I_{13/2}$ level is not affected through that resonant interaction between erbium ions, the process can occur between multiple neighbouring dopants until eventually the excitation is lost. This usually occurs through multiple energy-migration steps once a quenching centre such as OH- group impurity is met [45].

2.1.6 Pumping mechanisms and sensitisation

In a typical setup, erbium-doped systems are optically pumped using either 980 nm or 1480 nm light in order to excite the Er ion through ground state absorption onto $^4I_{11/2}$ or $^4I_{13/2}$ level, respectively. Both of these methods can be seen as three-level systems, where in case of the in-band pumping at 1480 nm, the process takes advantage of energy level splitting. The advantages of using direct $^4I_{13/2}$ pumping are a good modal overlap between the pump and signal, lower scattering losses and a higher absorption cross section of erbium at longer wavelengths compared to $^4I_{11/2}$ as shown in Figure 2-6. However, using 980 nm takes advantage of an almost complete lack of stimulated emission occurring as a result of this energy level leading to higher population inversion and, therefore, lower noise in the system. These advantages have been confirmed experimentally as the preferred pumping scheme for long-haul EDFAs [46].

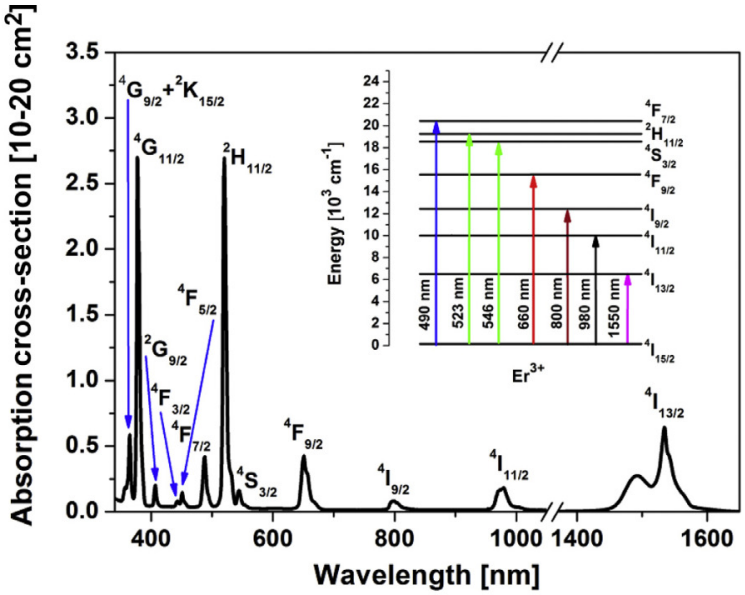

Figure 2-6: Erbium absorption cross-section when doped in phosphate glass [47]

However, in the case of compact devices, where efficiency is a key factor, absorption cross-sections of both energy levels are relatively weak, leading to low absorbance of pump power. In order to improve the gain of the device, various sensitizers have been proposed. The most widely used is co-doping erbium with ytterbium [48]–[51], but other methods such as silicon nanocrystals (Si NC's) [52]–[54] or organic cage complexes [55] have been put forward.

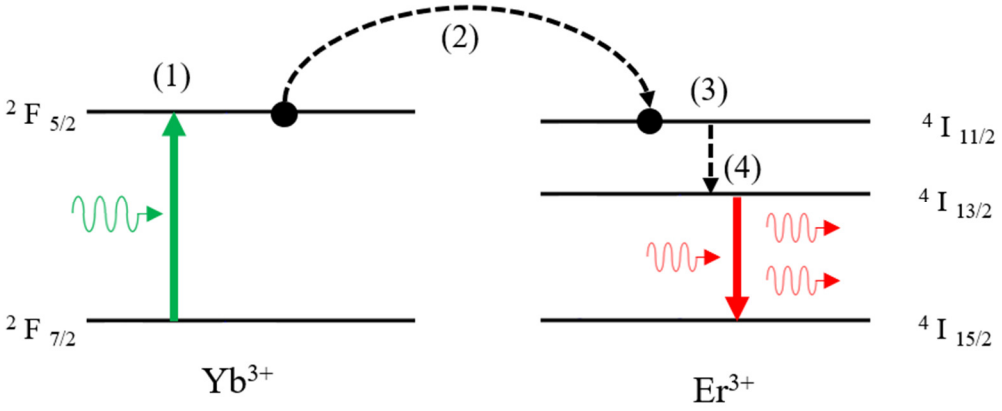

Figure 2-7: Energy processes involved in Er-Yb sensitisation

Yb offers an alternative absorption path from its $^2F_{7/2}$ to $^2F_{5/2}$ level which also corresponds to absorption around 980 nm. When a host material is co-doped with both erbium and ytterbium, the latter absorbs an incoming pump photon and then transfers it to neighbouring Er ions through the energy migration process described in the previous section. This process is detailed in Figure 2-7 where the Yb ion first absorbs a pump photon (1) through $^2F_{7/2} \rightarrow {}^2F_{5/2}$ transition and then transfers the energy onto the neighbouring Er ion via $^4I_{11/2}$ excitation (2). This is then followed by a non-radiative decay to $^4I_{13/2}$ and finally stimulated emission in the 1.5-1.6 µm range. Alternatively, the excited Yb ion can reemit a photon around 980 nm or a back-transfer from erbium to the ytterbium ion is possible, though unlikely due to the short multiphonon relaxation time of the $^4I_{13/2}$ level [56].

The benefit of the ytterbium ions' inclusion in the dopant mix in terms of absorption cross-section has been shown in phosphate glass where co-doping has led to a 7.6-fold increase in pump light absorption as shown in Figure 2-8. Additional advantages of using this co-dopant are the fact that it does not reabsorb the 1550 nm signal, but also has very similar ionic properties leading to an opportunity for co-doping with comparable or even higher concentrations than erbium in order to increase the device efficiency [57].

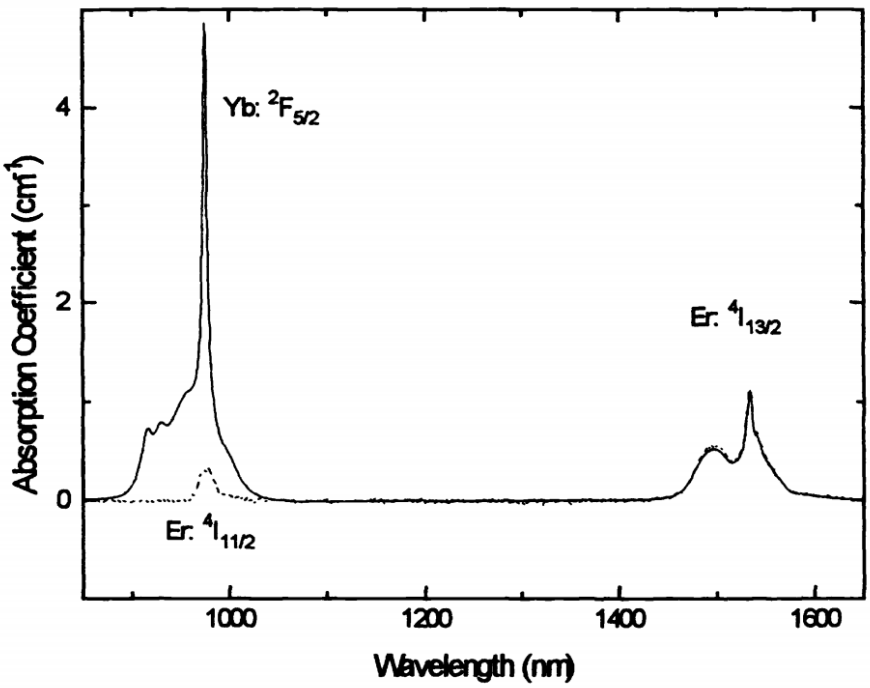

Figure 2-8: Absorption spectra of phosphate glass with 1.9 x 10^{20} cm^{-3} Er (dashed line) and 1.9/3.7 x 10^{20} Er/Yb cm^{-3} (solid line) [58]

A carefully designed system that takes advantage of Er-Yb co-doping offers a possibility for higher overall gain. Adding ytterbium ions effectively add another erbium excitation mechanism that in a highly pumped system competes with Er-Er energy transfer upconversion [59]. As a result, Yb ions act not only as sensitizers for EDWAs, but also help to reduce the concentration quenching effects and achieve higher gain per unit length through increased dopant density.

2.2 Material losses

In order for an erbium-doped system to produce gain, the stimulated emission must be greater than absorption. When an EDWA is unexcited the Er ions absorb the signal photons and reduce the signal intensity. That changes when the pump is turned on and population inversion is achieved resulting in emission becoming greater than absorption. In an ideal system, no other sources of losses would be present, but in practice a number of additional mechanisms contribute to the signal degeneration. Some of those losses depend on the device fabrication, for example scattering on a rough waveguide surface, but some are related to the host material itself.

Sources of losses in bulk materials include the intrinsic absorption of the material as well as absorption and scattering arising from the impurities. Those material losses intrinsically depend on the host chosen for device implementation and are required to be

kept as low as possible. Otherwise, any additional passive (non-erbium related) source of loss needs to be compensated for by generating higher gain from the erbium ions. In general, background losses should be kept under 1 dB/cm for efficient systems, but much lower values have been reported for phosphate glass – 0.4 dB/cm [60], aluminium oxide – 0.14 dB/cm [61] or lithium niobate – 0.1 dB/cm [62]. In order to create efficient EDWAs, it is important for the host material to have low background losses at both signal and pump wavelengths.

There are different terms that have been coined to describe gain in an amplifier system. Signal enhancement, sometimes referred as relative gain, describes the change in the output signal with and without pump excitation. Internal gain takes into account the background losses in the waveguide and refers to the difference between input and output powers. Finally, net gain expands on the on-chip (internal) gain by also considering external factors such as coupling losses.

2.3 The state of the art in EDWA

The need for a compact EDWA device has led to remarkable research activity to satisfy the predicted application needs using a variety of materials and systems. There are a range of parameters that need to be taken into account when an erbium-doped amplifier is designed. These need to be carefully controlled in order to maximise the gain for a given system. Minimising pump power and the device footprint, while ensuring a broadband operation, are key criteria that need to be met for future communications systems. Even though the exact specifications and performance depend on numerous design factors, a great number of parameters are determined by the host material used.

Many Er-doped devices have been put forward and fabricated using various techniques with some of the most promising attempts presented in Table 2-3. These devices have been proven to provide internal gain while promising compatibility with existing platforms such as silicon. The listed devices are compared in terms of not only the achieved internal gain at a peak wavelength, but also in terms of the Er/Yb concentrations, amplifier length and pumping scheme employed. In summary, pumping around 980 nm is assumed unless specified otherwise.

Table 2-3: Comparison of internal gain and operating conditions for EDWAs in different host materials

Host	Er/Yb conc. [$\times 10^{20}$ cm^{-3} or as quoted]	Length [cm]	Pump power [mW]	Peak internal gain [dB/cm]	Ref.
Phosphate glass	Er – 2.3 wt.% Yb – 3.6 wt.%	3.1	460	5.3	[60]
Aluminium oxide	Er – 2.12	2.1	80	2.0	[61]
Potassium double tungstate	Er – 1.9	0.68	600	7.95	[63]
Tantalum pentoxide	Er – 2.7	2.3	20	2.1	[64]
Soda-lime silicate glass	Er – 1.46 wt.%	4.5	280	3.3	[65]
PbO-GeO_2 glass	Er – 0.33 Yb – 20	1.0	100	6.0	[66]
Lithium niobate ($LiNbO_3$)	Not reported	4.6	200 (1486 nm)	3.0	[67]
Tellurium dioxide (TeO_2)	Er – 2.2	5.0	171	3.0	[68]
$NaYF_4$ in SU8 polymer	6.0 vol.%	1.2	80	6.6	[69]
$NaLuF_4$ in PMMA polymer	Er – 2.8 Yb – 28	1.3	400	11.6	[70]

2.3.1 Glasses

The limit of the solubility of Er ions and resulting gain quenching in silica glass have been initially addressed through introducing aluminium and phosphate into the mix leading to compact devices with a gain of up to 1.1 dB/cm [71]. Other glasses have been intensively researched as potential RE hosts due to their advantageous properties such as long luminescence lifetimes and increased erbium solubility [71]. The most promising amplifier candidates based on internal gain reported so far are listed in Table 2-3, but the losses have been overcome to a lesser degree in other types such as bismuthate [72], borosilicate [73] and fluoride [74] as well.

Phosphate glass has proven to be a particularly good host material with a number of reports demonstrating an internal gain of over 3 dB/cm around 1535 nm [75]–[77]. The highest reported signal enhancements in this host took advantage of both Yb co-doping as well as bi-pumping to ensure uniform population inversion along the device [60]. In another attempt, a very short, 3-mm-long, device with high doping concentrations (8 wt.% Er and 12 wt.% Yb) was fabricated through Ag-Na ion exchange and pumped at 150 mW to generate a net gain of 4.1 dB [57].

An extremely high ytterbium concentration was also used in PbO-GeO_2 glass where a 80-µm-wide pedestal structure delivered 6 dB of gain [66]. The benefit of very high Yb-co-doping resulted in a very efficient device that required only 100 mW of pump power to produce high signal enhancement. An alternative approach to reduce the energy requirements for a compact device has been to reduce the dimensions of the waveguide. This approach was demonstrated in a tantalum pentoxide (Ta_2O_5) where a waveguide with 5.2 μm^2 cross-section required only 20 mW to generate 2.8 dB gain over a 2.3-cm-long device [78].

Tellurite-based glasses have been actively investigated as RE hosts for a number of years due to their favourable material properties such as low material loss and high erbium solubility. This has culminated in the demonstration of waveguide amplifiers with a net gain over 140 nm bandwidth peaking with 15 dB at 1535 nm over a 5-centimetre-long waveguide [68]. The promising performance of the pure TeO_2-based system has led to investigation of the impact of adding different elements to the mix, such as gallium, tungsten or germanium [79]. Some promising spectroscopic properties when doped with erbium and early work towards EDWAs have been reported in tellurite modified with germanium-niobate [80] as well as a gain of 2.1 dB/cm at 1532 nm when the glass mix includes both zinc and magnesium [81].

A particularly attractive combination was obtained using zinc-sodium tellurite (TZN) glass doped with Er ions and incorporated into silica substrates through ultrafast laser plasma implantation (ULPI) [14]. This method has enabled the achievements of high erbium concentration without significant clustering confirmed by a record high lifetime-density product of 0.96×10^{19} $s.cm^{-3}$ [82]. Even though no EDWA device has been demonstrated with this material, homogenous thin films with a very high Er concentration of 1.63×10^{21} cm^{-3} and a long lifetime of 9.1 ms have been reported [83].

2.3.2 Aluminium Oxide

Another attractive material for erbium doping is aluminium oxide (Al_2O_3) as it offers the possibility of compact devices that are suitable for silicon integration based on the silicon-on-insulator (SOI) platform in Figure 2-9. This host has been actively used since the 1990s when the first promising devices were fabricated. A 4-cm-long amplifier occupying only 1 mm^2 of chip area providing a net gain of 2.3 dB when pumped at 9 mW and transparency power of 3 mW has been achieved in a small, $0.6 \times 2\ \mu m^2$ waveguide [84].

More recently a net gain over 80 nm bandwidth with a peak enhancement of 4.2 dB over 2.1 centimetres at 1533 nm as well as extremely low threshold pump power of 7 mW has been demonstrated [61]. Furthermore, a long lifetime of the excited state in such a system has provided low noise and cross-talk required for wavelength-division-multiplexed (WDM) transmission and allowed transmission rates of up to 170 Gbit/s [85]. The Al_2O_3-based systems have been shown to scale well and amplifiers of up to 24.5-cm-long generating over 20 dB net gain have been fabricated [86]. In this case, a low chip footprint was achieved through a compact spiral structure due to a relatively high refractive index contrast between the waveguide and the cladding.

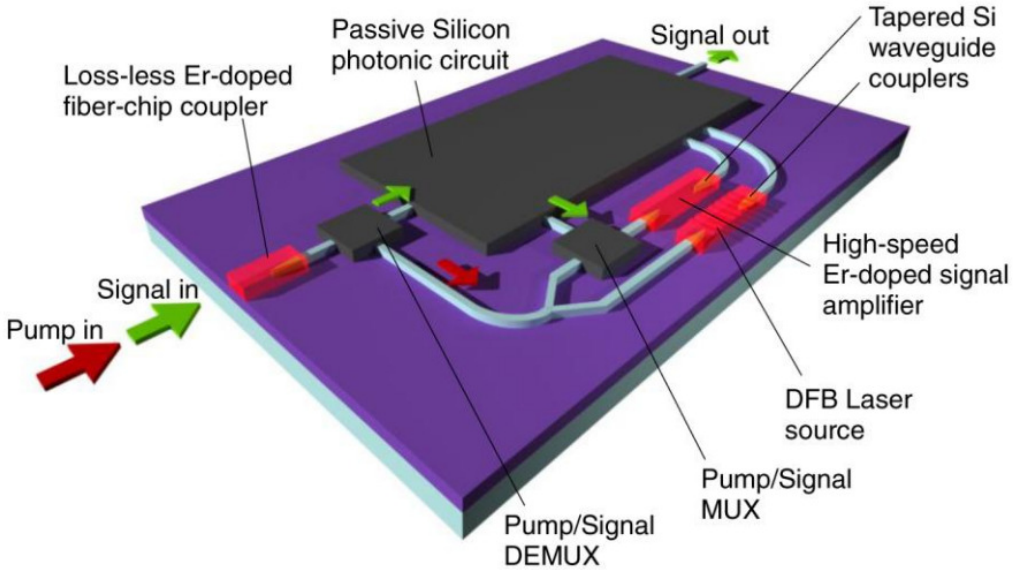

Figure 2-9: Schematic of a potential active component integration for SOI platform [87]

Even though an aluminium oxide host does not have the highest gain per unit length among the discussed hosts, it has proven to be enough to support CW lasing for a number of RE dopants [88]. For Er-based systems this has been achieved in a number of ways

including ring-resonators [89], the distributed Bragg reflector (DBR) [90] and distributed feedback (DFB) [91]. Despite all the progress reported on Er-doped Al_2O_3, the main factor limiting the gain per unit length in these systems with regard to the currently used fabrication methods is energy transfer upconversion [92]. However, there has been a recent progress in using atomic layer deposition (ALD) in order to fabricate highly-controlled micro-scale devices with the potential to achieve up to 20 dB/cm modal gain in sub-millimetre-long amplifiers [93].

2.3.3 Double tungstates

An alternative host that has been recently reported is potassium double tungstate. This crystalline matrix has been demonstrated to have broad-band emission, cross-sections that are 4 times as large compared to aluminium oxide and the ability to host Er concentrations of as high as 6.36×10^{20} cm^{-3} with relatively low ETU [94]. Early characterisation and simulations of $KY(WO_4)_2$-based amplifiers predicted extremely high gain of up to 40 dB over a 3-cm-long device due to high Er doping of 3.81×10^{20} cm^{-3} and very low propagation loss of 0.2 dB/cm [95].

Short, sub-centimetre devices have been reported with a measured gain of 12.1 dB/cm in 750-µm-long amplifiers and a slightly lower figure of 7.95 dB/cm for 6.75-mm-long structures [63]. A relatively low refractive index contrast of $\sim 1.2 \times 10^{-2}$ using this material as the Er host enabled the fabrication of relatively large devices with cross-sectional areas in the range of 50 μm^2. However, the large area and no Yb co-doping meant that not only was up to 256 mW of pump power required to reach the gain threshold but also 600 mW were needed to achieve the reported net gains.

2.3.4 Polymers

Polymers have been considered an attractive candidate for photonic integration despite difficulties with incorporating inorganic, rare-earth elements into these systems. The initial attempts to overcome the problems with dissolving erbium in organic host were made using polydentate cage complexes [96] or embedding the materials in silica before adding them into polymer systems [97]. Early promise was shown by using hydrophobic sol-gel materials, achieving signal enhancement of 0.8 dB/cm in a 7-mm-long waveguide [98] and then 1.8 dB/cm in a 1.3-cm-long ridge [99].

An alternative approach to solution processing has led to the demonstration of gain inside polymer-based EDWAs. A Er/Yb co-doped multimode structure was recently reported

with 7.2 dB/cm signal enhancement at 1533 nm [100], which was then further optimised to generate 16.5 dB over 2-cm-long structure pumped with 180 mW [101]. This approach has resulted in amplifiers with an internal gain not only in a SU8 host, but also 5.4 dB/cm in PMMA [102] and 7.2 dB/cm in a 0.5-cm-long copolymer mix device [103].

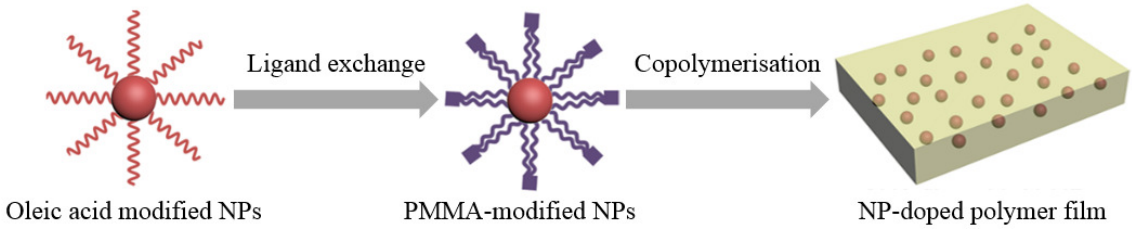

Figure 2-10: Fabrication workflow for a core-shell polymer structure after [69]

Increasingly popular techniques of introducing nanocrystals and nanoparticles (NPs) into a polymer host through an additional layer of coating have been developed [104] as shown in Figure 2-10. Even though initial attempts resulted in a very low gain per unit length [105], [106], new promising and optimised nanocrystals, such as $NaYF_4$ [107] or LaF_3 [108] were synthesised. More recently, auspicious devices have been demonstrated with various combinations of polymer hosts, NP compositions and linking components.

In 2015 an optical gain of 7.6 dB over a 15-mm-long PMMA-based waveguide was reported [109]. This was enabled by preparing a covalent-linking nanocomposite through copolymerisation of high concentration of oleic-acid-modified $NaYF_4$: Er^{3+}, Yb^{3+} NPs. A very similar process was used to combine SU8 polymer with n $BaYF_5$: 20%Yb^{3+}, 2% Er^{3+} leading to an optical gain of 10.4 dB over 1.1-cm-long waveguide when pumped with 212 mW [110]. This research area culminated in the highest reported gain of 11.6 dB/cm that was achieved in a rib waveguide using $NaYF_4$/$NaLuF_4$: 20%Yb^{3+}, 2%Er^{3+} in similar covalent-linking core-shell structures excited with a 400 mW laser at 980 nm [70]. One of the main complications with such a system was efficiency and sustainability when operated under hundreds of milliwatts of the pump power. This has recently been addressed through an EDWA demonstration with a gain of 6.6 dB/cm pumped with only 80 mW [69]. In order to improve performance, progress has been made by introducing cerium (Ce^{3+}) into the crystal structure to limit the upconversion effects [111], by reducing the size of the NPs in the polymer mix or by introducing new crystal structure types [112].

2.4 Conclusions

In this chapter, the properties of erbium ions are discussed together with a description of factors affecting the performance based on the host material. The key parameters for an efficient EDWA device are presented with particular focus on the gain-limiting upconversion processes, namely energy transfer upconversion and excited state absorption. The commonly used method of ytterbium sensitisation is introduced with an explanation of the resulting shift from in-band pumping at 1480 nm towards more efficient 980 nm scheme.

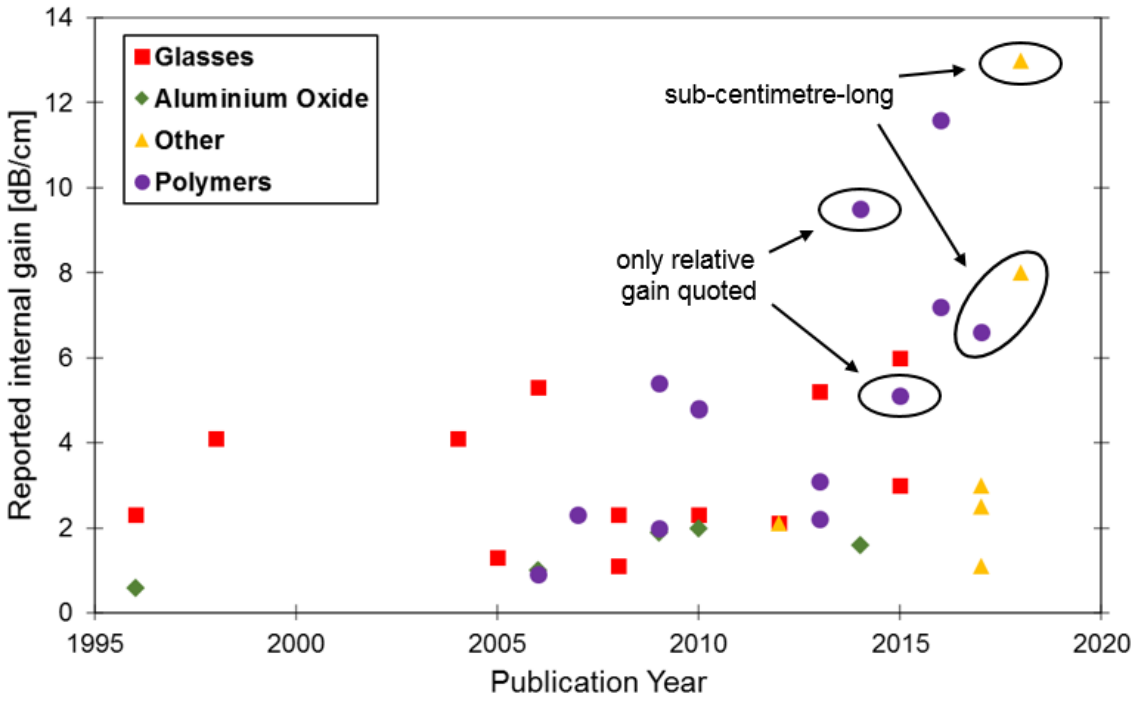

Figure 2-11: Summary of EDWA devices quoted in this chapter based on the year of publication

A review of current state-of-the-art EDWA systems is presented comparing amplifier performance achieved with different host materials. Great progress has been made in the field over the past 20 years, as summarised in Figure 2-11. Numerous investigated technologies, such as glasses, polymers and aluminium oxide have shown improving performance in terms of gain per unit length as well as amplification bandwidth and efficiency. This increasing research activity emphasises the application-driven interest in compact EDWAs, particularly in polymer-based devices used in this work.

2.5 References

[1] J. D. B. Bradley and M. Pollnau, "Erbium-doped integrated waveguide amplifiers and lasers," *Laser Photonics Rev.*, vol. 5, no. 3, pp. 368–403, 2011.

[2] C. Barnard, P. Myslinski, J. Chrostowski, and M. Kavehrad, "Analytical Model for Rare-Earth-Doped Fiber Amplifiers and Lasers," *IEEE J. Quantum Electron.*, vol. 30, no. 8, pp. 1817–1830, 1994.

[3] T. Danger, J. Koetke, R. Brede, E. Heumann, G. Huber, and B. H. T. Chai, "Spectroscopy and green upconversion laser emission of Er^{3+}-doped crystals at room temperature," *J. Appl. Phys.*, vol. 76, no. 3, pp. 1413–1422, 1994.

[4] M. Pollnau, "Rare-earth-ion-doped waveguide lasers on silicon chip," in *Proc. SPIE 9359, Optical Components and Materials XII*, 2015.

[5] W.-B. Sun *et al.*, "Optical damage resistant Ti-diffused Zr/Er-codoped lithium niobate strip waveguide for high-power 980 nm pumping," *Opt. Express*, vol. 25, no. 8, p. 8653, 2017.

[6] P. C. Becker, N. A. Olsson, and J. R. Simpson, "Rare Earth Ions - Introductory Survey," in *Erbium-doped Fiber Amplifiers: Fundamentals and Technology*, San Diego: Academic Press, 1999, pp. 87–130.

[7] C. R. Giles and E. Desurvire, "Modeling erbium-doped fiber amplifiers," *J. Light. Technol.*, vol. 9, no. 2, pp. 271–283, 1991.

[8] D. E. McCumber, "Einstein relations connecting broadband emission and absorption spectra," *Phys. Rev.*, vol. 136, no. 4A, pp. 16–19, 1964.

[9] W. J. Miniscalco and R. S. Quimby, "General procedure for the analysis of Er^{3+} cross sections," *Opt. Lett.*, vol. 16, no. 4, p. 258, 2008.

[10] T. Mann, R. Mathieson, M. Murray, B. Richards, and G. Jose, "Femtosecond laser ablation properties of Er^{3+} ion doped zinc-sodium tellurite glass," *J. Appl. Phys.*, vol. 124, no. 4, 2018.

[11] S. D. Jackson, "High-power erbium cascade fibre laser," *Electron. Lett.*, vol. 45, no. 16, p. 830, 2009.

[12] D. L. Veasey *et al.*, "Yb/Er-codoped and Yb-doped waveguide lasers in phosphate glass," *J. Non. Cryst. Solids*, vol. 263, pp. 369–381, 2000.

[13] G. N. Van Den Hoven, E. Snoeks, A. Polman, J. W. M. Van Uffelen, Y. S. Oei,

and M. K. Smit, "Photoluminescence characterization of Er-implanted Al_2O_3 films," *Appl. Phys. Lett.*, vol. 62, no. 24, pp. 3065–3067, 1993.

[14] S. A. Kamil, J. Chandrappan, M. Murray, P. Steenson, T. F. Krauss, and G. Jose, "Ultrafast laser plasma doping of Er^{3+} ions in silica-on-silicon for optical waveguiding applications," *Opt. Lett.*, vol. 41, no. 20, p. 4684, Oct. 2016.

[15] P. F. Wysocki, J. B. Judkins, R. P. Espindola, M. Andrejco, and A. M. Vengsarkar, "Broad-band erbium-doped fiber amplifier flattened beyond 40 nm using long-period grating filter," *IEEE Photonics Technol. Lett.*, vol. 9, no. 10, pp. 1343–1345, 1997.

[16] M. Digonnet and J. R. Simpson, "Rare Earth Doped Fiber Fabrication: Techniques and Physical Properties," in *Rare-Earth-Doped Fiber Lasers and Amplifiers*, 2nd ed., New York: CRC Press, 2001.

[17] M. Shimizu, M. Yamada, M. Horiguchi, and E. Sugita, "Concentration effect on optical amplification characteristics of Er-doped silica single-mode fibers," *IEEE Photonics Technol. Lett.*, vol. 2, no. 1, pp. 43–45, Jan. 1990.

[18] G. N. van den Hoven, E. Snoeks, A. Polman, C. van Dam, J. W. M. van Uffelen, and M. K. Smit, "Upconversion in Er□implanted Al_2O_3 waveguides," *J. Appl. Phys.*, vol. 79, no. 3, pp. 1258–1266, 2002.

[19] F. Auzel and P. Goldner, "Towards rare-earth clustering control in doped glasses," *Opt. Mater. (Amst).*, vol. 16, no. 1–2, pp. 93–103, 2001.

[20] L.-D. Sun, H. Dong, P.-Z. Zhang, and C.-H. Yan, "Upconversion of Rare Earth Nanomaterials," *Annu. Rev. Phys. Chem.*, vol. 66, no. 1, pp. 619–642, 2015.

[21] J. D. B. Bradley, L. Agazzi, D. Geskus, F. Ay, K. Wörhoff, and M. Pollnau, "Gain bandwidth of 80 nm and 2 dB/cm peak gain in Al_2O_3:Er^{3+} optical amplifiers on silicon," *J. Opt. Soc. Am. B*, vol. 27, no. 2, p. 187, 2010.

[22] Y. C. Yan, A. J. Faber, H. De Waal, P. G. Kik, and A. Polman, "Erbium-doped phosphate glass waveguide on silicon with 4.1 dB/cm gain at 1.535 μm," *Appl. Phys. Lett.*, vol. 71, no. 20, pp. 2922–2924, 1997.

[23] J. Chandrappan *et al.*, "Doping silica beyond limits with laser plasma for active photonic materials," *Opt. Mater. Express*, vol. 5, no. 12, p. 2849, 2015.

[24] E. Snoeks, G. N. van den Hoven, A. Polman, B. Hendriksen, M. B. J. Diemeer, and F. Priolo, "Cooperative upconversion in erbium-implanted soda-lime silicate

glass optical waveguides," *J. Opt. Soc. Am. B*, vol. 12, no. 8, p. 1468, 2008.

[25] P. Golding, S. Jackson, T. King, and M. Pollnau, "Energy transfer processes in-doped and-codoped ZBLAN glasses," *Phys. Rev. B - Condens. Matter Mater. Phys.*, vol. 62, no. 2, pp. 856–864, 2000.

[26] S. A. Vázquez-Córdova *et al.*, "13 dB/cm gain per unit length at 1.53 μm in $KGd_xLu_yEr_{1-x-y}(WO_4)_2$ channel waveguides, allowing for ~40 dB total gain," in *Lasers Congress 2016 (ASSL, LSC, LAC)*, 2016, p. ATu6A.3.

[27] S. Suntsov, C. E. Rüter, and D. Kip, "Er:Ti:$LiNbO_3$ ridge waveguide optical amplifiers by optical grade dicing and three-side Er and Ti in-diffusion," *Appl. Phys. B Lasers Opt.*, vol. 123, no. 4, pp. 1–7, 2017.

[28] X. Zhai *et al.*, "Enhancement of 1.53 μm emission band in $NaYF_4:Er^{3+},Yb^{3+},Ce^{3+}$ nanocrystals for polymer-based optical waveguide amplifiers," *Opt. Mater. Express*, vol. 3, no. 2, p. 270, Feb. 2013.

[29] F. Auzel, "Upconversion and Anti-Stokes Processes with f and d Ions in Solids," *Chem. Rev.*, vol. 104, no. 1, pp. 139–174, 2004.

[30] R. S. Quimby, W. J. Miniscalco, and B. Thompson, "Clustering in erbium-doped silica glass fibers analyzed using 980 nm excited-state absorption," *J. Appl. Phys.*, vol. 76, no. 8, pp. 4472–4478, 1994.

[31] T. Ohtsuki, S. Honkanen, S. I. Najafi, and N. Peyghambarian, "Cooperative upconversion effects on the performance of Er^{3+}-doped phosphate glass waveguide amplifiers," *J. Opt. Soc. Am. B*, vol. 14, no. 7, p. 1838, 2008.

[32] E. S. Waveguides, F. Di Pasquale, and M. Federighi, "Modelling of Uniform and Pair-Induced Upconversion Mechanisms in High-Concentration," *Lightwave*, vol. 13, no. 9, pp. 1858–1864, 1995.

[33] H. Masuda, A. Takada, and K. Aida, "Modeling the Gain Degradation of High Concentration Erbium-Doped Fiber Amplifiers by Introducing Inhomogeneous Cooperative Up-Conversion," *J. Light. Technol.*, vol. 10, no. 12, pp. 1789–1799, 1992.

[34] P. Myslinski, D. Nguyen, and J. Chrostowski, "Effects of Concentration on the Performance of Erbium-Doped Fiber Amplifiers," *J. Light. Technol.*, vol. 15, no. 1, pp. 112–120, 1997.

[35] M. Pollnau, "Analysis of heat generation and thermal lensing in erbium 3-μm

lasers," *IEEE J. Quantum Electron.*, vol. 39, no. 2, pp. 350–357, 2003.

[36] L. Agazzi, K. Wörhoff, M. Pollnau, K. Worhoff, and M. Pollnau, "Energy-Transfer-Upconversion Models, Their Applicability and Breakdown in the Presence of Spectroscopically Distinct Ion Classes: A Case Study in Amorphous $Al_2O_3:Er^{3+}$," *J. Phys. Chem.*, vol. 117, no. 13, pp. 6759–6776, 2013.

[37] B.-C. Hwang, S. Jiang, T. Luo, J. Watson, G. Sorbello, and N. Peyghambarian, "Cooperative upconversion and energy transfer of new high Er^{3+}- and Yb^{3+}–Er^{3+}-doped phosphate glasses," *J. Opt. Soc. Am. B*, vol. 17, no. 5, p. 833, 2007.

[38] Y. Hu *et al.*, "Numerical analyses of the population dynamics and determination of the upconversion coefficients in a new high erbium-doped tellurite glass," *J. Opt. Soc. Am. B*, vol. 18, no. 12, pp. 1928–1934, 2001.

[39] P. G. Kik and A. Polman, "Cooperative upconversion as the gain-limiting factor in Er doped miniature Al_2O_3 optical waveguide amplifiers," *J. Appl. Phys.*, vol. 93, no. 9, pp. 5008–5012, 2003.

[40] K. Suh *et al.*, "Cooperative upconversion and optical gain in ion-beam sputter-deposited Er_xY_2-$xSiO_5$ waveguides," *Opt. Express*, vol. 18, no. 8, p. 7724, 2010.

[41] F. Di Pasquale and M. Federighi, "Improved gain characteristics in high-concentration Er^{3+}/Yb^{3+} codoped glass waveguide amplifiers," *IEEE J. Quantum Electron.*, vol. 30, no. 9, pp. 2127–2131, 1994.

[42] M. Pollnau, D. R. Gamelin, S. R. Lüthi, H. U. Güdel, and M. P. Hehlen, "Power dependence of upconversion luminescence in lanthanide and transition-metal-ion systems," *Phys. Rev. B*, vol. 61, no. 5, pp. 3337–3346, Feb. 2000.

[43] W. J. Miniscalco, "Erbium-Doped Glasses for Fiber Amplifiers at 1500 nm," *J. Light. Technol.*, vol. 9, no. 2, pp. 234–250, 1991.

[44] P. G. Kik and A. Polman, "Erbium-Doped Optical-Waveguide Amplifiers on Silicon," *MRS Bull.*, vol. 23, no. 04, pp. 48–54, Apr. 1998.

[45] A. Polman, "Erbium implanted thin film photonic materials," *J. Appl. Phys.*, vol. 82, no. 1, pp. 1–39, 1997.

[46] R. G. Smart, J. L. Zyskind, and D. J. DiGiovanni, "Experimental comparison of 980 nm and 1480 nm-pumped saturated in-line erbium-doped fiber amplifiers suitable for long-haul soliton transmission systems," *IEEE Photonics Technol. Lett.*, vol. 5, no. 7, pp. 770–773, 2002.

[47] D. Pugliese *et al.*, "Concentration quenching in an Er-doped phosphate glass for compact optical lasers and amplifiers," *J. Alloys Compd.*, vol. 657, pp. 678–683, 2016.

[48] J. Nilsson, P. Scheer, and B. Jakorzynska, "Modelling and Optimization of Short Yb^{3+}-Sensitized Er^{3+}-Doped Fiber Amplifiers," *IEEE Photonics Technol. Lett.*, vol. 6, no. 3, pp. 383–385, 1994.

[49] F. Di Pasquale and M. Federighi, "Improved Gain Characteristics in High-Concentration Er^{3+}/Yb^{3+} Codoped - Glass Waveguide Amplifiers," *IEEE J. Quantum Electron.*, vol. 30, no. 9, pp. 2127–2131, 1994.

[50] C. E. Chryssou, F. Di Pasquale, and C. W. Pitt, "Improved Gain Performance In Yb^{3+}-Sensitized Er^{3+}-Doped Alumina (Al_2O_3) Channel Optical Waveguide Amplifiers," *J. Light. Technol.*, vol. 19, no. 3, pp. 345–349, 2001.

[51] J. B. Gruber, D. K. Sardar, B. Zandi, J. A. Hutchinson, and C. W. Trussell, "Modeling the absorption spectra of Er^{3+} and Yb^{3+} in a phosphate glass," *J. Appl. Phys.*, vol. 94, no. 8, pp. 4835–4840, 2003.

[52] P. G. Kik and A. Polman, "Exciton-erbium interactions in Si nanocrystal-doped SiO_2," *J. Appl. Phys.*, vol. 88, no. 4, pp. 1992–1998, 2000.

[53] N. Daldosso *et al.*, "Refractive index dependence of the absorption and emission cross sections at 1.54 μm of Er^{3+} coupled to Si nanoclusters," *Appl. Phys. Lett.*, vol. 88, no. 16, pp. 86–89, 2006.

[54] D. Navarro-Urrios *et al.*, "Assessment of the main material issues for achieving an Er coupled to silicon nanoclusters infrared amplifier," *Phys. E Low-Dimensional Syst. Nanostructures*, vol. 41, no. 6, pp. 1029–1033, 2009.

[55] A. Polman and F. C. J. M. van Veggel, "Broadband sensitizers for erbium-doped planar optical amplifiers: review," *J. Opt. Soc. Am. B*, vol. 21, no. 5, p. 871, 2004.

[56] C. Strohhöfer and A. Polman, "Relationship between gain and Yb^{3+} concentration in Er^{3+}-Yb^{3+} doped waveguide amplifiers," *J. Appl. Phys.*, vol. 90, no. 9, pp. 4314–4320, 2001.

[57] F. D. Patel, S. DiCarolis, P. Lum, S. Venkatesh, and J. N. Miller, "A compact high-performance optical waveguide amplifier," *IEEE Photonics Technol. Lett.*, vol. 16, no. 12, pp. 2607–2609, 2004.

[58] S. Honkanen, T. Ohtsuki, S. Jiang, S. I. Najafi, and N. Peyghambarian, "High Er

concentration phosphate glasses for planar waveguide amplifiers," in *Rare-Earth-Doped Devices*, 2004, vol. 2996, no. May 1997, pp. 32–40.

[59] J. F. Philipps, T. Töpfer, H. Ebendorff-Heidepriem, D. Ehrt, and R. Sauerbrey, "Energy transfer and upconversion in erbium-ytterbium-doped fluoride phosphate glasses," *Appl. Phys. B Lasers Opt.*, vol. 74, no. 3, pp. 233–236, 2002.

[60] G. Della Valle, S. Taccheo, P. Laporta, G. Sorbello, E. Cianci, and V. Foglietti, "Compact high gain erbium-ytterbium doped waveguide amplifier fabricated by Ag-Na ion exchange," *Electron. Lett.*, vol. 42, no. 11, p. 632, 2006.

[61] J. D. B. Bradley, L. Agazzi, D. Geskus, F. Ay, K. Wörhoff, and M. Pollnau, "Gain bandwidth of 80 nm and 2 dB/cm peak gain in $Al_2O_3:Er^{3+}$ optical amplifiers on silicon," *J. Opt. Soc. Am. B*, vol. 27, no. 2, pp. 187–196, 2010.

[62] R. Brinkmann, I. Baumann, M. Dinand, W. Sohler, and H. Suche, "Ti:$LiNb0_3$ Waveguide Amplifiers," *IEEE J. Quantum Electron.*, vol. 30, no. 10, pp. 2356–2360, 1994.

[63] S. A. Vázquez-Córdova *et al.*, "High optical gain in erbium-doped potassium double tungstate channel waveguide amplifiers," *Opt. Express*, vol. 26, no. 5, pp. 6260–6266, 2018.

[64] A. Z. Subramanian, G. S. Murugan, M. N. Zervas, and J. S. Wilkinson, "Spectroscopy, Modeling, and Performance of Erbium-Doped Ta_2O_5 Waveguide Amplifiers," *J. Light. Technol.*, vol. 30, no. 10, pp. 1455–1462, 2012.

[65] G. Nykolak, M. Haner, P. C. Becker, J. Shmulovich, and Y. H. Wong, "Systems Evaluation of an Er^{3+}-Doped Planar Waveguide Amplifier," *IEEE Photonics Technol. Lett.*, vol. 5, no. 10, pp. 1185–1187, 1993.

[66] F. A. Bomfim, D. M. da Silva, L. R. P. Kassab, and M. I. Alayo, "Production of Yb^{3+}/Er^{3+} codoped PbO-$Ge0_2$ pedestal type waveguides for photonic applications," in *30th Symposium on Microelectronics Technology and Devices (SBMicro)*, 2015.

[67] D. Brüske, S. Suntsov, C. E. Rüter, and D. Kip, "Efficient ridge waveguide amplifiers and lasers in Er-doped lithium niobate by optical grade dicing and three-side Er and Ti in-diffusion," *Opt. Express*, vol. 25, no. 23, p. 29374, 2017.

[68] K. Vu, S. Farahani, and S. Madden, "980nm pumped erbium doped tellurium oxide planar rib waveguide laser and amplifier with gain in S, C and L band," *Opt.*

Express, vol. 23, no. 2, p. 747, 2015.

[69] G. F. R. Chen, X. Zhao, Y. Sun, C. He, M. C. Tan, and D. T. H. Tan, "Low Loss Nanostructured Polymers for Chip-scale Waveguide Amplifiers," *Sci. Rep.*, vol. 7, no. 1, pp. 1–8, 2017.

[70] M. Zhang *et al.*, "High-gain polymer optical waveguide amplifiers based on core-shell $NaYF_4$/$NaLuF_4$: Yb^{3+}, Er^{3+} NPs-PMMA covalent-linking nanocomposites," *Sci. Rep.*, vol. 6, 2016.

[71] W. Huang, R. R. A. Syms, E. M. Yeatman, M. M. Ahmad, T. V. Clapp, and S. M. Ojha, "Fiber-device-fiber gain from a sol-gel erbium-doped waveguide amplifier," *IEEE Photonics Technol. Lett.*, vol. 14, no. 7, pp. 959–961, 2002.

[72] R. R. Thomson, N. D. Psaila, S. J. Beecher, and A. K. Kar, "Ultrafast laser inscription of a high-gain Er-doped bismuthate glass waveguide amplifier," *Opt. Express*, vol. 18, no. 12, p. 13212, 2010.

[73] P. Camy *et al.*, "Ion-Exchanged Planar Lossless Splitter At 1.5 μm," *Electron. Lett.*, vol. 32, no. 4, pp. 321–323, 1996.

[74] I. Vasilief *et al.*, "Propagation losses and gain measurements in erbium-doped fluoride glass channel waveguides by use of a double-pass technique," *Appl. Opt.*, vol. 44, no. 22, p. 4678, 2005.

[75] K. Liu and E. Y. B. Pun, "Modeling and experiments of packaged Er^{3+}-Yb^{3+} co-doped glass waveguide amplifiers," *Opt. Commun.*, vol. 273, no. 2, pp. 413–420, 2007.

[76] J. Hoyo *et al.*, "Femtosecond laser written 16.5 mm long glass-waveguide amplifier and laser with 5.2 dB cm-1 internal gain at 1534 nm," *Laser Phys. Lett.*, vol. 10, no. 10, 2013.

[77] Y. Dai, G. Jin, and G. Shao, "The Analysis of Intensity Profiles of Pump and Signal Light in Er-doped Waveguide Amplifier," *Mod. Phys. Lett. B*, vol. 22, no. 28, pp. 2747–2758, Nov. 2008.

[78] A. Z. Subramanian, G. S. Murugan, M. N. Zervas, and J. S. Wilkinson, "High index contrast Er:Ta_2O_5 waveguide amplifier on oxidised silicon," *Opt. Commun.*, vol. 285, no. 2, pp. 124–127, 2012.

[79] P. Joshi *et al.*, "Erbium-ion-doped tellurite glasss fibers and waveguides - Devices and future prospective: Part I," *Int. J. Appl. Glas. Sci.*, vol. 4, no. 3, pp. 192–201,

2013.

[80] C. Zhao, G. F. Yang, Q. Y. Zhang, and Z. H. Jiang, "Spectroscopic properties of GeO_2- and Nb_2O_5-modified tellurite glasses doped with Er^{3+}," *J. Alloys Compd.*, vol. 461, no. 1–2, pp. 617–622, 2008.

[81] J. I. Mackenzie, G. S. Murugan, T. Suzuki, Y. Ohishi, A. W. Yu, and J. B. Abshire, "Er-doped Tellurite glasses for planar waveguide power amplifier with extended gain bandwidth," in *Proc. SPIE 8235, Solid State Lasers XXI: Technology and Devices*, 2012, p. 823514.

[82] J. Chandrappan *et al.*, "Target dependent femtosecond laser plasma implantation dynamics in enabling silica for high density erbium doping," *Sci. Rep.*, vol. 5, 2015.

[83] J. Chandrappan *et al.*, "Doping silica beyond limits with laser plasma for active photonic materials," *Opt. Mater. Express*, vol. 5, no. 12, pp. 2849–2861, 2015.

[84] G. N. van den Hoven, R. J. I. M. Koper, A. Polman, C. van Dam, J. W. M. van Uffelen, and M. K. Smit, "Net optical gain at 1.53 μm in Er-doped Al_2O_3 waveguides on silicon," *Appl. Phys. Lett.*, vol. 68, no. 14, pp. 1886–1888, Apr. 1996.

[85] J. D. B. Bradley *et al.*, "170 Gbit/s transmission in an erbium-doped waveguide amplifier on silicon," *Opt. Express*, vol. 17, no. 24, pp. 22201–22208, 2009.

[86] S. A. Vázquez-Córdova *et al.*, "Erbium-doped spiral amplifiers with 20 dB of net gain on silicon," *Opt. Express*, vol. 22, no. 21, pp. 25993–26004, 2014.

[87] L. Agazzi *et al.*, "Monolithic integration of erbium-doped amplifiers with silicon-on-insulator waveguides," *Opt. Express*, vol. 18, no. 26, p. 27703, 2010.

[88] M. Pollnau and J. D. B. Bradley, "Optically pumped rare-earth-doped Al_2O_3 distributed-feedback lasers on silicon [Invited]," *Opt. Express*, vol. 26, no. 18, p. 24164, 2018.

[89] J. D. Bradley, R. Stoffer, L. Agazzi, F. Ay, K. Wörhoff, and M. Pollnau, "Integrated Al_2O_3:Er^{3+} ring lasers on silicon with wide wavelength selectivity," *Opt. Lett.*, vol. 35, no. 1, p. 73, 2009.

[90] E. H. Bernhardi, Q. Lu, H. A. G. M. Van Wolferen, K. Wörhoff, R. M. De Ridder, and M. Pollnau, "Monolithic distributed Bragg reflector cavities in Al_2O_3 with quality factors exceeding 10^6," *Photonics Nanostructures - Fundam. Appl.*, vol. 9,

no. 3, pp. 225–234, 2011.

[91] E. H. Bernhardi *et al.*, "Ultra-narrow-linewidth, single-frequency distributed feedback waveguide laser in $Al_2O_3:Er^{3+}$ on silicon," *Opt. Lett.*, vol. 35, no. 14, p. 2394, 2010.

[92] L. Agazzi, K. Worhoff, and M. Pollnau, "Energy-Transfer-Upconversion Models, Their Applicability and Breakdown in the Presence of Spectroscopically Distinct Ion Classes: A Case Study in Amorphous $Al_2O_3:Er^{3+}$," *J. Phys. Chem.*, vol. 117, no. 13, pp. 6759–6776, 2013.

[93] X. Leroux *et al.*, "Ultra-high on-chip optical gain in erbium-based hybrid slot waveguides," *Nat. Commun.*, vol. 10, no. 1, pp. 1–9, 2019.

[94] S. A. Vázquez-Córdova *et al.*, "Spectroscopy of erbium-doped potassium double tungstate waveguides," in *Proceedings of SPIE - The International Society for Optical Engineering*, 2017, vol. 10106.

[95] S. A. Vazquez-Cordova *et al.*, "13 dB/cm gain per unit length at 1.53 μm in $KGd_xLu_yEr_{1-x-y}(WO_4)_2$ channel waveguides, allowing for ~40 dB total gain," in *Lasers Congress 2016 (ASSL, LSC, LAC)*, 2016, p. ATu6A.3.

[96] L. H. Slooff, A. Polman, M. P. Oude Wolbers, F. C. J. M. Van Veggel, D. N. Reinhoudt, and J. W. Hofstraat, "Optical properties of erbium-doped organic polydentate cage complexes," *J. Appl. Phys.*, vol. 83, no. 1, pp. 497–503, 1998.

[97] L. H. Slooff *et al.*, "Rare-earth doped polymers for planar optical amplifiers," *J. Appl. Phys.*, vol. 91, no. 7, pp. 3955–3980, 2002.

[98] P. Etienne, P. Coudray, J. Porque, and Y. Moreau, "Active erbium-doped organic – inorganic waveguide," *Opt. Commun.*, vol. 174, pp. 413–418, 2000.

[99] S. Bo *et al.*, "LaF_3:Er,Yb doped sol–gel polymeric optical waveguide amplifiers," *Appl. Phys. B*, vol. 91, no. 1, pp. 79–83, 2008.

[100] W. H. Wong, E. Y. B. Pun, and K. S. Chan, "Er^{3+}–Yb^{3+} codoped polymeric optical waveguide amplifiers," *Appl. Phys. Lett.*, vol. 84, no. 2, pp. 176–178, 2004.

[101] W. H. Wong, K. S. Chan, and E. Y. B. Pun, "Ultraviolet direct printing of rare-earth-doped polymer waveguide amplifiers," *Appl. Phys. Lett.*, vol. 87, no. 1, pp. 1–4, 2005.

[102] D. Zhang, C. Chen, D. Zheng, T. Li, L. Song, and Z. Zhen, "Erbium-ytterbium

codoped waveguide amplifier fabricated with solution-processable complex," *Appl. Phys. Lett.*, vol. 94, no. 4, pp. 4–7, 2009.

[103] Y. Zheng *et al.*, "Metal-cladding directly defined active integrated optical waveguide device based on erbium-containing polymer," *RSC Adv.*, vol. 6, no. 4, pp. 3224–3230, 2016.

[104] J. Wang, J. Hu, D. Tang, X. Liu, and Z. Zhen, "Oleic acid (OA)-modified LaF_3:Er,Yb nanocrystals and their polymer hybrid materials for potential optical-amplification applications," *J. Mater. Chem.*, vol. 17, no. 16, pp. 1597–1601, 2007.

[105] A. Q. Le Quang *et al.*, "Demonstration of net gain at 1550 nm in an erbium-doped polymersingle mode rib waveguide," *Appl. Phys. Lett.*, vol. 89, no. 14, p. 141124, Oct. 2006.

[106] D. Zhang *et al.*, "Optical gain at 1535 nm in LaF_3: Er,Yb nanoparticle-doped organic-inorganic hybrid material waveguide," *Appl. Phys. Lett.*, vol. 91, no. 16, pp. 1–4, 2007.

[107] K. L. Lei *et al.*, "Long aliphatic chain coated rare-earth nanocrystal as polymer-based optical waveguide amplifiers," *J. Mater. Chem.*, vol. 20, no. 35, pp. 7526–7529, 2010.

[108] S. H. Bo *et al.*, "Core-shell LaF_3 :Er,Yb nanocrystal doped sol-gel materials as waveguide amplifiers," *Appl. Phys. B Lasers Opt.*, vol. 97, no. 3, pp. 665–669, 2009.

[109] T. Wang *et al.*, "Optical waveguide amplifiers based on $NaYF_4$: Er^{3+}, Yb^{3+} NPs-PMMA covalent-linking nanocomposites," *Opt. Mater. Express*, vol. 5, no. 3, p. 469, 2015.

[110] P. Zhao *et al.*, "Optical Amplification at 1525 nm in $BaYF_5$: 20% Yb^{3+} , 2% Er^{3+} Nanocrystals Doped SU-8 Polymer Waveguide," *J. Nanomater.*, vol. 2014, pp. 1–6, 2014.

[111] Y. Zhang, Y. Shi, Z. Qin, M. Song, and W. Qin, "Synthesis of Small Ce^{3+}-Er^{3+}-Yb^{3+} Tri-Doped $BaLuF_5$ Active-Core-Active-Shell-Active-Shell Nanoparticles with Strong Down Conversion Luminescence at 1.5 μm," *Nanomaterials*, vol. 8, no. 8, p. 615, 2018.

[112] Y. Zhang *et al.*, "$KMnF_3$:Yb^{3+},Er^{3+} Core-Active-Shell Nanoparticles with Broadband Down-Shifting Luminescence at 1.5 μm for Polymer-Based

Waveguide Amplifiers," *Nanomaterials*, vol. 9, no. 3, p. 463, 2019.

3 Design and Modelling of EDWAs

In the previous chapters, potential applications for a compact EDWA have been presented and key physical mechanisms governing the behaviour of erbium-doped materials have been discussed. In this section, the design of an amplifier system is explained focusing on key waveguide parameters and the impact they have on the performance of the device.

The aim of this work is to develop an EDWA compatible with the polymer platform, sometimes referred to as erbium-doped polymer waveguide amplifier (EDPWA). In order to achieve this, a choice of right organic host is discussed. The benefits of polymer in terms of fabrication ease and scalability have already been explained, but progress in material engineering offers a wide range of potential types with different properties available. Based on the chosen siloxane polymer, optical waveguide theory is employed to understand the light behaviour in the system as well as derive necessary parameters, such as cross-section and modal overlap, required for an EDWA analysis.

The derived design specifications are then combined with the Er properties and fed into a rate-equations-based model in order to predict and optimise the achievable performance. The used model takes into account introduced material and system properties allowing for qualitative discussion of their impact. Physical factors such as ion concentration, dopant composition and upconversion rate are investigated and analysed in terms of their impact on the achievable gain. The potential for reaching an internal gain of 10 dB/cm in a short waveguide under realistic operational conditions compatible with polymer waveguides is explored. Scalability options for the EDWA system are also examined and power efficiency in systems of different length is discussed.

In this chapter, a standard, symmetric channel geometry is assumed to be used as a benchmark for comparison with other systems reported in literature as well as polymer-platform compatible designs presented in detail in later chapters of this thesis. While used simulation parameters correspond to these reported for ULPI fabricated erbium samples, similar methodology can be applied to other Er-based systems. Focus is placed on the upconversion parameter as it corresponds to the adverse effect of ion clustering predicted for devices with high rare-earth doping at a concentration of ~ 10^{21} cm^{-3}.

Finally, a number of designs are put forward at the end of this chapter as a result of the simulation analysis. These are based on the most promising approaches to combine polymer host with erbium dopants, namely ion implantation and nanoparticle (NP) doping. The benefits and potential issues with each approach are compared and contrasted. The proposed systems are created to ensure compatibility with the polymer

platform as well as potential for providing compact EDWAs that can be integrated with other functionalities.

3.1 Amplifier Design Considerations

The Er-doped material characteristics and properties discussed in Chapter 2 are important indicators of the EDWA performance, but there are other practical aspects of the design that need to be taken into account. In order to get a comprehensive view of the system, optical waveguiding theory is introduced to characterise the potential EDWA devices. This method allows for establishing final design parameters for a system: an amplifier's cross-section and mode confinement in the active region. An optimal choice of polymer material is discussed with key properties required in terms of fabrication as well as system design.

3.1.1 Optical Waveguide Theory

Optical waveguides are multi-layer structures designed to confine light so that it propagates along a predetermined path. It is usually achieved by keeping the light signal within a core area surrounded by a lower refractive index cladding. This process can be controlled by setting appropriate refractive indices values for the structure so that light is trapped inside of the desired layer. In order to numerically investigate the wave propagation, one has to solve the wave equation with carefully set boundary conditions. However, there also exists an analytical approach to understand the light confinement principles. Very often a wave-guiding problem can be intuitively approximated with ray optic theory, where the conditions required for light guiding can be derived using Snell's law [1].

3.1.1.1 Ray Tracing

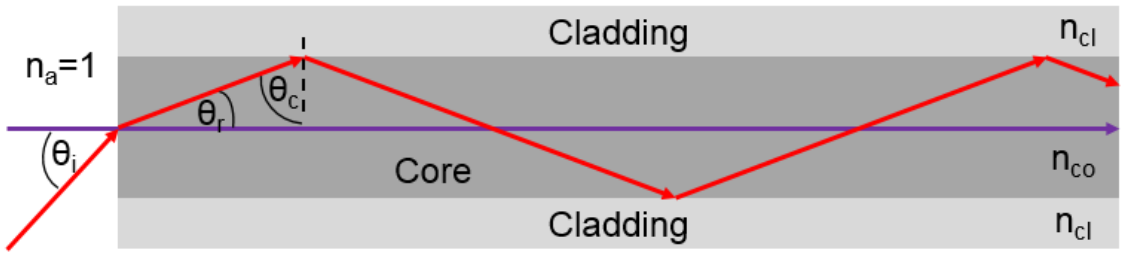

Figure 3-1: Illustration of a guided ray of light

In a simple case, where a core layer of higher refractive index n_{co} is surrounded by a lower refractive index cladding n_{cl}, light is coupled into a waveguide as shown in Figure 3-1.

Depending on the incident angle θ_i at the interface, a ray of light can be either guided or leak out of the structure. A guided ray travels through a waveguide without losing any power due to total internal reflection phenomena (TIR) while a leaky ray is only partially transmitted and at every reflection at the core-cladding interface part of the power is lost.

Refraction occurs at the input of the waveguide as the ray is incident on the interface with the core. Reflected and refracted waves can be calculated using the formula given in Equation (3.1).

$$n_a \sin\theta_i = n_{co} \sin\theta_r \tag{3.1}$$

where $\boldsymbol{\theta_r}$ is the refractive angle. A ray that was not initially reflected then reaches the core-cladding interface where it undergoes another refraction. There is an incident angle $\boldsymbol{\theta_c}$, usually referred to as the critical angle, for which the refracted angle is 90° and the Snell's law in this case can be simplified to:

$$\sin\theta_c = \frac{n_{cl}}{n_{co}} \tag{3.2}$$

If the incidence angle is greater than $\boldsymbol{\theta_c}$, total internal reflection occurs and no light is transmitted into the cladding medium. When the Equations (3.1) and (3.2) are combined, the maximum incident angle allowing for light confinement, also called numerical aperture (***NA***), can be defined.

$$NA = \sin\theta_i \, n_a = n_{co} \cos\theta_c = \sqrt{{n_{co}}^2 - {n_{cl}}^2} \tag{3.3}$$

3.1.1.2 Light Modes

As shown in Figure 3-1, an electromagnetic wave propagates through the structure bouncing between the two core-cladding interfaces. This wave can be described using wave vector $\boldsymbol{k}$ that has components along all the directions even though only two dimensions are considered in this planar waveguide example. Propagating light forms a standing wave pattern along the direction normal to the propagation vector with a phase shift introduced by both making the round trip as well as the reflections at the core-cladding interfaces. For the wave to be continued the total phase shift must be an integral multiple of 2π. Therefore, a discrete number of incident angles exists and each of these corresponds to a different mode of propagation. Every possible mode propagating through the waveguide can be described using polarisation and mode number, where the latter

indicates the integral multiple of 2π used to calculate it. For example, the fundamental TE mode is referred as TE_0.

It is possible to estimate the total number of modes supported by a given waveguide by remembering that the incidence angle is limited by the critical angle. This can be written down as shown in Equation (3.4) with a detailed derivation presented in [2].

$$m_{max} = \frac{2n_{co}a\cos\theta_c}{\lambda_0} \tag{3.4}$$

where: $\boldsymbol{m_{max}}$ is the maximum number of supported modes, $\boldsymbol{a}$ is the thickness of the waveguide and $\boldsymbol{\lambda_0}$ is the free-space wavelength of light.

This work focuses on a specific form of light transmission, where only a single mode is guided within the structure. It is possible to rearrange the above equation in order to obtain a condition for the monomode operation in terms of waveguide thickness, light wavelength as well as the refractive indices of core and cladding materials. This can be done by assuming that $\boldsymbol{m_{max}}$ is equal to one and setting this as the boundary condition for the critical angle. The resultant expression given in Equation (3.5).

$$\theta_c = \cos^{-1}\frac{\lambda_0}{2n_{co}a} \tag{3.5}$$

A more useful approach is to use normalised frequency (V Number) [1] that is commonly used for step-index fibres and apply it to a 2D slab waveguide under consideration here. This method allows to estimate the point at which the m^{th} mode is guided in the waveguide in terms of minimum refractive indices difference between core and cladding materials as shown in the Equation (3.6) [2]. A more detailed derivation with examples of curves for lowest modes plotted for a number of different waveguides can be found in [3].

$$\Delta n = n_{co} - n_{cl} = \frac{m^2{\lambda_0}^2}{4(n_{co}+n_{cl})a^2} \tag{3.6}$$

3.1.1.3 Electromagnetic Waves Model

The above approach is useful as it provides a simple way of estimating the number of modes, particularly in larger structures, but it does not provide any information about the electromagnetic field distribution of light inside the waveguide. In order to obtain more

insight into the mode propagation, one has to solve Maxwell's wave equations, which for an electric field in a linear medium with no discontinuities in space or time is:

$$\nabla^2\overrightarrow{E(\tilde{r},t)} = \frac{n(\tilde{r})^2}{c^2}\frac{\delta^2\overrightarrow{E(\tilde{r},t)}}{\delta t^2} \tag{3.7}$$

Where $\overline{\boldsymbol{E}}$ is electric field vector, $\tilde{\boldsymbol{r}}$ the radius vector, $\boldsymbol{n}(\tilde{\boldsymbol{r}})$ the refractive index and $\boldsymbol{c}$ is the speed of light in vacuum. It can rewritten for a monochromatic wave as [4]:

$$\nabla^2\overrightarrow{E(\tilde{r})} + k^2 n(\tilde{r})^2\overrightarrow{E(\tilde{r})} = 0 \tag{3.8}$$

where $k = {}^{\omega}/_{c} = {}^{2\pi}/_{\lambda_0}$ is the propagation constant and $\boldsymbol{\omega}$ is the radian frequency. This is a general equation, which can be specified for a uniform plane wave propagating along the z-direction (that is $\overrightarrow{E(\tilde{r})} = \overrightarrow{E(x,y)}\exp(-j\beta z)$, where β is the propagation constant) to be:

$$\frac{\delta\overrightarrow{E(x,y)}}{\delta x^2} + \frac{\delta\overrightarrow{E(x,y)}}{\delta y^2} + [k^2 n(\tilde{r})^2 - \beta^2]\overrightarrow{E(x,y)} = 0 \tag{3.9}$$

All the solutions to the above equation can be either sinusoidal or exponential functions depending on whether the third term in Equation (3.9) is positive or negative [5]. Every set of appropriate values of β and $\overrightarrow{E(x,y)}$ for a given waveguide forming a solution to the above equation is known as a mode with a well-defined effective mode index ($\boldsymbol{n_{eff}}$) given by Equation (3.11).

$$n_{eff} = \frac{\beta}{k} \tag{3.10}$$

In order for a mode to be confined in the core layer and guided by the waveguide, it is required that $\boldsymbol{n_{cl} < n_{eff} < n_{co}}$. The modes that fulfil this condition propagate in the core medium and exponentially decay in the cladding. On the other hand, when the effective refractive index of a mode is below that of a cladding, the mode is no longer guided and becomes a radiation mode.

In addition to this, the boundary conditions for two perfect dielectrics must be satisfied, therefore, the electric field and its derivatives must be continuous across the core-cladding

interfaces. The field distribution varies for all the modes existing in the waveguide with an example of three lowest order modes shown in Figure 3-2.

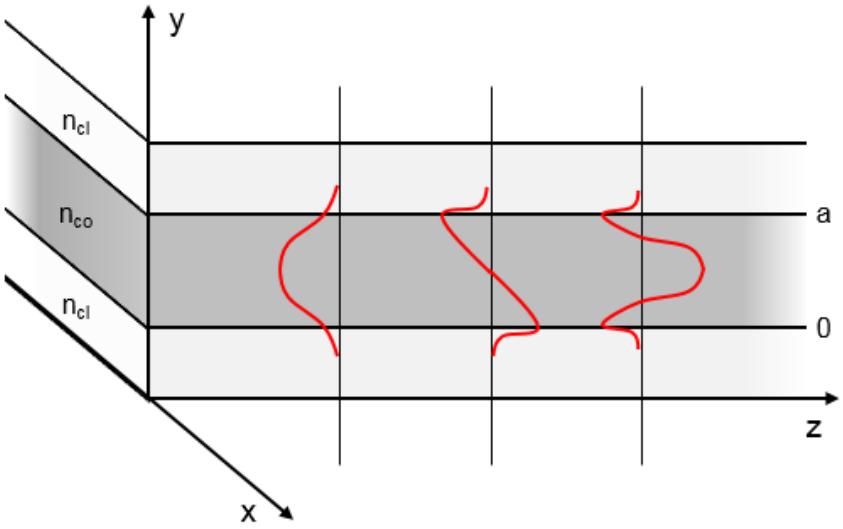

Figure 3-2: Field distribution of low order modes in a symmetric slab waveguide

Figure 3-2 clearly indicates that different modes have sinusoidal field distribution with most of the field trapped inside of the core medium. However, at the interface with the cladding layers, it does not decay to zero, but a portion of the field leaks into the cladding medium. This indicates that the power is not completely confined in the waveguide, but the tails of the evanescent field are present in the surroundings. In order to quantify this phenomenon a parameter called mode confinement factor is used to describe the fraction of the total power of a given mode confined within the guide layer. Based on the slab waveguide example, the formula can be written as follows:

$$\Gamma = \frac{\int_0^a {E_x}^2(y)dy}{\int_{-\infty}^{\infty} {E_x}^2(y)dy} \tag{3.11}$$

where $\boldsymbol{\Gamma}$ is the confinement factor and $\boldsymbol{a}$ is the thickness of the core layer in the slab waveguide. This property of a mode becomes an important factor in EDWA design as it allows one to quantify the proportion of the signal and pump light interacting with the erbium ions.

Calculations of the mode profiles become considerably more complex in waveguide systems with two-dimensional confinement. In most of the cases, waveguide structures are created with a combination of various materials with different refractive indices surrounding the core leading to asymmetric modal shape. As a result, it is necessary to use numerical methods to accurately investigate light behaviour in polymer waveguide

amplifier systems. This is done throughout this work using commercially available FimmWave software that employs the finite difference method.

3.1.2 Polymer Materials

There exist a range of polymer materials that have been used to fabricate waveguides and more complex integrated components. The majority of them can be classified into one of the following general groups: acrylates, polyimides, epoxies and siloxanes [6]. Despite the great variety of polymers available, the most commonly used and widely available are SU-8 [7] and PMMA [8]. The availability of different materials exhibiting different properties means that the right one needs to be chosen for a given application. There are many criteria affecting this choice as shown in Table 3-1, but most impactful for EDWA applications are the absorption loss, refractive index difference, thermal stability and fabrication method.

Table 3-1: Key polymer material properties [9]

Low absorption loss
Low polarisation dependent loss
Low birefringence
Thermal stability
Adhesion (to substrates, self, electrodes)
Stability with humidity
Stability with optical power
Patternability with low scattering loss
Machinability (cleaving, dicing, polishing)
Large thermo-optic coefficient (dn/dT)
Manufacturability with repeatable properties
Ability to vary refractive index profile

Initially the development of polymer materials and optimisation of their properties has been focused on wavelengths around 850 nm with low-cost and high-speed optical backplanes in mind [10],[11]. As a result of this research, a new class of polymer materials with favourable mechanical, thermal and optical properties for direct integration onto printed circuit boards (PCBs) have been developed [12]. Siloxanes have become one of the leading types of polymer materials as they exhibit all the necessary properties to withstand the manufacturing processes of PCBs (solder reflow), good environmental

stability, long lifetimes and low absorption at the datacommunications' wavelength of 850 nm (~ 0.04 dB/cm) [13].

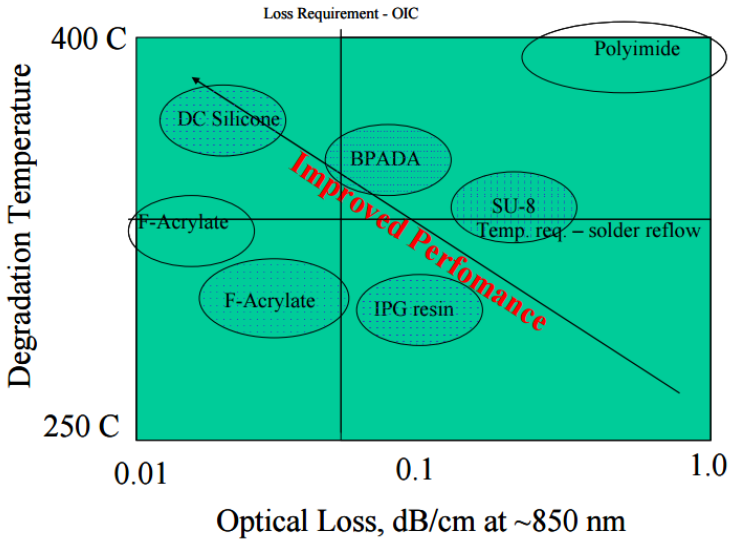

Figure 3-3: Comparison of various polymer types for datacom applications [14]

Siloxanes are unusual in their structure as the backbone is composed of alternating silicon and oxygen atoms without a typical presence of carbon in the polymer chain. This results in the material being more suitable for operation in harsher environments [15]. Not only do they exhibit resistance to high temperature exposure occurring during the PCB manufacturing process as shown in Figure 3-3, but also are not affected by increased transmission loss due to discoloration caused by thermal ageing [16]. A standard board manufacturing process may require several soldering cycles that expose the material to temperatures in range of 250 °C. The polymer has to withstand that process without losing mechanical integrity leading to performance degradation. Furthermore, the reliability under harsh environmental conditions such as heat or humidity is one of the key factors supporting use of Dow Corning silicone material (type of polydimethylsiloxane – PDMS polymer) in communications applications. It has also been proven to maintain good performance under extensive periods of time in hot and humid environment [17].

The current interest in migrating this technology to longer telecommunications' wavelengths (1310 nm and 1550 nm) and to single mode waveguides has led to advancements in polymer materials engineered for this purpose. Some of the most promising materials have been listed in Table 3-2, but a larger number of types can be found in literature [18].

Table 3-2: Optical polymers developed for telecom applications

Manufacturer	Polymer Type [Trade Name]	Patterning Techniques	Propagation loss at 1550 nm [dB/cm]
Amoco [19]	Fluorinated polyimide [Ultradel]	Photoexposure / wet etch	1.0
DuPont [20]	Cyclotene	RIE	1.5
NTT [18]	Halogentaed acrylate	RIE	1.7
NTT [18]	Deuterated polysiloxane	RIE	0.43
Optical Crosslinks [21]	Acrylate [Polyguide]	Diffusion	0.6
Nissan Chemical [22]	Hybrid [Sunconnect]	Photoexposure	0.49
Dow Corning [23]	Polysiloxane	Photoexposure	1.5

Many of the aforementioned benefits for siloxane polymers are also applicable to the fabrication of compact EDWAs for applications other than optical backplanes. Thermal and environmental stability are key requirements for optical devices that require relatively high pumping power densities due to high Er concentrations involved. The siloxane materials used in this work have been developed by Dow Corning. They have been improved over the years to maintain their reliability and advantageous performance in PCB-integrated systems while improving their performance at higher telecom wavelengths. The latest material used in this work, named WG-2020 Optical Waveguide Core and WG-2021 Optical Waveguide Cladding, have been engineered not only to improve propagation losses at 1310 nm and 1550 nm, but also to allow for relaxed waveguide size restrictions due to a carefully designed refractive index difference.

Finally, all the elements required in a practical system, such as bends, crossings or splitters have been demonstrated in this material showing suitability for high transmission rate applications in more complex, integrated systems [23], [24]. The combination of all of the above factors combined with very low birefringence and high processability (adhesion, coating, dicing, etc.) makes Dow Corning polymer a good candidate for waveguide implementation in this work.

3.1.3 Waveguide Losses

There are a number of sources of loss in a Er-doped waveguide amplifier in addition to the Er absorption loss described in Chapter 2. In telecommunications systems a term

insertion loss is often used, which refers to the total difference between the optical power entering and leaving the system expressed as a ratio in decibels. In a typical optical fibre network it is also called fibre-to-fibre loss as the device is placed in-between input and output fibres.

3.1.3.1 Coupling Losses

In case of EDWAs, presence of the coupling loss necessitates a distinction between net and internal gain quoted for a given amplifier. One of the advantages of system integration on a single PIC is that this additional loss source can be greatly reduced or even eliminated depending on the design. However, if the erbium-doped device is to be externally pumped as well as the 1550 nm signal is coupled in and out of the device via optical fibres, coupling losses need to be accounted for.

In general, two contributors can be distinguished for this power degradation mechanism. The first one, called Fresnel loss, is related to the signal reflection of the waveguide facet and for a perfectly flat surface the reflected proportion of the incident field amplitude (***R***) is given by Equation (3.12).

$$R = \left[\frac{(n_2 - n_1)}{(n_2 + n_1)}\right]^2 \tag{3.12}$$

where n_1 and n_2 are the refractive indices of the media outside and inside of the waveguide. In a more realistic scenario, every facet will have certain roughness associated with it. As a result of that, the incoming light beam will reflect at slightly different angles leading to higher losses. In order to minimise the Fresnel loss, the refractive index contrast and waveguide surface roughness need to be kept as low as possible.

An additional source of loss when coupling a signal between different guiding elements is mode mismatch. Different geometries and sizes of the optical fibre and typical waveguides mean that the optical mode profiles do not match. This is usually taken into account by using a coupling efficiency factor (η_c) that can be quantified with a mode overlap integral given in Equation (3.13).

$$\eta_c = \frac{|\int E_1^* E_2 \, dA|^2}{\int |E_1|^2 dA \int |E_2|^2 dA} \tag{3.13}$$

where E_1 and E_2 are complex electric field amplitude distributions of a given mode over area A. The mode mismatch loss is the calculated by multiplying the signal energy with $1 - \eta_c$ to account for the light that is not coupled into the waveguide.

Both of the above coupling losses can be estimated through theoretical modelling of the above equations. A lot of studies have been performed to find ways of quantifying and minimising the loss, including for interfaces between optical fibres and rectangular waveguides [25].

3.1.3.2 Internal Losses

Attenuation of a light signal as it propagates through a waveguide is an important design parameter for EDWAs. There are multiple sources of loss in an optical transmission, but three main internal sources can be distinguished.

- Scattering Loss

First contributor that is important in dielectric waveguides used in this work is the scattering loss. This source of loss is a result of imperfections such as impurities or defects in the guiding layer itself or surface roughness at the core-cladding interface. Even if the fabrication process is optimised to reduce the volume imperfections to minimum some wavelength-dependent scattering is always present due to the Rayleigh scattering. It is particularly relevant in EDPWAs as the polymer host is doped with erbium particles and as a result non-negligible, excess scattering is introduced onto the beam propagation path resulting in some photon energy moving in other directions. The additional loss introduced ($\alpha_{Rayleigh}$) can be estimated using the following formula:

$$\alpha_{Rayleigh}\left[{}^{dB}/_{m}\right] = 4.34 \times C_{Rayleigh} \times N \times \Gamma \qquad (3.14)$$

where N is the particle density [m^{-3}] and Γ is the overlap factor between the guided mode and the waveguide region with scattering particles. The Rayleigh scattering coefficient ($C_{Rayleigh}$ [m^2]) can be calculated using Equation (3.15) [26].

$$C_{Rayleigh} = \frac{(2\pi)^5}{48} \times \frac{d^6}{\lambda^4} \times n_m^4 \times \left(\frac{n_n^2 - n_m^2}{n_n^2 + 2n_m^2}\right)^2 \qquad (3.15)$$

where d is the diameter of the particle [m], λ is the signal wavelength [m] and n_m and n_n correspond to the refractive indices of the host matrix and the particle, respectively. This method has been proven to work well to estimate the volume scattering loss in case of

nanoparticles doped material where the NP size is over an order of magnitude smaller than light wavelength, distance between particles is comparable to their size and their size is narrowly distributed without clustering [27].

The second source of scattering occurs due to thickness fluctuations in different layer interfaces between core and cladding. This is particularly problematic in multi-mode structures where more interaction between light and surface takes place. This loss can be estimated using ray optic theory [28] and is proportional to the surface roughness and inversely proportional to the refractive index contrast [29]. As a result, it is not expected to play a significant role in this work as the developed EDPWAs are single mode structures with low refractive index contrast and siloxane polymers chosen have been shown to have surface roughness below 50 nm [30].

- Absorption Loss

Another key type of loss in a waveguide is the absorption loss occurring when photon's energy is transferred into the host material's atoms. It depends on the molecular structure of the used material and is particularly important in semiconductors, but also present in glasses and dielectrics. A lot of effort has been made in polymer engineering in order to reduce losses at various wavelengths. This has been particularly important in organic materials designed for telecommunications applications where a shift from original low-loss window of 850 nm towards second and third communications windows of 1310 nm and 1550 nm respectively has been underway [31].

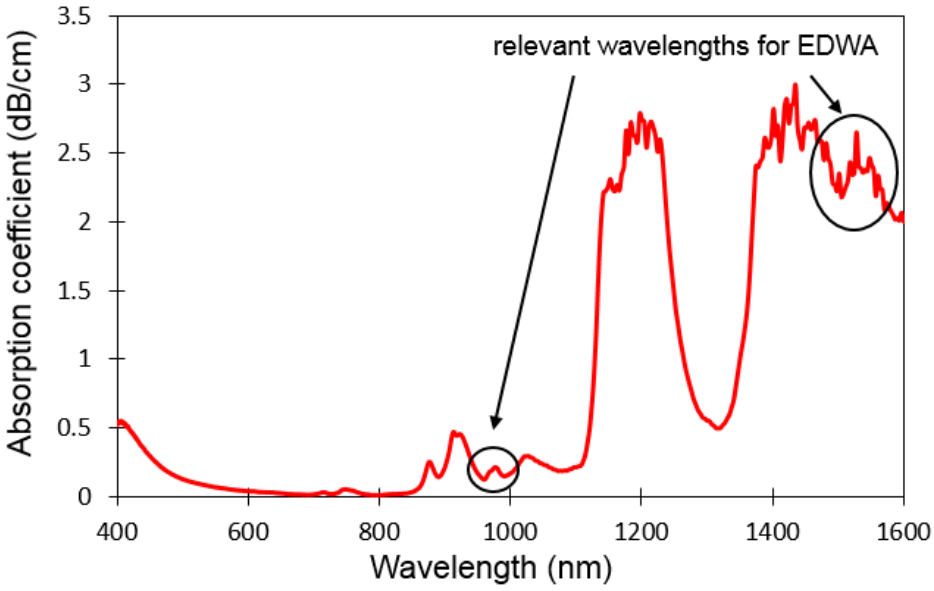

Figure 3-4: Straight waveguide loss variance with light wavelength for Dow Corning siloxane polymer measured on a 10-cm-long multimode waveguide [13]

Even though it may be complicated to measure accurately the internal losses of a waveguide, several techniques exist to achieve this. The most popular, albeit destructive, method is through a cut-back comparison of different length's of waveguides [32].

The internal loss of an older generation of the same type of the polymer material as used in this work has already been done as shown in Figure 3-4. The two key EDWA spectral regions of 980 nm for pumping and 1550 nm for signal are highlighted showing losses of around 0.2 dB/cm and 2.4 dB/cm, respectively. It must be kept in mind that these values were measured for a waveguide with a larger cross-section and as a result in multi-modal operation. Therefore, the above values are only taken as reference as they will vary depending on the waveguide geometry and size used for more compact devices in this work.

- Bending Loss

Finally, a potential source of signal loss, particularly relevant for photonic integrated circuits is linked to components with non-straight features and corners. Bending loss is determined by a combination of factors such as the curve radius, refractive index difference and waveguides size. It is more problematic for low-index-contrast systems, such as polymers, as it limits the density and size of used components. This work mainly focuses on straight waveguides, so it is not considered an important source of attenuation.

3.1.4 Refractive index

Another important factor when designing waveguide-based systems is the refractive indices of core and cladding layers. The advantage of siloxanes is that they have a wide range of values ranging between 1.4 and 1.54 [33] and can be tuned accurately depending on what is required for a given application. The great amount of control allows for a very small refractive index difference ($\boldsymbol{\Delta n}$) between core and cladding of approximately 0.0065 and gives an opportunity for generation of single mode features with relatively large cross-sections.

Dow Corning WG2020 and WG2021 polymers used have been provided with refractive index data for 470-1310 nm range. In order to calculate the values for other required wavelengths a Sellmeier formula [34] has been employed as presented in Equation (3.16).

$$n(\lambda) = \sqrt{1 + \sum_j \frac{B_j \lambda^2}{\lambda^2 - C_j}} \tag{3.16}$$

where $n(\lambda)$ is a wavelength-dependent refractive index while B_j and C_j are pairs of constants used to describe the relationship. A non-linear regression algorithm [35] was used to fit known data points into the formula and derive the coefficients. It has been first run on a well-defined fused silica glass [36] and then the polymer data giving the coefficient pairs listed in Table 3-3.

Table 3-3: Derived Sellemier coefficients for fused silica glass and Dow Corning WG2020 and WG2021 polymers

Coefficient	Fused silica glass		WG2020		WG2021	
	2 pairs	3 pairs	2 pairs	3 pairs	2 pairs	3 pairs
B_1	1.1037	0.7025	0.8412	0.7873	0.8318	0.7808
C_1	0.09	0.0687	0.015675	0.015675	0.014568	0.014568
B_2	0.5229	0.4016	0.4412	0.3879	0.4318	0.3819
C_2	7.6752	0.1165	0.015675	0.015675	0.014593	0.014593
B_3	-	0.8973	-	0.1073	-	0.1009
C_3	-	9.8952	-	0.015675	-	0.014593

For all of the above coefficients the correlation factor between the generated plots and original points was above 0.999 and the root mean square error (RMSE) below 0.0005. The resultant coefficients have been used to plot the refractive index for all three materials in Figure 3-5.

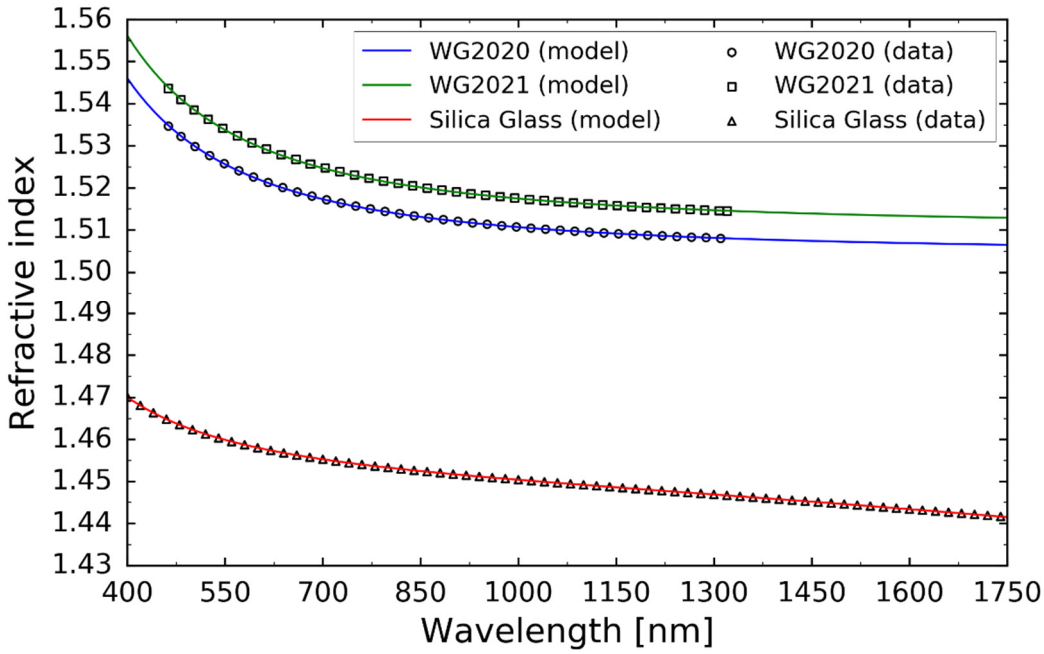

Figure 3-5: Refractive index variance with light wavelength for Dow Corning siloxanes and fused silica as a reference

When designing a waveguide-based amplifier for a single-mode operation one has to keep in mind the fact that the refractive index of the polymer is different at the two spectral regions of interest. The values used for the simulations and simulations of various designs presented in this work are listed in Table 3-4.

Table 3-4: Key refractive index values used in this work

Material	980 nm	1550 nm
WG-2020 core	1.5178	1.5135
WG-2021 cladding	1.5110	1.5071
Refractive index contrast	0.0068	0.0064
Fused silica glass substrate	1.4507	1.4440

3.2 Waveguide Architectures and Simulations

The waveguide theory introduced in section 3.1.1 has been based on a planar structure with only one dimensional confinement. In practice three-dimensional waveguides are used and the light is controlled in both x- and y-directions to maximise the mode overlap in the active EDWA region as well as implemented in more complex structures such as

bends and splitters. There exists a number of practical designs for such structures with the most common geometries shown in Figure 3-6.

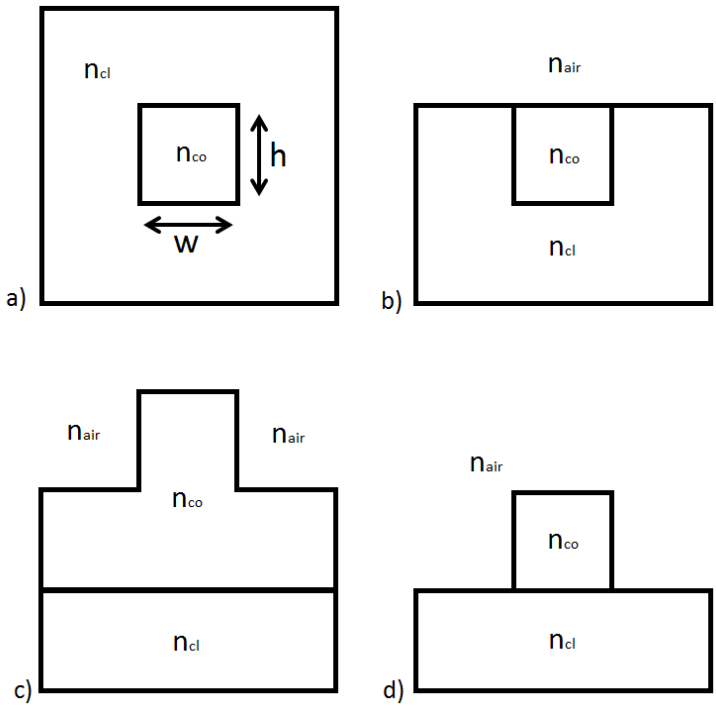

Figure 3-6: Waveguide geometries: a) channel, b) embedded, c) rib, d) ridge

The above structures can be implemented using the introduced polymer core and cladding materials, but also combined with other media such as silica glass or Er-doped polymers. With the exception of the channel waveguide, the above designs have different refractive indices (air - n_{air} or cladding - n_{cl}) surrounding the core medium n_{co} introducing an asymmetric shape to the modes propagating through the structure. As a result, the calculations of mode profiles are much more complex than in the case of a slab waveguide presented before. The pure TE or TM modes are no longer supported in these structures, hence an approximate analysis of TEM hybrid modes polarised along the x- and y-axis that resemble the basic light modes in a 2D structure has to be employed throughout this work.

3.2.1 Channel Polymer Waveguide

The initial simulated system assumes a channel waveguide of square cross-section. This is a standard architecture employed in many EDWA systems and offers a good benchmark for other structures. Another benefit of starting with a simple and symmetric case is that it allows for intuitive assessment of the mode orders supported by the structure with examples shown in Figure 3-7.

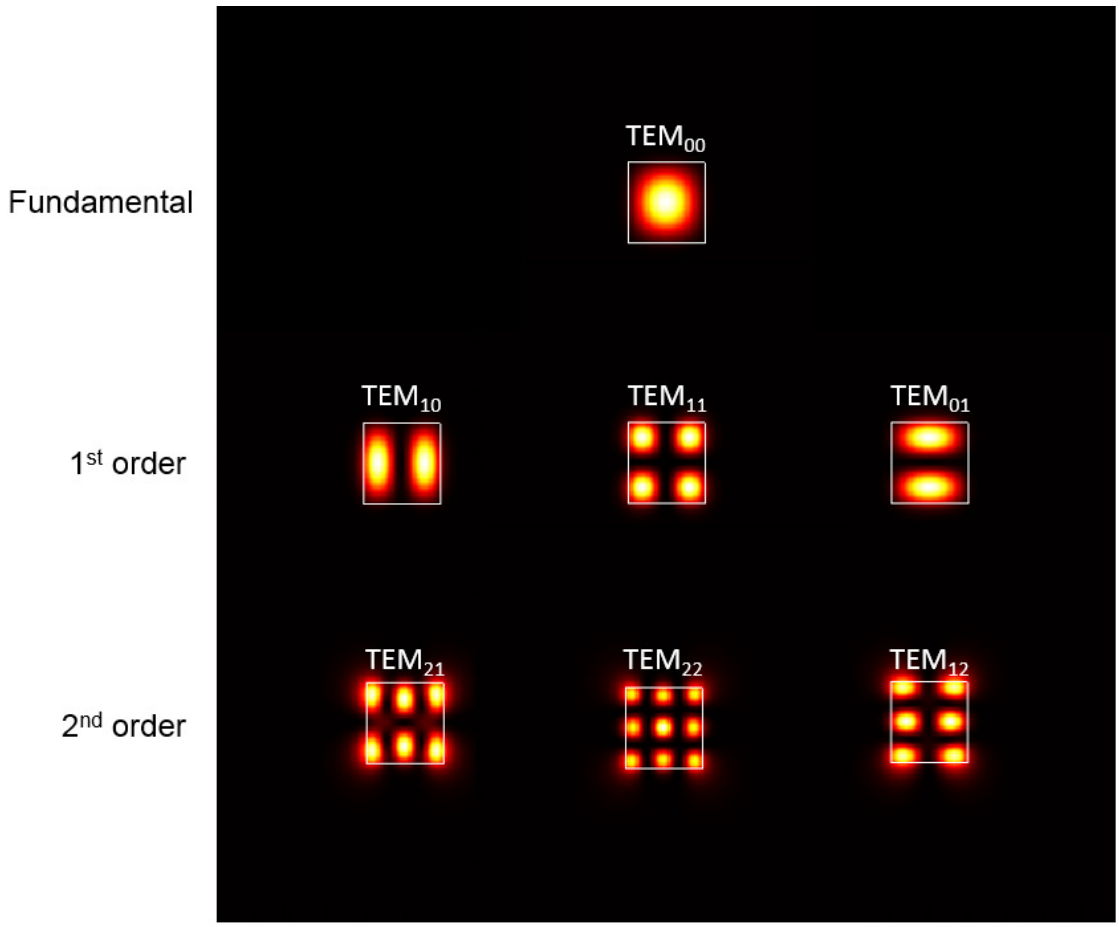

Figure 3-7: Examples of light intensity profiles and their orders in a square waveguide

The refractive index data for Dow Corning WG2020 core and WG2021 is used to begin with. These results offer a chance to simulate a benchmark system with minimum achievable refractive index contrast of 0.0064 for a 1550 nm signal. The results of these simulations shown in Figure 3-8 (a) allow one to quantify the maximum size of a channel waveguide to support single mode operation. In case of the EDWA signal band, the maximum size of a waveguide side is estimated to be approximately 7.5 μm before the first order modes become weakly guided. This size limit is even stricter when simulations are run at the EDWA pump band of 980 nm as shown in Figure 3-8 (b). Even though the refractive index contrast is only slightly greater, the waveguide width and height requirement is reduced to 4.5 μm. While it is crucial for the system to remain single mode (SM) around 1550 nm, it is not a firm requirement for the pump wavelength. It has been shown in literature that even though a multimode behaviour at 980 nm reduces the potential efficiency of an amplifier device due to lower confinement, high gain is still possible [37]. The difference in achievable gain is relatively small and can be minimised by either pumping the device from both ends or adjusting the optimal EDWA length.

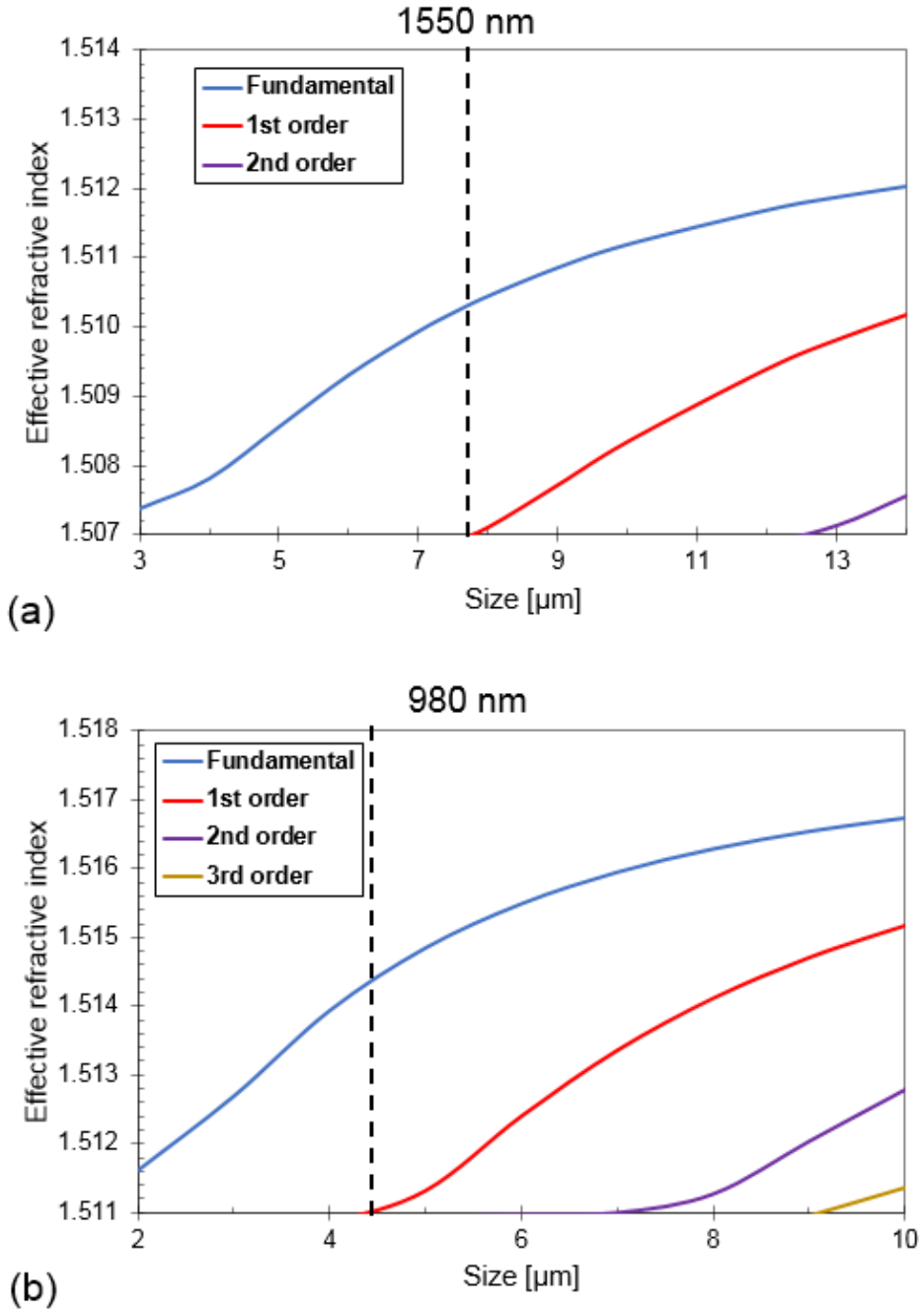

Figure 3-8: Mode orders supported in a square polymer channel waveguide at (a) 1550 nm and (b) 980 nm

3.2.2 Channel Er-doped Waveguide

A polymer-only system is a good starting point for analysis, however, an introduction of erbium ions into the material results in an increase of the refractive of this region. In general, the higher the dopant concentration, the higher the refractive index of the active core of the waveguide [38]. In this report, an introduction of 1 wt.% Er (equivalent to an erbium concentration of approximately 0.91×10^{21} cm^{-3}) into the material results in a refractive index increase of 0.093 in this layer at 1550 nm.

It is therefore crucial for the change in the refractive index to be taken into account when designing EDWA devices. One of the possible approaches is to fix the device size and investigate the limit in the refractive index contrast for SM operation as shown in Figure 3-9. In case of a channel waveguide device with fixed a 2×2 μm^2 area, a refractive index difference between cladding and Er-doped core can be slightly over 0.09 for single mode operation. The advantage of keeping the size and refractive index contrast as close as possible to the transition point of the monomode operation is that the fundamental mode confinement factor is maximised leading to more efficient EDWA performance.

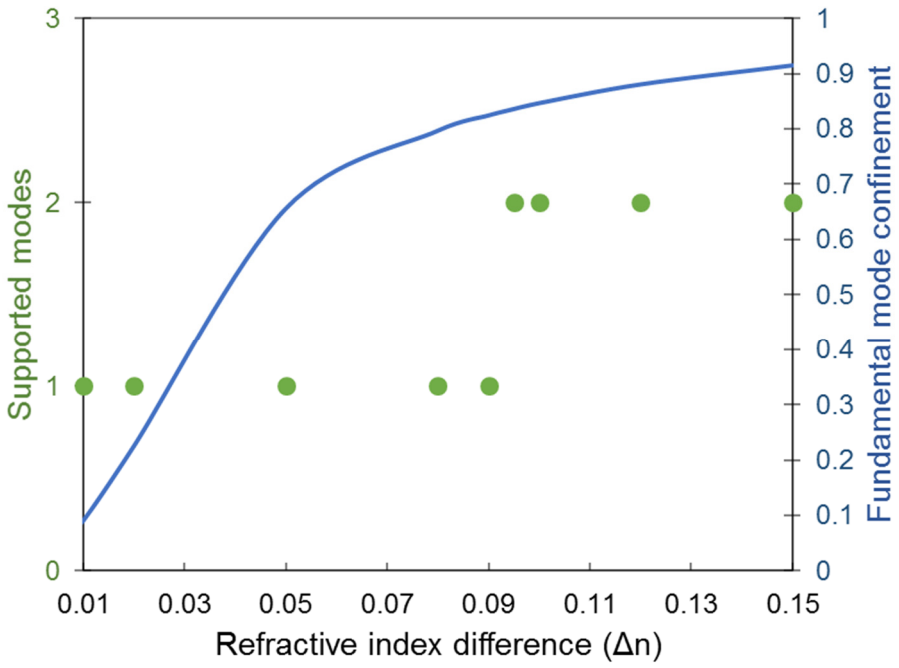

Figure 3-9: Number of supported modes and fundamental mode confinement dependence on refractive index contrast in a 2×2 μm^2 channel waveguide

Even though the channel size of 2×2 μm^2 is chosen as a benchmark for the full EDWA model based on the polymer platform employed in this work, alternative combinations of size and core refractive index can be used. A non-exhaustive list of potential combinations is plotted in Figure 3-10.

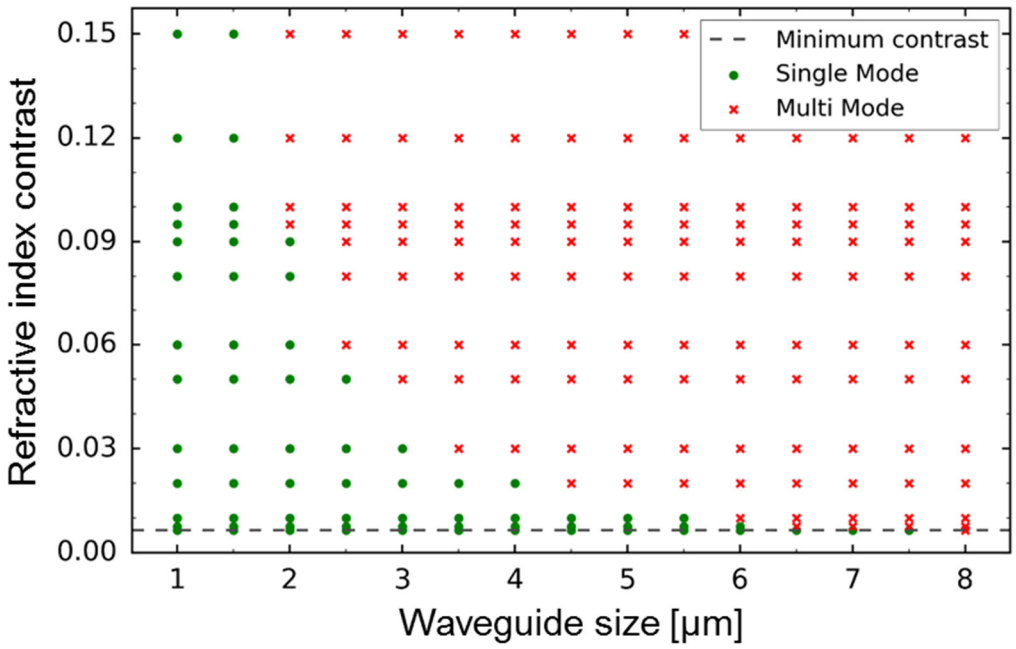

Figure 3-10: Single- and multi-mode regimes of operation for polymer doped with erbium

In the above figure, a discrete range of refractive index contrasts and square channel waveguide sizes is shown. The distinction between SM and MM is based on the number of modes fulfilling the guiding requirement of $n_{cl} < n_{eff} < n_{co}$. The wavelength is assumed to be 1550 nm and the refractive index of the polymer cladding remains unchanged at 1.5071. The investigated waveguide size range starts at a micron and increases to the point where SM operation is not possible even in an all-polymer system. Not surprisingly, a trade-off between the allowable waveguide dimension and the refractive index contrast is observed. Therefore, it must be kept in mind when designing practical EDWAs that by increasing the doping concentration the maximum size of the waveguide becomes further limited in order to ensure single mode operation.

3.3 EDWA Model

All the key characteristics of an erbium system and the resulting EDWA parameters have been covered in Chapter 2 and the remaining amplifier design parameters based on the polymer platform introduced in the previous section. Once all of these are combined, behaviour of the erbium-doped waveguide amplifier can be predicted.

An EDWA can be modelled using rate equations for a multi-level system. The energy diagram for relevant levels including interactions between erbium and ytterbium ions is

shown on Figure 3-11. Throughout this work a 976-nm pump is used for both simulations and experimentally, due to the Yb co-doping efficiency benefit explained in the previous chapter.

When pumped at this wavelength, the photons are absorbed by either erbium resulting in ion being promoted from level $^4I_{15/2}$ to $^4I_{11/2}$ or ytterbium where a corresponding change from level $^2F_{7/2}$ to $^2F_{5/2}$ occurs. The corresponding pumping rates are $\boldsymbol{W_{13}}$ and $\boldsymbol{W_{56}}$. If the case of the second transition, it is then usually followed by a fast energy transfer to a neighbouring erbium ion's state $^4I_{11/2}$ at a rate of $\boldsymbol{C_{cr}}$. From the excited state the ions then non-radiatively decay to the metastable level $^4I_{13/2}$ with a corresponding rate of $\boldsymbol{A_{32}}$. This process is typically very rapid in range of a few to few hundred microseconds depending on the phonon energies of the host material. The lifetime at the metastable level is usually found to be in range of a few milliseconds, resulting in a build-up of Er ions that later go back to the ground state radiatively through either stimulated or spontaneous emission. These energy transfers have been used to describe EDFA systems used in telecoms, but in case of EDWAs additional transitions need to be taken into account due to the very high dopant densities leading to upconversion phenomena. As a result, the model also includes a probable transfer from level $^4I_{13/2}$ to $^2H_{11/2}$ that accounts for processes of excited state absorption and energy transfer upconversion explained in the previous chapter.

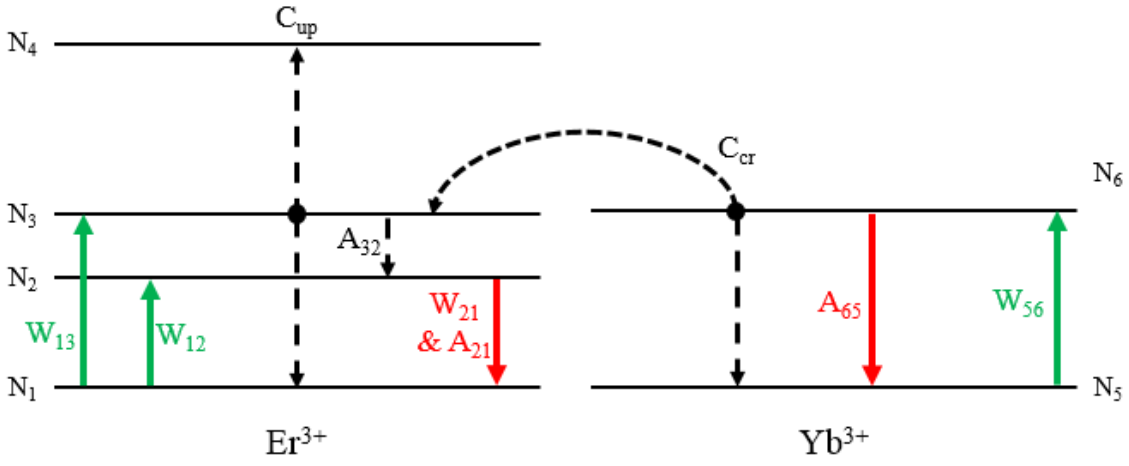

Figure 3-11: Energy diagram with key state transitions in an erbium-ytterbium co-doped system

All the above interactions can then be combined and modelled by using rate equations. The erbium populations and changes between them due to different excitation and emission processes are described as follows.

$$\frac{dN_1}{dt} = -W_{13}N_1 + W_{21}N_2 - W_{12}N_1 + A_{21}N_2 + C_{up}{N_2}^2 - C_{cr}N_1N_4 + C_{up}{N_3}^2 - C_{cr}N_1N_6 \tag{3.17}$$

$$\frac{dN_2}{dt} = W_{12}N_1 - A_{21}N_2 - W_{21}N_2 + A_{32}N_3 - 2C_{up}{N_2}^2 + 2C_{cr}N_1N_4 \tag{3.18}$$

$$\frac{dN_3}{dt} = W_{13}N_1 - A_{32}N_3 + A_{43}N_4 - 2C_{up}{N_3}^2 + C_{cr}N_1N_6 \tag{3.19}$$

$$\frac{dN_5}{dt} = -W_{56}N_5 + A_{65}N_6 + C_{cr}N_1N_6 \tag{3.20}$$

$$N_1 + N_2 + N_3 + N_4 = N_{Er} \tag{3.21}$$

$$N_5 + N_6 = N_{Yb} \tag{3.22}$$

where N_1, N_2, N_3, and N_4 are the populations of the erbium levels $^4I_{15/2}$, $^4I_{13/2}$, $^4I_{11/2}$, and $^2H_{11/2}$, respectively. The ytterbium levels of $^2F_{7/2}$, and $^2F_{5/2}$, are represented by N_5 and N_6, while the total concentrations of Er^{3+} and Yb^{3+} are N_{Er} and N_{Yb}. C_{up} and C_{cr} are coefficients corresponding to upconversion and cross-relaxation between various energy levels needed to represent energy transfer between Er-Yb neighbours as well as the cooperative upconversion process. A_{21} and A_{65} are the spontaneous emissions from both ion types while A_{32} and A_{43} are non-radiative relaxations between different energy levels. The stimulated transitions are represented by W terms and calculated with the following formulas:

$$W_{21} = \frac{\sigma_{21}(\nu_s)}{h\nu_s} I_s(x,y,z,t,\nu_s) + \sum_j \frac{\sigma_{21}(\nu_j)}{h\nu_j} [I_{ASE+}(x,y,z,t,\nu_j) + I_{ASE-}(x,y,z,t,\nu_j)] \tag{3.23}$$

$$W_{12} = \frac{\sigma_{12}(\nu_s)}{h\nu_s} I_s(x,y,z,t,\nu_s) + \sum_j \frac{\sigma_{12}(\nu_j)}{h\nu_j} [I_{ASE+}(x,y,z,t,\nu_j) + I_{ASE-}(x,y,z,t,\nu_j)] \quad (3.24)$$

$$W_{13} = \frac{\sigma_{13}(\nu_p)}{h\nu_p} [I_{p+}(x,y,z,t,\nu_p) + I_{p-}(x,y,z,t,\nu_p)] \quad (3.25)$$

$$W_{56} = \frac{\sigma_{56}(\nu_p)}{h\nu_p} [I_{p+}(x,y,z,t,\nu_p) + I_{p-}(x,y,z,t,\nu_p)] \quad (3.26)$$

where σ_{12}, σ_{13} and σ_{21}, σ_{56} are the absorption and emission cross-sections for a given energy transition, respectively. Signal, pump and ASE signal intensities and photon frequencies are represented by I_s, I_p, I_{ASE}, and ν_s, ν_p, ν_{ASE}, respectively, while h is the Planck's constant. In order to get more accurate results, both ASE (I_{ASE}) and directionality of the signals (+/- indicators) have been taken into account. In case of the amplified spontaneous emission, the erbium emission bandwidth is divided into a finite number of spectral intervals to reflect the noise generated in the amplifier. The power change along the length of the amplifier is described by using the propagation equations for all three signals (P_p, P_s, P_{ASE}) shown below.

$$\frac{dP_{p\pm}(z)}{dz} = -P_{p\pm}(z) \iint_A \psi_p(x,y) \left[\sigma_{13}(\upsilon_p) N_1(x,y,z) + \sigma_{56}(\upsilon_p) N_5(x,y,z)\right] dxdy - l_p P_{p\pm}(z) \quad (3.27)$$

$$\frac{dP_s(z,\upsilon_s)}{dz} = P_s(z,\upsilon_s) \iint_A \psi_s(x,y) [\sigma_{21}(\upsilon_s) N_2(x,y,z) - \sigma_{12}(\upsilon_s) N_1(x,y,z)] dxdy - l_s P_s(z) \quad (3.28)$$

$$\frac{dP_{ASE\pm}(z,\upsilon_j)}{dz} = \pm P_{ASE\pm}(z,\upsilon_j) \iint_A \psi_s(x,y) \left[\sigma_{21}(\upsilon_j) N_2(x,y,z) - \sigma_{12}(\upsilon_j) N_1(x,y,z)\right] dxdy \pm h\upsilon_j \Delta\upsilon_j \iint_A \psi_s(x,y) \sigma_{21}(\upsilon_j) N_2(x,y,z)\, dxdy \mp l_j P_{ASE\pm}(z,\upsilon_j) \quad (3.29)$$

where parameters l_s, l_p and l_j correspond to losses in the waveguide for signal, pump and ASE respectively. $\Psi_p(x,y)$ and $\Psi_s(x,y)$ are the normalised field intensity profiles, while Δv_j and A represent spectral resolution of ASE and cross-section area of the ion-doped region.

In order reduce the number of parameters in Equations (3.27)-(3.29), mode overlap factors are introduced. These are used to represent the overlap integral between the optical field distribution of a given signal and the dopant ions [39].

$$\Gamma_p = \iint_A \psi_p(x,y) N_i(x,y)\, dxdy \tag{3.30}$$

$$\Gamma_s = \iint_A \psi_s(x,y) N_i(x,y)\, dxdy \tag{3.31}$$

where $N_i(x,y)$ is the normalised cross-sectional Er-Yb ion distribution. Throughout the simulations performed in this work, the overlap factor is considered to be equal to the overlap between the guided mode and the total ion concentration as well as independent of the optical power. These are valid approximations in systems with dopant population well-confined to the active region and intensity not varying significantly over the transverse dopant profile. The system is investigated in a steady state, when the rate of change is equal to zero, i.e. $dN_i/dt=0$, with Equations (3.30)-(3.31) substituted into Equations (3.27)-(3.29) as shown below.

$$\frac{dP_{p\pm}(z)}{dz} = -\Gamma_p[\sigma_{13}N_1(z) + \sigma_{56}N_5(z)]P_{p\pm}(z) - l_p P_{p\pm}(z) \tag{3.32}$$

$$\frac{dP_s(z,\upsilon_s)}{dz} = \Gamma_s[\sigma_{21}(\upsilon_s)N_2(z) - \sigma_{12}(\upsilon_s)N_1(z)]P_s(z,\upsilon_s) - l_s P_s(z) \tag{3.33}$$

$$\begin{aligned}\frac{dP_{ASE\pm}(z,\upsilon_j)}{dz} = {} & \pm\Gamma_s\left[\sigma_{21}(\upsilon_j)N_2(z) - \sigma_{12}(\upsilon_j)N_1(z)\right]P_{ASE\pm}(z,\upsilon_j) \\ & \pm h\upsilon_j\Delta\upsilon_j\Gamma_s\sigma_{21}(\upsilon_j)N_2(z) \mp l_j P_{ASE\pm}(z,\upsilon_j)\end{aligned} \tag{3.34}$$

The model is solved numerically and run using commercially available VPI Photonics software that employs the above equations. The length of the amplifier is divided into smaller sections of length Δz and then solved at each interval and calculated until the difference in gain figure between the consecutive iterations is below 0.001 dB.

3.4 Theoretical EDWA Studies

The parameters used for theoretical EDWA feasibility studies in this chapter are listed in Table 3-5. The simulations are based on a channel waveguide with cross-section of 2×2 μm^2 with overlap factors derived through FimmWave simulations. The maximum available dopant concentration of 1.63 × 10^{27} m^{-3} is used as this corresponds to the reported value for the ion implantation technique used in this work [40]. Remaining parameters are selected based on literature reports on similar systems where various types of erbium particles are doped in to polymer systems.

Table 3-5: Key EDWA simulation parameters and their sources used in this section

Parameter	Sym.	Value used	Reported for similar systems
Er concentration	N_{Er}	max 1.63 × 10^{27} m^{-3} [40]	-
Yb concentration	N_{Yb}	max 1.63 × 10^{27} m^{-3} [40]	-
Er lifetime	τ_{Er}	9.1 ms [40]	up to 13.2[38] ms
Yb lifetime	τ_{Yb}	1.5 ms [37]	0.78[41] – 2.0[42] ms
Er absorption (1533)	σ_{12}	5.13 × 10^{-25} m^2	3.45-16.2 [43] × 10^{-25} m^2
Er emission (1533)	σ_{21}	5.13 × 10^{-25} m^2	3.79-18.6 [43] × 10^{-25} m^2
Er absorption (975)	σ_{13}	2.54 × 10^{-25} m^2 [44]	2.0[45] – 9.9[46] × 10^{-25} m^2
Yb absorption (975)	σ_{56}	1.42 × 10^{-24} m^2 [37]	0.25[42] -10[47] × 10^{-24} m^2
Er-Yb cross-relaxation	C_{cr}	2.3 × 10^{-22} m^3s^{-1}	0.7[42] – 3.4[48] × 10^{-22} m^3s^{-1}
Upconversion coefficient	C_{up}	varied	0.8[37] – 10[42] × 10^{-23} m^3s^{-1}
Overlap factors	Γ_s,Γ_p	0.83, 0.81	-
Active region area	A	4 μm^2	-
Background loss	l_s,l_p,l_j	1 dB/cm	-

In addition to the values used in this work, a range of reported parameters from various sources is listed as a reference. This shows that very often implementations of similar devices and corresponding models result in different values of the same parameter

depending on the fabrication technique as well as complexity of the simulation. Furthermore, a lot of modelling work based on Al_2O_3 systems have been done in the past leading to development of sophisticated models and highly accurate parameter values confirmed by multiple sources [49]–[52] which is not always the case with other materials as seen by some of the parameter value ranges in Table 3-5.

The amplifier length step size for the simulations was fixed at 100 μm and the input power was set at 10 μW while the pump power was varied to see how it impacts the achievable gain. In the rest of this section different design parameters are varied in order to optimise the structure of the EDWA in terms of the achievable internal gain and to investigate feasibility of obtaining 10 dB/cm gain using the polymer platform combined with ion implantation technique.

3.4.1 Concentration

The first investigated design parameter was the concentration of erbium ions in a 1-cm-long waveguide. The pump power incident on the device was varied between 0 and 600 mW while all the other design parameters were kept constant. The maximum reported erbium concentration achieved through ULPI was 1.63×10^{27} m^{-3} and this value was used as the highest level. The upconversion factor was kept at 0.8×10^{-23} m^3s^{-1} [37] for this part of analysis.

Figure 3-12 shows the change in internal gain with an increase of the pumping power for a number of selected erbium ion concentrations. At lower Er doping levels, the maximum gain can be achieved with relatively low power before it becomes constant and an increased pumping has little effect. For example, at Er concentration of 1.63×10^{26} m^{-3} the maximum gain of approximately 1.6 dB is reached at 300 mW, but only a third of this power is needed to gain 1.4 dB. As the concentration is increased, the maximum achievable gain becomes higher culminating with 20.5 dB at the highest concentration at the maximum power of 600 mW. However, a number of observations can be made with respect to this trend. The higher the number of erbium ions, the greater the pump power needed to reach the gain saturation point. In most practical devices, the sustainability and availability of intensive pumping may be limited. Therefore, it can be observed that having maximum possible Er concentration is desirable for systems where more than 180 mW of pump power is available. Below this level, it is beneficial to reduce the number of dopant ions as higher internal gain can be obtained.

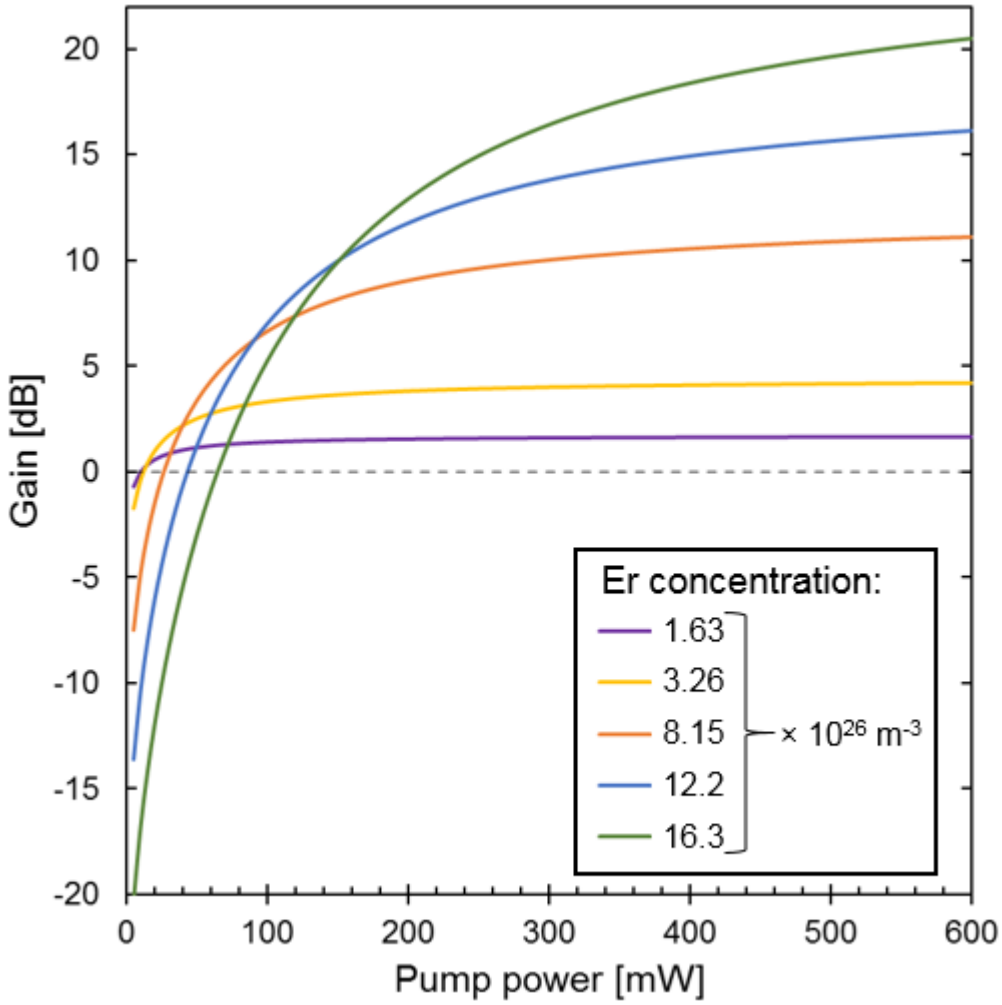

Figure 3-12: Dependence of internal gain on pump power for different erbium concentrations

In order to understand better the mechanisms behind the benefit of lowering the erbium concentration, analysis of the population of the excited $^4I_{13/2}$ state along the devices is needed. Figure 3-13 tracks the percentage of Er ions that can be found on this level when the EDWA device is pumped at a relatively low 50 mW. It can be observed that by increasing the number of erbium ions at a fixed pump power the population inversion becomes lower. In case of 1.63 × 10^{26} m^{-3} ions, 50 mW is enough to reach the gain saturation which is confirmed by having a constant inversion percentage along the device. It is worth noticing that due to the upconversion process happening inside of the amplifier, it is impossible to have 100% of Er ions in the $^4I_{13/2}$ state as a proportion of them will be excited to even higher levels. At this pump power the highest gain of 3.4 dB is achieved when Er concentration is at 8.15 × 10^{26} m^{-3} which corresponds to a relatively high population inversion with a large number of dopants. After this point, the increase in concentration leads to a reduced gain due to insufficient power to maintain a large

population inversion. When the number of ions is so high that the level drops below 50%, the absorption process dominates over stimulated emission and results in signal loss at the far end of the device from the pump.

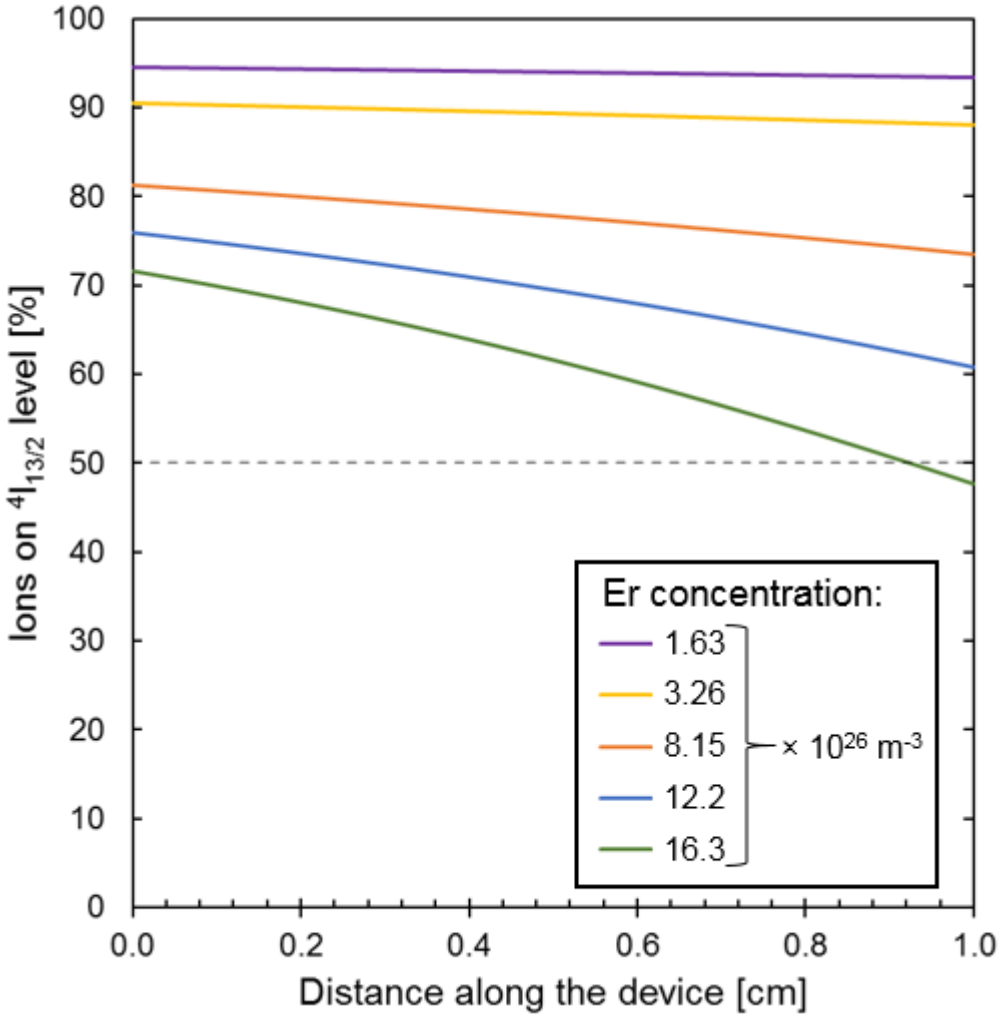

Figure 3-13: Er population inversion along EDWA pumped at 50 mW with various dopant concentrations

Fabrication techniques used in this work offer flexibility in terms of the ion concentration which means that the system can be optimised with power requirements in mind. Figure 3-14 presents optimal dopant concentrations for a number of pump powers. Depending on application, a maximal pump intensity may be a limiting factor which then results in reduced need for extremely high dopant concentrations. The maximum concentration of 1.63×10^{27} m^{-3} provides the highest gain at high power above 180 mW, but below this it is beneficial to reduce the erbium content. For example, if only 50 mW of pump power is available the optimal concentration for this 1-cm-long EDWA is much lower at approximately 6.5×10^{26} m^{-3}.

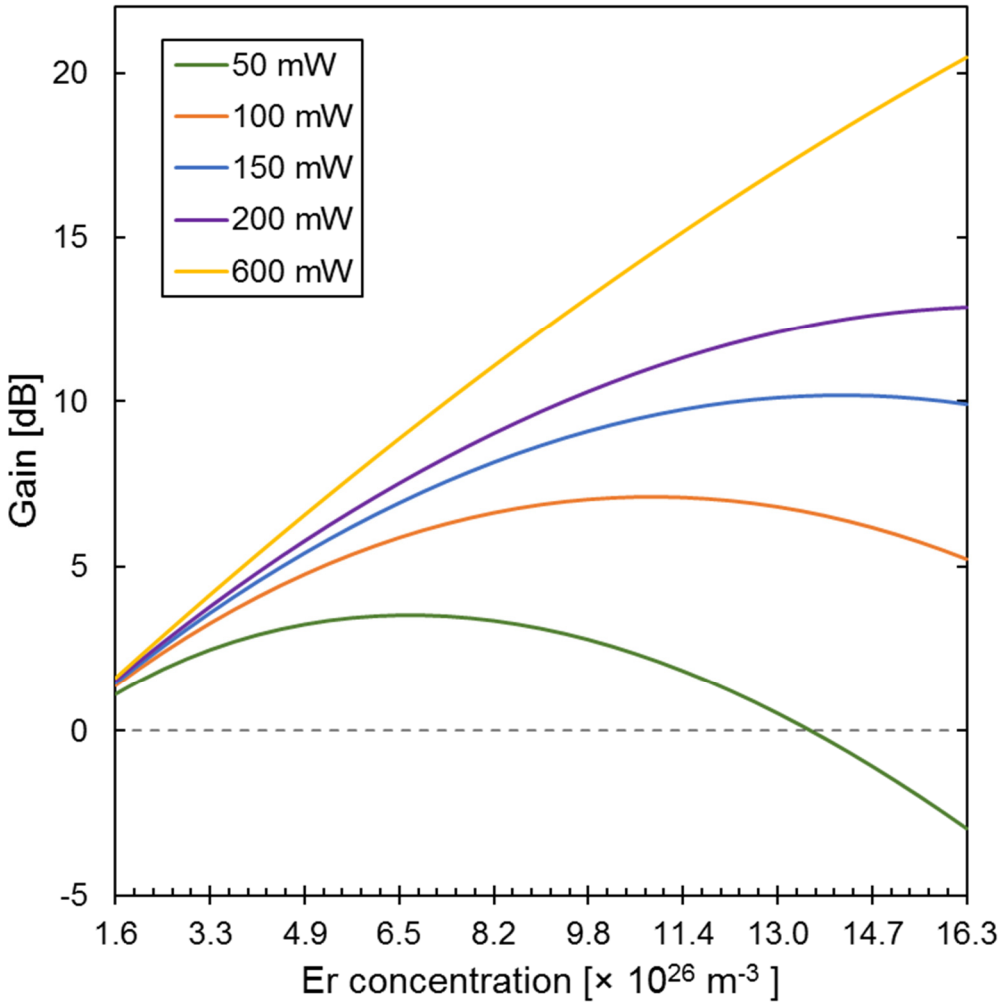

Figure 3-14: Optimal erbium doping concentration for a range of pumping powers

3.4.2 Length and Scalability

A practical EDWA requires high gain per unit length as investigated in pervious section, but in many cases 1-cm-long device will not be able to provide enough gain. As a result, it important to investigate how well the device scales. Figure 3-15 shows results of such gain analysis for EDWA devices of varied Er concentration and a fixed pump power of 200 mW. Initially, for every ion concentration the internal gain scales linearly with length. However, the greater the concentration the sooner this relationship ceases to apply. At 8.15×10^{26} m^{-3} this is still the case up to 5 centimetres when pumped at 200 mW. As the concentration is increased, the pump power becomes insufficient to create population inversion along the entire length of the device. Throughout a short distance along the device the population inversion becomes lower and eventually drops below 50% resulting in signal reabsorption happening at faster rate than stimulated emission as discussed in the previous section.

In the figure below, it can be noticed that Er concentrations of 8.15, 12.2 and 16.3 × 10^{26} m^{-3} provide maximal gain of 23.1 dB, 19.4 dB and 15.6 dB for different EDWA lengths of 3.9, 2.4 and 1.6 cm, respectively. Despite the fact that, with a careful erbium concentration selection, the internal gain of EDWA increases with distance, resulting improvement is not linear. Using the optimised gains for lengths of 1.6, 2.4 and 3.9 cm, the corresponding gain per unit length is 9.8, 8.1 and 5.9 dB/cm. It is therefore important to keep in mind that while with careful design a higher overall gain is possible with increased distance, the efficiency becomes lower. With the design used in this model, a maximum gain of 24 dB over 5-cm-long EDWA is achievable when pumped at 200 mW and Er concentration is set at 6.1 × 10^{26} m^{-3}.

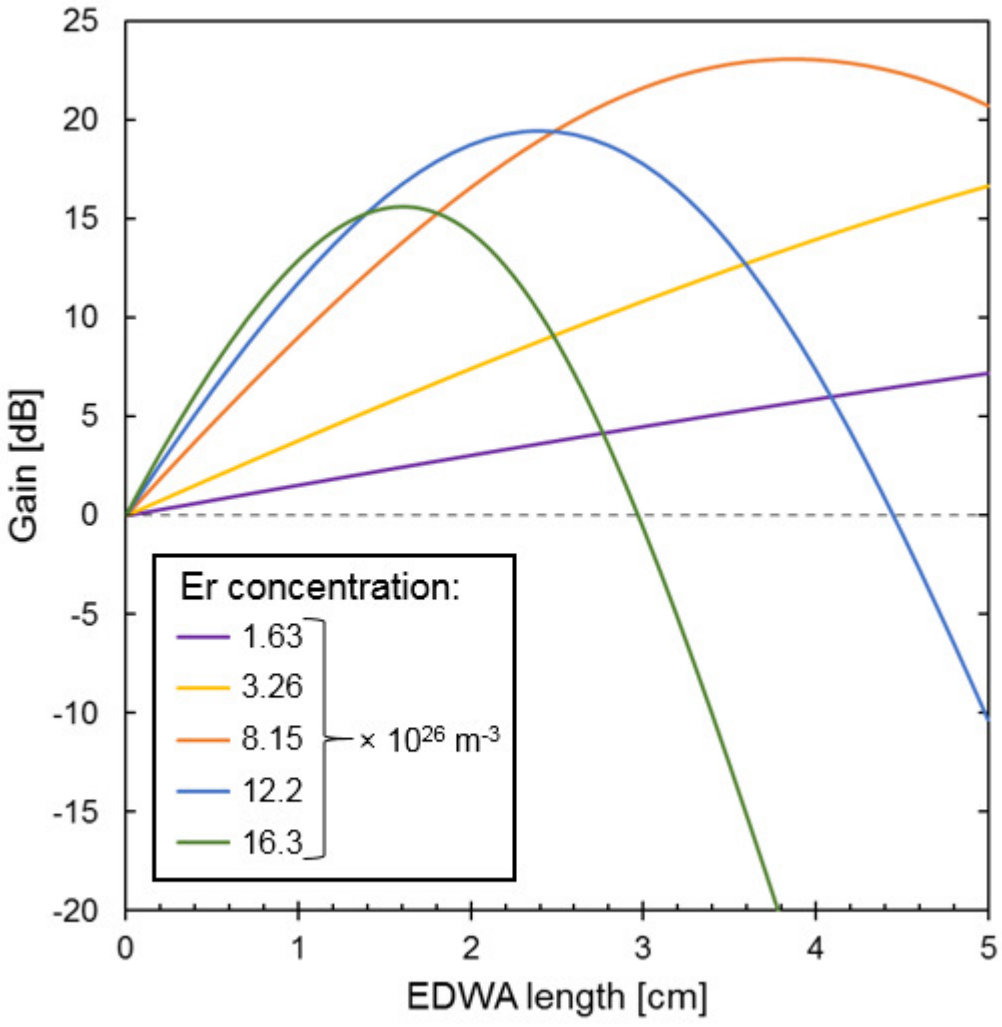

Figure 3-15: Dependence of internal gain on EDWA length for different erbium concentrations pumped at 200 mW

The above analysis assumed that the pump power is fixed at 200 mW, but in the same way as for the 1-cm-long device, a different value may be available for different

applications. Figure 3-16 depicts the impact of changing the assumed power while keeping the Er concentration at a constant level of 8.15×10^{26} m^{-3}. As in case of varying the concentration, there is a different optimal device length depending on the supplied power. Across the investigated range of 50 to 600 mW, the maximum gain increases from 3.6 dB in a 1.3-cm-long amplifier to 36.3 dB in a 5-cm-long one.

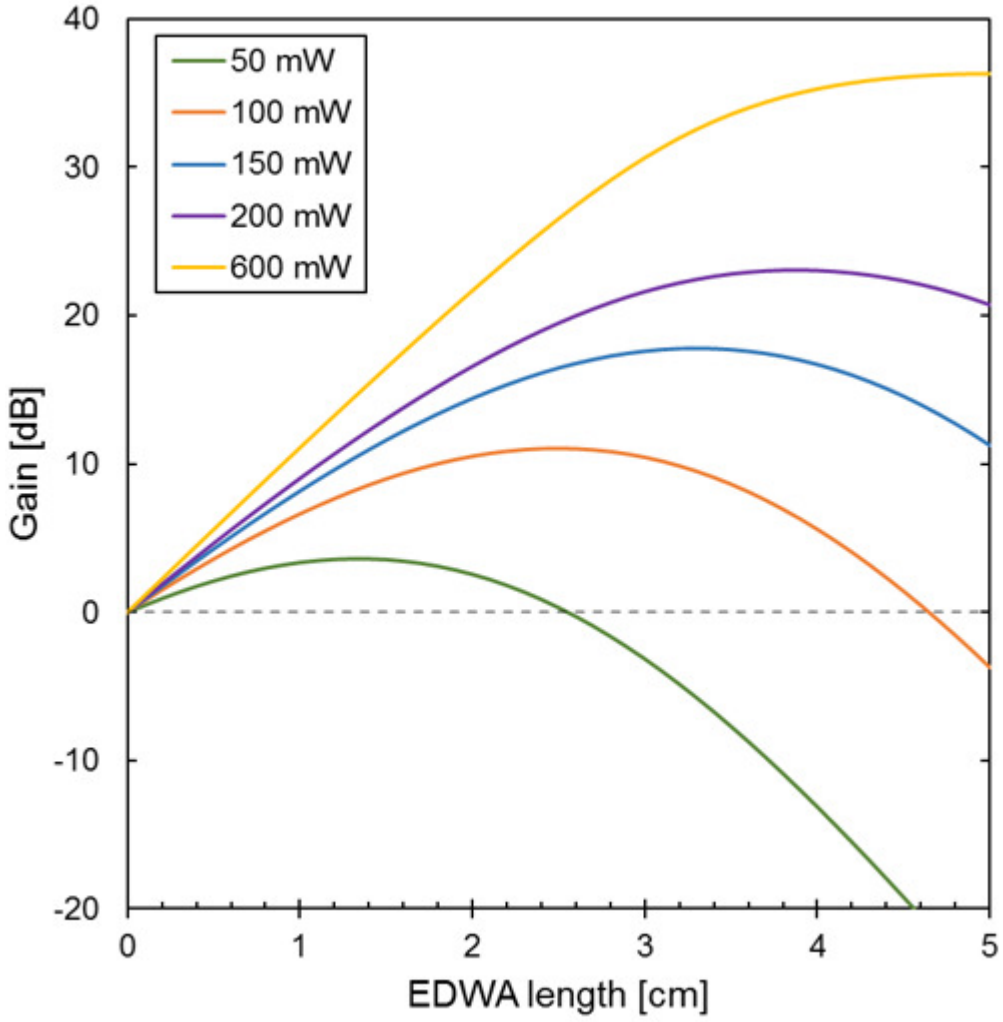

Figure 3-16: Dependence of internal gain on EDWA length for different pump powers at a fixed Er concentration of 8.15×10^{26} m^{-3}

The pump of 50 mW is not enough for a longer and a heavily doped device as only short part of the amplifier is inverted after this point the absorption becomes more and more dominant leading to high losses. In order to avoid that, the device can be either shortened or the concentration reduced. For a 5-cm-long EDWA with Er concentration of 8.15×10^{26} m^{-3} pump power of 600 mW is very close to optimum as around this value the gain reaches its saturation point and the maximum value. It is important to realise that even though at this point the absorption and emission processes become equal at the end

of the device, there is still a lot of pump photons that have not been absorbed and leave the amplifier. In order to minimise this inefficiency, the pump absorption has to be increased which typically is achieved through ytterbium co-doping as explained in previous chapter.

3.4.3 Upconversion

In the previous section an upconversion value of 0.8×10^{-23} m^3s^{-1} was assumed based on a similar material with a comparable dopant concentration [37]. In practice this may not be the case and the impact of change in this parameter has been analysed. In order to understand the impact of the cooperative upconversion processes on design parameters of erbium concentration, pump power and scalability these parameters were varied as shown in Figure 3-17, Figure 3-18 and Figure 3-19 respectively.

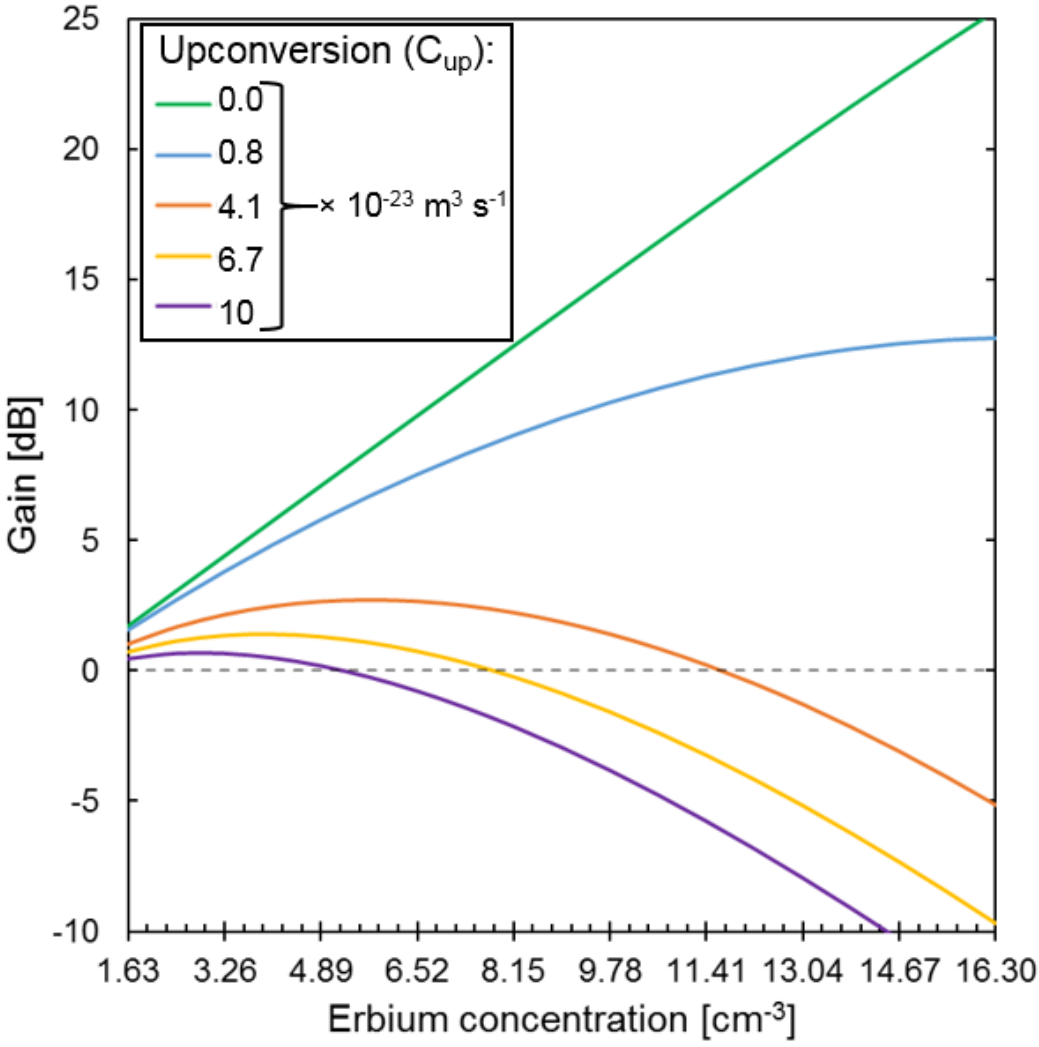

Figure 3-17: Upconversion impact on optimal erbium concentration based on a 1-cm-long EDWA pumped at 200 mW

Figure 3-17 shows that if it wasn't for the upconversion process, the internal gain of the EDWA would scale linearly with the erbium concentration. However, by accounting for the upconversion processes, the achievable gain shifts further away from this ideal scenario. At the point when it becomes higher than 1×10^{-23} m^3s^{-1} (last three simulated curves), increasing the erbium concentration increases the impact of upconversion faster than gain leading to less efficient devices. In these cases it is beneficial to reduce the doping concentration to increase the achievable gain in the EDWA.

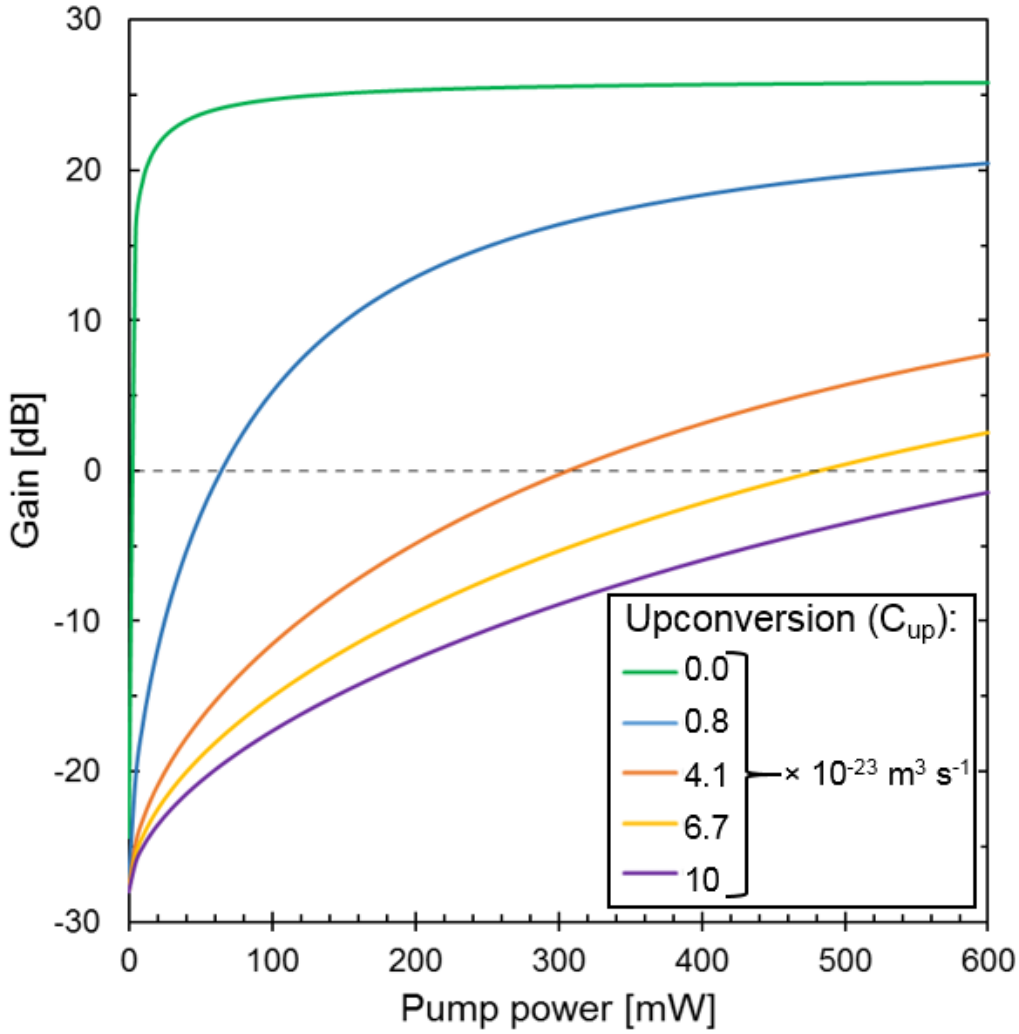

Figure 3-18: Upconversion impact evolution with pump power based on a 1-cm-long EDWA doped with 1.63×10^{27} m^{-3} Er ions

While reducing erbium concentration for a given upconversion parameter in the amplifier system is beneficial, higher pump power always leads to higher gain as presented in Figure 3-18. Even though higher upconversion coefficient always results in lower gain at a given pump power, a net gain is achievable if enough power is provided. From a practical perspective, energy efficiency of an amplifier is very sensitive to variation in

upconversion. In a case with no upconversion, a gain figure of 20 dB/cm only requires 20 mW of pump power. When the CUC parameter is increased to a level of 0.8×10^{-23} m^3s^{-1} used in previous section, almost 600 mW are needed to reach this level. For the coefficient above that, reaching this gain becomes impossible within a power constraint of a practical system.

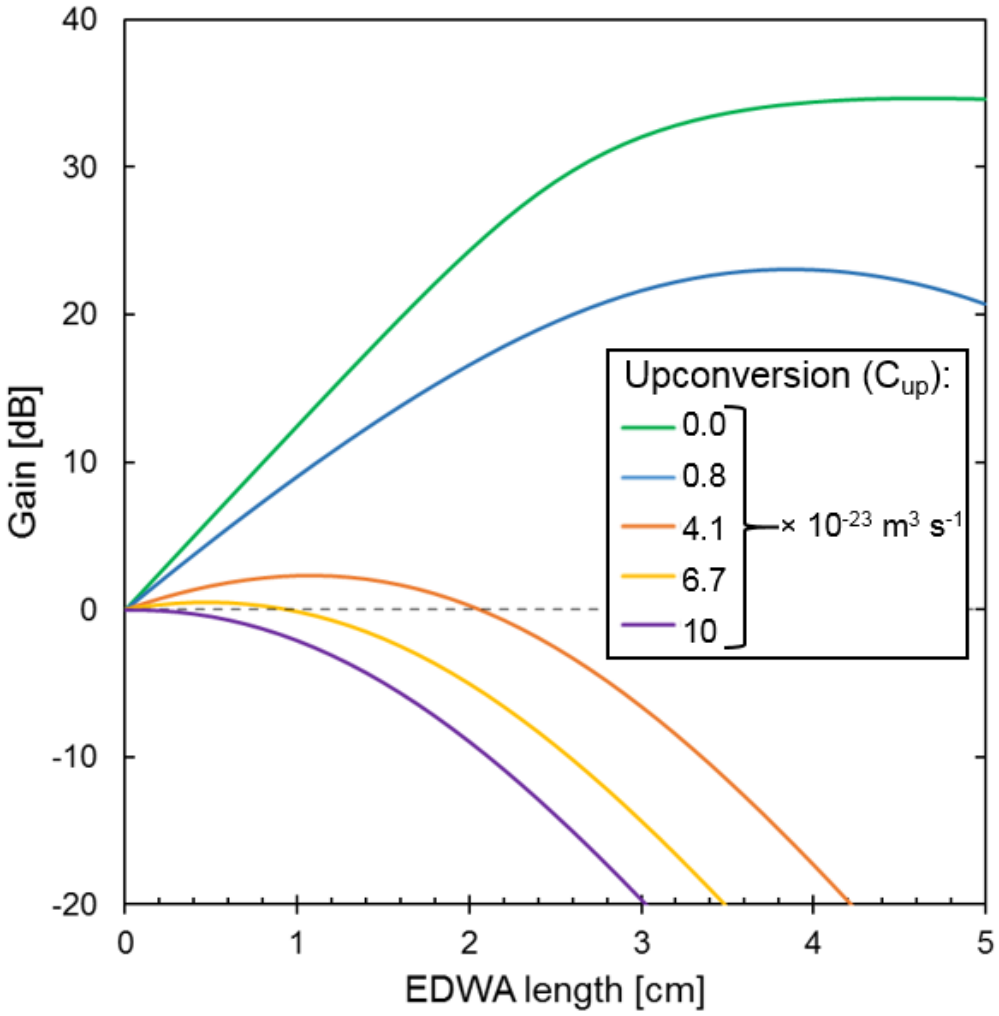

Figure 3-19: Upconversion effect on amplifier scalability based on an EDWA doped with 8.15×10^{26} m^{-3} Er ions pumped at 200 mW

In Figure 3-19, the effect of upconversion on scalability of an amplifier is shown. In all cases, initially the gain increases with length of the device till it reaches saturation point. The higher the upconversion, the lower the gain value and the shorter the optimal device for a given pumping and Er concentration. Without upconversion, 34.6 dB from 4.3 cm is possible, but with 0.8×10^{-23} m^3s^{-1} it drops to 23.1 dB at 3.9 cm. Furthermore, an increase of about an order of magnitude to 10×10^{-23} m^3s^{-1} makes a practical design

impossible as with the design specifications assumed in this section internal gain is not possible at all.

As in the simulation papers referred at the beginning of this section, a single value of upconversion is used across the entire concentration range of this work. However, it has been experimentally shown on example of Al_2O_3 using both Zubenko method [53] and a quenched ion model that the upconversion parameter increases linearly with erbium concentration [54]. With this assumption, the upconversion coefficient and erbium concentration were scaled linearly at the same time to investigate how this change affected the optimal operating points for the devices in term of pump power and length.

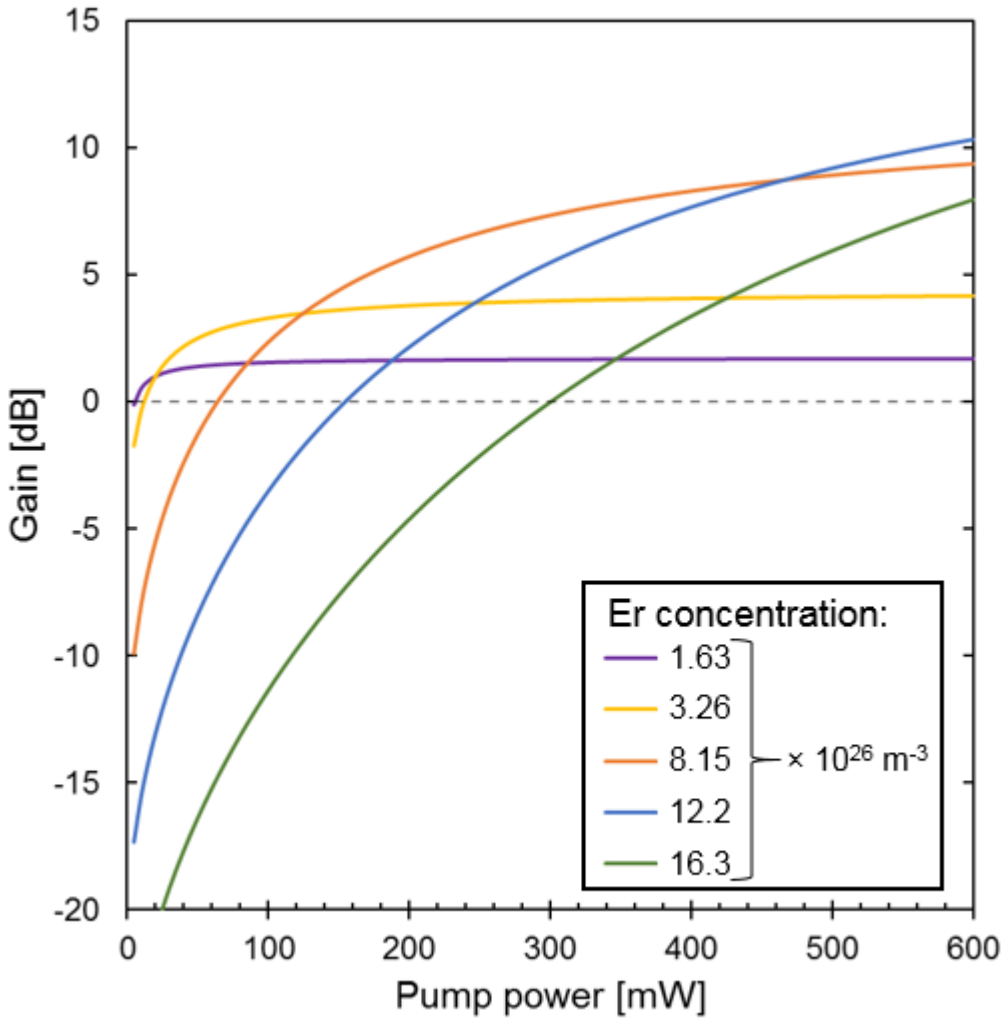

Figure 3-20: Dependence of internal gain on pump power for different erbium concentrations with linearly scaled upconversion coefficient

Figure 3-20 shows a result of a 1-cm-long amplifier with upconversion and Er concentration scaled linearly in range of 1.63-16.3 × 10^{26} m^{-3} and 0.4-4 × 10^{-23} m^3s^{-1} respectively. These results can be compared with Figure 3-12 where a fixed value for

upconversion was used. Not surprisingly, the increase in the upconversion reduces the achievable gain particularly at high Er concentrations. Previously, maximum gain of 12.9 dB from a 1-cm-long device pumped at 200 mW was achieved with the maximum available erbium concentration. With increasing upconversion, relatively more power is needed to obtain comparable gain and, as a result, within a 200 mW power limit lower gain of 5.7 dB is achievable by keeping erbium concentration at 8.15×10^{26} m^{-3}, half of the ULPI maximum value.

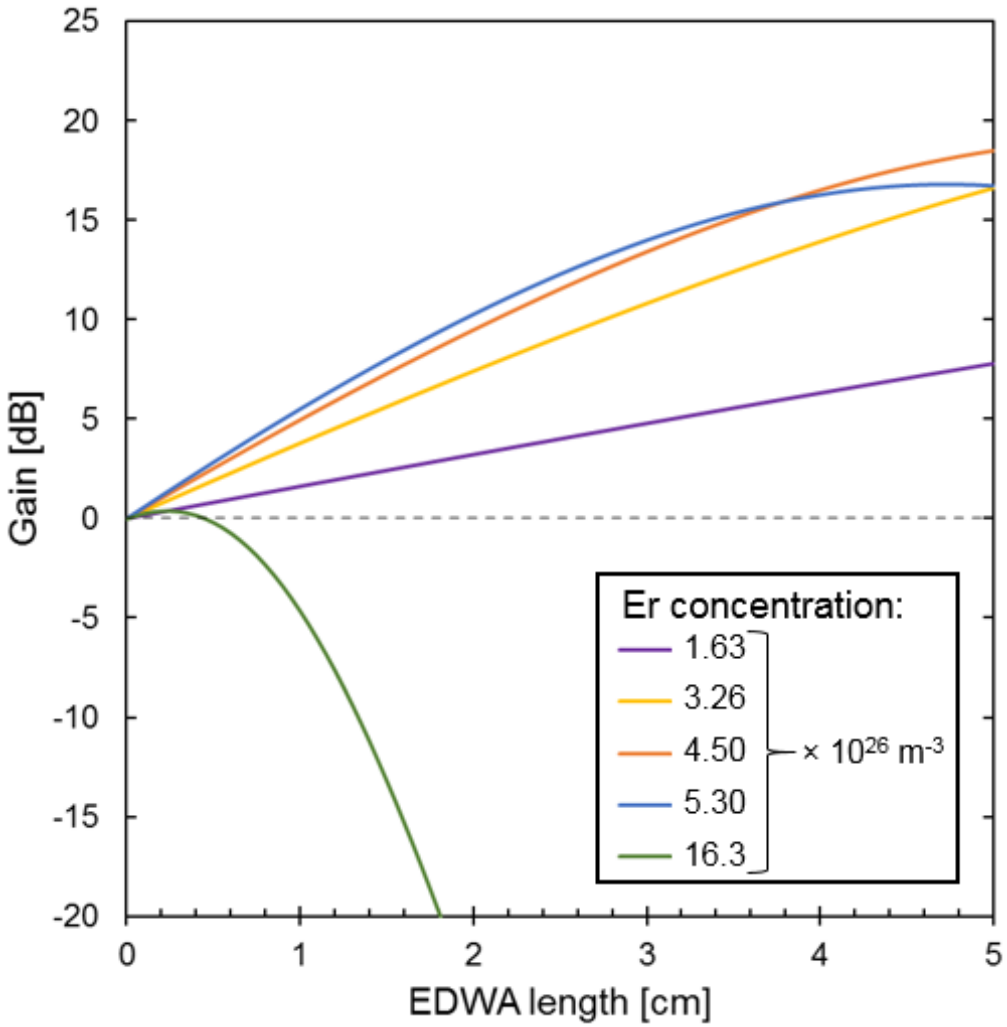

Figure 3-21: Dependence of internal gain on EDWA length for different erbium concentrations with linearly scaled upconversion coefficient pumped at 200 mW

An analogous analysis was performed to investigate the impact on EDWA scalability as presented in Figure 3-21. As in the results for a fixed upconversion parameter (Figure 3-15), increasing the length of the amplifier at a fixed pump power benefits from reduction in erbium concentration. This is compounded with the scaling of the upconversion factor leading to even lower concentrations being preferred, particularly for longer devices. The updated model predicts a maximum internal gain of 18.5 dB and

14 dB from 5- and 3-cm-long devices with re-optimised Er concentrations of 4.5 and 5.3×10^{26} m^{-3}, respectively. The values are lower at all the investigated lengths due to the upconversion scaling, but the difference becomes smaller as the length of the amplifier increased and corresponding number of dopants decreased.

3.4.4 Er/Yb Ratio

The previous section discussed the adverse impact of upconversion in the amplifier system showing that increasing Er content beyond certain point causes reduction in EDWA gain. One of common methods to counteract this process is through addition of ytterbium ions into the mix. The co-doping has been long used to sensitize the amplifier resulting in more efficient use of the pump power. However, an additional benefit comes from the fact that adding Yb introduces an alternative transition path that is competing with upconversion process. Simulations in this section assume constant total dopant concentration of 1.63×10^{27} m^{-3} where the difference between this number and a later quoted Er concentrations gives the number of ytterbium ions.

The impact of erbium-ytterbium co-doping is first investigated by looking at the gain evolution with pump power for a number of different concentrations. Figure 3-22 shows the same Er concentration and upconversion values as presented in Figure 3-20 where only the effects of linear upconversion scaling were investigated. When comparing the two, the positive impact at low erbium doping is clearly visible as the full potential of the EDWA is realised at much lower pump powers. The maximum gain of 1.7 dB and 4.2 dB for Er concentrations of 1.63 and 3.26×10^{26} m^{-3} is achieved at pump powers of approximately 4.5 and 10 mW. This highlights the pump power absorption efficiency and upconversion reduction provided by Yb as without it the corresponding pump powers were 85 mW and 130 mW, respectively.

In case of 1:1 ratio of dopants at 8.15×10^{26} m^{-3} each, first a rapid increase to an internal gain of approximately 8.8 dB at 130 mW can be observed and then a slow increase to 10.4 dB at 600 mW. The initial raise is a result of Yb efficiently absorbing and transferring the energy to neighbouring Er ions. However, the erbium population is high enough for upconversion to still have an effect on the performance of the amplifier. The relatively high number of ions on the $^4I_{13/2}$ level results in upconversion becoming a factor affecting the excited population and therefore preventing a fuller population inversion. This can be contrasted with behaviour of an amplifier at the same Er concentration

without Yb co-doping where only a slow gain build-up stage with no initial high increase at low pump powers was visible as shown in Figure 3-20.

As the Er concentration is further increased, the benefit of co-doping becomes smaller. When looking at 12.2 × 10^{26} m^{-3} Er with and without the additional 4.1 × 10^{26} m^{-3} Yb only a relatively small difference can be observed. It is more pronounced at medium pump powers compared to lower and higher as the relative improvement is 1.8, 4.1 and 2 dB at 100, 200 and 500 mW, respectively. At low pump powers the erbium-induced signal reabsorption closer to the end of the device reduces the initial Yb benefits. When the pump power is increased this process becomes less significant as higher population inversion is achieved and higher relative improvement is achieved. At high pump powers the absorption effectiveness of ytterbium becomes a smaller factor due to the very high pump density.

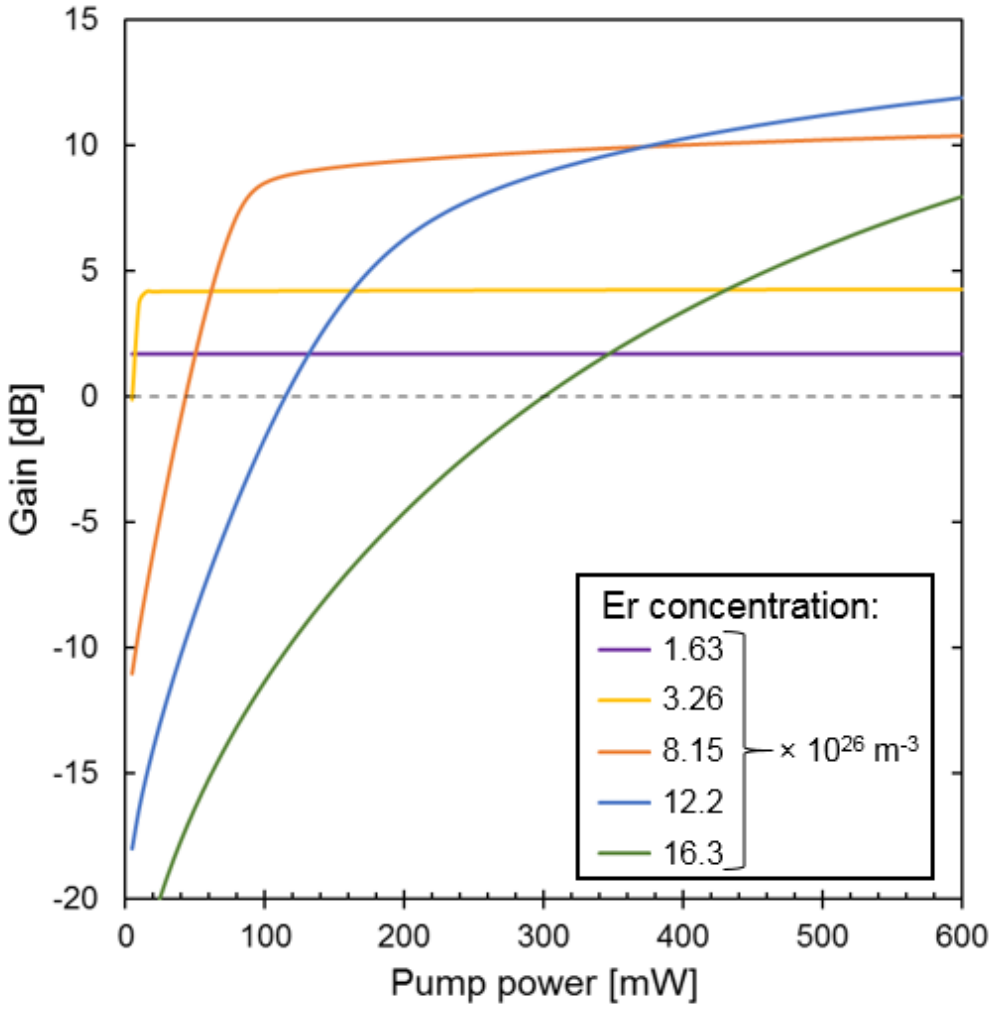

Figure 3-22: Internal gain dependence on pump power for a 1-cm-long Er-Yb co-doped amplifier with linearly scaled upconversion factor

In Figure 3-23 the benefits of ytterbium are depicted in the process of device optimisation for various amplifier lengths and they offer a chance for a direct comparison with Er-only results presented in Figure 3-21. The presented concentrations have been adjusted to show maximum gain at different lengths up to 5 centimetres. When the Er-Yb mix is used, a much sharper gain peak at a fixed pump power of 200 mW is visible compared to Er only systems. With careful optimisation the maximum gain is achieved at the desired length as for example for a 1.7-cm-long design gain of 14.3 dB can be obtained with Er:Yb ratio of 8.97:7.33 $\times 10^{26}$ m^{-3}. A much sharper response can be explained with two effects taking place along the device. Initially, a much faster increase of gain with length is a result of ytterbium ions efficiently absorbing pump power. However, this fast absorption leaves less pump power further along the EDWA leading to an increased reabsorption before the signal is coupled out of the device.

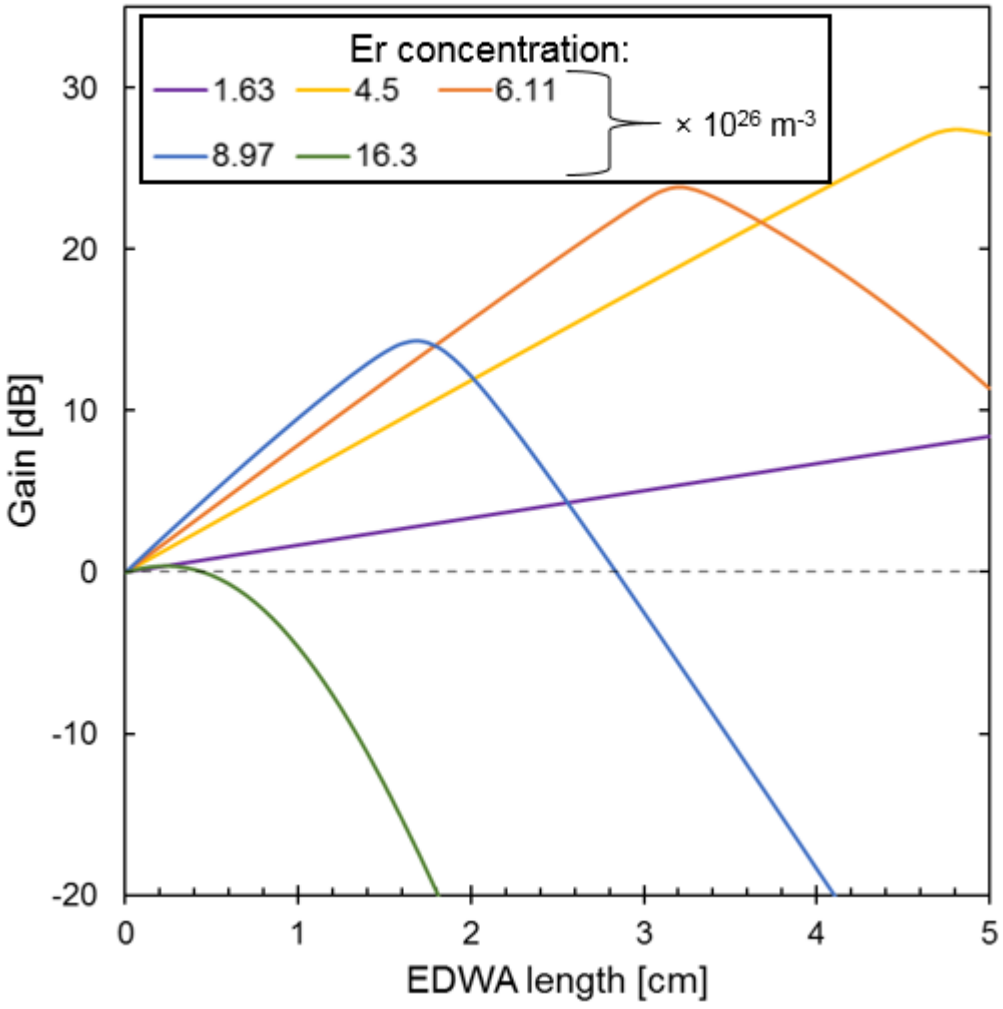

Figure 3-23: Internal gain optimisation for Er-Yb co-doped amplifiers of different lengths with linearly scaled upconversion factor

The introduction of ytterbium to the EDWA results in increased internal gain for all investigated amplifier lengths. It is important to adjust both Er and Yb concentrations for a specific length and pump power in a given system. Table 3-6 shows that under various upconversion and doping assumptions different optimal Er/Yb concentrations need to be chosen leading to a maximum gain. As explained throughout this section, a more realistic assumption about the upconversion factor scaling with concentration reduces the potential performance of the amplifier. However, by introducing ytterbium co-doping this effect can be counteracted and partially reversed leading to a better performance.

In the end, a short channel amplifier with optimised Er-Yb ratio based on system parameters expected form similar systems in literature should be able to reach a gain of almost 10 dB/cm without a need for pump powers above 200 mW. With this supply power limit in mind, the system can be readjusted to maximise the gain for longer designs, but the increase is not linear.

Table 3-6: Summary of optimised EDWAs based on a channel structure pumped at 200 mW with different Er concentrations and upconversion estimates

Length	Optimised parameter	Er + fixed upconversion	Er + scaled upconversion	Er-Yb + scaled upconversion
1 cm	**Gain [dB]**	**12.9**	**5.9**	**9.6**
	Er/Yb [$\times 10^{26}$ m^{-3}]	16.3	6.9	9/7.3
3 cm	**Gain [dB]**	**21.9**	**14.0**	**23.0**
	Er/Yb [$\times 10^{26}$ m^{-3}]	9.0	5.3	6.1/10.2
5 cm	**Gain [dB]**	**23.8**	**18.5**	**27.2**
	Er/Yb [$\times 10^{26}$ m^{-3}]	6.1	4.5	4.5/11.8

3.5 Device Structures

The above modelling and analysis have been performed on a square channel waveguide, but in practice alternative designs have to be considered in order to accommodate for the fabrication process. In this work two different approaches towards EDPWA have been taken with the fabrication techniques described in Chapter 4. In the first case, ultrafast laser plasma implantation (ULPI) is performed on samples to introduce rare-earth ions into the host material [55]. As a result of this process ideal channel structures are difficult to achieve as shown in Figure 3-24 (a) and (b). An alternative method of nanoparticle

dissolution in polymer is also studied, but in this case square channel waveguides were achieved.

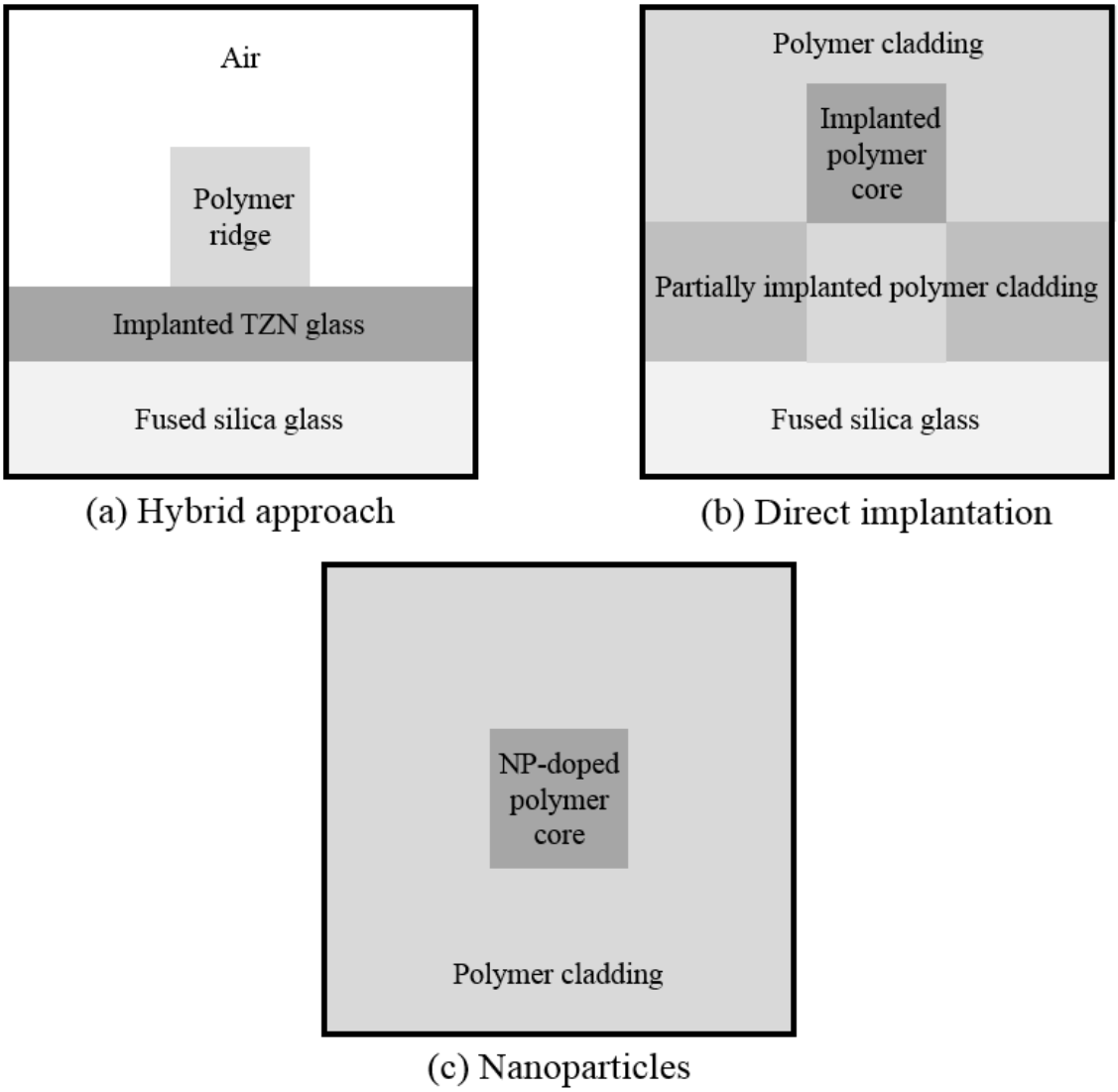

Figure 3-24: Waveguide structures used throughout this work. Shading represents the relative refractive index of the material

3.5.1 Hybrid Structure

This approach is based on a silica glass substrate that is implanted with Er-doped TZN particles to form erbium-doped tellurite-modified silica (EDTS) as described in [56]–[58]. Then a polymer ridge is deposited on top to create an strip-loaded structure where the fundamental mode is index-guided in the highest refractive index region underneath the polymer stripe [59].

The dimensions of the polymer strip and thickness of the Er-doped glass layer need to be controlled in order to achieve good performance. Figure 3-25 shows a well-designed structure with only a single mode trapped in the active region underneath the ridge in the

middle. Even though more transverse magnetic (TM) modes exist due to the planar nature of the structure they are not confined in the desired area. If the thickness of the EDTS layer is too thin or too thick, the fundamental mode shifts to the polymer ridge or multiple transverse electric (TE) modes become possible respectively. The size of the polymer waveguide is also important as by making it too large more than one TM mode can emerge leading to lower device efficiency.

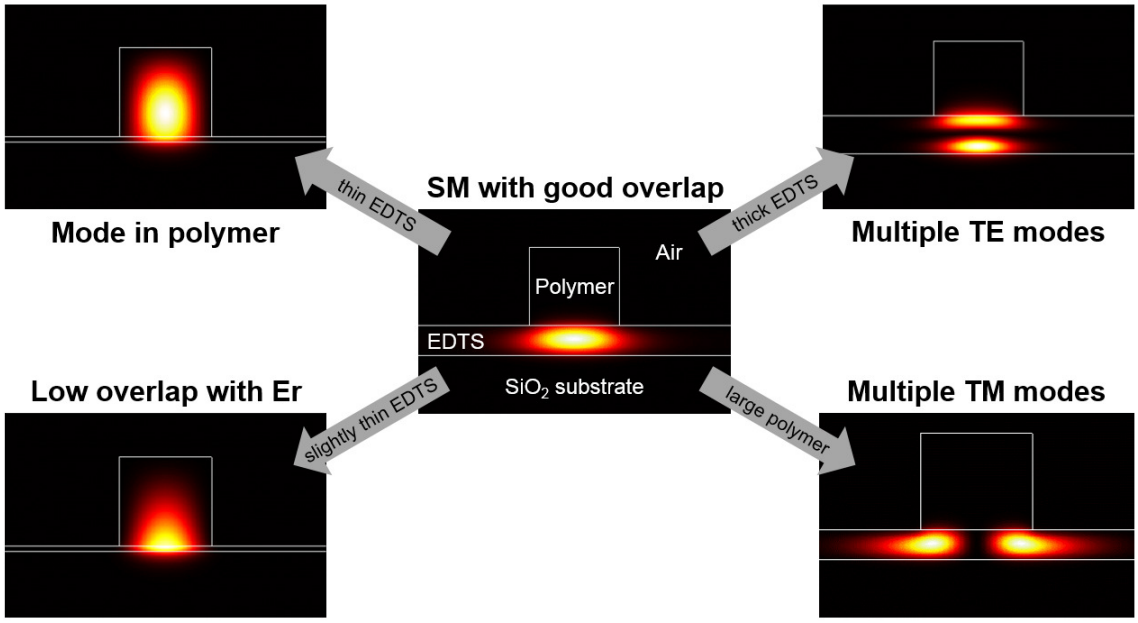

Figure 3-25: Guided mode intensity profiles obtained through FimmWave simulations for hybrid structures

This method employed to combine available EDTS samples with the polymer platform is described in more detail in Chapter 5. More quantitative analysis of the above SM conditions is performed based on the variable properties of the available samples such as the refractive index of the Er-doped layer that depends on the ion doping concentration.

3.5.2 Direct Implantation

This approach assumes direct ion implantation via ULPI process into polymer samples. This can be achieved either by performing this process on a planar polymer thin film leading to a strip-loaded architecture or on pre-fabricated polymer waveguides.

In the first case, a similar analysis to the hybrid approach is performed to ensure good operation. Alternatively, instead of adding a ridge for strip-loading an etching process can be employed to form waveguides that can later be covered with polymer cladding to form an asymmetric structure with fused silica glass substrate as presented in Figure 3-26.

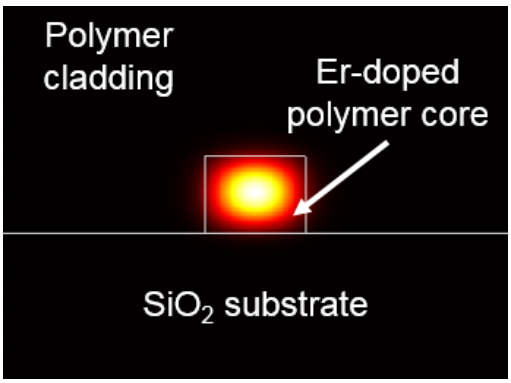

Figure 3-26: Asymmetric channel waveguide structure with glass substrate and polymer cladding

In case of the pre-fabricated polymer waveguides, the polymer features are prepared first using standard techniques such as spin-coating and photolithography. This is then followed by ULPI process that, depending on the operating conditions, can lead to either implantation into the polymer core and uncovered cladding or to deposition on top of the polymer features. The latter structures then can be tested for evanescent tail amplification as the light is not fully confined in the polymer core.

3.5.3 Nanoparticles

The last approach to EDPWAs used in this work is based on introducing Er-doped nanoparticles into the polymer host. This approach has been highly successful in recent years and a number of synthesis methods has been proposed [60]–[62] with some of the highest gain per unit lengths reported so far, as summarised in Chapter 2.

Once a core material is doped with NPs, the fabrication process follows this as for any polymer. In this work spin-coating and UV photolithography have been used to generate features such as waveguides. Since this process has allowed for fabrication of square channel waveguides, the same design procedure as in section 3.2 was used. In case of a uniformly NP-doped material, the refractive index of the core and, consequently, the refractive index contrast depend on the doping concentration. In order to ensure a single mode operation, a right feature size for a given NP density must be selected. The waveguide losses for NP-doped polymer are a combination of polymer absorption and scattering losses due to the particle presence as discussed in detail in Chapter 6.

3.6 Conclusions

In this chapter, the previously discussed erbium material properties are supplemented with the amplifier design parameters required for accurate modelling of EDWAs. The optical waveguide theory is introduced to describe and characterise behaviour of light inside of a guiding structure.

The range of available polymer materials is presented with particular focus on siloxanes chosen for amplifier implementation in this work. These materials have been shown to have all the necessary optical, mechanical and thermal properties required for the application environments of EDWA amplifiers. The chosen Dow Corning polymer has been shown in multi-mode waveguides to have propagation loss of about 0.2 dB/cm around pump wavelength of 980 nm and a higher loss of over 2 dB/cm across erbium emission spectrum. What is more, core and cladding material refractive indices indicate a possibility of fabricating single mode features of size up to 7.5×7.5 μm^2.

The increased refractive index resulting from Er doping into the polymer core reduces the SM maximum waveguide size. However, even when the effect of erbium concentration of 1.63×10^{27} m^{-3} is accounted for, a SM operation at 1550 nm is possible when a waveguide size is reduced to 2×2 μm^2. In this case SM operation is not achieved for the pump light leading to reduced device efficiency due to lower overlap with active region.

A full EDWA model based on multi-level equations with processes such as upconversion and energy transfer is used to investigate the potential of combining polymer platform with erbium through techniques such as ULPI. Realistic assumptions based on previously reported characterisation results on similar systems have been made and led to a thorough analysis of impact of erbium concentration increase. While using maximum achievable Er of 1.63×10^{27} m^{-3} does not lead to highest gain due to unfavourable upconversion scaling effects, optima have been found for various operating conditions such as pump power and length. It has also been shown that a gain of almost 10 dB/cm, comparable to the best reported in literature, can be achieved at relatively low pump power of 200 mW with help of a carefully optimised Er-Yb co-doping.

Finally, device structures alternative to channel waveguide are discussed based on the two employed Er-doping techniques: ion implantation and nanoparticle dissolution. Due to their different fabrication methods, slightly adjusted designs are proposed for a final EDWA device. The fabrication procedures for both are described in detail in Chapter 4

while further modelling, characterisation and measurement results specific to ultrafast laser plasma implanting and NP dissolving are presented in Chapters 5 and 6 respectively.

3.7 References

[1] A. Snyder and J. Love, "Optical Waveguide Theory," Springer US, 1983.

[2] P. K. Basu and M. J. Deen, "Guided Lightwaves: Introduction," in *Silicon Photonics: Fundamentals and Devices*, First., John Wiley & Sons, Ltd, 2012, pp. 265–302.

[3] H. Kogelnik and V. Ramaswamy, "Scaling Rules for Thin-Film Optical Waveguides," *Appl. Opt.*, vol. 13, no. 8, pp. 1857–1862, 1974.

[4] T. Tamir, G. Griffel, and H. L. Bertoni, *Guided-Wave Optoelectronics*. Berlin: Springer-Verlag, 1995.

[5] R. Hunsperger, *Integrated Optics - Theory and Technology*, Fourth. Berlin: Springer-Verlag, 1995.

[6] M. Zhou, "Low-loss polymeric materials for passive waveguide components in fiber optical telecommunication," *Opt. Eng.*, vol. 41, no. 7, pp. 1631–1643, 2002.

[7] M. Immonen, M. Karppinen, and J. Kivilahti, "Investigation of environmental reliability of optical polymer waveguides embedded on printed circuit boards," *Microelectron. Reliab.*, vol. 47, no. 2–3, pp. 363–371, 2005.

[8] D. Bosc, A. Maalouf, F. Henrio, and S. Haesaert, "Strengthened poly(methacrylate) materials for optical waveguides and integrated functions," *Opt. Mater. (Amst).*, vol. 30, no. 10, pp. 1514–1520, 2008.

[9] L. A. Eldada, "Polymer integrated optics: promise versus practicality," in *Organic Photonic Materials and Devices IV*, 2002, vol. 4642, no. June 2002, pp. 11–22.

[10] N. Bamiedakis, A. Hashim, J. Beals, R. V. Penty, and I. H. White, "Low-cost PCB-integrated 10-Gb/s optical transceiver built with a novel integration method," *IEEE Trans. Components, Packag. Manuf. Technol.*, vol. 3, no. 4, pp. 592–600, 2013.

[11] H. J. Yan, M. Immonen, L. X. Zhu, T. Rapala-Virtanen, P. Chen, and J. Wu, "Development of electro-optical PCBs with embedded waveguides for data center and high performance computing applications," *Opt. Interconnects XIV*, vol. 8991, no. March 2014, p. 899113, 2014.

[12] R. Dangel *et al.*, "Polymer waveguides for electro-optical integration in data centers and high-performance computers," *Opt. Express*, vol. 23, no. 4, pp. 4736–4750, 2015.

[13] R. S. E. John *et al.*, "Thermally stable, low loss optical silicones: A key enabler for electro-optical printed circuit boards," *J. Light. Technol.*, vol. 33, no. 4, pp. 814–819, 2015.

[14] J. V. DeGroot, "Cost Effective Optical Waveguide Components for Printed Circuit Applications," in *Proc. SPIE 6781, Passive Components and Fiber-based Devices IV;*, 2007, vol. 6781.

[15] A. W. Norris *et al.*, "High reliability of silicone materials for use as polymer waveguides," *Linear Nonlinear Opt. Org. Mater. III*, vol. 5212, no. November 2003, p. 76, 2003.

[16] L. Eldada and L. W. Shacklette, "Advances in polymer integrated optics," *IEEE J. Sel. Top. Quantum Electron.*, vol. 6, no. 1, pp. 54–68, Jan. 2000.

[17] K. Su, J. V. DeGroot, A. W. Norris, and P. Y. Lo, "Silicone Materials for Optical Applications," in *Proc. SPIE 6029, ICO20: Materials and Nanostructures*, 2006.

[18] H. Ma, A. K. Y. Jen, and L. R. Dalton, "Polymer-based optical waveguides: Materials, processing, and devices," *Adv. Mater.*, vol. 14, no. 19, pp. 1339–1365, 2002.

[19] K. D. Singer, T. C. Kowalczyk, H. D. Nguyen, A. J. Beuhler, and D. A. Wargowski, "Cross-linked polyimides for integrated optics," *Sol-Gel Polym. Photonic Devices A Crit. Rev.*, vol. 10290, no. July 1997, p. 102900I, 2017.

[20] R. G. Hunsprenger, "Polymer and Fiber Integrated Optics," in *Integrated Optics: Theory and Technology*, Fifth., Springer, 2013, p. 74.

[21] J. E. Marchegiano, B. L. Booth, C. T. Chang, R. J. Furmanak, D. M. Graham, and R. M. Yohannan, Jr., "Polyguide technology for passive optical interconnects," in *Wavelength Division Multiplexing Components*, 1996, vol. 2690, no. May 1996, pp. 361–368.

[22] H. Nawata *et al.*, "Organic-inorganic hybrid material, SUNCONNECT® for optical interconnects," *IEEE CPMT Symp. Japan 2015 Packag. is Everywhere, ICSJ 2015*, pp. 126–129, 2015.

[23] J. Beals, J. V. DeGroot, N. Bamiedakis, I. H. White, T. V. Clapp, and R. V. Penty,

"Cost-Effective Multimode Polymer Waveguides for High-Speed On-Board Optical Interconnects," *IEEE J. Quantum Electron.*, vol. 45, no. 4, pp. 415–424, 2009.

[24] R. Dangel *et al.*, "Polymer waveguides for electro-optical integration in data centers and high-performance computers," *Opt. Express*, vol. 23, no. 4, p. 4736, 2015.

[25] L. O. Lierstuen and A. S. Sudbø, "Coupling losses between standard single-mode fibers and rectangular waveguides for integrated optics," *Appl. Opt.*, vol. 34, no. 6, p. 1024, 2009.

[26] D. R. Buffman, "Particles Small Compared with the Wavelength," in *Absorption and Scattering of Light by Small Particles*, Weinheim, Germany: Wiley-VCH Verlag GmbH, 2007, pp. 130–157.

[27] W. Blanc and B. Dussardier, "Formation and applications of nanoparticles in silica optical fibers," *J. Opt.*, pp. 1–13, 2015.

[28] P. K. Tien, "Light waves in thin films and integrated optics.," *Appl. Opt.*, vol. 10, no. 11, pp. 2395–413, 1971.

[29] S. Laval, E. Cassan, L. Vivien, and F. Grillot, "Influence of waveguide geometry on scattering loss effects in submicron strip silicon-on-insulator waveguides," *IET Optoelectron.*, vol. 2, no. 1, pp. 1–5, Feb. 2008.

[30] N. Riegel, C. Middlebrook, K. Kruse, and M. Roggemann, "Using the 3D beam propagation method to model the effects of lithographic roughness on the attenuation of highly multimodal polymer waveguides," *J. Vac. Sci. Technol. B, Nanotechnol. Microelectron. Mater. Process. Meas. Phenom.*, vol. 31, no. 3, p. 031206, 2013.

[31] L. A. Eldada, R. Blomquist, L. W. Shacklette, and M. J. McFarland, "High-performance polymeric componentry for telecom and datacom applications," *Opt. Eng.*, vol. 39, no. 3, pp. 596–609, 2000.

[32] K. K. Tung, W. H. Wong, and E. Y. B. Pun, "Polymeric optical waveguides using direct ultraviolet photolithography process," *Appl. Phys. A Mater. Sci. Process.*, vol. 80, pp. 621–626, 2005.

[33] K. Su, J. V. DeGroot, Jr., A. W. Norris, and P. Y. Lo, "Siloxane materials for optical applications," in *Proc. SPIE 6029*, 2006, p. 60291C.

[34] B. Tatian, "Fitting refractive-index data with the Sellmeier dispersion formula," *Appl. Opt.*, vol. 23, no. 24, p. 4477, 2009.

[35] G. A. F. Seber and C. J. Wild, *Nonlinear regression*. New York: Wiley, 2004.

[36] I. H. Malitson, "Interspecimen Comparison of the Refractive Index of Fused Silica," *J. Opt. Soc. Am.*, vol. 55, no. 10, p. 1205, Oct. 1965.

[37] N. Lou, G. Liang, J. Hao, R. Gu, and Q. Li, "Improved gain characteristics by forward- backward pumped configuration in erbium-ytterbium–doped phosphate glass waveguide amplifier," *Opt. Eng.*, vol. 46, no. 4, 2007.

[38] J. Chandrappan *et al.*, "Target dependent femtosecond laser plasma implantation dynamics in enabling silica for high density erbium doping," *Sci. Rep.*, vol. 5, 2015.

[39] F. Di Pasquale and M. Federighi, "Improved Gain Characteristics in High-Concentration Er^{3+}/Yb^{3+} Codoped - Glass Waveguide Amplifiers," *IEEE J. Quantum Electron.*, vol. 30, no. 9, pp. 2127–2131, 1994.

[40] J. Chandrappan *et al.*, "Doping silica beyond limits with laser plasma for active photonic materials," *Opt. Mater. Express*, vol. 5, no. 12, p. 2849, 2015.

[41] G. Bilir, A. Kaya, H. Cinkaya, and G. Eryürek, "Spectrochimica Acta Part A : Molecular and Biomolecular Spectroscopy Spectroscopic investigation of zinc tellurite glasses doped with Yb^{3+} and Er^{3+} ions," *Mol. Biomol. Spectrosc.*, vol. 165, pp. 183–190, 2016.

[42] S. Ghatrehsamani and G. E. Town, "Optical Gain in Polymer Composite Materials With P_2O_2:Er^{3+}/Yb^{3+} Codoped Nanoparticles," *IEEE J. Quantum Electron.*, vol. 53, no. 2, pp. 2–6, 2017.

[43] Y. Benmadani, A. Kermaoui, M. Chalal, W. Khemici, A. Kellou, and F. Pellé, "Erbium doped tellurite glasses with improved thermal properties as promising candidates for laser action and amplification," *Opt. Mater. (Amst).*, vol. 35, no. 12, pp. 2234–2240, 2013.

[44] T. Mann, R. Mathieson, M. Murray, B. Richards, and G. Jose, "Femtosecond laser ablation properties of Er^{3+} ion doped zinc-sodium tellurite glass," *J. Appl. Phys.*, vol. 124, no. 4, p. 044903, 2018.

[45] Y. Dai, G. Jin, and G. Shao, "The Analysis of Intensity Profiles of Pump and Signal Light in Er-doped Waveguide Amplifier," *Mod. Phys. Lett. B*, vol. 22, no. 28, pp.

2747–2758, Nov. 2008.

[46] C. Zhao, G. F. Yang, Q. Y. Zhang, and Z. H. Jiang, "Spectroscopic properties of GeO_2- and Nb_2O_5-modified tellurite glasses doped with Er^{3+}," *J. Alloys Compd.*, vol. 461, no. 1–2, pp. 617–622, 2008.

[47] M. Zhang *et al.*, "High-gain polymer optical waveguide amplifiers based on core-shell $NaYF_4$/$NaLuF_4$: Yb^{3+}, Er^{3+} NPs-PMMA covalent-linking nanocomposites," *Sci. Rep.*, vol. 6, no. November, pp. 1–8, 2016.

[48] M. Zhang *et al.*, "High-gain polymer optical waveguide amplifiers based on core-shell $NaYF_4$/$NaLuF_4$: Yb^{3+}, Er^{3+} NPs-PMMA covalent-linking nanocomposites," *Sci. Rep.*, vol. 6, 2016.

[49] C. Strohhofer and A. Polman, "Absorption and emission spectroscopy in Er^{3+}–Yb^{3+} doped aluminum oxide waveguides," *Opt. Mater. (Amst).*, vol. 21, no. 4, pp. 705–712, 2003.

[50] J. D. B. Bradley *et al.*, "170 Gbit/s transmission in an erbium-doped waveguide amplifier on silicon," *Opt. Express*, vol. 17, no. 24, pp. 22201–22208, 2009.

[51] J. Yang, M. Pollnau, K. Wörhoff, R. M. de Ridder, E. H. Bernhardi, and J. D. B. Bradley, "Rare-earth-ion Doped Waveguide Amplifiers and Lasers in Alumina and Polymers," p. FWD1, 2013.

[52] C. E. Chryssou, F. Di Pasquale, and C. W. Pitt, "Improved Gain Performance In Yb^{3+}-Sensitized Er^{3+}-Doped Alumina (Al_2O_3) Channel Optical Waveguide Amplifiers," *J. Light. Technol.*, vol. 19, no. 3, pp. 345–349, 2001.

[53] D. Zubenko and M. Noginov, "Different mechanisms of nonlinear quenching of luminescence," *Phys. Rev. B - Condens. Matter Mater. Phys.*, vol. 55, no. 14, pp. 8881–8886, 1997.

[54] L. Agazzi, K. Wörhoff, M. Pollnau, K. Worhoff, and M. Pollnau, "Energy-Transfer-Upconversion Models, Their Applicability and Breakdown in the Presence of Spectroscopically Distinct Ion Classes: A Case Study in Amorphous Al_2O_3:Er^{3+}," *J. Phys. Chem.*, vol. 117, no. 13, pp. 6759–6776, 2013.

[55] B. D. O. Richards *et al.*, "Tm^{3+} Tellurite-modified-silica glass thin films fabricated using ultrafast laser plasma doping," *IEEE J. Sel. Top. Quantum Electron.*, vol. 25, no. 4, pp. 1–8, 2019.

[56] J. Chandrappan *et al.*, "Enabling silica for high density rare earth doping for

integrated opto- electronic systems," vol. 65, no. 2011, p. 241905, 2015.

[57] J. Chandrappan, V. Khetan, M. Ward, M. Murray, and G. Jose, "Devitrification of ultrafast laser plasma produced metastable glass layer," *Scr. Mater.*, vol. 131, pp. 37–41, 2017.

[58] Z. Zolnai *et al.*, "Ultrafast laser plasma assisted rare-earth doping for silicon photonics," *CLEO*, vol. 1, p. ATu3K.5, 2016.

[59] J. S. Chang, I. Y. Kim, G. Y. Sung, and J. H. Shin, "Population inversion and low cooperative upconversion in Er-doped silicon-rich silicon nitride waveguide," *Opt. Express*, vol. 19, no. 9, p. 8406, 2011.

[60] Y. Liu, D. Tu, H. Zhu, and X. Chen, "Lanthanide-doped luminescent nanoprobes: Controlled synthesis, optical spectroscopy, and bioapplications," *Chem. Soc. Rev.*, vol. 42, no. 16, pp. 6924–6958, 2013.

[61] X. Zhai *et al.*, "Polymer-Based Optical Waveguide Amplifiers," *Opt. Mater. Express*, vol. 3, no. 2, pp. 270–277, 2013.

[62] M. Haase and H. Schäfer, "Upconverting nanoparticles," *Angew. Chemie - Int. Ed.*, vol. 50, no. 26, pp. 5808–5829, 2011.

4 Fabrication and Er-doped Thin Film Characterisation

Three different approaches to designing polymer-compatible EDWAs have been presented in the previous chapter. Each of these designs requires a different fabrication process flow to implement the proposed systems. The hybrid structure and direct implantation EDWAs take advantage of the novel ULPI process to implant erbium ions into glass or polymer substrate respectively. Alternatively, the nanoparticle dispersion approach allows for pre-mixing of the materials followed by standard polymer fabrication techniques.

In this chapter, commonly used polymer fabrication techniques are presented with particular focus on the UV photolithography process suitable for siloxane materials. The employed fabrication steps are described in detail showing how the final features are manufactured. The wafers are patterned using a mask designed with the doping processes in mind and accommodating for the different waveguide sizes required by different amplifier architectures. The background losses of the fabricated polymer waveguides are then characterised, background loss being a key parameter for polymer-based EDWA designs.

The doping technologies, namely ultrafast laser plasma implantation and nanoparticle dispersion, are also described in the chapter. These fabrication processes are used to prepare three types of Er-doped thin films: erbium-doped tellurite-modified silica (EDTS), Er-implanted polymer and nanoparticle dispersed polymer. These planar erbium layers are then characterised through a visual inspection, including scanning electron microscopy (SEM), photoluminescence (PL) spectrum analysis and lifetime measurements. Based on the thin film characterisation most promising approaches and samples are chosen for amplifier studies in Chapters 5 and 6 of this thesis.

4.1 Polymer Component Fabrication

One of the aforementioned advantages of polymers is their ease of processing as well as the variety of methods that can be employed to process them. Some of the most common fabrication techniques are discussed in this section, followed by a description of the detailed process employed in this thesis work.

4.1.1 Fabrication Techniques

Polymers can be used to create a wide range of waveguides and waveguide components with a variety of fabrication methods. Different fabrication methods may be required depending on the type of polymer, but in many cases multiple options are available for a

given material. Thin films can be deposited by a range of methods such as spin-coating, doctor-blading or drop casting on various substrates (glass, silicon, FR4). There are advantages and disadvantages for each method: for example spin coating allows for formation of uniform layers of controllable thickness while making removal of striations difficult. Most common methods for patterning and generation of waveguides can be performed on a wafer scale, such as photoresist, lithography and embossing or one feature at the time as in case of direct laser writing and a mosquito method [1]–[3].

Photoresist-based patterning (Figure 4-1 (a)) is based on a standard semiconductor processing technique where a photoresist is deposited and ultra-violet (UV) patterned on the polymer layer. After removing the undeveloped material with solvent, etching is used to translate the pattern onto the polymer itself. Reactive ion etching (RIE) can be used but a problem with using conventional RIE is that it often results in large surface roughness. To reduce this phenomenon and the adverse effect it has on sidewall scattering losses, alternative processes such as inductively coupled plasma (ICP) etching have been proposed. Careful calibration of the ICP process parameters including RF power, chamber pressure and oxygen flow rate led to sub-20-nanometre root-mean-square roughness [4].

Direct lithographic patterning process is used to make waveguides based on photosensitive polymers. The structures are prepared through wet etching of a polymer film after it has been selectively exposed to UV light through a mask. Compared to photoresist-based pattering (Figure 4-1 (b)), this technique has a simplified and faster process in addition to usually resulting in a lower surface roughness [5].

Soft lithography techniques such as embossing, moulding or stamping are a well-known microfabrication methods [6]. In order to use this method, a PDMS mould needs to be prepared first, which is usually achieved through casting polydimethylsiloxane on a micro-structured silicon master [7]. The structures are then replicated by pressing the mould against a substrate with polymer melt as shown in Figure 4-1 (c) on an example of micromoulding in capillaries (MIMIC) process. These techniques are considered to be cost efficient and offer large-scale fabrication, but the surface roughness is usually relatively large.

A variety of other techniques exist, but two mask-free approaches have caught a lot of attention. Laser direct writing and mosquito method both offer a flexible method of generating patterns in polymer with rapid prototyping capabilities and a relaxed limitation in terms of the maximum area and waveguide length generated as no mask is needed.

While the first uses a laser beam spot to outline the desired pattern, the latter uses a syringe needle inserted into a cladding material to inject core monomer along the pre-programmed path before UV exposure of the entire system [8], [9]. These methods offer an option to write features within restricted regions without affecting the surrounding as well creation of novel structures. Despite their serial nature, progress has been made to increase the speed of the pattern generation [10].

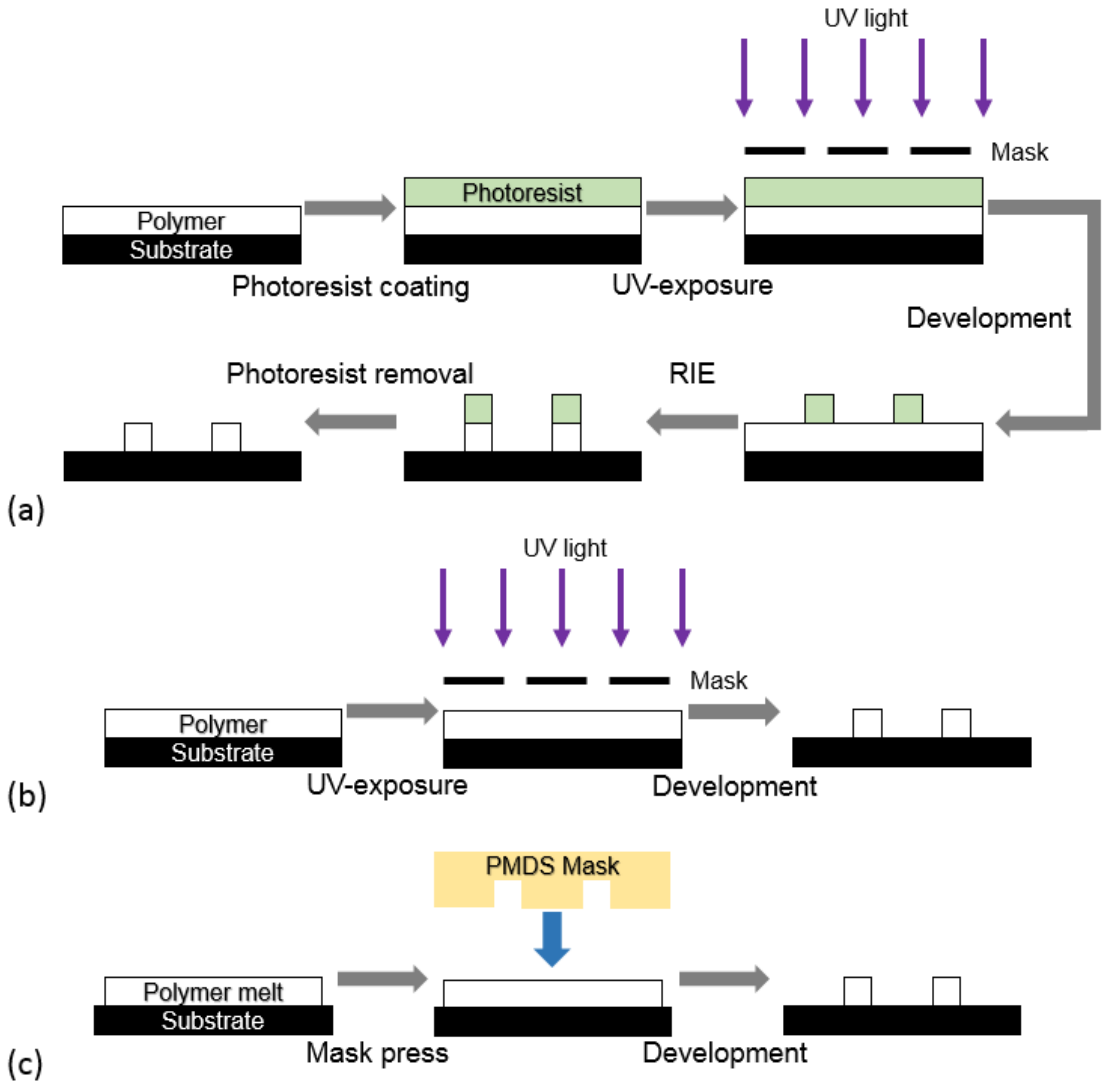

Figure 4-1: Schematic illustration of polymer patterning techniques (a) photoresist-based, (b) direct lithographic and (c) MIMIC

Different patterning techniques have their advantages and disadvantages as summarised in Table 4-1. For the purpose of this work, the relatively simple photolithography method is used. It has been chosen with the available fabrication facilities in mind as well as the fact that the chosen siloxane polymers are photosensitive to UV exposure. More details on the details and optimisation of the fabrication processes for different EDWA amplifier designs is given is Chapter 4.

Table 4-1: Trade-off of common polymer patterning methods

Patterning method	Advantages	Disadvantages
Photoresist-based	Standard semiconductor processing technology	Rough surface, mask required, high cost
Direct Lithography	Simple process	Mask required
Laser Writing	Rapid prototyping, mask-free	Features like Y-splitters problematic, serial nature
Mosquito	Rapid prototyping, graded index	Complex features problematic, serial nature
Soft Lithography (moulding / embossing)	Cost-efficient, large scale	Rough surface (< 150 nm)

4.1.2 Siloxane Waveguide Fabrication

There is a number of processing steps involved in fabrication of polymer waveguides based on the Dow Corning siloxanes as summarised in Figure 4-2. Initially, the substrate is prepared before any polymer deposition can take place to remove potential contaminants from the surface. Then flat horizontal layers of a defined thickness are obtained through spin coating and solidified using a combination of UV photolithography and thermal treatment often referred to as baking. In order to obtain features, such as waveguides, a mask is used to expose only required areas to the UV light. The remaining polymer is then removed from a substrate to uncover the final design through development.

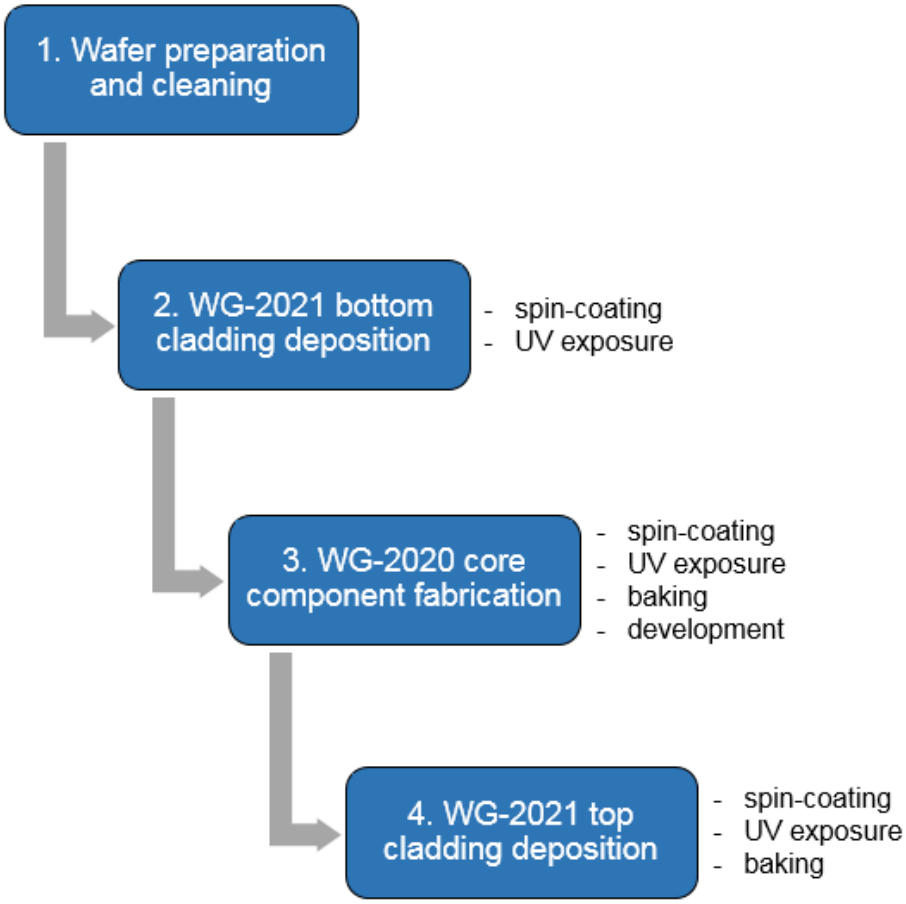

Figure 4-2: Fabrication process flow for siloxane polymers used in this thesis

4.1.2.1 Spin-coating

The polymer materials come in form of a highly viscous liquid that is poured onto a substrate or preceding polymer layer. The underlying wafer can be made from a wide range of materials, but in this work fused silica and silicon are used as they are compatible with the laser plasma implantation process described in the following section. Spin-coating is used to equally distribute the polymer onto a 100 mm diameter round substrate. The thickness of the resulting layer is determined by two parameters: rotation speed and time.

For the WG-2021 cladding material, the thickness of the layer is not required to be carefully controlled, particularly for a glass substrate, which has lower refractive index than the polymers used (detailed values shown in section 3.1.4). In case of silicon wafers, the thickness of the polymer cladding layer separating the substrate from waveguides has been maintained at more than a magnitude larger than the wavelength of the light to ensure that the signal doesn't leak out of the desired region.

In case of the core WG-2020 material the thickness is controlled to a much greater extent as the dimensions of the waveguides are crucial for maintaining a single mode operation.

The relationship between the rotation speed and the corresponding layer thickness for a fixed 1-minute-long spinning is shown in Figure 4-3. The presented values have been obtained at a room temperature for a wafer-scale deposition with the polymer material diluted with toluene at a ratio of 4:1. Increasing the rotation speed of the spin-coating reduces the thickness of the resulting polymer layer. In case of Dow Corning WG-2020, rising the speed from 1000 to 4000 rpm resulted in a change in polymer layer thickness from an average of 13 μm to 7 μm. However, the rate of change slows at higher speeds and ultimately is limited by the viscosity of the material used. Alternative means of controlling the thickness of the layer are through changing polymer-to-toluene ratio or spinning time [11].

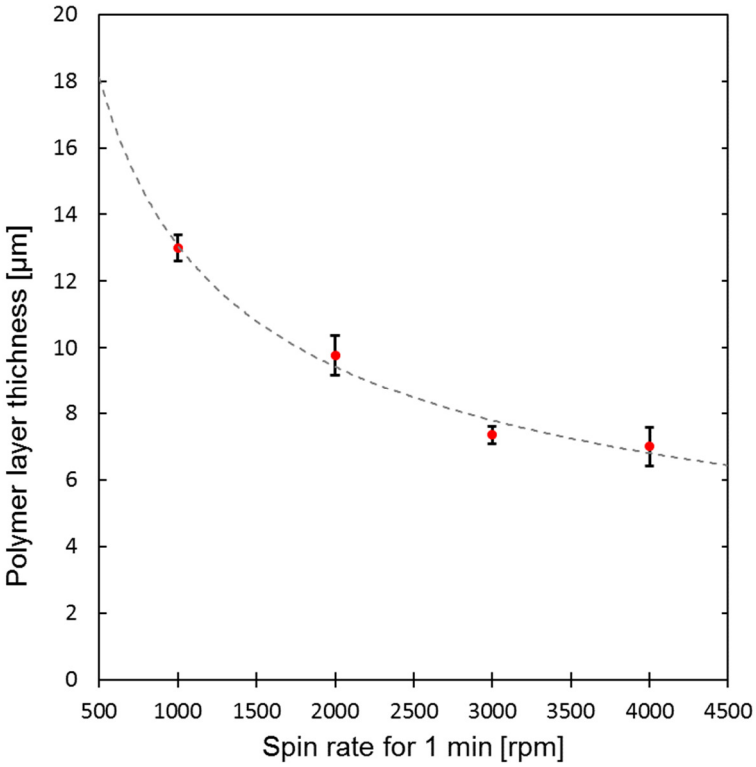

Figure 4-3: Measured dependence of Dow Corning WG-2020 layer thickness on spin-coating speed

After the spin-coating process is finished, the polymer remains in a liquid form as the solvents are still present in the material. The solvents can be evaporated by baking and photolithography. Heating the wafer to a temperature in range of from 110 ˚C to 130 ˚C (referred to as “soft baking”) removes some of the solvent and has been shown to improve adhesion as well [12]. Usually it is accompanied with a photolithography processing step in order to create a more permanent and good quality layers or generate features when combined with an exposure through a mask.

4.1.2.2 UV Photolithography

Contact photolithography is normally used in order to obtain very high-resolution features. If, however, the mask touches the liquid polymer it can stick to the metal patterns making it impossible to use again [13]. As a result, photolithography is used in a proximity mode where the mask is set in a small distance, in range of tens of microns, above the polymer. In this way it can be used repetitively to pattern entire wafers at once and ensure high process throughput leading to cost-efficient fabrication.

Introducing a gap between the two objects reduces the achievable resolution of the process due to a light diffraction through the patterns on the mask. The quality and minimum size depends on the separation distance that can be reduced through ensuring that the polymer layer is as uniform as possible. Spin-coating results in a relatively flat surface in the middle of the wafer with slightly thicker sides because of more material accumulating at the edges as shown in Figure 4-4. This difference between edges and the centre of the layer is proportional to the target polymer thickness and can be reduced through techniques such as chemical [14] or mechanical edge bead removal. The latter has been performed using a mesitylene-coated polyester swab after spin-coating. This has resulted in a thickness variation as low as 15 µm (measured with KLA Tencor Alpha-Step D-600 profilometer) enabling close proximity of the mask to the exposed polymer in the following lithography steps.

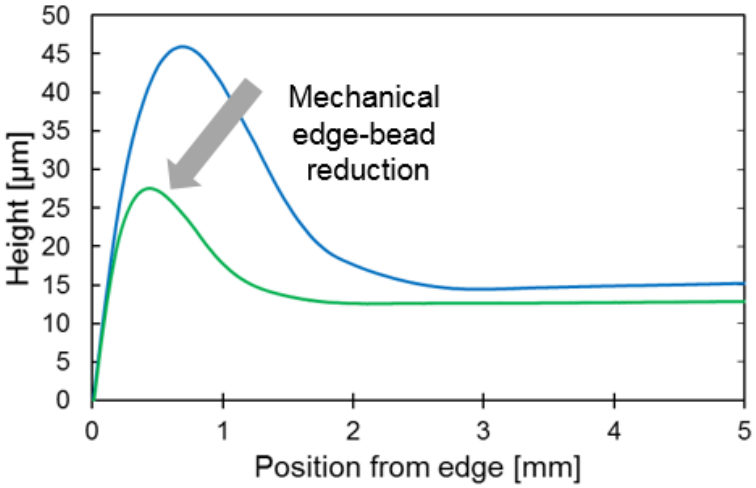

Figure 4-4: Reduction in the size of the edge-bead of the WG-2021 bottom cladding before (blue) and after (green) mechanical edge-bead removal

Furthermore, the UV exposure dose has an additional effect on the height of the developed features. The mask used in this work has waveguides of varying width leading to a different amount of light shone on the spin-coated polymer. Figure 4-5 shows a result of

a 6-µm-thick layer exposed through mask slots of varying width. A variation is observed with the smallest 3 µm features having an average height of 3.2 µm and then increasing till eventually reaching 5.6 µm for the widest 10 µm waveguides. The benefit of this phenomena is that waveguides of almost square cross-sections can be achieved for even the smallest design sizes. To obtain similar width-to-height proportions for the largest features, the spinning speed has to be reduced to start with a thicker layer pre-exposure.

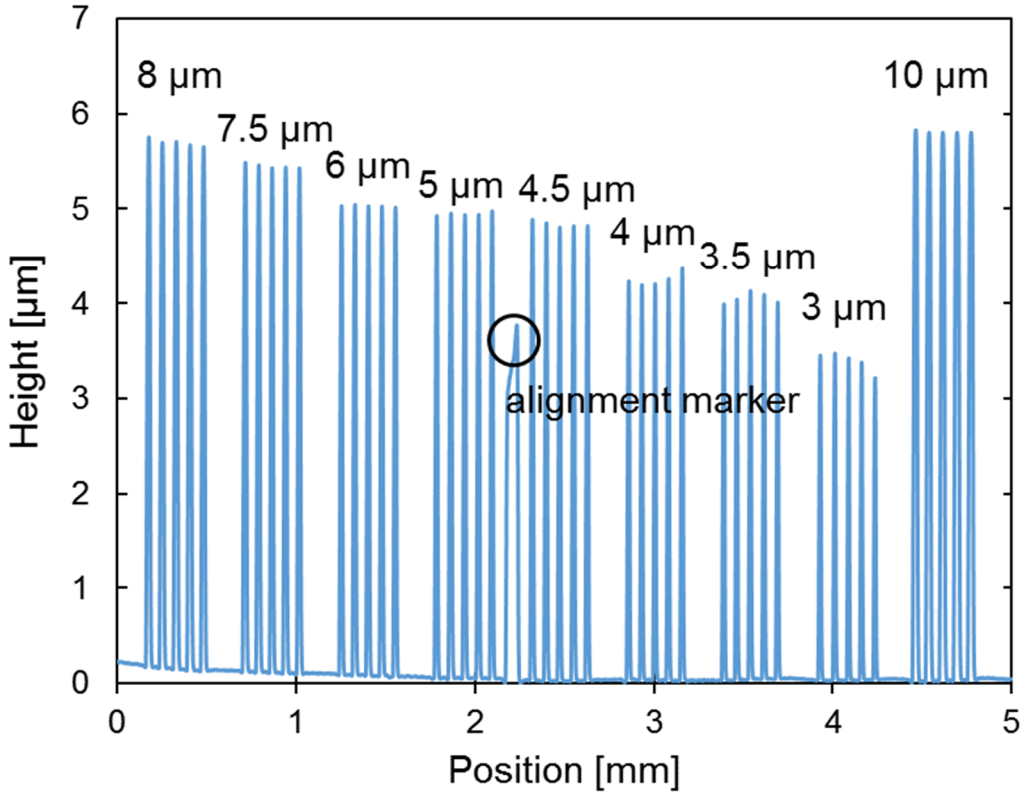

Figure 4-5: Height variation of polymer features with different waveguide widths (marked) spin-coated at 4000 rpm and UV exposed for 30 seconds

4.1.2.3 Optimised wafer fabrication procedure

The final procedure for wafer-scale fabrication using Dow Corning siloxanes with both glass and silicon substrates has been optimised as shown in Table 4-2 for single mode waveguides. This procedure has been used as a benchmark for all-polymer, undoped systems. This process has been then adjusted to accommodate for plasma implantation and NP dispersion Er doping procedures as discussed in later sections. Another important factor that affected the optimal deposition parameters has been the size of the sample. While the below methodology has been prepared for wafers with diameter of 100 millimetres, adjustments have been made for smaller samples.

Table 4-2: Detailed procedure for wafer-scale polymer fabrication

Step	Material	Spin Rate (RPM)	UV exposure	Temperature (°C)	Time (min)
Coating	WG-2021	800			1
UV Exposure			flood		1
Coating	WG-2020	4000			1
Prebake				110	5
UV Exposure			proximity		0.5
Post Bake				130	5
Develop	mesitylene				1
Post Bake				180	5
Coating	WG-2021	500			1
UV Exposure			flood		1
Post Bake				130	5
Hard Bake				180	30

4.1.3 Lithography Mask Design

Implementation of the designs put forward in Chapter 3 using photolithography requires a metal mask with which to pattern waveguides by blocking the UV light. The maximum size of the single mode waveguides depends on the refractive index contrast which is a function of the erbium concentration in the polymer. In order to accommodate for this variation, a versatile mask is prepared allowing for waveguide sizes in range of 3 μm to 10 μm. Furthermore, one of the limitations of the ULPI setup is that it can only implant samples up to size of 2×3 cm^2. This is accounted for in the final design by dividing the wafer area into six smaller pieces of this size as well as additional, longer sections used for alternative fabrication methods. A detailed mask design showing the component and section positioning is attached in the Appendix.

4.1.3.1 Bends

In addition to straight waveguides, the mask design included a number of additional features required for more complex system architectures. One of the key basic geometries are 90° and 180° bends. Using FimmWave simulations based on siloxane core and cladding materials, loss per 90° bend is estimated depending on factors such as refractive index contrast, waveguide width (square channels assumed) and bending radius. All of the aforementioned factors have an impact on the additional loss introduced as the signal

propagates along the waveguide. The mask used in this work is designed with a range of waveguide widths meaning that different sizes have varying requirements for low loss bending. Figure 4-6 shows loss results for a number of SM waveguide designs with different combinations of size and refractive index contrast. In order to maintain the single mode operation, as the refractive index contrast between Er-doped core and cladding increases the waveguide size has to be reduced. It is observed that an additional benefit of higher doping is reduced bending radius for a given loss leading to more compact design. In an unaltered polymer system, a radius of 5.7 mm is required to have an excess bending loss of 0.5 dB while a highly doped system with refractive index contrast of 0.02 and a smaller waveguide of 3 μm achieves the same with radius of 1.2 μm.

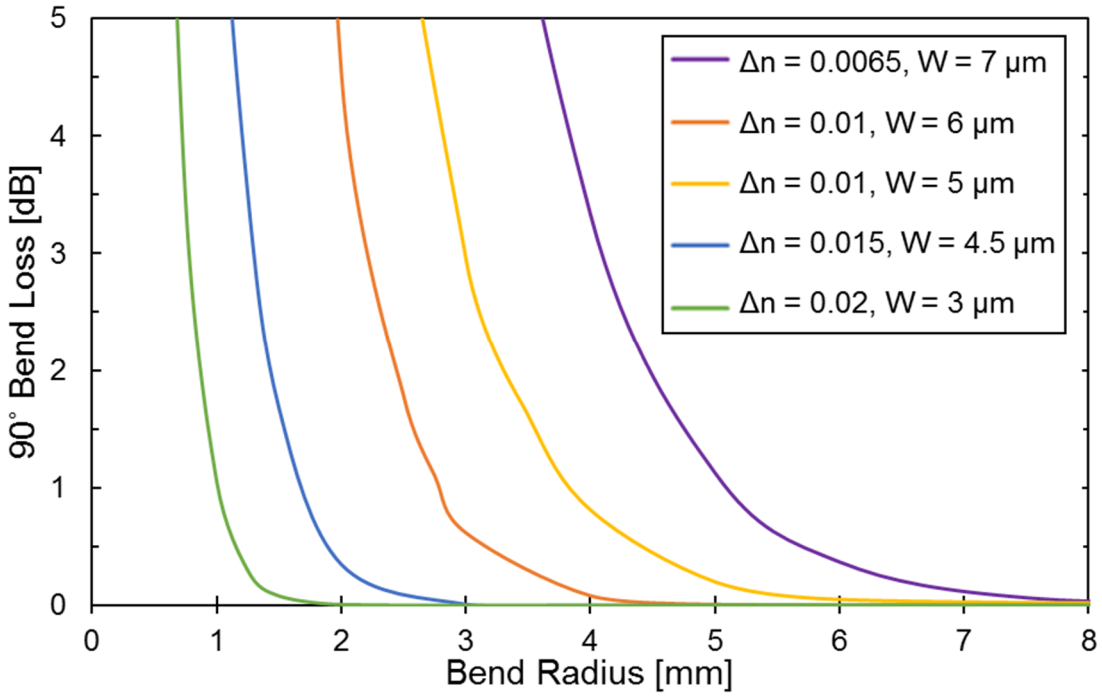

Figure 4-6: 90° bend loss variation with bending radius for a number of SM polymer waveguides

In order to accommodate for the range of requirements, the final mask design is made to accommodate for a wide range of bending radii for the waveguide sizes from 3 μm to 10 μm. Additionally, to increase the length limit of a straight waveguide on samples used in the project U-turns consisting of two such bends are used. In this way, a potential amplifier length is raised to 5.7 cm on a 2×3 cm^2 sample as shown in Figure 4-7 b) with red light illumination.

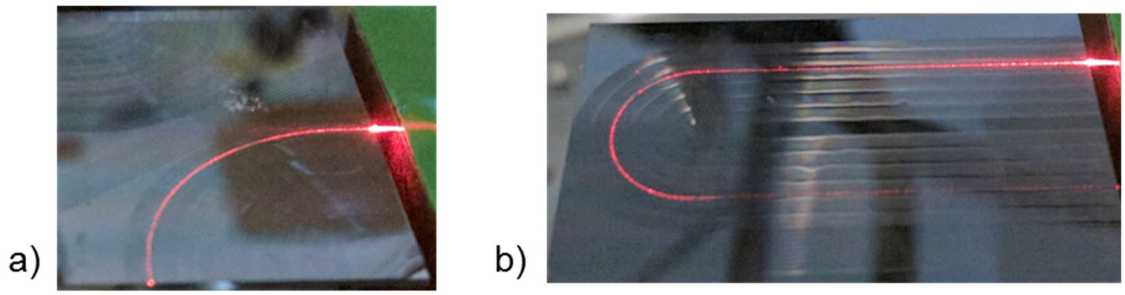

Figure 4-7: Red light illuminated a) 90° and b) 180° bends

4.1.3.2 Curves

Curves are useful features included in the mask design that are a basis for both S-bends and Y-splitters Figure 4-8. The losses in this type of structures are minimised by ensuring a minimal change in direction at any given point. In this work it is implemented using parametric Bezier curves that have found many applications over the years, particularly in computer graphics and animation, to model smooth curves that can be indefinitely scaled [15].

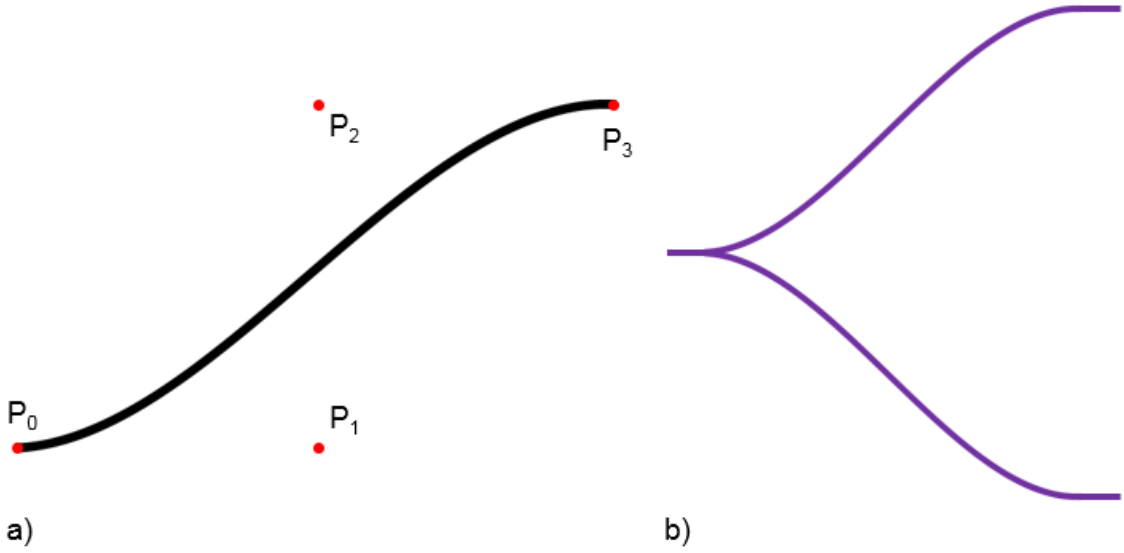

Figure 4-8: Bezier curve used to model a) S-bend and b) Y-splitter

The S-bends and Y-splitters are based on a cubic Bezier curves that can be defined using four points: $\boldsymbol{P_0}$ to $\boldsymbol{P_3}$ as marked in Figure 4-8 a). It starts at $\boldsymbol{P_0}$ going towards $\boldsymbol{P_1}$ and eventually comes to $\boldsymbol{P_3}$ from the direction of $\boldsymbol{P_2}$, where the middle two point are there to provide direction. Mathematically, the path of the curve is described using the Equation (4.1).

$$B(t) = (1-t)^3\, P_0 + 3(1-t)^2 t\, P_1 + 3(1-t)t^2\, P_2 + t^3\, P_3 \qquad (4.1)$$

where $0 \leq t \leq 1$ and, for S-curve, x-coordinate of $\boldsymbol{P_1}$ and $\boldsymbol{P_2}$ as well as y-coordinate of both $\boldsymbol{P_0}$, $\boldsymbol{P_1}$ and $\boldsymbol{P_2}$, $\boldsymbol{P_3}$ pairs are kept equal to one another. Using this method, a number of splitters and S-bends of varying angles is included in the final mask design as shown in Figure 4-9.

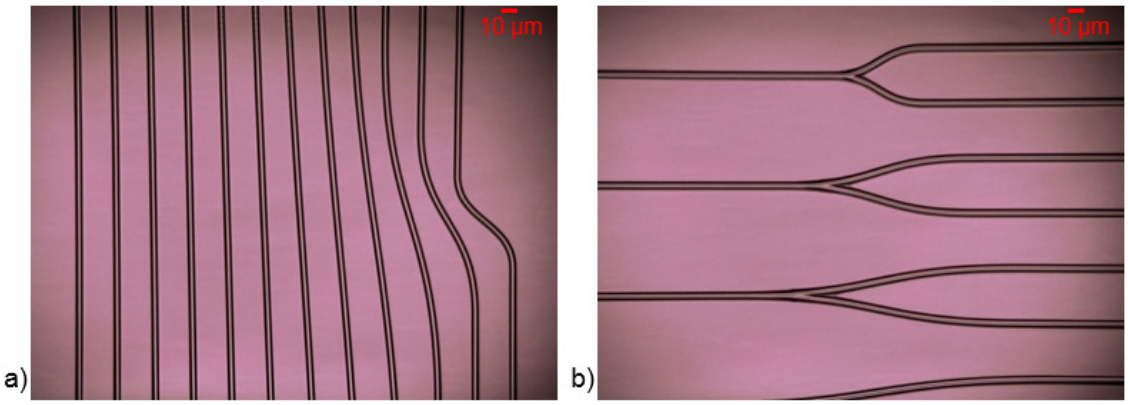

Figure 4-9: Examples of a) S-bends and b) Y-splitters based on Bezier curves

4.1.4 Cut-back measurements

Measuring a fibre-to-fibre signal with and without a sample gives a good idea of the overall loss in the device, but it is more useful to find what the contribution of internal loss is. One of the most common techniques to achieve this is the cut-back method [16], [17]. It is a straightforward albeit destructive procedure that requires a section of the original waveguide to be removed after each measurement. The reduction in the total loss between the consecutive measurements is attributed to the internal loss in the removed section. In the simplest case with a single cut, the internal loss can be found using Equation (4.2), but in practice the procedure is repeated a number of times and a linear fit is found to estimate coupling and internal losses.

$$\alpha\ [^{dB}/_{cm}] = \frac{10 \log_{10} {}^{P_1}/_{P_2}}{L_1 - L_2} \tag{4.2}$$

A set of polymer only straight waveguides with various widths were prepared using the wafer-scale fabrication procedure listed in Table 4-2. The sample with waveguides was then diced from a wafer and investigated using a cut-back setup presented in Figure 4-10 a). A tuneable laser (HP 8168E) was used to measure loss in the waveguide across the 1475-1575 nm erbium emission spectrum combined with a multimode fibre is used at the output to maximise amount of light captured and reduce measurement inaccuracy due to changing facets. In order to align the sample, visible (633 nm) laser was used to take

advantage of high scattering loss at this wavelength and, therefore, clearly visible signal path along the sample as shown in Figure 4-10 b).

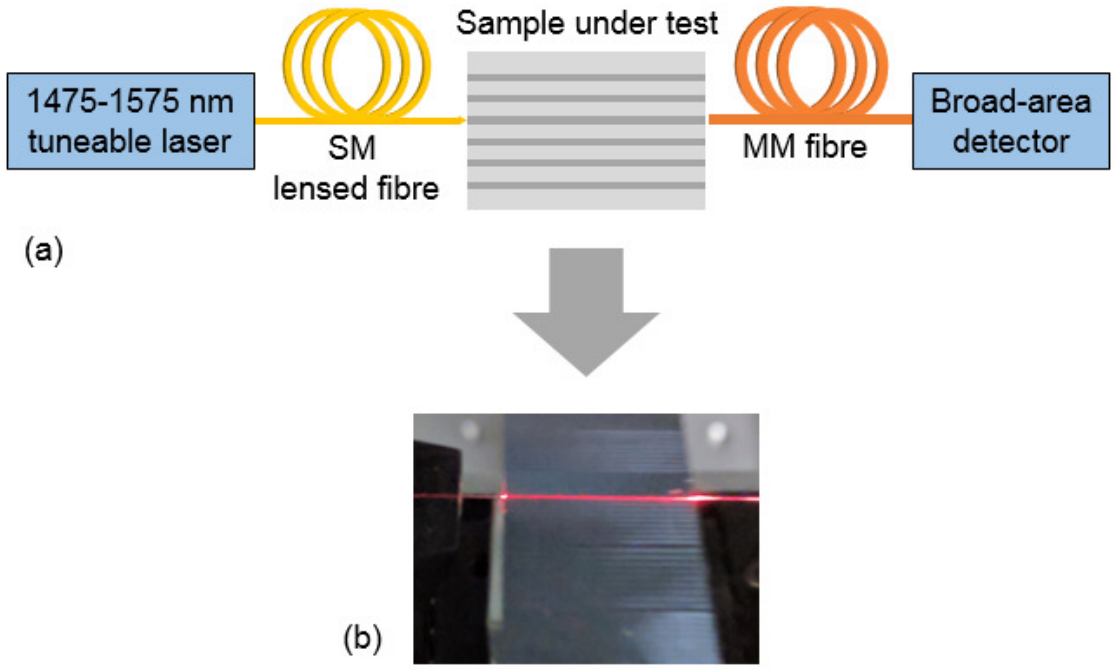

Figure 4-10: Cut-back measurement setup showing a) experimental schematic and b) straight waveguide sample under red light illumination

After completion of a set of measurements the sample was then diced at the output end using a Disco DAD341 machine. The procedure was repeated a number of times in order to have enough data points to estimate contributions of internal and coupling losses to the total loss measured through linear fitting.

4.1.5 Waveguide Loss Results

The cut-back procedure was performed on waveguides of different widths to estimate their internal loss as shown in Figure 4-11 a). The values were obtained through a methodology presented in Figure 4-11 b) on an example of a 6-μm-wide waveguide at signal wavelength of 1550 nm.

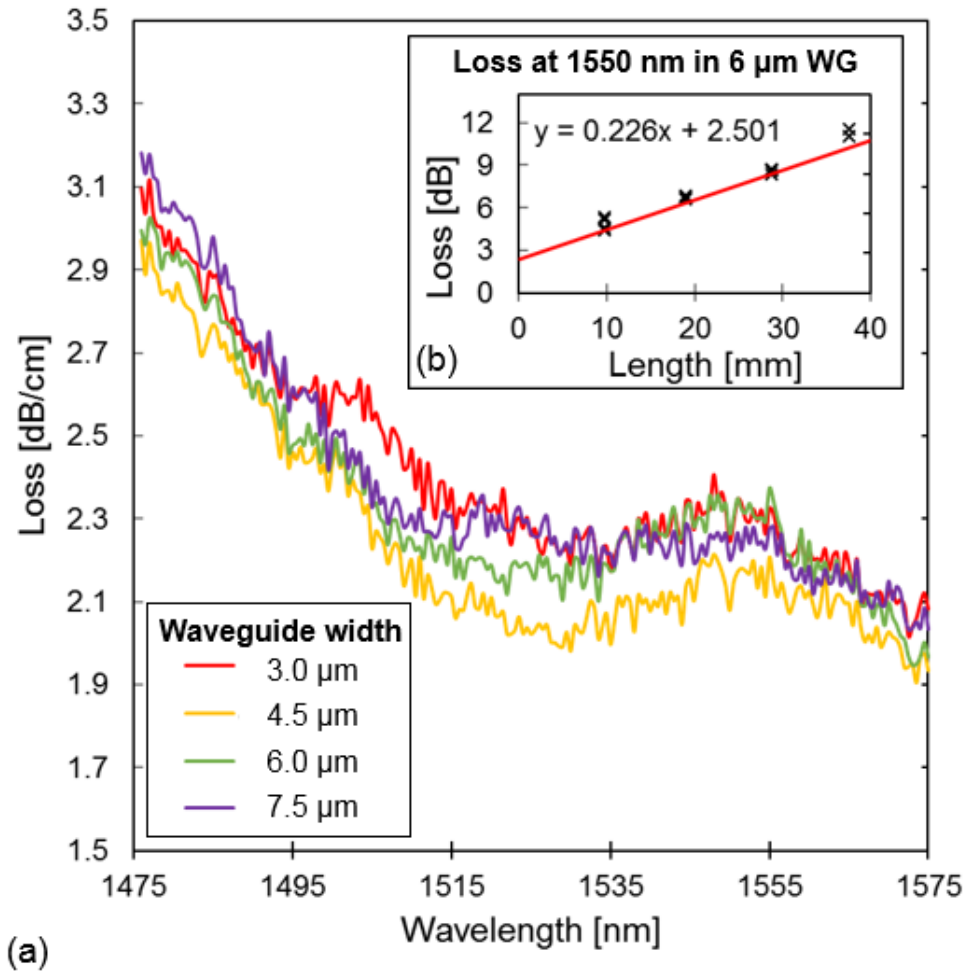

Figure 4-11: Polymer waveguide cut-back results a) internal loss across 1475-1575 nm spectral range and b) on an example of a 6-µm-wide waveguide at 1550 nm

The sample with initial length of 37.5 mm was measured and then cut and re-measured three more times at lengths of 28.7, 18.9 and 9.8 mm. For each length multiple measurements were taken and averaged and a method of least squares was used to find the best linear fit. The y-axis intersection gives the value for coupling loss while the slope of the calculated line is the internal loss per unit length.

The results for the internal loss show higher signal degradation at lower end of the investigated spectrum with loss exceeding 3 dB/cm around 1475 nm indicating that EDWA in-band pumping at 1480 nm would be inefficient. As the wavelength is increased towards 1530 nm corresponding to erbium emission peak the loss drops to approximately 2.2 dB/cm and stays constant till a smaller peak at 1550 nm. After this point it reduces again to slightly over 2 dB/cm at the highest measurement wavelength of 1575 nm. The spectral shape of the internal loss across the investigated signal wavelengths remains almost the same for measured waveguide widths and only small variation in magnitude is observed in the range of 3 µm to 7.5 µm.

The measured internal loss of 2.2 dB/cm at 1530 nm is higher than some of the best values reported in other specialist polymers mentioned in Chapter 3. However, it is lower than in case of most common, commercially available materials such as SU-8 where 2.6 dB/cm at Er peak emission wavelength has been reported [18]. In contrary to some of the lower loss materials, siloxane polymers used in this work have the benefit of being UV sensitive required for the lithography process as well as having a high degradation temperature [19] important for ultrafast laser plasma implantation process described in the next section.

4.2 Er-doped Thin Films

The next step towards realisation of EDWAs, after investigation of polymer waveguides, is demonstration of planar Er-doped planar films. These can be used not only to optimise the fabrication steps necessary for obtaining high quality doped material without damaging the host but also assessing best methods of combining doped and undoped layers to form waveguides. Furthermore, erbium thin films can be used investigate the key amplifier properties such as Er emission spectrum and $^4I_{13/2}$ metastable lifetime. These results then offer a possibility of comparing NP-dissolved and ULPI-implanted polymer films against an erbium-doped tellurite-modifies silica (EDTS) glass obtained through ion implantation process.

4.2.1 Doping Technologies

In this thesis two promising erbium doping techniques are investigated. ULPI is chosen due to the fact that it has demonstrated some of the highest reported erbium concentrations up to 1.63×10^{21} cm^{-3} while maintaining very long metastable lifetimes around 9.16 ms [20]. An alternative approach of nanoparticle dispersion in a still liquid polymer matrix is investigated as it has already been shown to generate relatively high internal gain of 6.6 dB/cm [18]. In contrary to the suggested approach of using additional polymer materials to form complex active core shells, in this work doped material is prepared through a membrane filtering process.

4.2.1.1 Ultrafast Laser Plasma Implantation

Ultrafast lasers have been reliably used for material processing, micromachining and surface ablation [21]. For many years nanosecond pulsed laser deposition (ns-PLD) has been considered a promising doping method as it has been shown to produce NPs with process-controllable size, morphology and composition [22]. Fabrication of NPs using even shorter, femtosecond pulses (fs-PLD) has also been validated on a range of dielectric

materials such as aluminium or various glasses [23], [24]. Decreasing the duration of the pulses has been demonstrated not only to improve the properties of the fabricated thin films in terms of NP size uniformity and agglomeration, but also provide greater degree of control of the nanoparticle size [25]. The ULPI process used in this thesis for fabrication glass and some of the polymer Er-doped thin films is based on the fs-PLD [26] as shown in Figure 4-12 and has been performed by project collaborators from the University of Leeds.

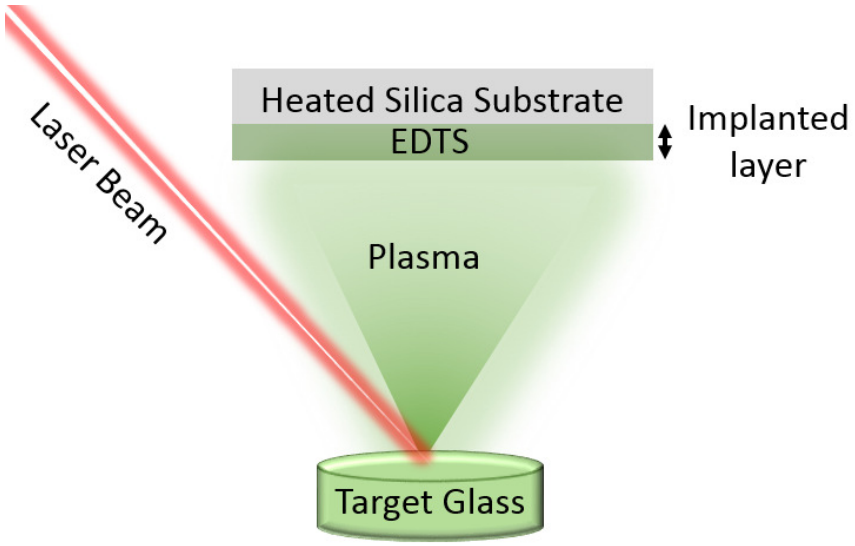

Figure 4-12: ULPI fabrication schematic showing formation of the EDTS layer

First, tellurite glass targets required for deposition are prepared using standard glass melting and quenching processes [27], which allow for good control of the concentration and ratio of erbium and ytterbium ions in the final deposited layer. The prepared target is then placed in a vacuum chamber in front of a deposition substrate. The high-energy femtosecond pulses are then used to ablate the prepared target leading to generation of a highly energetic plasma that expands towards a heated-up substrate surface. Silica temperatures in range of 600 °C to 800 °C assist the diffusion process resulting in a homogenous Er-doped thin film layer deposited on the substrate [28].

The ULPI process has been mainly used for rare-earth ion implantation into silica glass to form EDTS layer that is used in this work to investigate hybrid structures where the fabrication process is completed by addition of polymer ridges on top of the deposited erbium layer. However, the process has also been modified in order to deposit erbium into a siloxane polymer thin film layer on top of a substrate as described in the next section.

4.2.1.2 Nanoparticle Dispersion

An alternative technique of fabricating polymer-based EDWAs is dispersing Er-doped nanoparticles in the polymer matrix. A lot of work has been done to address inorganic material insolubility in polymers through, for example, active core-shells, leading to the promising results summarised in Chapter 2.

In this work, ceria-based (CeO_2) nanoparticles and siloxane polymer materials are combined to develop a cost-effective method of producing Er-doped polymer thin films and waveguides with strong photoluminescence properties required for EDWA applications. Er:Gd co-doped ceria nanoparticles (EGC NPs) are synthesised using a novel Leeds Alginate Process (LAP) sol-gel method developed for a single-step fabrication of complex functional ceramic oxide NPs of highly controlled composition [29]–[31].

The LAP process has been used by collaborators at the University of Leeds to prepare $Ce_{0.8}Er_{0.1}Gd_{0.1}O_{1.9}$ nanoparticles using the procedure shown in Figure 4-13. Commercially available nitrates: $Ce(NO_3)_3{\cdot}6H_2O$ (>99% of purity), $Er(NO_3)_3{\cdot}6H_2O$ (>99.9% of purity) and $Gd(NO_3)_3{\cdot}6H_2O$ (>99.9% of purity) are used to prepare the dopants. Two separate solutions are prepared under magnetic stirring – one with metal complex and one with sodium alginate, before the sodium alginate solution (SAL) is added into the metal complex solution using a steel needle attached to a syringe. The resulting gel beads are kept for 14 hours before the wet metal-alginate material is dried at 90 °C for 24 hours. The final nanoparticles are then obtained through a calcination process from the dry beads taking place at 500 °C for 2 hours in ambient atmosphere. The optimum process parameters, such as calcination temperature, have been experimentally determined on dried beads of similar composition [31].

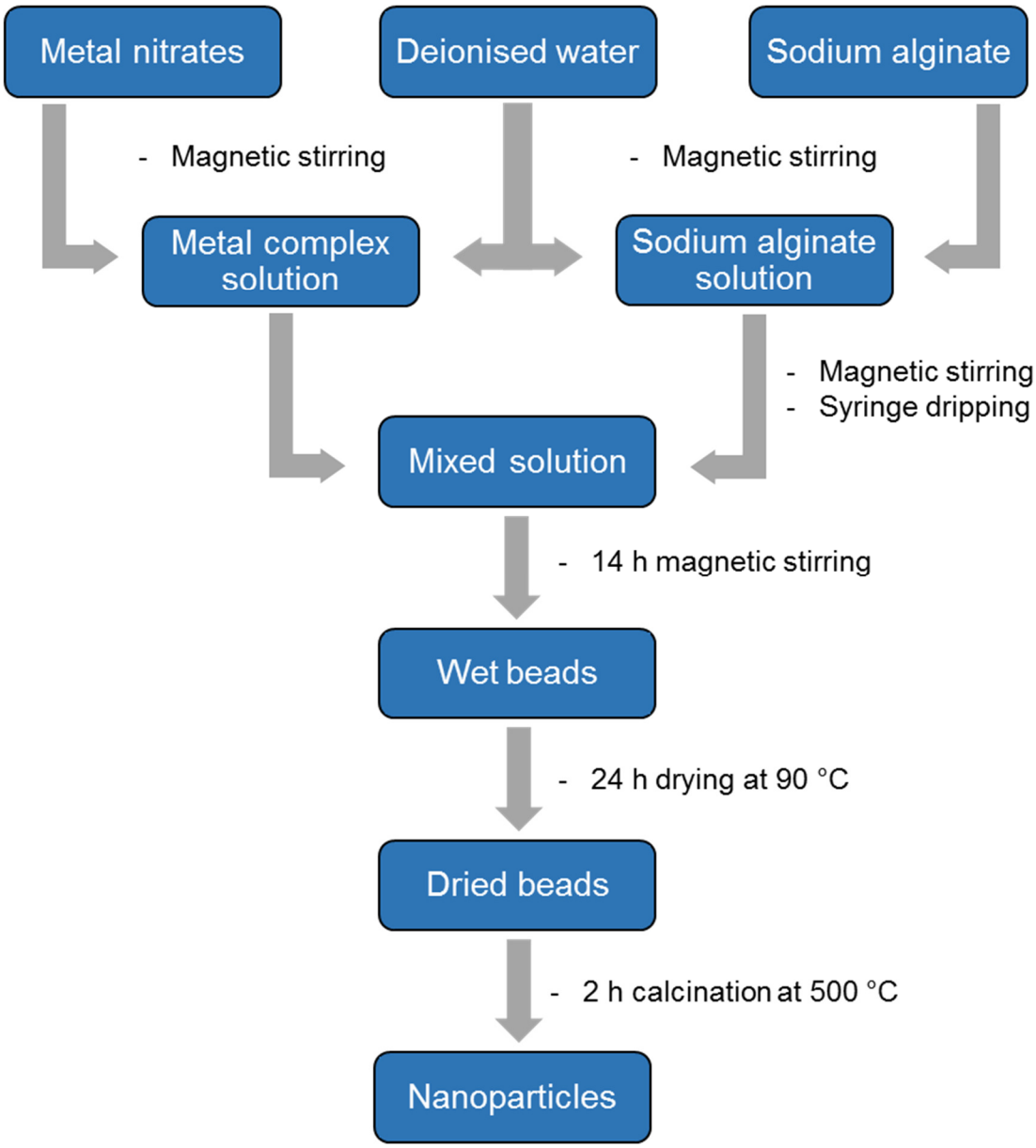

Figure 4-13: Fabrication process flow for ceria nanoparticles used in this thesis

4.2.2 Fabrication Processes

Three different approaches to making Er-doped polymer-based amplifiers are investigated with the detailed fabrication steps and process optimisations presented in this section. Hybrid structures and direct implantation both take advantage of the ULPI technology, but the key difference is that silica glass (UQG Optics Spectrosil 2000) and siloxane polymer (Dow Corning WG-2020) are used as a substrate respectively. The third method is based on combination of the same polymer material with ceria nanoparticles to then produce thin films via spin-coating.

4.2.2.1 ULPI – Glass Substrate

The ULPI fabrication has been carried out by Dr Eric Kumi-Barimah as a part of a collaboration work on the Seamatics project. The Functional Materials group at the University of Leeds has the required implantation setup to create Er-doped thin films and the expertise in operating it. ULPI is a complex and relatively new process where many operating parameters affect the final Er-doped layer. Some of the key process variables include target glass composition, laser pulse energy, substrate temperature, pressure in the vacuum chamber and duration of the process. These parameters have been studied on the setup used to prepare samples for this thesis as summarised based on published data in Figure 4-14 in terms of the key design properties of Er concentration and refractive index.

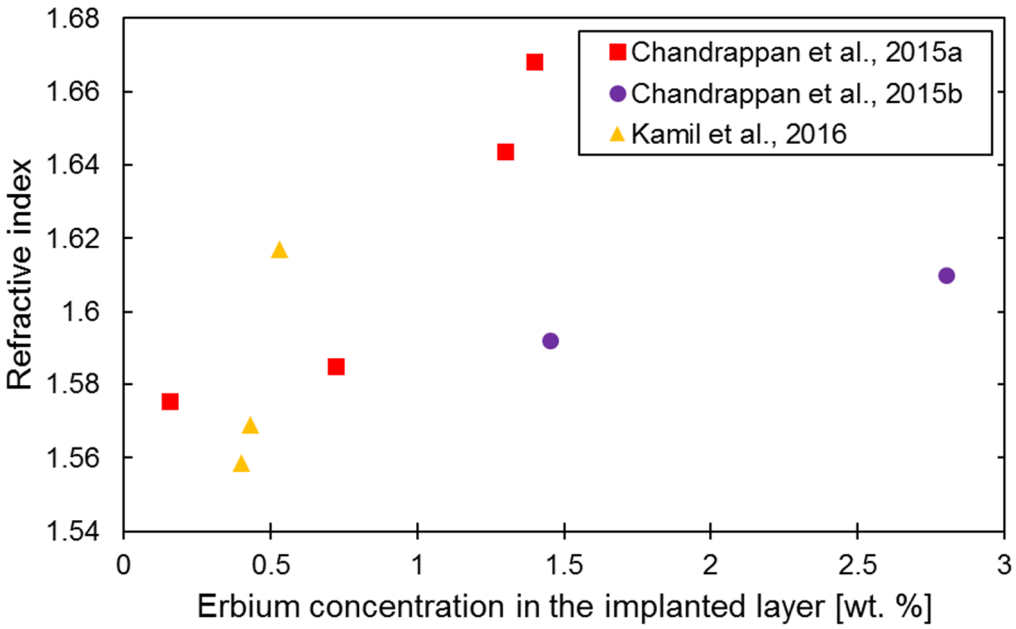

Figure 4-14: Summary of refractive index and Er concentration data based data published on ULPI setup used in this work

In general, an increasing erbium concentration results in higher refractive index, but there are a number of other important factors. When the only varied parameter is the erbium content in the target glass (red squares), the resultant EDTS layer shows that higher Er concentration leads to higher refractive index when target glass composition $(80\text{-}x)TeO_2\text{-}10ZnO\text{-}10Na_2O\text{-}xEr_2O_3$ is varied for x = 0.125,0.5,0.75 and 1 [32]. Similar experiments under an altered deposition procedure is performed on higher dopant concentrations of 1 and 2 wt.% in the target glass (purple circles) showing a similar increasing trend, but at a different rate [33]. However, it is not the only factor affecting thin film properties as even with identical target glasses and changing only the laser

energy (yellow triangles corresponding to 50, 60 and 80 μJ) the implanted layer erbium concentration increases from 0.4 to 0.53 wt.% and refractive index grows from 1.5587 to 1.6172 [34].

The samples received for analysis in EDWA studies based on EDTS layer for polymer-glass hybrid structures are listed in Table 4-3 with all the known implantation parameters and the measured layer thickness. The corresponding dopant concentrations in the EDTS layers are estimated to be $1.63 \times 10^{27} m^{-3}$ for T-series and $0.91 \times 10^{27} m^{-3}$ for the other thin films. Samples O6, C1 and C2 are deposited on a maximum substrate size fitting the ULPI chamber (2×3 cm^2) while T26 and T28 are half this size (2×1.5 cm^2).

Table 4-3: Summary of implantation parameters for EDTS samples

Sample Name	Target composition [TeO-ZnO-Na_2O-Er_2O_3-Yb_2O_3 wt.%]	Laser energy [μJ]	Deposition time [h]	Chamber pressure [mTorr]	Measured EDTS thickness [μm]
T26	85.4-5.5-7.2-1.9-0	60	8	95	2.05
T28	85.4-5.5-7.2-0.6-1.3	65	4	65	2.54
O6	79-10-10-1-0	300	4	80	0.62
C1	79-10-10-1-0	150	4	80	0.84
C2	79-10-10-1-0	160	4	80	1.20

4.2.2.2 ULPI – Polymer Substrate

Ultrafast laser plasma implantation into polymer has not been attempted prior to this work therefore the process is adjusted for this type of substrate. The polymer samples are spin-coated onto a silica substrate at 2000 rpm for 1 minute, UV-exposed for 1 minute and hard-baked at 180 °C to form a uniform ~ 10-μm-thick layer. The wafers are then cut into 2×3 cm^2 pieces suitable for the ULPI chamber.

The target Er-TZN glass used for direct implantation into polymer layer has a composition of $79.5TeO_2$-$10ZnO$-$10NaO_2$-$0.5Er_2O_3$ (wt.%). As in case of implanting into a glass substrate, a number of parameters are varied to find best quality of thin film. The substrate temperature is reduced from 700-750 °C used for silica glass to 100 °C in order to minimise polymer damage. The implantation time and laser energy are also reduced as keeping the sample for over 1 hour in the chamber results in polymer film peeling off the substrate. In the end, the two most promising samples which have been used for further analysis have corresponding ULPI parameters summarised in Table 4-4.

Table 4-4: Summary of implantation parameters for polymer samples

Sample Name	Laser energy [µJ]	Deposition time [h]	Substrate temperature [°C]	Chamber pressure [mTorr]
F1	45	0.75	100	70
F3	60	0.75	100	70

A visual inspection of the two Er-implanted polymer samples uncovered a granular character of the surface that led to a SEM check to obtain more information on the surface quality as shown in Figure 4-15. The two images revealed that the process parameters such as temperature and laser energy, set at much lower values than for EDTS implantation, have led to the ablated target glass particles deposition on top of the polymer layer rather than implantation into it. Furthermore, the higher energy deposition of sample F3 resulted in the average deposited Er-TZN glass particle size of ~ 21 nm to be larger than for F1 where ~ 11 nm are observed.

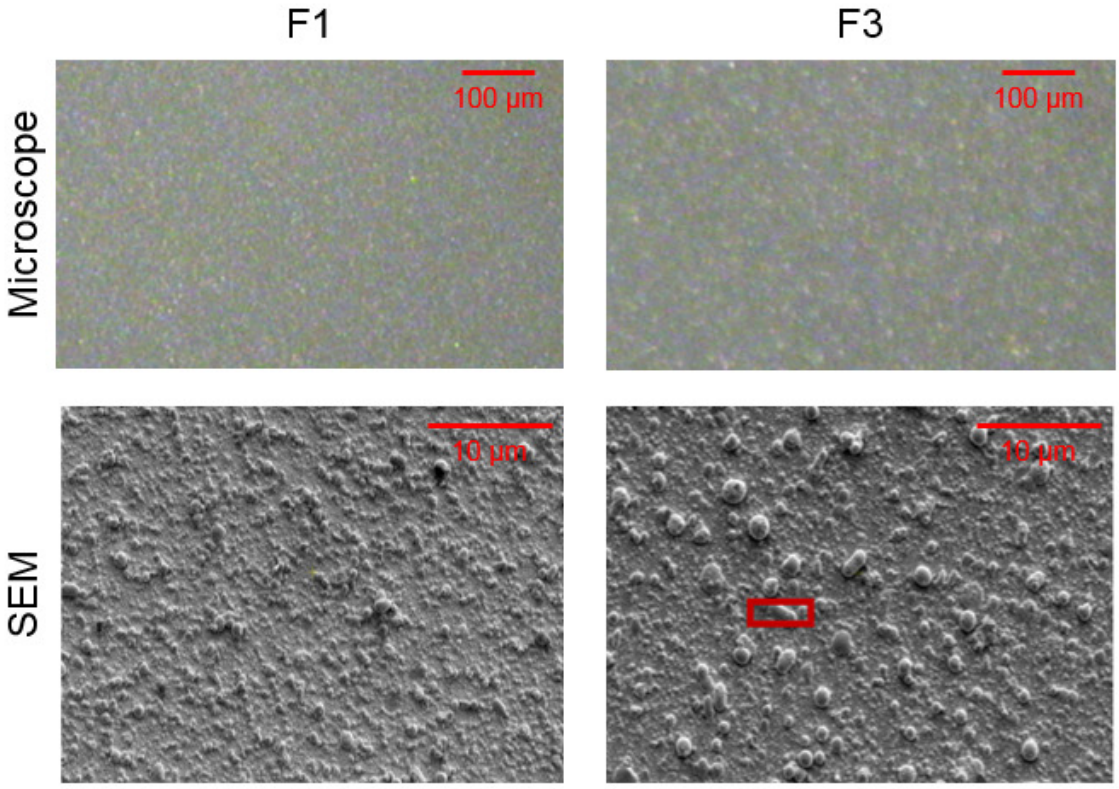

Figure 4-15: Visual inspection of ULPI on polymer samples using a microscope and SEM on samples F1 and F3 [35]

4.2.2.3 Nanoparticles

The polymer thin films doped with ceria nanoparticles have been prepared using the fabrication procedure shown in Figure 4-16. The EGC NPs are dispersed in toluene and polymer at various concentrations with the amount of toluene kept at a constant 20 wt.% as used for polymer-only systems. The weight ratio of the polymer (***80% – x***) and nanoparticles (***x***) is varied with NP content being in range from 0.1 wt.% to 12.5 wt.% of the total mix. After all the components are combined together, the mixture is stirred overnight and then undergoes ultrasonication process to reduce particle agglomeration in the solution [36]. The process is completed by membrane filtration though a commercially available (Whatman) syringe filters before deposition on a small 15×20 mm^2 silica glass sample. The optional filtering step is added to the procedure in order to remove any larger NP agglomerations in the material and reduce the luminescence quenching.

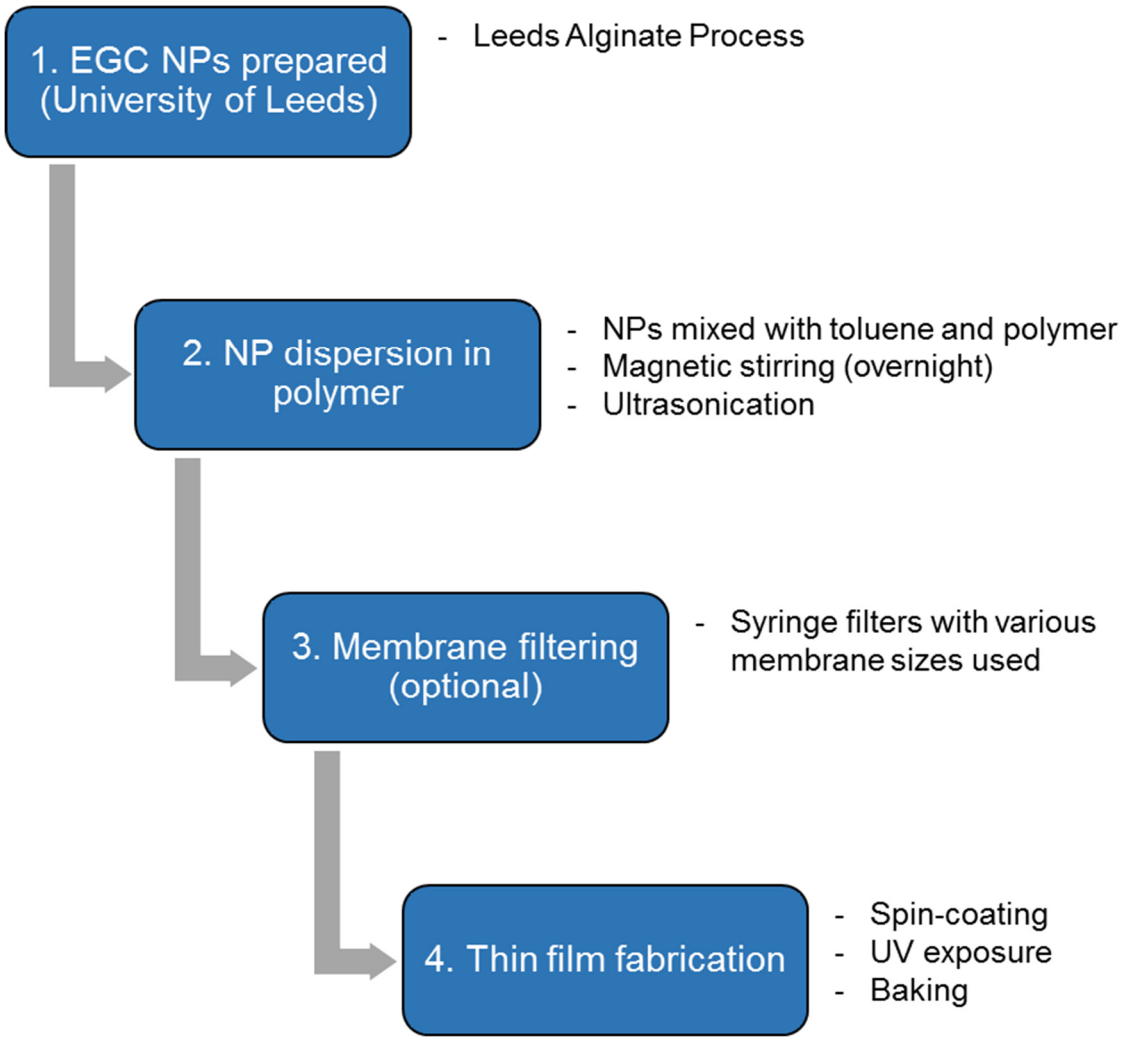

Figure 4-16: Fabrication process flow for NP-dispersed polymer thin films

The first batch is prepared using readily available at the time, un-optimised NPs has been used to determine the most suitable membrane filter size. The same 0.1 wt.% EGC concentrations is used to prepare a set of samples without filtering as well as with membrane sizes of 20, 200 and 1200 nm. The resultant thin films are then compared in terms of their relative PL intensity and FWHM as shown in the next section.

Based on these results, a second batch of NP-doped polymer materials is prepared using fabrication-optimised EGC nanoparticles. The powdered nanoparticles have been measured by project collaborators using high resolution transmission electron microscopy (HRTEM) as shown in Figure 4-17. The image shows that the agglomerated cubical-shaped particles have size in range of 7 to 10 nm before the dispersion in the polymer matrix.

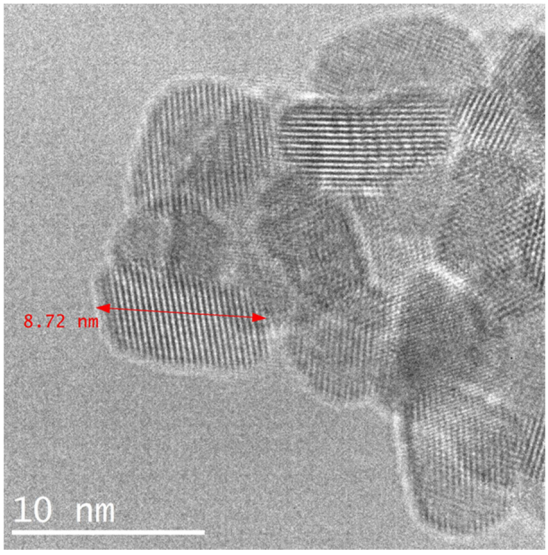

Figure 4-17: HRTEM image of EGC NPs taken at University of Leeds

The same dispersion process is used with the key difference being the nanoparticle concentration is increased from 0.1 wt.% to higher values in range from 1 wt.% to 12.5 wt.%. The effect of filtering is investigated by comparing unfiltered and filtered material in the same way as for the first batch. As a result of the initial material analysis, only the smaller (20 and 200 nm) membrane filters are considered. During the fabrication process it has been revealed that due to the higher concentrations involved the 20 nm filter would block before a deposition process on a glass sample is finished. Therefore, ten thin films are prepared based on EGC nanoparticle concentrations of 1, 2.4, 5.1, 9.2, 12.5 wt.% with and without a filtering step before thin film deposition. The resultant thin films are visually inspected using a microscope as shown in Figure 4-18. It is observed that without filtering large agglomerations of inorganic nanoparticles are present in the mix. They are

often larger in size then the waveguide features designed for this work, making the additional filtering step necessary for better quality film fabrication. Even with the proposed filtering step, sub-micron spots are noticed on the final thin film suggesting that additional clustering may occur between the filtering and sample fabrication completion.

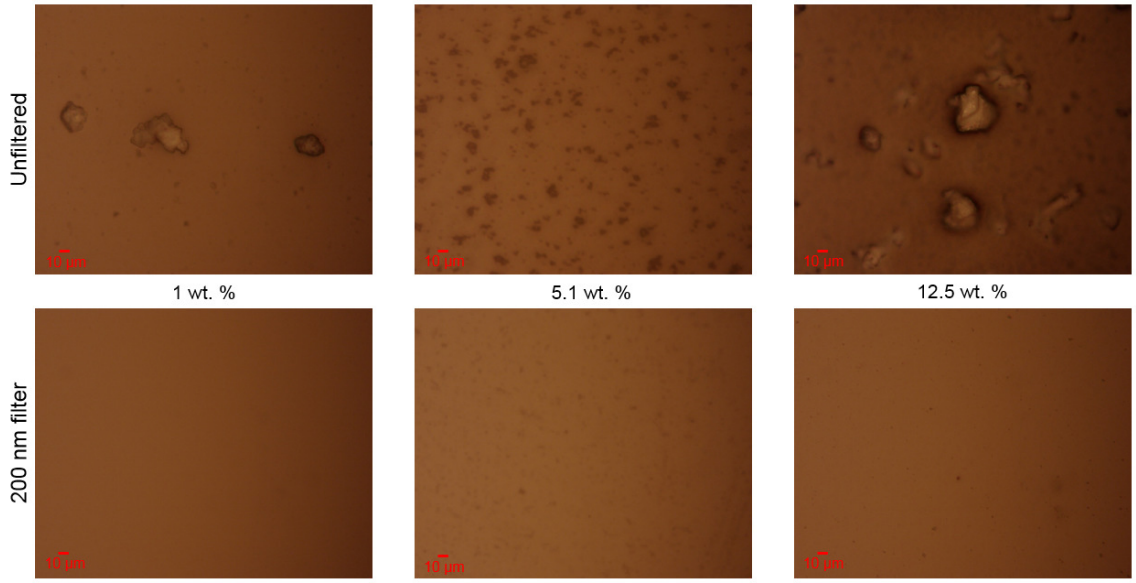

Figure 4-18: Microscope pictures of filtered and unfiltered EGC NP-doped polymer thin films at various dopant concentrations

4.3 Thin Film Characterisation and Comparison

4.3.1 Characterisation Methodology

Optical characterisation of the erbium-doped thin films is performed in order to extract the key parameters required for characterising EDWA performance. The key properties that are determined though thin film measurements are not only the emission spectrum, in particular full width at half maximum (FWHM) and peak wavelength, but also lifetime of the erbium ions. These results then are combined to derive emission and absorption cross-sections required for full amplifier studies as presented in Chapters 5 and 6.

The photoluminescence spectrum of the EDTS layer is measured at a room temperature using the setup shown in Figure 4-19. A pump laser diode (BL976-PAG500) emitting at 976 nm is used to excite an erbium-doped thin film sample mounted on a 3-axis stage. The pump light is then filtered out (FELH1500 long-pass filter with 1500 nm cut-off wavelength) before the signal is collected using multi-mode fibre connected to an optical spectrum analyser (Yokogawa AQ6370D). Optimal alignment and focusing is achieved with a set of four lenses mounted on movable stages.

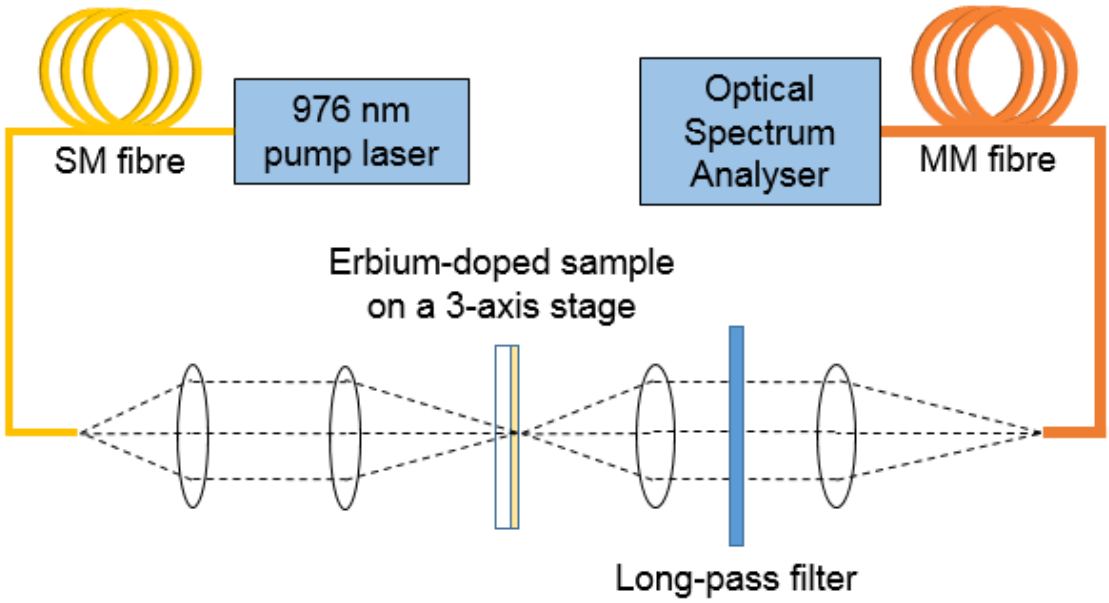

Figure 4-19: Photoluminescence measurement setup

The lifetime and photoluminescence spectrum of the polymer films is measured by collaborators at a room temperature using a more sensitive integrated setup with the FS920 spectrometer (Edinburgh Instruments) under a 976 nm laser-diode excitation. The pump light is prevented from reaching the spectrometer by using a long-pass filter with a cut-off wavelength of 1100 nm.

4.3.2 Photoluminescence Spectrum and Erbium Lifetime

4.3.2.1 ULPI Glass

The photoluminescence emission spectra across the telecommunications C-band of the five EDTS samples are plotted in Figure 4-20. The results are normalised with respect to the emission peak of the strongest sample – T28 in order to assess the relative intensity of the light. It is noticed that the T-series samples are performing the best in terms of intensity which is expected due to their higher dopant concentration and greater thickness. The main difference between samples T26 and T28 is that the latter is co-doped with ytterbium at a ratio of 1:2 Er:Yb. This suggested that even at extremely short pump interaction distances adding ytterbium to the mix can beneficial in terms of NIR emission strength. The remaining three samples have the same, lower erbium concentration and, as a result of the implantation process parameters, have slightly different thicknesses. The similarity of the target material is apparent when the peak emission intensity is found to be approximately 1534 nm for all the investigated samples.

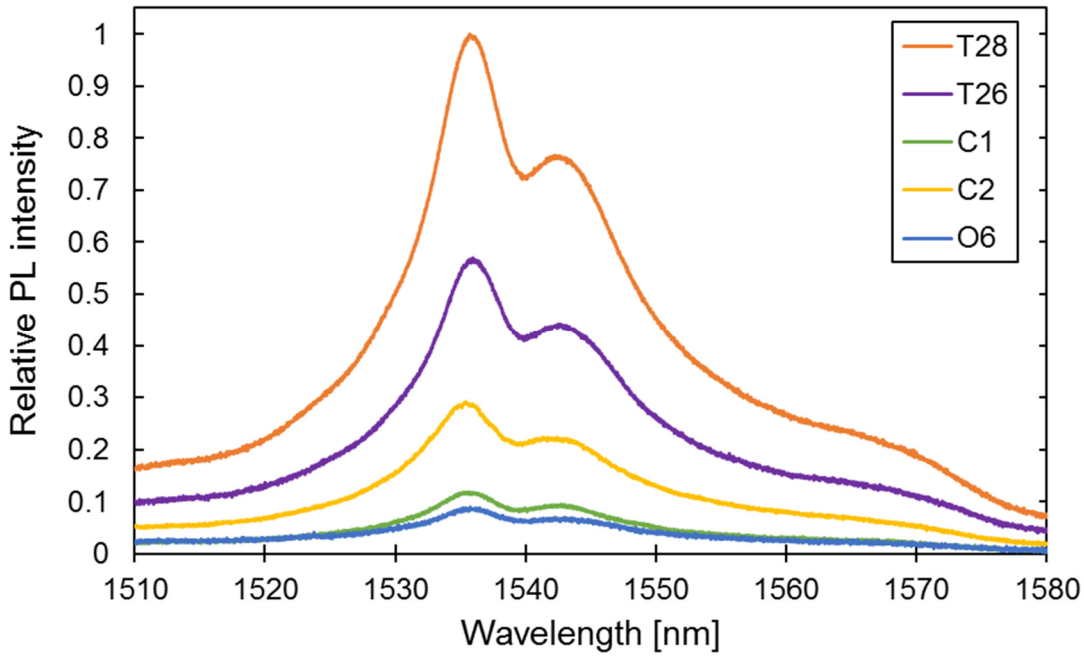

Figure 4-20: PL spectra of EDTS samples normalised against the strongest emitting sample T28

The measured relative intensity peaks of 0.09, 0.11 and 0.29 for thickness of 0.62, 0.84 and 1.2 μm are observed for samples O6, C1 and C2, respectively. The intensity difference is adjusted by the sample thickness and dopant concentration in order to see the impact of other factors on the film quality and compared to the thickest sample T28 as shown in Figure 4-21. The results indicate that a large part of the previously observed discrepancies is an effect of these two variables as the differences between samples became much smaller. There is still a deviation in the emission intensity indicating other implantation parameters play a role in the resultant film quality. Additionally, FWHM results confirm spectral shape similarity between the samples as not only the peak emission intensity is approximately the same but also the spectral width is very close to 20 nm for all the EDTS samples.

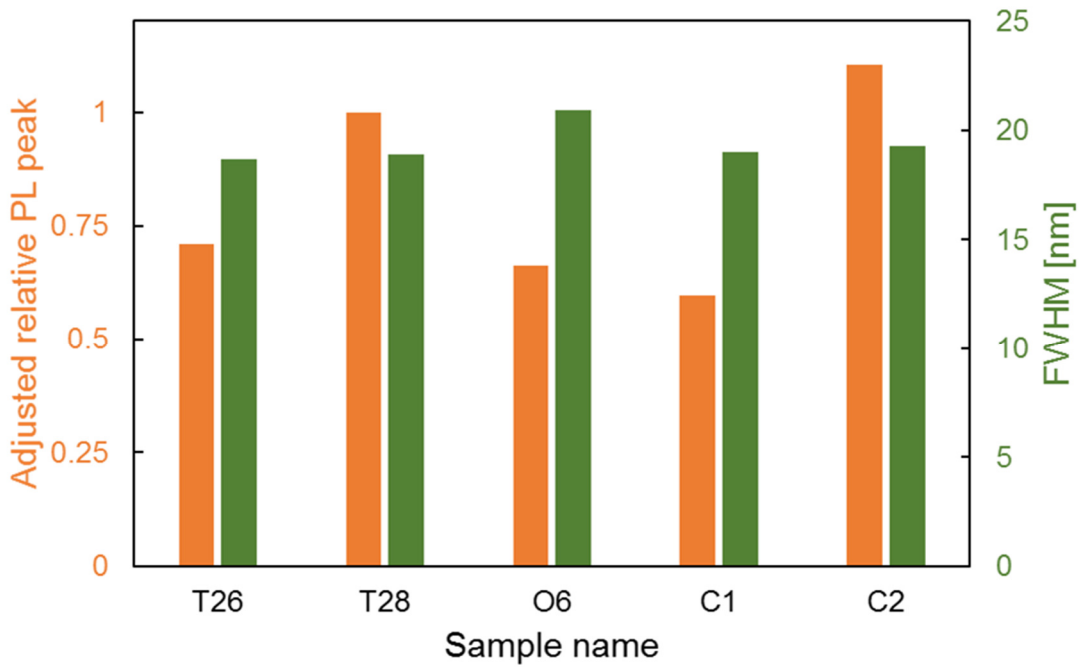

Figure 4-21: EDTS sample comparison in terms of the relative PL peak adjusted by sample thickness & dopant concentration and FWHM

Even though the spectral shape of all the samples is very similar, they differ in terms of their metastable lifetimes. The strongest emitting thin films from the T-series have very good lifetime of lifetimes of 11.8 and 12.1 ms for T26 and T28, respectively. Remaining samples have not only weaker PL intensity but also shorter Er lifetimes of 2.2 and 4.9 ms for C1 and C2 respectively indicating that they are less suitable for EDWA fabrication in terms of these properties and sample T28 is the most promising candidate for hybrid structure studied in detail in Chapter 5.

4.3.2.2 ULPI Polymer

The same measurement procedure is performed on the most promising polymer samples F1 and F3 as shown in Figure 4-22. It is apparent that the polymer-doped samples have much weaker photoluminescence signals compared to the strongest EDTS sample. At their peaks they only reach 0.04 and 0.08 emission coming from the T28 sample. Part of the difference arises from the fact that a target glass with only 0.5 wt.% Er is used for ULPI, but this does not explain the entire observed difference. Another important reason expected to contribute to the reduced NIR emission is the clustering seen in Figure 4-15.

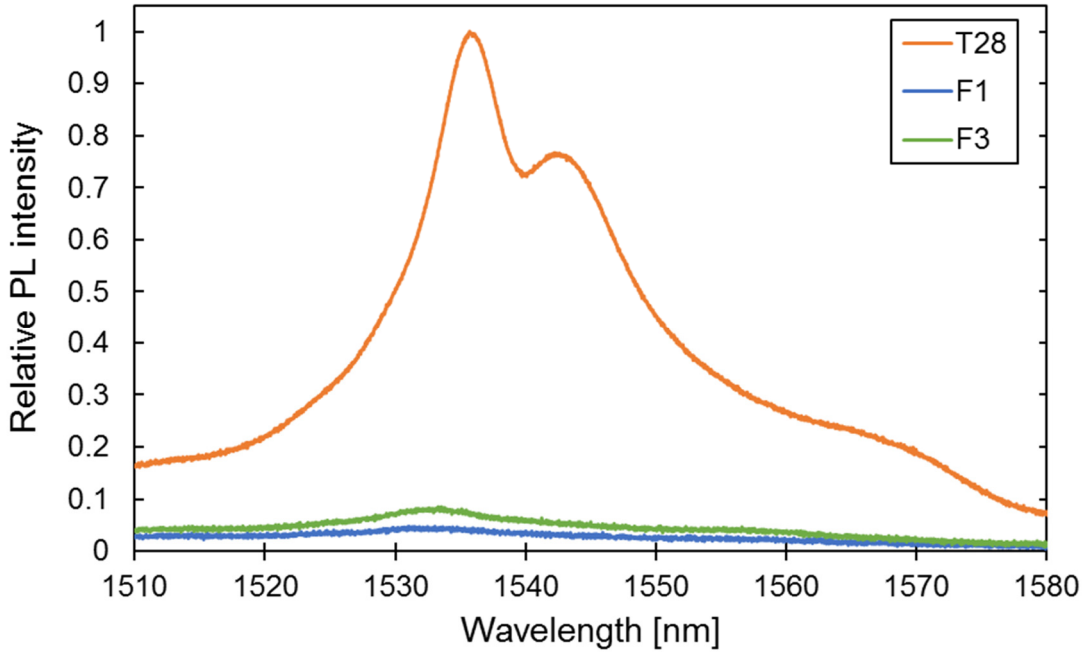

Figure 4-22: PL spectra of implanted polymer thin films normalised against the strongest emitting EDTS sample T28

Furthermore, a broader FWHM of 39 nm is observed for the F-series polymer samples peaking at wavelength of 1533 nm. Compared to the EDTS the peak occurs at a slightly lower wavelength and the spectrum is slightly broader. In terms of their lifetime, 3.5 and 4.2 ms are measured for F1 and F3 respectively, which is shorter than the EDTS T-series samples but comparable to the remaining glass-doped thin films.

4.3.2.3 Nanoparticles

Figure 4-23 shows a result of varying the filter size on the PL intensity of the first batch of the polymer doped with low concentration of 0.1 wt.% where all the investigated samples have the same peak emission wavelength of 1532 nm. Compared to the base case where no filtering is used, both 20 and 200 nm show a stronger photoluminescence signal while a larger 1200 nm filter reduced the light emission intensity. Using small membrane filters is believed to remove agglomeration sizes above their size. However, by comparing results for 20 and 200 nm pores, it can be seen that having too small membrane is detrimental as it results in removal of too many EGC NPs and lower intensity. In contrary to beneficial impact of these two filters, 1200 nm membrane has led to lower PL signal compared to the unfiltered benchmark indicating removal of some Er particles but without the benefit of quenching reduction.

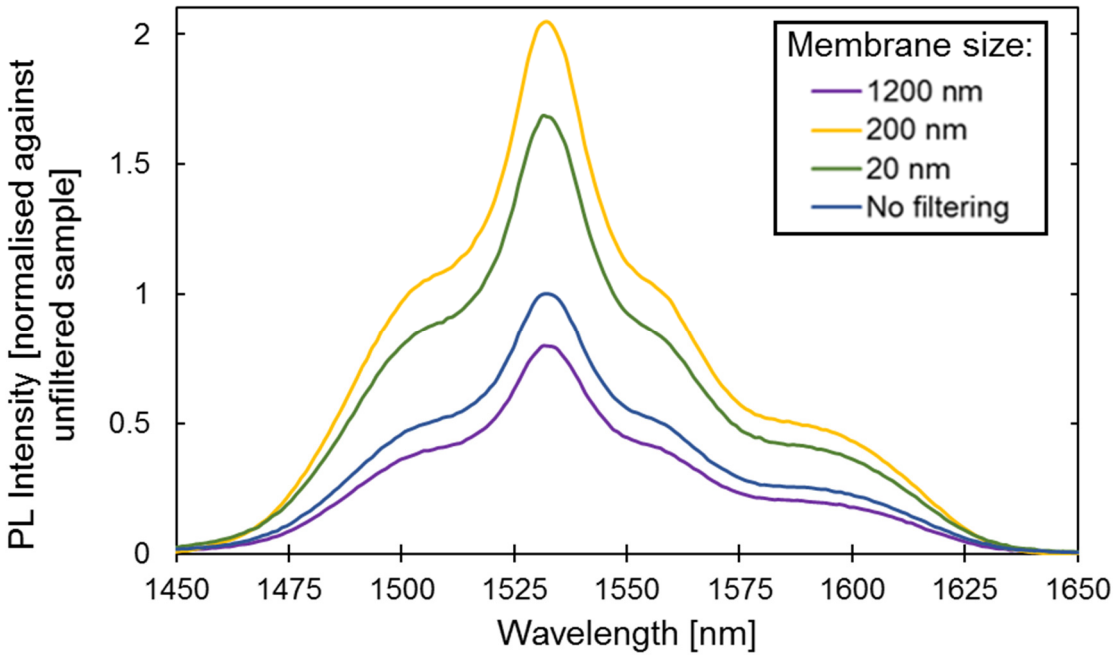

Figure 4-23: Relative PL intensity of the first batch of EGC NPs normalised with respect to unfiltered sample

Further analysis of the filtering effect is performed based on another important material property from a perspective of the amplifier operation. FWHM, which determines the amplification spectrum of the EDWA, is measured for the different filter sizes. Figure 4-24 shows that, as expected from the PL intensity graph, there is not much disparity in this thin film property and a relatively constant value around 55 nm is observed. The value for unfiltered sample is approximately 53.5 nm and using filters increased it slightly by 1.4, 4.4 and 3.1 nm for membrane sizes of 1200, 200 and 20 nm respectively.

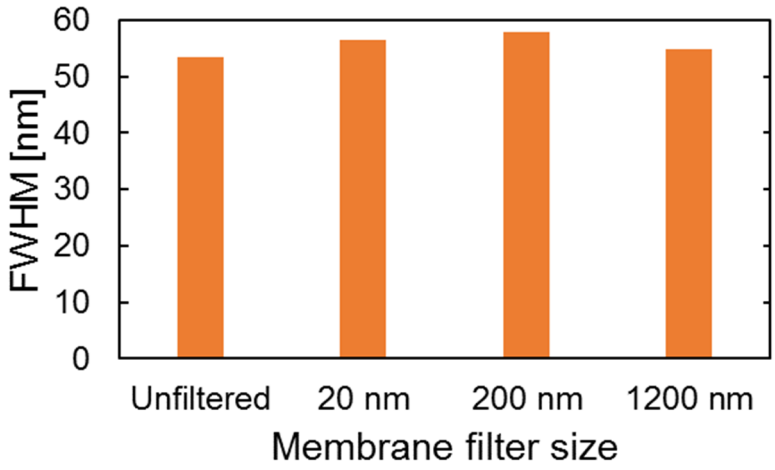

Figure 4-24: FWHM measurement results of the first batch of EGC NPs

Similar photoluminescence studies of the thin films from the second batch with higher dopant concentration of optimised NPs are carried out for both filtered and unfiltered samples as shown in Figure 4-25. The same scales are chosen to present the improvement between films obtained with additional 200-nm-membrane filtering step (Figure 4-25 a)) and without (Figure 4-25 b)). Despite the differences in the intensity depending on the concentration, all the measured films exhibit very similar spectral shape peaking at approximately 1532 nm.

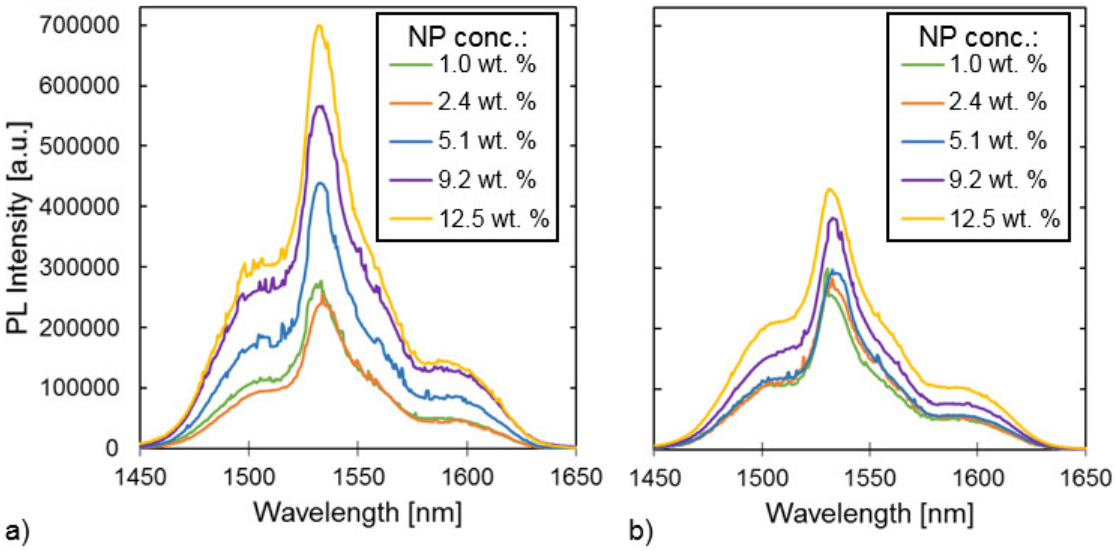

Figure 4-25: Photoluminescence intensity of EGC NP-doped polymer thin films at various concentrations a) with and b) without filtering

The improvement in PL intensity with increasing NP concentration and as a result of filtering is summarised in Figure 4-26 where not only intensity but also FWHM and Er metastable level lifetimes are compared across the obtained thin films. Figure 4-26 a) shows the relative peak (1532 nm) PL intensity normalised against the unfiltered film of the lowest concentration. In an ideal system with no clustering and perfectly uniform distribution, the emission value for higher concentrations would increase in line with the NP ratio. However, by observing the progression for unfiltered samples almost no change is observed for 2.4 and 5.1 wt.% samples while the highest doped films improve PL intensity by 28% and 44% for 9.2 and 12.5 wt.% respectively. There is an improvement in the emission intensity, but it is much lower than expected suggesting a significant concentration quenching and poor dispersion uniformity. A very similar trend emerges for filtered samples, where for smallest two concentrations a minimal reduction in the emission intensity is detected compared to unfiltered samples indicating some dopants being removed without any benefit to signal strength. Only at the higher concentrations

there is a more pronounced improvement of 59%, 105% and 154% compared to the unfiltered 1 wt.% sample for filtered concentrations of 5.1, 9.2 and 12.4 wt.% respectively. It is believed based on PL intensity that the filtering step helps to remove the largest NP clusters leading to improved performance, but the dispersion is still not completely uniform as the relative intensities are lower than expected from the relative dopant concentration.

Despite the fact that similar spectral responses with peak around 1532 nm are observed (Figure 4-25), there is some degree of variation between samples in terms of their FWHM as shown in Figure 4-26 b). A large FWHM is key requirement for a broadband amplifier and is a useful performance parameter to study in practical designs. In most of the prepared films, the emission spectral width around 35 nm, from 1520 to 1555 nm covering most of the telecom C-band (1525-1565 nm). However, in case of the lowest NP concentration of 1 wt.% it is much lower at 22.1 and 28.8 nm while for the highest 12.5 wt.% it becomes 41.4 and 33.3 nm for unfiltered and filtered films respectively. This would suggest that this is an effect related more to clustering rather than the concentration as the FWHM is much more uniform for filtered thin films.

The final comparison criteria for the NP dispersed thin films is the lifetime of the $^4I_{13/2}$ erbium level measured at the peak wavelength. As in case of the FWHM values, no clear trend emerges across the samples when looking for an effect of filtering. In both cases, the peak lifetime occurs at NP concentration of 2.4 wt.% and then slightly shortens as the concentration is increased. This is expected as higher concentrations tend to increase quenching effects, however in case of doping with NPs it appears to be more affected by the nanoparticle composition than the dispersion uniformity in the polymer. In the ECG NP-doped polymer, increasing concentration from 2.4 to 12.5 wt.% reduced the lifetime by 0.7 and 0.4 ms for unfiltered and filtered samples respectively. This is a much smaller change compared to the difference between second and first NP batches where the average lifetimes are 5.7 and 3.1 ms respectively. The shorter lifetime of the first batch of un-optimised EGC NPs is measured despite the dopant concentration being only 0.1 wt.% compared to second batch's 1-12.5 wt.% of the total mix.

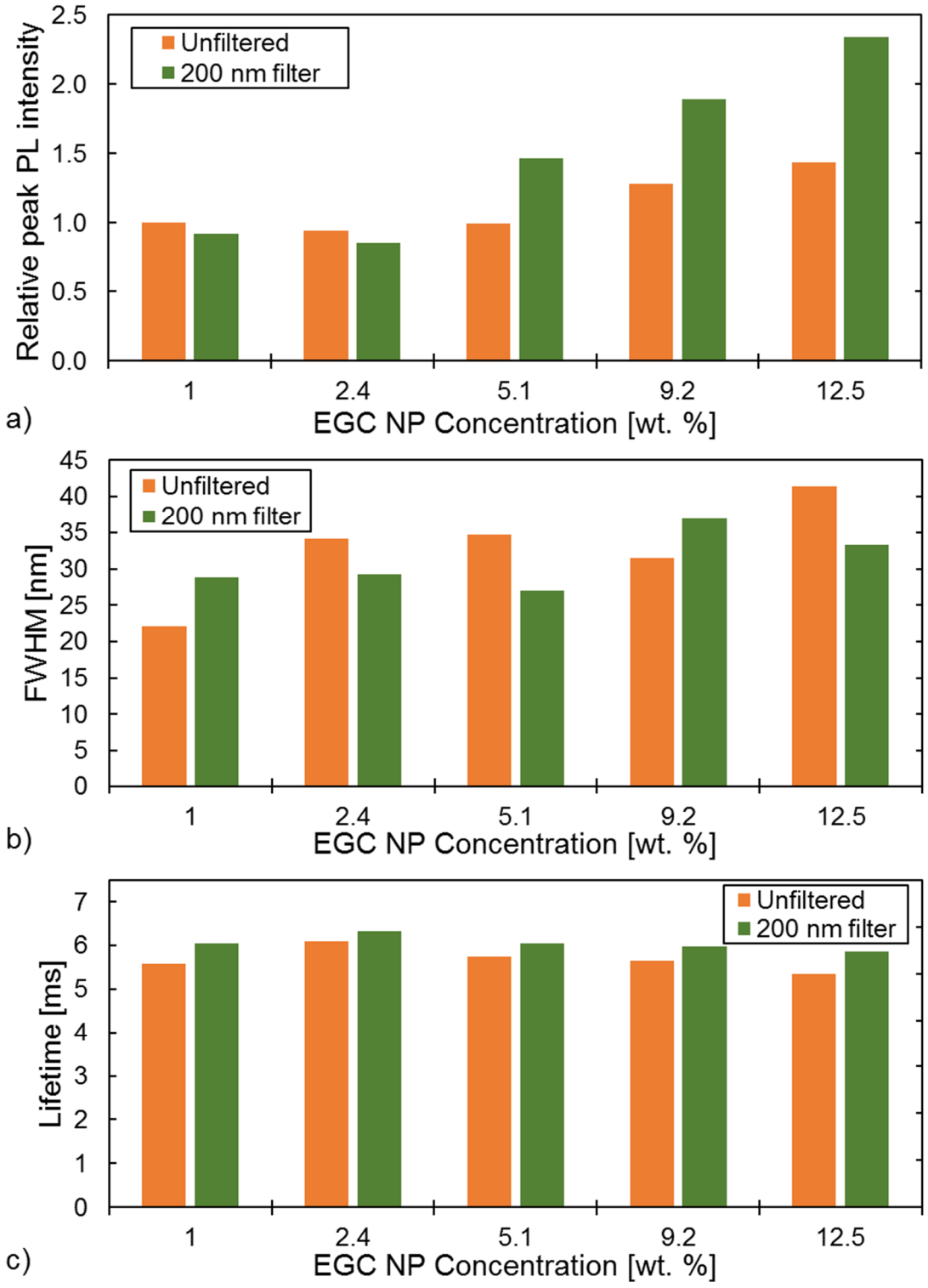

Figure 4-26: EGC thin film comparison in terms of a) relative peak PL intensity, b) FWHM and c) Er lifetime

4.3.3 Result Comparison and Discussion

The samples prepared with different methods presented in previous sections have been compared with one another with the aim to find best representatives of a given batch. It is also important to compare the thin films between the methods as shown in Figure 4-27. In order to address discrepancies between films such the thicknesses and Er-concentrations, the results for a given group have been averaged and normalised.

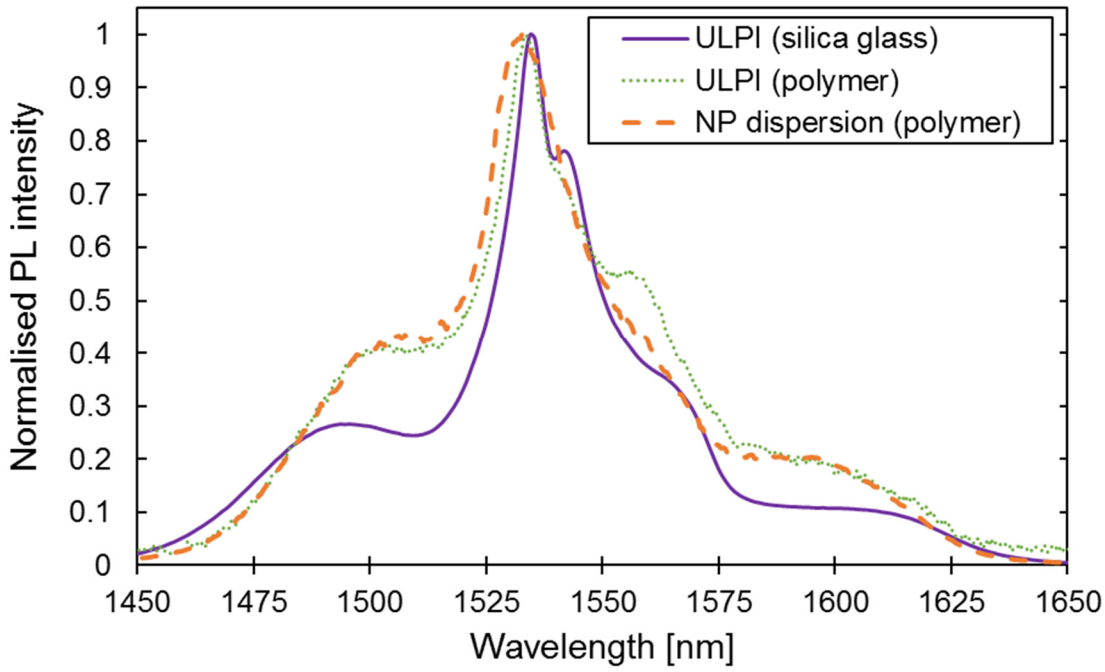

Figure 4-27: Comparison of normalised average PL emission spectral shapes for the investigated doping approaches

Even though the resultant photoluminescence emission spectra vary between the thin film types, they all have emission peak around 1533 nm. Interestingly, the materials prepared using ULPI method show distinctively different spectral shapes based on the substrate used. The two shapes can be traced to reports in literature [37], where Er-doped TZN glass properties are investigated. It has been shown that as a result of implantation in silica the emission spectrum becomes narrower, 1540 nm secondary peak more pronounced and the signal around 1510 nm is much lower as seen in this work. Furthermore, the shape of ULPI-made polymer with its secondary peaks around 1500 and 1550 nm matches very closely the shape of bulk TZN target glass. This indicates that the implanted material does not mix well with the polymer host and the observed signal comes from the target glass deposited on top of the sample as seen via visual inspection in Figure 4-15. This hypothesis is also supported by the very short lifetime in implanted

polymer where the measured values around 4 ms come very close to 4.4 ms reported in bulk target glass of the same Er content in the mix [35]. In case of a materials with well distributed Er-TZN particles a much longer lifetime is expected as seen in the T-series samples [38].

The spectral shape difference of the ECG NP dispersed thin film is a natural outcome of a different composition of the nanocrystals with erbium content. Even though there are no reports on similar material to compare the spectra, polymer-hosted nanocrystals with erbium-cerium mix have been described to have a singular peak at a wavelengths slightly shorter than 1535 nm [39]. Additionally, the measured lifetimes around 6 ms are comparable to the best values reported in literature for NP dispersed in polymer hosts [18].

4.4 Conclusions

In this chapter polymer platform fabrication methods are discussed and an optimised UV photolithography process for siloxane-based materials is presented. The fabricated waveguides are then used to estimate background loss throughout Er-emission spectrum from 1475 to 1575 nm via cutback method measurements showing a signal reduction of approximately 2.2 dB/cm around the erbium peak emission wavelength of 1530 nm. This value is comparable to other commercial polymer materials, such as SU-8, which do not possess thermal stability of siloxanes required for PCB integration or long-term high energy EDWA pumping. Even though the measured loss is relatively low for a polymer material, it is an additional contributor to the signal strength degradation that needs to be accounted for and compensated through amplification.

Two promising techniques of erbium-doping, namely ultrafast laser plasma implantation and nanoparticle dispersion, are described and their fabrication processes explained. These processes are then used to fabricate three distinct types of Er-doped thin films. ULPI is used to implant both polymer directly and a silica glass substrate for hybrid structures. The latter forms EDTS layer with high dopant concentration of 1.63×10^{27} m^{-3} while maintaining long Er lifetime of 12.1 ms. This result is used as a benchmark to compare with previously unattempted direct polymer implantation. Analysis of thin films obtained in this way shows a number of challenges arising from the combination of high-temperature and high-energy process even with siloxanes that are known for being polymers with a good thermal resistance. After ULPI process adjustments, thin films are found to have a dopant layer deposited on top of them rather

than implanted. As a result, the characterisation of their PL properties demonstrates a broader emission spectrum and shorter lifetime closely matching this of a bulk target glass rather than uniformly implanted EDTS.

The alternative method of nanoparticle dispersion in undeveloped polymer is also studied on thin films. Two batches of prepared material are used to improve the fabrication process in terms of the emission properties. The initial assessment shows that by adding an additional filtering step in the thin film preparation procedure stronger photoluminescence is observed and largest NP agglomerations are removed. The lifetime of the ECG NP dispersed thin film at highest prepared weight ratio of 12.5% remains at approximately 6 ms which is longer than in case of the ULPI polymer films range of 3.5-4.2 milliseconds.

The comparison of the thin film properties has led to the conclusion that most promising approaches to polymer-platform-compatible EDWA designs are hybrid approach using EDTS layer as explained in the previous chapter and direct doping via NP dispersion. More detailed studies on the first of the methods including design and fabrication optimisation are presented in Chapter 5. Waveguide systems based on the ECG-doped siloxane polymer with relevant experimental and simulation results are described in Chapter 6 of this thesis.

4.5 References

[1] B. W. Swatowski *et al.*, “Flexible, stable, and easily processable optical silicones for low loss polymer waveguides,” in *Proc. SPIE 8622, Organic Photonic Materials and Devices XV*, 2013.

[2] E. Zgraggen *et al.*, “Laser direct writing of single-mode polysiloxane optical waveguides and devices,” *J. Light. Technol.*, vol. 32, no. 17, pp. 3036–3042, 2014.

[3] K. Yasuhara, F. Yu, and T. Ishigure, “Circular core single-mode polymer optical waveguide fabricated using the Mosquito method with low loss at 1310/1550 nm,” *Opt. Express*, vol. 25, no. 8, p. 8524, 2017.

[4] X. Sun *et al.*, “Optimized inductively coupled plasma etching for poly(methyl-methacrylate- glycidly-methacrylate) optical waveguide,” *Thin Solid Films*, vol. 520, no. 18, pp. 5946–5951, 2012.

[5] M. C. Fu, T. Higashihara, and M. Ueda, “Recent progress in thermally stable and photosensitive polymers,” *Polym. J.*, vol. 50, no. 1, pp. 57–76, 2018.

[6] Y. Xia and G. M. Whitesides, "Soft Lithography," *Annu. Rev. Mater. Sci.*, vol. 28, no. 1, pp. 153–184, 1998.

[7] H. Ma, A. K. Y. Jen, and L. R. Dalton, "Polymer-based optical waveguides: Materials, processing, and devices," *Adv. Mater.*, vol. 14, no. 19, pp. 1339–1365, 2002.

[8] X. Xu, L. Ma, S. Jiang, and Z. He, "Circular-core single-mode polymer waveguide for high-density and high-speed optical interconnects application at 1550 nm," *Opt. Express*, vol. 25, no. 21, p. 25689, Oct. 2017.

[9] R. Pitwon *et al.*, "Competitive Evaluation of Planar Embedded Glass and Polymer Waveguides in Data Center Environments," *Appl. Sci.*, vol. 7, no. 9, p. 940, 2017.

[10] L. Eldada and L. W. Shacklette, "Advances in polymer integrated optics," *IEEE J. Sel. Top. Quantum Electron.*, vol. 6, no. 1, pp. 54–68, Jan. 2000.

[11] W. J. Daughton, "An Investigation of the Thickness Variation of Spun-on Thin Films Commonly Associated with the Semiconductor Industry," *J. Electrochem. Soc.*, vol. 129, no. 1, p. 173, 2006.

[12] MicoChemicals, "Baking Steps in Photoresists Processing," *AZ Electronic Materials*, pp. 1–3, 2013.

[13] M. Diemeer, L. Hilderink, R. Dekker, and A. Driessen, "Low-Cost and Low-Loss Multimode Waveguides of Photodefinable Epoxy," *IEEE Photonics Technol. Lett.*, vol. 18, no. 15, pp. 1624–1626, 2006.

[14] I. Jekauc, M. Watt, T. Hornsmith, and J. Tiffany, "Necessity of Chemical Edge Bead Removal in Modern Day Lithographic Processing," in *Proc. of SPIE 5376, Advances in Resist Technology and Processing XXI*, 2004, pp. 1255–1264.

[15] M. E. Mortenson, *Mathematics for Computer Graphics Applications*, Second. New York: Industrial Press, 1999.

[16] Z. Cai, W. Qiu, G. Shao, and W. Wang, "A new fabrication method for all-PDMS waveguides," *Sensors Actuators, A Phys.*, vol. 204, pp. 44–47, 2013.

[17] I. P. Kaminow and L. W. Stulz, " Loss in cleaved Ti-diffused LiNbO 3 waveguides ," *Appl. Phys. Lett.*, vol. 33, no. 1, pp. 62–64, 2003.

[18] G. F. R. Chen, X. Zhao, Y. Sun, C. He, M. C. Tan, and D. T. H. Tan, "Low Loss Nanostructured Polymers for Chip-scale Waveguide Amplifiers," *Sci. Rep.*, vol. 7,

no. 1, pp. 1–8, 2017.

[19] R. S. E. John *et al.*, "Thermally stable, low loss optical silicones: A key enabler for electro-optical printed circuit boards," *J. Light. Technol.*, vol. 33, no. 4, pp. 814–819, 2015.

[20] J. Chandrappan *et al.*, "Doping silica beyond limits with laser plasma for active photonic materials," *Opt. Mater. Express*, vol. 5, no. 12, p. 2849, 2015.

[21] K. Sugioka and Y. Cheng, "Ultrafast lasers-reliable tools for advanced materials processing," *Light Sci. Appl.*, vol. 3, no. 390, pp. 1–12, 2014.

[22] Z. Zhao *et al.*, "Tellurite glass thin films on silica and polymer using UV (193 nm) pulsed laser ablation," *J. Phys. D. Appl. Phys.*, vol. 44, no. 9, pp. 0–6, 2011.

[23] S. Eliezer *et al.*, "Synthesis of nanoparticles with femtosecond laser pulses," *Phys. Rev. B - Condens. Matter Mater. Phys.*, vol. 69, no. 14, pp. 1–6, 2004.

[24] P. Balling and J. Schou, "Femtosecond-laser ablation dynamics of dielectrics: Basics and applications for thin films," *Reports Prog. Phys.*, vol. 76, no. 3, 2013.

[25] I. Mirza, G. O'Connell, J. J. Wang, and J. G. Lunney, "Comparison of nanosecond and femtosecond pulsed laser deposition of silver nanoparticle films," *Nanotechnology*, vol. 25, no. 26, 2014.

[26] T. Mann, R. Mathieson, M. Murray, B. Richards, and G. Jose, "Femtosecond laser ablation properties of Er^{3+} ion doped zinc-sodium tellurite glass," *J. Appl. Phys.*, vol. 124, no. 4, p. 044903, 2018.

[27] A. Jha *et al.*, "Review on structural, thermal, optical and spectroscopic properties of tellurium oxide based glasses for fibre optic and waveguide applications," *Int. Mater. Rev.*, vol. 57, no. 6, pp. 357–382, 2012.

[28] J. Chandrappan, V. Khetan, M. Ward, M. Murray, and G. Jose, "Devitrification of ultrafast laser plasma produced metastable glass layer," *Scr. Mater.*, vol. 131, pp. 37–41, 2017.

[29] Z. Wang, G. M. Kale, and M. Ghadiri, "Synthesis and characterization of $Ce_xGd_{1-x}O_{2-\delta}$ nanopowders employing an alginate mediated ion-exchange process," *Chem. Eng. J.*, vol. 198–199, pp. 149–153, 2012.

[30] S. Rahayu, J. S. Forrester, G. M. Kale, and M. Ghadiri, "Promising solid electrolyte material for an IT-SOFC: Crystal structure of the cerium gadolinium holmium

oxide $Ce_{0.8}Gd_{0.1}Ho_{0.1}O_{1.9}$ between 295 and 1023 K," *Acta Crystallogr. Sect. C Struct. Chem.*, vol. 74, no. 2, pp. 236–239, 2018.

[31] Z. Wang, G. M. Kale, and M. Ghadiri, "Sol-gel production of $Ce_{0.8}Gd_{0.2}O_{1.9}$ nanopowders using sucrose and pectin as organic precursors," *J. Am. Ceram. Soc.*, vol. 95, no. 9, pp. 2863–2868, 2012.

[32] J. Chandrappan *et al.*, "Target dependent femtosecond laser plasma implantation dynamics in enabling silica for high density erbium doping," *Sci. Rep.*, vol. 5, 2015.

[33] J. Chandrappan *et al.*, "Doping silica beyond limits with laser plasma for active photonic materials," *Opt. Mater. Express*, vol. 5, no. 12, pp. 2849–2861, 2015.

[34] S. A. Kamil, J. Chandrappan, M. Murray, P. Steenson, T. F. Krauss, and G. Jose, "Ultrafast laser plasma doping of Er^{3+} ions in silica-on-silicon for optical waveguiding applications," *Opt. Lett.*, vol. 41, no. 20, p. 4684, Oct. 2016.

[35] E. K. Barimah, M. W. Ziarko, N. Bamiedakis, I. H. White, R. V. Penty, and G. Jose, "Erbium-doped glass nanoparticle embedded polymer thin films using femtosecond pulsed laser deposition," *Opt. Mater. Express*, vol. 8, no. 7, p. 1997, 2018.

[36] Y. Gokce, B. Cengiz, N. Yildiz, A. Calimli, and Z. Aktas, "Ultrasonication of chitosan nanoparticle suspension: Influence on particle size," *Colloids Surfaces A Physicochem. Eng. Asp.*, vol. 462, pp. 75–81, 2014.

[37] Z. Zolnai *et al.*, "Ultrafast laser plasma assisted rare-earth doping for silicon photonics," *CLEO*, vol. 1, p. ATu3K.5, 2016.

[38] J. Chandrappan *et al.*, "Enabling silica for high density rare earth doping for integrated opto- electronic systems," vol. 65, no. 2011, p. 241905, 2015.

[39] X. Zhai *et al.*, "Enhancement of 1.53 μm emission band in $NaYF_4:Er^{3+},Yb^{3+},Ce^{3+}$ nanocrystals for polymer-based optical waveguide amplifiers," *Opt. Mater. Express*, vol. 3, no. 2, p. 270, Feb. 2013.

5 STUDIES OF HYBRID EDWAS

The hybrid polymer-glass approach to fabricating EDWAs takes advantage of the available highly-doped EDTS thin films investigated in Chapter 4. The benefit of using this approach comes from a more mature ULPI fabrication process in silica glass compared to a polymer that has in turn led to more promising thin film characteristics in terms of their lifetime and photoluminescence intensity.

In this chapter, the methodology for designing such amplifiers is explained in order to maintain single mode operation for both channel and strip-loaded waveguides. The corresponding waveguide size and the modal overlap information is then combined in a full amplifier model with absorption and emission cross-sections derived from the material properties. The cross sections are obtained through a combination of McCumber and Füchtbauer-Ladenburg methods.

Hybrid EDWAs based on known sample properties are simulated using the rate-equations model introduced in Chapter 3. The potential amplifier gain is assessed for both channel and strip-loaded geometries to compare the potential of both approaches. These are not only optimised in terms of their Er-Yb ratios, but also operating factors, such as available pump power, are accounted for in the simulations. Based on these results, as well as other factors such as fabrication process, strip-loaded structures are prepared using available EDTS thin films. The polymer ridge deposition process is optimised to combine two dissimilar materials to form the designed waveguides.

Furthermore, the prepared hybrid amplifier samples are experimentally investigated via SEM, surface roughness inspection, near-field profile and ASE measurements. Assessment of these results has led to a conclusion that while the strip-loaded hybrid approach has a potential to form polymer platform compatible EDWAs, better quality samples with lower surface roughness are required for practical devices.

5.1 Parameter Extraction

A number of physical and design parameters are needed in order to simulate an EDWA device. While many of the properties have been measured on the Er-doped thin films in the previous chapter, several characteristics depend on the chosen waveguide geometry.

The single mode operation for a square channel waveguide is modelled in Chapter 3, therefore focus on asymmetric geometries is placed in this section. Size and refractive index requirements for such designs are described as well as references to the available

thin film samples are made. Additionally, emission and absorption cross sections are derived from the EDTS thin film measurements based on the most promising sample T28.

5.1.1 SM operation in hybrid amplifiers

The dimensions of the polymer ridge and the thickness of the doped layer affect the operating conditions. The focus is placed on the latter as the polymer waveguide minimum size is determined to be approximately 3.5×3.5 μm^2. These dimensions are limited by a combination of the material, where polymer viscosity limits the minimum layer thickness, and the fabrication procedure used. Figure 5-1 shows the investigated geometries for hybrid EDWAs based on an EDTS layer implanted into a silica glass substrate. The first approach assumes a square channel fabricated by etching the planar Er-doped layer which is later cladded with a polymer material to reduce the refractive index difference between remaining EDTS core and the surrounding material as shown in Figure 5-1 (a). The additional step of the cladding addition allows for a reduced size limit for single mode operation through reduction of the refractive index contrast.

The channel waveguide is used as a benchmark for the strip-loaded geometry which only requires a single preparation step. In order to generate this structure a polymer strip is deposited on top of the EDTS layer using waveguide fabrication techniques presented in Chapter 4. The resulting device uses the principle of index guiding to contain the fundamental mode underneath the ridge [1].

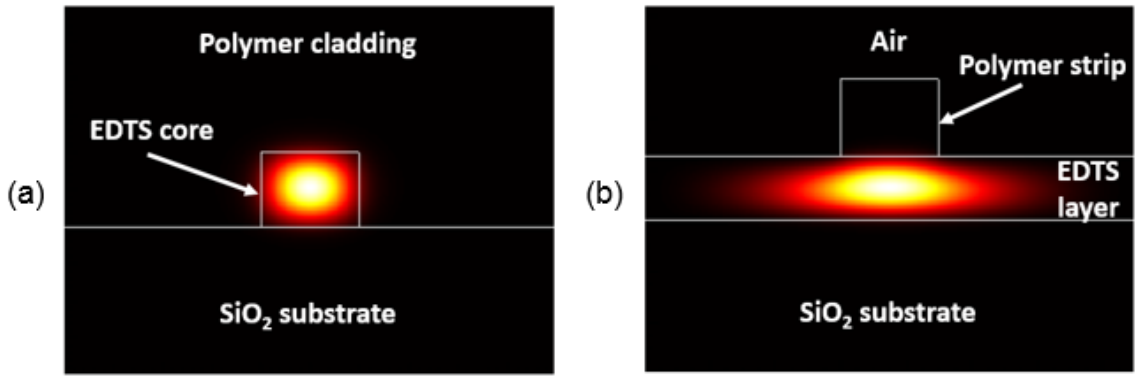

Figure 5-1: Investigated hybrid waveguide geometries: (a) square channel, (b) strip-loaded with fundamental mode shown (λ = 1550 nm)

Two physical properties of the Er-doped thin film, namely refractive index and thickness, determine the conditions for the single mode of operation in the case of a fixed polymer strip size. The refractive index of the EDTS layer is predominantly determined by the erbium and ytterbium co-dopant concentration in the target glass while the thickness of

the implanted layer depends on the ULPI parameters such as duration. These two parameters also determine the mode overlap with the active erbium-doped region as presented in Figure 5-2 for the signal wavelength. In an efficient amplifier, the overlap is kept as high as possible in order to maximise light interaction with Er ions.

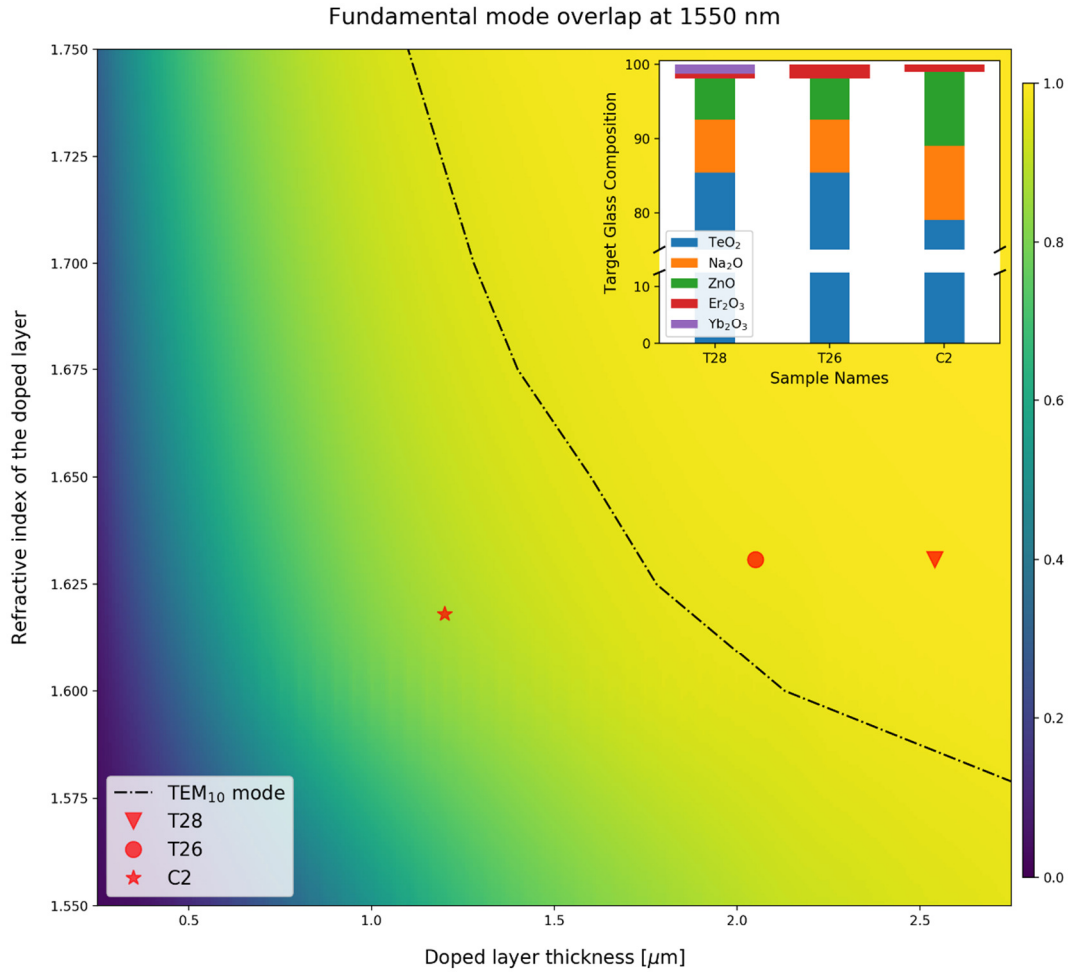

Figure 5-2: Fundamental mode overlap dependence on doped layer thickness and refractive index with marked three most promising EDTS samples

The highest fundamental mode overlap is achieved by increasing both refractive index and thickness of the doped layer. The limiting factor to this rise is that at a certain point it leads to first order transverse-electric mode being guided underneath the polymer ridge. At this stage the amplifier becomes less efficient as the two coexisting modes have lower total overlap due to the TEM_{10} mode being more weakly confined in the active region. Designing the device to operate in this regime is not optimal. However even highly multimode EDWAs have been shown to achieve gain [2].

The three EDTS samples with the most promising photoluminescence emission strengths and metastable lifetimes are also plotted in Figure 5-2 to predict their behaviour. The

target glass with higher dopant concentration used on the T-series samples leads to a higher refractive index compared to C2. It is observed that both T26 and T28 are thicker than the modelled single mode operation limit. As a result, a less efficient operation is expected from these samples compared to the theoretically predicted hybrid strip-loaded amplifiers.

5.1.2 Emission and absorption cross sections

The emission cross section of a given Er-doped material can be approximated using Füchtbauer-Ladenburg method discussed in Chapter 2 (Equation 2.3). The three physical properties required by this method are: metastable level lifetime, doped layer refractive index and normalised emission spectrum. All the above parameters have been measured for EDTS samples as shown on an example of T28 in Figure 5-3.

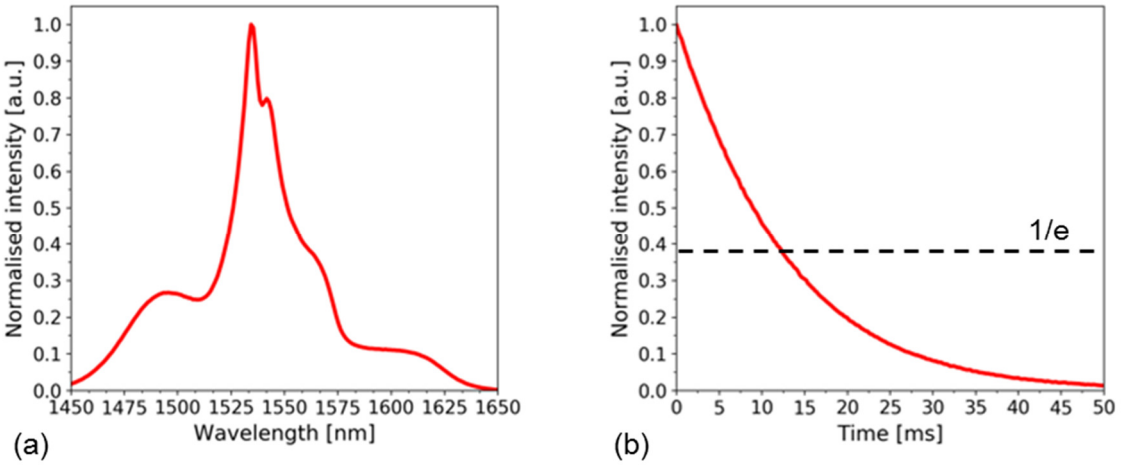

Figure 5-3: Optical characterisation results for T28 sample.
(a) PL intensity profile, (b) metastable lifetime

Figure 5-3(a) presents the normalised PL emission spectrum in the 1450 nm to 1650 nm range demonstrating a strong peak at 1534.4 nm and a FWHM of 24.2 nm. Even though the exact spectral shape of the emission depends on the host material and target glass composition, a comparable linewidth has been observed from similar types of materials [3]. Figure 5-3(b) presents the single exponential decay with time of the normalised spontaneous emission light intensity at the peak of 1534 nm. The lifetime of the Er ions in the material is calculated by a standard procedure of finding the amount of time it takes for the signal to drop to 36.8% (1/e level) of the initial value. The existence of a long metastable time that the erbium ion remains in the $I_{13/2}$ energy level, which in this case is estimated to be 12.1 ms, shows promise for implementation of efficient optical amplifiers using ULPI fabricated EDTS layer.

The effective emission cross section $\boldsymbol{\sigma_e}$ between the excited ($I_{13/2}$) and ground ($I_{15/2}$) levels using the shape of the photoluminescence spectrum is calculated as shown in Figure 5-4. The corresponding absorption spectrum required to implement a full EDWA model is calculated based on the McCumber theory [4] using the extracted emission cross section. According to the procedure proposed by Miniscalco and Quimby [5], and confirmed for a range of various materials, these two quantities are related with the equation below:

$$\sigma_a(\nu) = \sigma_e(\nu)e^{h\nu-\varepsilon/kT} = \sigma_e(\nu)e^{h(\nu-\nu_0)/kT} \tag{5.1}$$

where $\boldsymbol{\sigma_a}$ and $\boldsymbol{\sigma_e}$ are absorption and emission cross-sections respectively, $\boldsymbol{h}$ and $\boldsymbol{k}$ are Planck and Boltzmann constants, $\boldsymbol{T}$ is the temperature, $\boldsymbol{\varepsilon}$ is the net free energy required to excite one Er ion from $I_{15/2}$ to $I_{13/2}$ and $\boldsymbol{\nu}$ corresponds to the wave frequency. Equation (**5.1**) is used to calculate the corresponding absorption cross-section of the fabricated EDTS layer and is plotted in Figure 5-4.

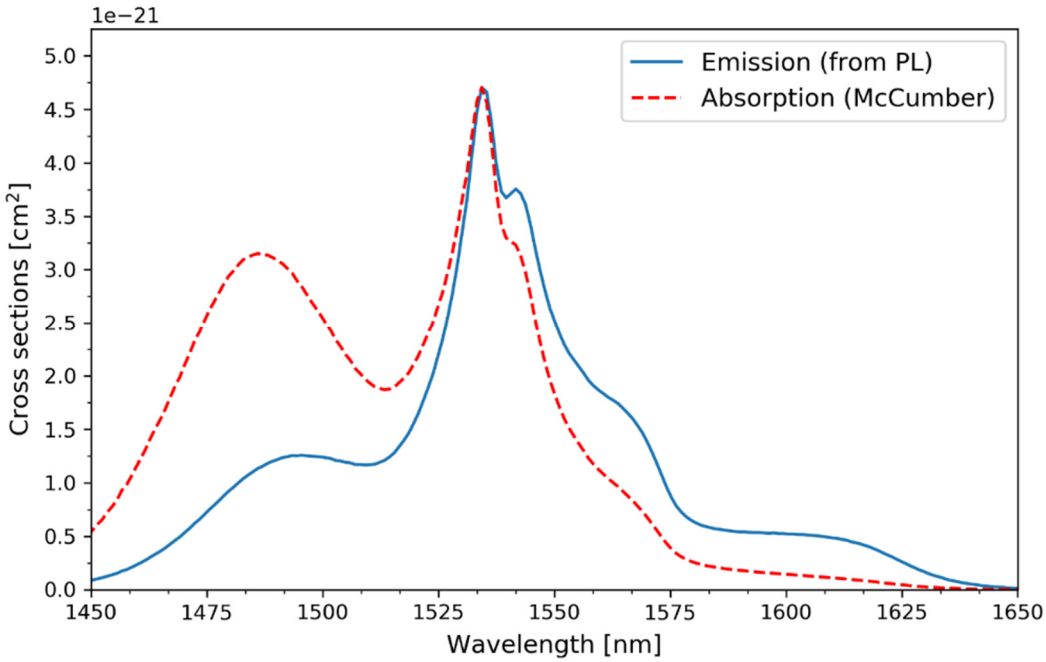

Figure 5-4: Emission and absorption cross-sections of the EDTS layer based on sample T28

The obtained results show that the fabricated sample exhibits absorption and emission cross-sections maxima of very similar magnitude of 4.7×10^{-21} cm^2 at 1534 nm. The spectral shape also highlights a secondary absorption peak around 1485 nm which corresponds to a potential in-band pumping of the $I_{13/2}$ level without a high probability of the resultant emission occurring at wavelengths below 1525 nm. The obtained cross-section results for the EDTS layer agree well with the previous literature reports on

similar materials (Table 5-1). Although a TZN material of this composition has not been investigated before, similar Er-doped tellurite-based glass thin films have been shown to possess cross-sections in range from 3.45 to 8.81 × 10^{-21} cm^2 [6]. The target material with most resembling chemical constituents of $75TeO_2–20ZnO–3Na_2O–2Er_2O_3$ has been measured to have absorption and emission cross sections of 3.46 and 3.79 × 10^{-21} cm^2 respectively [7]. Even though higher cross sections have been reported as summarised in Table 5-1, the TZN-doped into silica used here offers comparable cross sections while maintaining an Er ion lifetime longer than alumina (7.5 ms) [8], tantala (2.4 ms) [9] or tellurite glasses (3.5 ms) [10].

Table 5-1: Erbium cross sections in various host materials

Host material	Absorption cross section [× 10^{-21} cm^2]	Emission cross section [× 10^{-21} cm^2]	Ref.
$75TeO_2–20ZnO–3Na_2O–2Er_2O_3$	3.5	3.8	[7]
Phosphate glass	5.4	5.3	[11]
Alumina (Al_2O_3)	5.6	4.2	[8]
Tantala (Ta_2O_5)	4.8	4.4	[9]
$85.4TeO_2–5.5ZnO–7.2Na_2O–0.6Er_2O_3$-$1.3Yb_2O_3$	4.7	4.7	-

5.2 Hybrid Structures Modelling

The hybrid geometries described in the previous section are simulated using a multi-level rate equations model implemented in the VPI Photonics software. The available parameters, measured on the T28 sample, are used, and supplemented with values obtained from similar materials where necessary as listed in Chapter 3.

5.2.1 Waveguide Configurations

The channel and strip-loaded waveguide designs that can be implemented using the Er-doped thin films (Figure 5-1) are compared with one another in terms of their performance potential. In both cases the dimensions of the waveguide are chosen to ensure single mode operation based on the refractive indices of the glass layer, the polymer materials and the light wavelength.

Both of the above geometries are simulated using the Fimmwave software package in order to check the required feature sizes and determine their operating parameters. The key derived values for the EDWA simulations are listed in Table 5-2 below for both configurations. In order to obtain these, an EDTS refractive index of 1.631 is used as measured for the T-series samples with the highest dopant concentration of 1.63×10^{21} cm^{-3}.

Table 5-2: Key waveguide simulation parameters extracted

Parameter	Channel	Strip-loaded
Size [μm]	1.9 × 1.9	1.5 (EDTS thickness)
Overlap factor at signal wavelength (1550 nm)	0.87	0.94
Overlap factor at signal wavelength (980 nm)	0.85	0.91
Effective Er overlap area [μm^2]	3.60	8.96

Both of the above geometries show high overlap factors with the Er-doped area, which is crucial for efficient utilisation of the dopant ions. The main difference between the two configurations can be noted when comparing their effective overlap areas. The strip-loaded waveguide exhibits a larger effective Er overlap area which indicates its stronger potential for forming a higher gain amplifier. This is due to a larger total number of the dopant ions interacting with both pump and signal light. The drawback of a larger overlap area is a requirement for more pump power in order to achieve a population inversion in the device. Additionally, the implementation of a channel waveguide based on the EDTS requires minimally smaller single mode dimensions compared to the ideal square channel theoretically discussed in Chapter 3. This is due to an asymmetry introduced to the system by having the core surrounded with polymer from three sides while the substrate underneath is a lower refractive index silica glass.

Both configurations are modelled and their behaviour studied in the next sections. The channel waveguide is a typical configuration used in many system applications and the simulation studies are applicable to similar erbium-doped amplifiers obtained using different fabrication techniques, for example, NP dispersion in polymer as described in Chapter 6. This standard device geometry also provides a good performance reference for the alternative hybrid approach of having a strip-loaded EDWA. This configuration is investigated due to its fabrication process requiring only a polymer ridge deposition on top of the EDTS layer.

5.2.2 Channel Amplifier

The gain performance of a 1-cm-long device is obtained using multi-level rate equations implemented using the VPI Photonics software. The model parameters listed in Chapter 3 are used with adjustments for values experimentally extracted based on sample T28 and hybrid structure studies.

The main unknown aspects for this structure are the upconversion factor and the waveguide background loss. As a result, the rest of the parameters (total ion concentration, lifetime and cross-sections) are kept constant, while these two are varied to assess their impact on the amplifier's performance and optimum design. Three values are used for the background loss: 0.3, 1 and 3 dB/cm, as 0.3 dB/cm represents a very good quality waveguide, 1 dB/cm represents an average quality waveguide and 3 dB/cm a worst-case scenario. In terms of the upconversion factor, a similar approach is initially undertaken with three values chosen based on values reported in other Er-doped glass systems: 0.8, 5 and 10×10^{-23} m^3s^{-1}. These three scenarios are used to assess impact of this energy transfer process, followed by a linear scaling of the upconversion with the Erbium concentration as proposed in Chapter 3.

The optimum performance of the EDWA is found by varying the ratio of erbium and ytterbium while maintaining the total ion concentration of 1.63×10^{21} cm^{-3} constant. This is investigated through an observation of the amplifier's gain at the peak emission wavelength of 1534 nm for a given pump power.

Figure 5-5 shows the optimised internal gain that could be achieved from a 1-cm-long device as a function of the pump power (from 0 to 600 mW) and Er:Yb ratio (from 1:99 to 99:1). Figure 5-5 (a-c) show how the background loss affects the device performance. Comparison of the three graphs indicates that the background loss reduces the achievable gain of the device for a given pump power. Although the highest gain can be achieved by using a 600 mW pump power, this power is too high for practical applications and as a result, a more realistic pump power of 200 mW is used for comparing the different plots (red dashed line in plots).

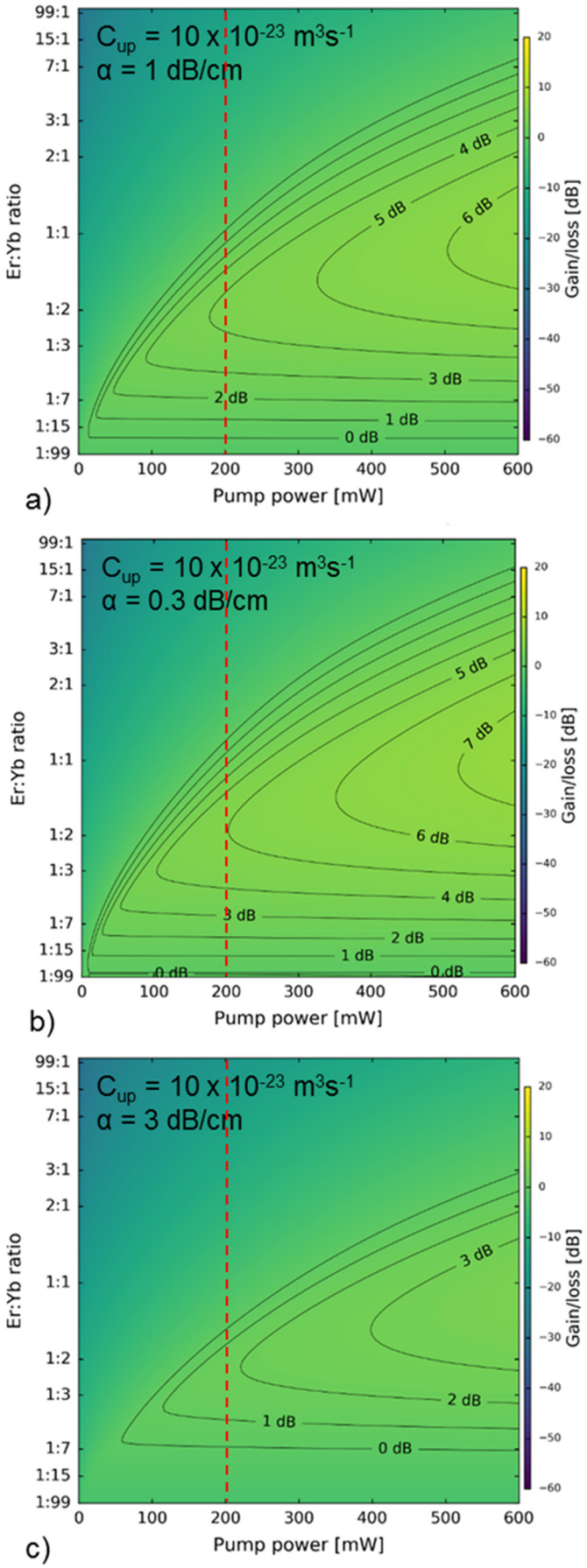

Figure 5-5: Gain and Er:Yb ratio optimisation for a 1-cm-long EDWA with varied upconversion and background losses

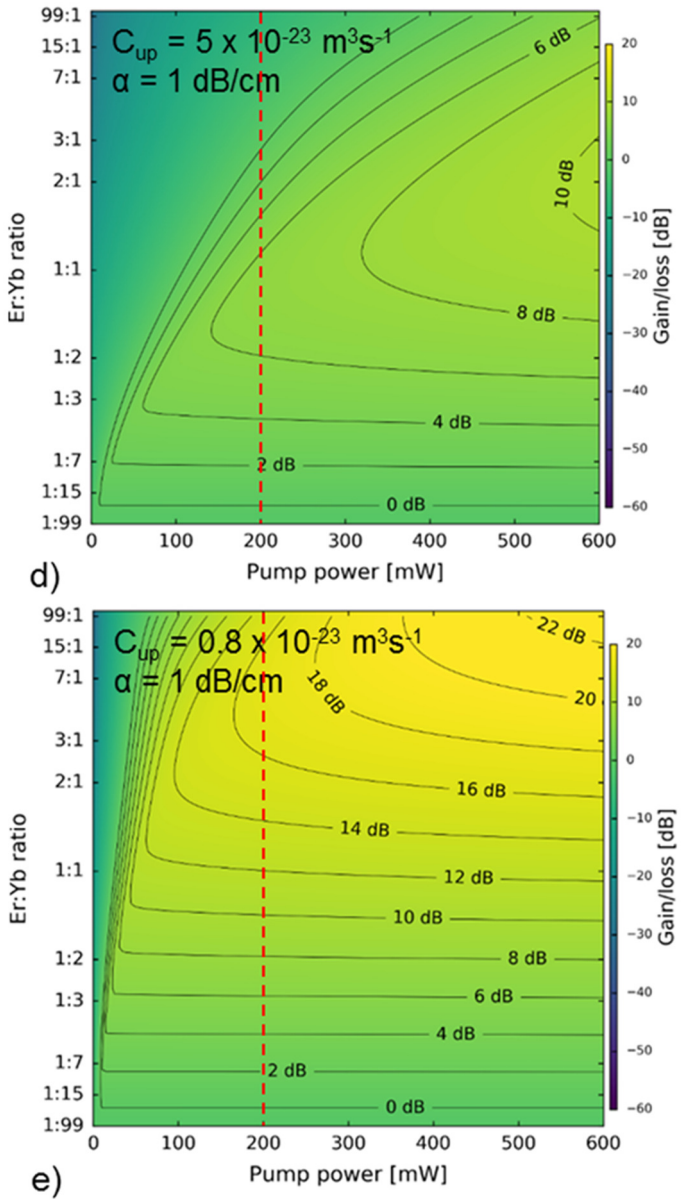

Figure 5-5: Gain and Er:Yb ratio optimisation for a 1-cm-long EDWA with varied upconversion and background losses (cont.)

For an EDWA with a 1 dB/cm loss (Figure 5-5 a), a maximum gain of 4.2 dB can be achieved with an Er:Yb ratio slightly below 1:2. When the loss in the waveguide is changed to 0.3 dB or 3 dB, the maximum gain at 1534 nm becomes 5 dB and 1.9 dB respectively, as shown in Figure 5-5 (b) and (c). The 2 dB loss increase results in a 2.3 dB gain drop, while the 0.7 dB loss reduction yields a 0.8 dB gain increase. Changing the background loss affects the intensity of the pump signal along the device length and therefore the population inversion along the device and the achievable gain itself. However, the variation of the waveguide loss does not significantly affect the optimum Er:Yb ratio for this device, which is found to be approximately 1:2.

A more pronounced effect on the optimum device structure is observed when the upconversion factor impact is investigated. In the initial scenario shown in Figure 5-5 a), a strong upconversion effect due to very high erbium concentration is assumed. However, introduction of ytterbium as a co-dopant not only acts as a sensitizer for the pump signal, but it also reduces the effect of upconversion [12] due to adding an additional energy transition in the system as explained in Chapter 3. Therefore, Figure 5-5 d) and e) present simulation results where the upconversion factor is reduced from 10×10^{-23} m^3s^{-1} to 5 and 0.8×10^{-23} m^3s^{-1} respectively. For a design with the pump power limited to 200 mW, the reduction in the upconversion coefficient results in a significant increase in the maximum achievable internal gain: from 4.2 dB to 6.8 dB and 16.8 dB for the two values studied. A reduction in the upconversion coefficient by a factor of 2 and 10 increased the internal gain by 2.6 and 12.6 dB respectively.

The change in the value of the upconversion coefficient significantly affects the optimum Er:Yb ratio for the amplifier, changing it from ~ 1:2 to ~ 1:1 and ~ 7:1 for the upconversion coefficients of 5 and 0.8×10^{-23} m^3s^{-1} respectively. An alternative method of linearly scaling the upconversion factor between 0.08 and 8×10^{-23} m^3s^{-1} with the erbium ion population in range of $0.0163\text{-}1.63 \times 10^{21}$ cm^{-3} is used to compare the previous fixed value findings with a more dynamic approach.

Figure 5-6 shows the results for a 1-cm-long hybrid channel amplifier with a 1 dB/cm background loss. The maximum gain when pumped at 200 mW (red dashed line) is 7.7 dB/cm which corresponds to an optimised Er:Yb ratio of ~ 1:1. This is approximately 1 dB/cm higher than in case of a fixed upconversion factor 5×10^{-23} m^3s^{-1} at the same dopant ratio. These results highlight the importance of the upconversion factor for optimising the amplifier design and achieving a high gain in this material system.

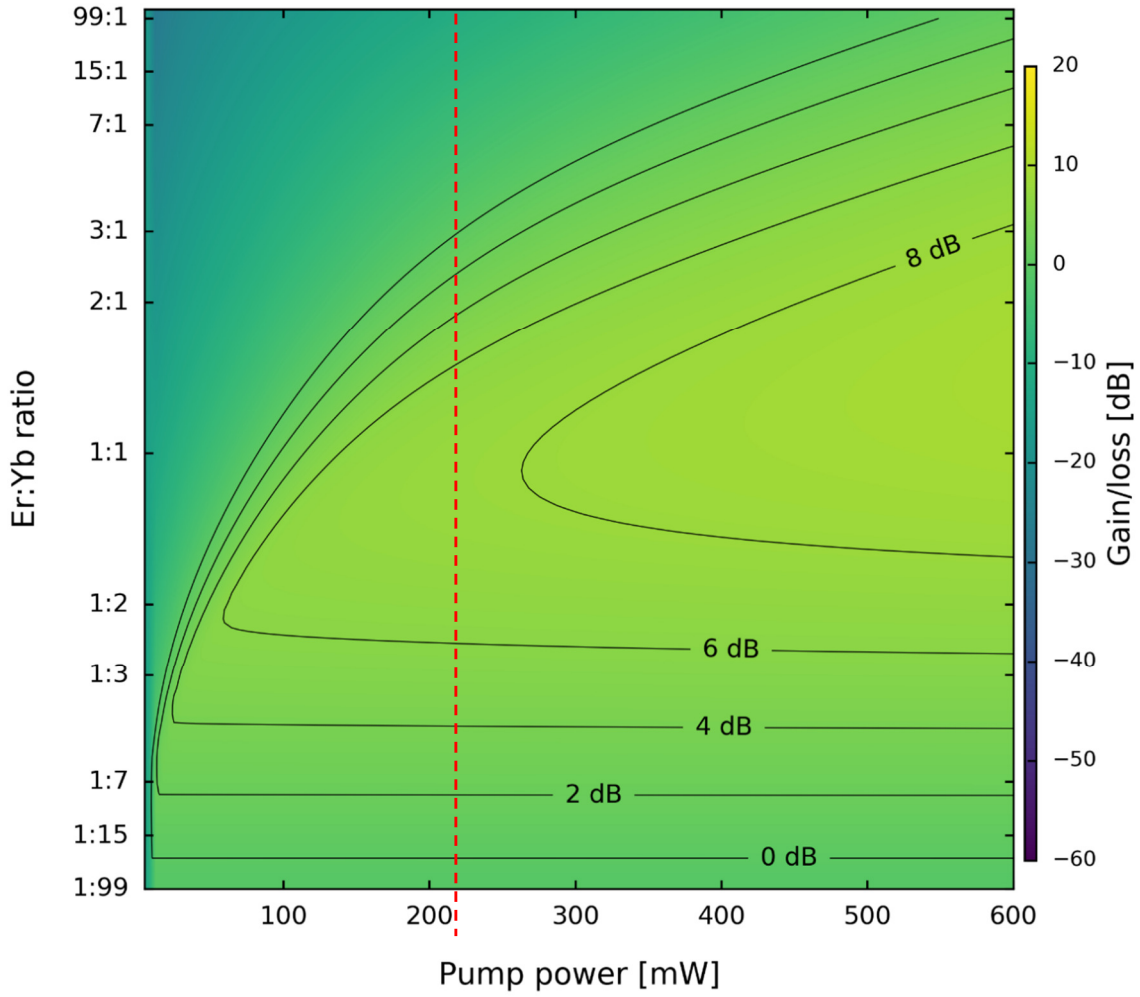

Figure 5-6: Gain and Er:Yb ratio optimisation for a 1-cm-long channel EDWA with 1 dB/cm background loss and linearly scaled upconversion factor

A summary of the simulation results for the optimised hybrid channel EDWAs is shown in Table 5-3. These highlight that change in the background loss has a negligible effect on the optimal dopant ratios while the upconversion factor strongly influences the device design. In the most realistic approach, where the upconversion factor is linearly scaled with the Er concentration, the best operating condition for this EDWA design is found when the structure is doped with 7.5:8.8 × 10^{20} cm^{-3} Er:Yb with corresponding upconversion factor of 3.7 × 10^{-23} m^3s^{-1}. Additionally, this methodology can be easily applied to any changes in the operating conditions for the system, such as pump power, where a new optimal dopant ratio and corresponding gain can be estimated using the presented plots.

Table 5-3: Summary of the simulation results for an optimised channel EDWA

Operating Conditions		**Optimisation Results**	
Upconversion coefficient [$\times 10^{-23}$ m^3s^{-1}]	Background loss [dB/cm]	Maximum internal gain [dB/cm]	Optimum Er:Yb ratio
Varying background loss			
10	0.3	1.9	1:2
	1.0	4.2	1:2
	3.0	5.0	1:2
Varying upconversion coefficient			
0.8	1.0	16.8	7:1
5		6.8	1:1
10		4.2	1:2
linearly scaled		7.7	1:1

5.2.3 Strip-loaded Amplifier

The same analysis is performed on the second hybrid waveguide geometry and the respective results for a linearly scaled upconversion factor are shown in Figure 5-7. The first key observation is a lower potential gain despite the presence of more dopant ions in the amplifier, due to a larger overlap area. The maximum gain of 7.4 dB/cm when pumped with 200 mW is lower than this achieved from the channel structure (7.7 dB/cm). This is due to the fact that at a fixed pump power a lower population inversion can be achieved in a device with a higher volume, thus, resulting in a lower overall gain.

In order to counteract the reduced pump energy density, a larger number of ytterbium ions is required. The optimum Er:Yb ratio for a strip-loaded device that is 1-cm-long is ~ 1:2 compared to ~ 1:1 in the channel structure operated under the same conditions. Despite the difference in the active area and optimal Er:Yb ratio, the achievable gain at 200 mW is only 0.3 dB/cm lower than in case of a channel structure showing that the strip-loaded geometry is a viable alternative if the amplifier is carefully designed.

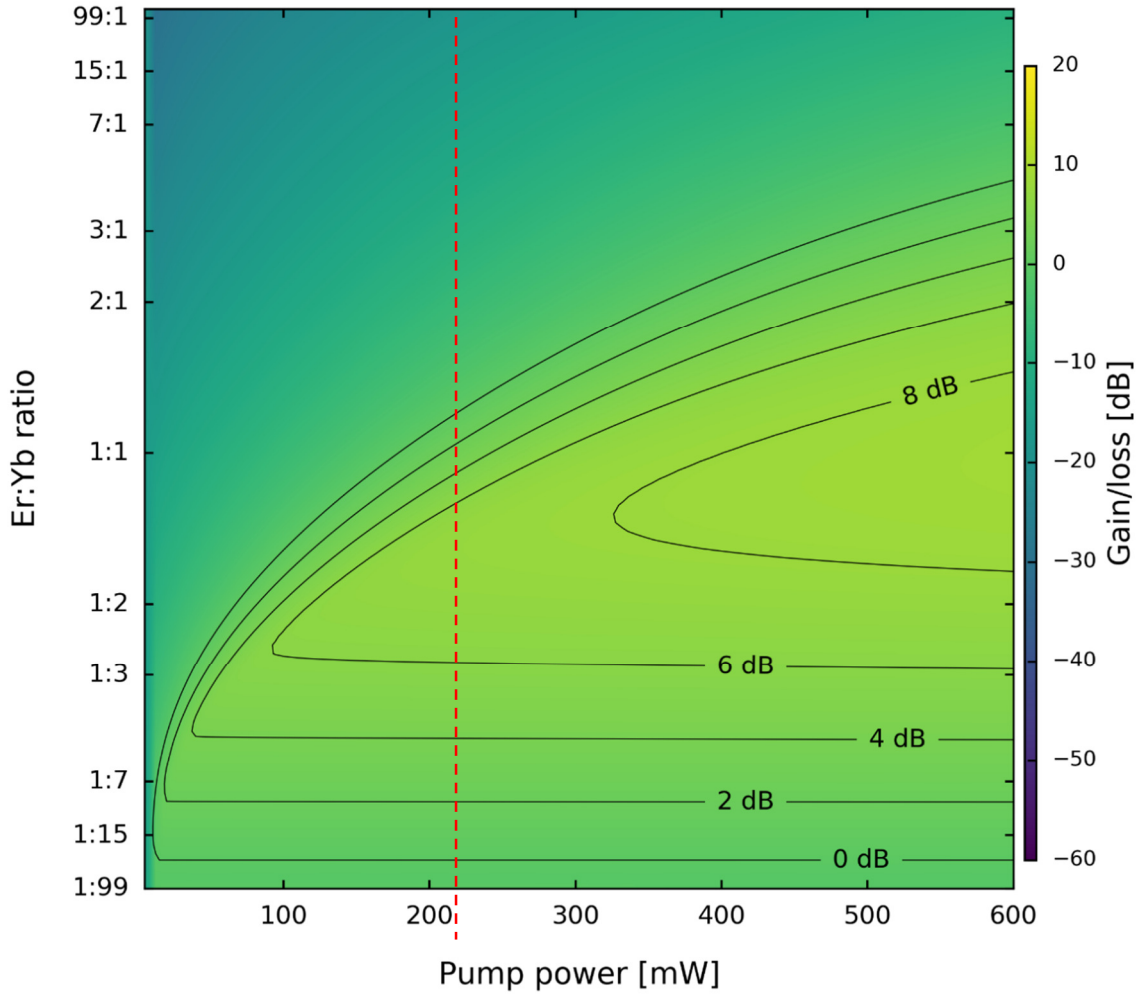

Figure 5-7: Gain and Er:Yb ratio optimisation for a 1-cm-long strip-loaded EDWA with 1 dB/cm background loss and linearly scaled upconversion factor

The optimised strip-loaded EDWA is further investigated in terms of its spectral response and efficiency as shown in Figure 5-8. It can be observed in Figure 5-8 (a) that when the amplifier is not pumped, very high absorption is observed across the erbium spectrum peaking around -12 dB/cm at 1534 nm. As the pump laser is turned on and with power increased loss becomes smaller and eventually an internal gain is observed. The design is optimised for a 200-mW operation (Er:Yb ratio of 37:63) leading to a gradual gain increase until this pump power is reached. Increasing the pump intensity beyond this point brings almost no benefit to the amplified signal.

The pump power of approximately 85 mW is needed for the erbium absorption and background loss to be perfectly countered by amplification resulting in device transparency at 1534 nm. Additionally, when operated at the designed optimum of 200 mW, the amplifier is observed to provide internal gain over a wide bandwidth of 137 nm, from 1475 nm to 1612 nm.

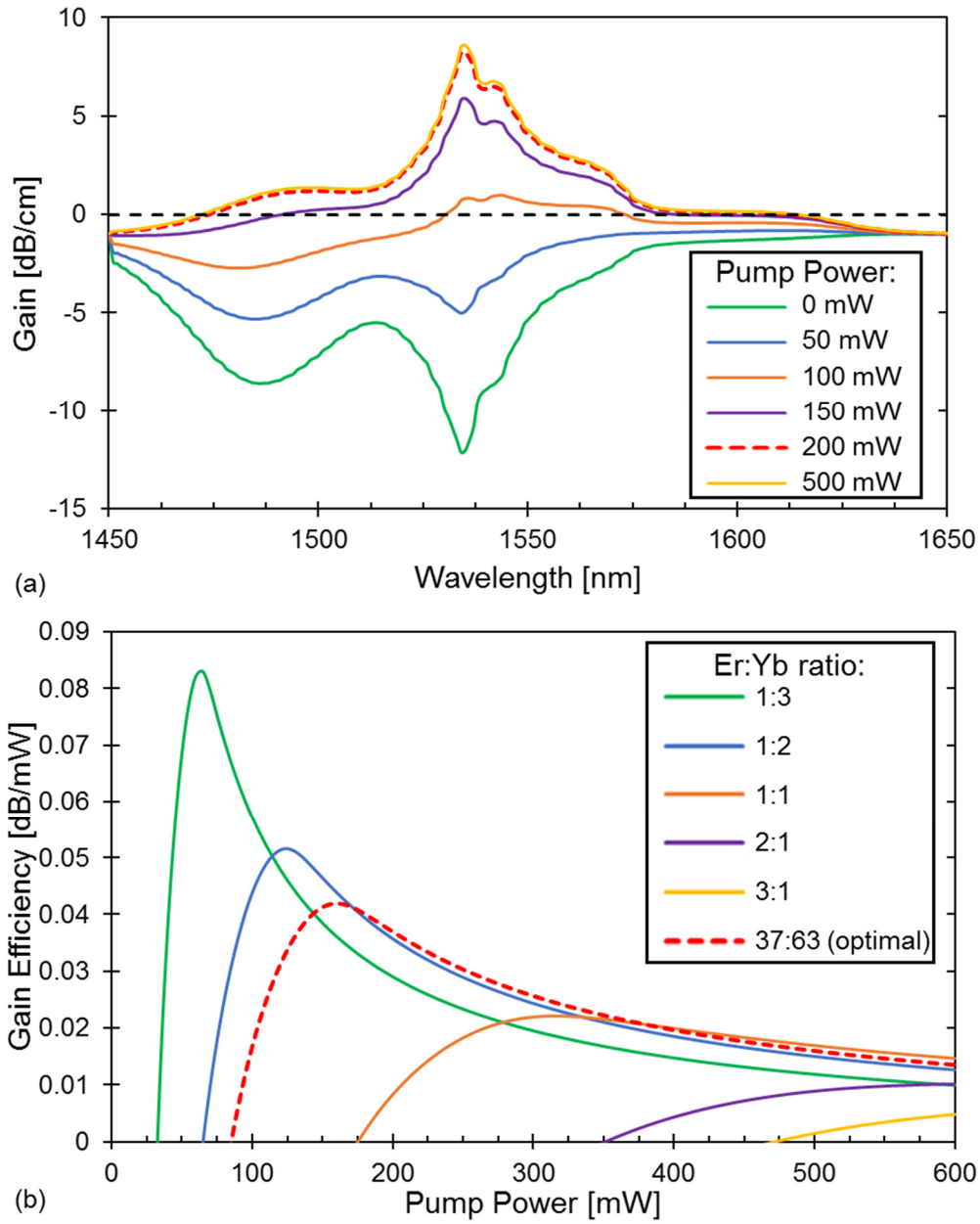

Figure 5-8: Strip-loaded waveguide EDWA results showing (a) gain spectrum for various pump powers at Er:Yb ratio fixed at 1:2 and (b) amplifier efficiency at various dopant rations

In terms of the amplifier efficiency, Figure 5-8 (b) indicates that, peak performance occurs at different pump powers depending on the Er:Yb ratio used. Based on the plotted examples, it can be observed that by increasing the ytterbium content the efficiency is increased, particularly at low pump powers. Introducing more erbium ions reduces the overall efficiency and shifts the peak gain to higher pump powers.

When the two hybrid systems are compared, it is found that a channel geometry offers a higher gain when operated at the same maximum power of 200 mW. The difference is minimised to 0.3 dB/cm by carefully optimising both designs in terms of their Er:Yb

ratios. The highest gain per 1-cm-long waveguide of 7.7 dB/cm and 7.4 dB/cm at 1534 nm is predicted for channel and strip-loaded EDWAs with erbium-to-ytterbium ratios of approximately 1:1 and 1:2, respectively. These results are obtained based on known EDTS thin film properties and assuming background loss to be 1 dB/cm while the upconversion factor is linearly scaled with the erbium concentration.

5.3 Strip-loaded Waveguide Fabrication

The fabrication procedure for siloxane waveguides has been presented in Chapter 4 for a wafer-scale system with polymer core and cladding. This methodology is adjusted for the hybrid polymer-on-glass devices due to two main factors: the size of the substrate is reduced from a 100-mm-diameter wafer to a 20 × 30 mm^2 rectangle and the waveguides are deposited on EDTS directly, without a planar layer of polymer cladding. The modified procedure is presented in Figure 5-9 with key adjustments to process parameters highlighted in steps 3 to 6.

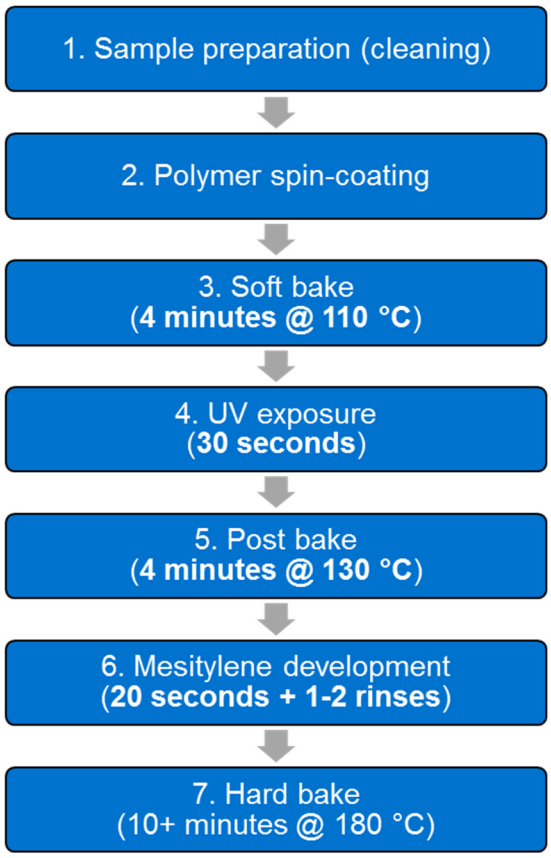

Figure 5-9: Polymer ridge deposition procedure on EDTS samples

The initial two steps of the fabrication process were kept unchanged. The only variation attempted was to use plasma cleaning (40 ccm oxygen at 149 mTorr for 1 minute) to remove impurities from the glass surface. While it was found to be useful in terms of

polymer adhesion by relaxing the carefully optimised processing steps, it was not necessary for a successful ridge deposition. The duration of the process steps 3-6 is shown in Figure 5-10 in addition to highlighting how the unsuccessful attempts have led to the final protocol.

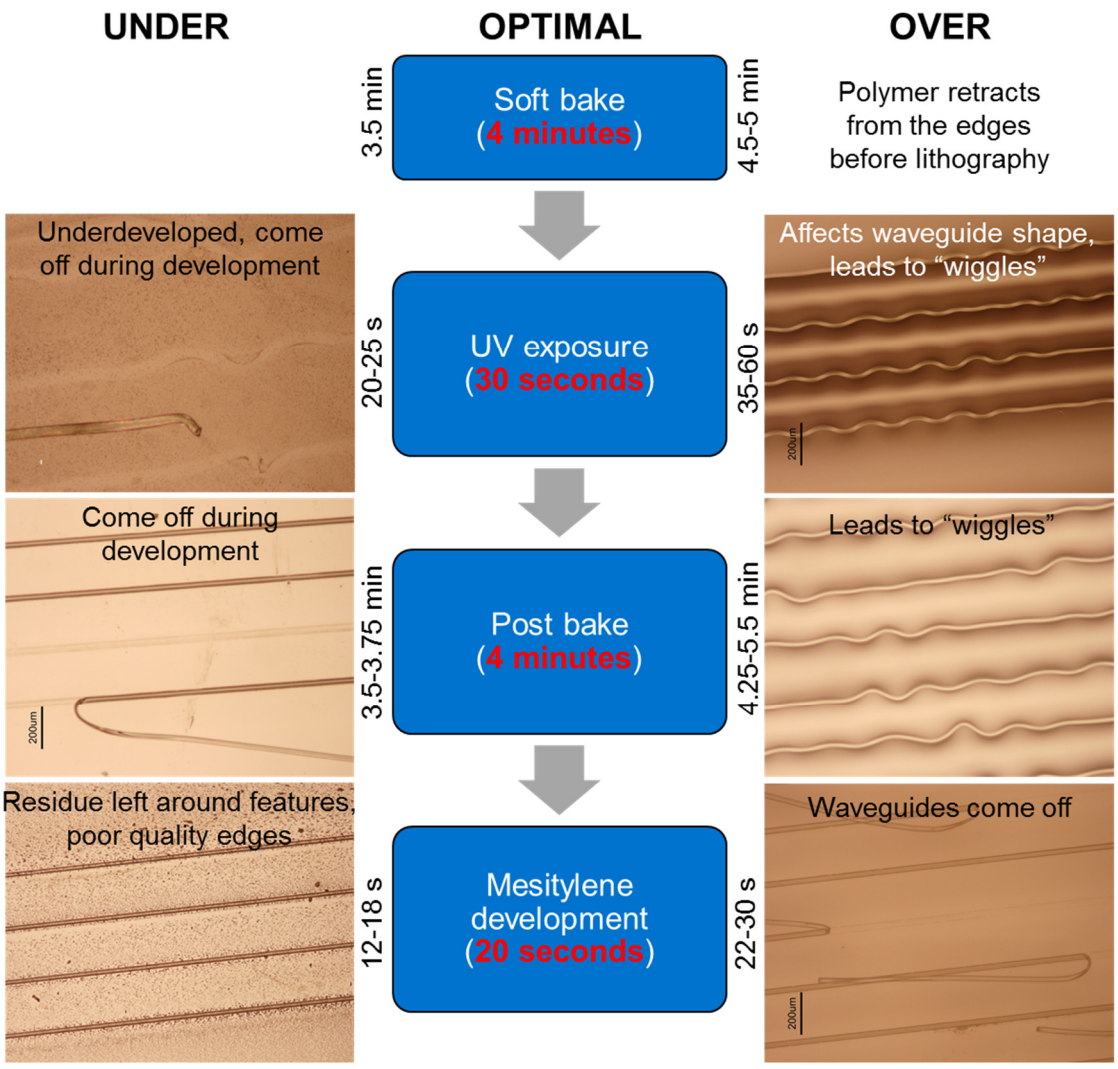

Figure 5-10: Effects of under- and over-optimal processing times during different fabrication steps of the strip-loaded hybrid structures

In general, the soft bake step was found to have the smallest impact on the quality of the final waveguides. The duration at which the spin-coated polymer was heated up had to be reduced from the original 5 minutes due to a visible deposited layer retraction from the edges towards the centre of the sample. Further reduction beyond 4 minutes was determined not to make any observable difference at this fabrication stage. Therefore, it was kept at this duration to maximise the amount of solvent evaporated in the process.

Duration of the UV exposure and the post bake step were established to be crucial factors in forming good quality features. In case when either or both of these times had been set

too short, the resulting waveguides were underdeveloped and come off during the later stages. Contrarily, running these processes for too long resulted in well-developed features that did not properly adhere to the glass surface and formed wave-like patterns instead of straight lines (Figure 5-10).

The last crucial fabrication step was mesitylene development performed in order to remove any undeveloped material from the surface. As in the previous steps optimal process time was found by varying the duration while keeping all the other steps unchanged. In case of a too short development, visible residue traces were observed on the sample surface with a particularly high density around the waveguides. Alternatively, developing the sample for too long caused the mesitylene to detach the waveguides together with undeveloped polymer material.

5.4 Experimental Studies

Based on the optimised fabrication procedure, three thin-film samples presented in Chapter 4 were used for waveguide fabrication. Strip-loaded hybrid waveguides were made using samples T28, O6 and C2 due to their promising planar layer characterisation results. The latter two were initially 20 × 30 mm^2 large while T28 was half of this size (20 × 15 mm^2). The final length of the waveguides deposited along the longer side was shorter than these lengths due to an edge removal needed to create accessible waveguide facets on both ends of the samples.

5.4.1 Visual Inspection

The three samples were prepared using the optimised fabrication process presented and waveguides were deposited in order to create hybrid strip-loaded devices. The initial investigation was performed using an optical microscope in order to visually assess the quality of the devices as shown in Figure 5-11. In terms of the waveguide quality, samples T28 and O6 looked more promising than C2 where traces of undeveloped polymer could not be removed without damaging the waveguides themselves. Furthermore, the best fabricated structures were 9-µm-wide as the optimisation only allowed for formation of non-wavy (Figure 5-10) waveguides in a relatively narrow size range that did not cover the entire width range available on the designed mask.

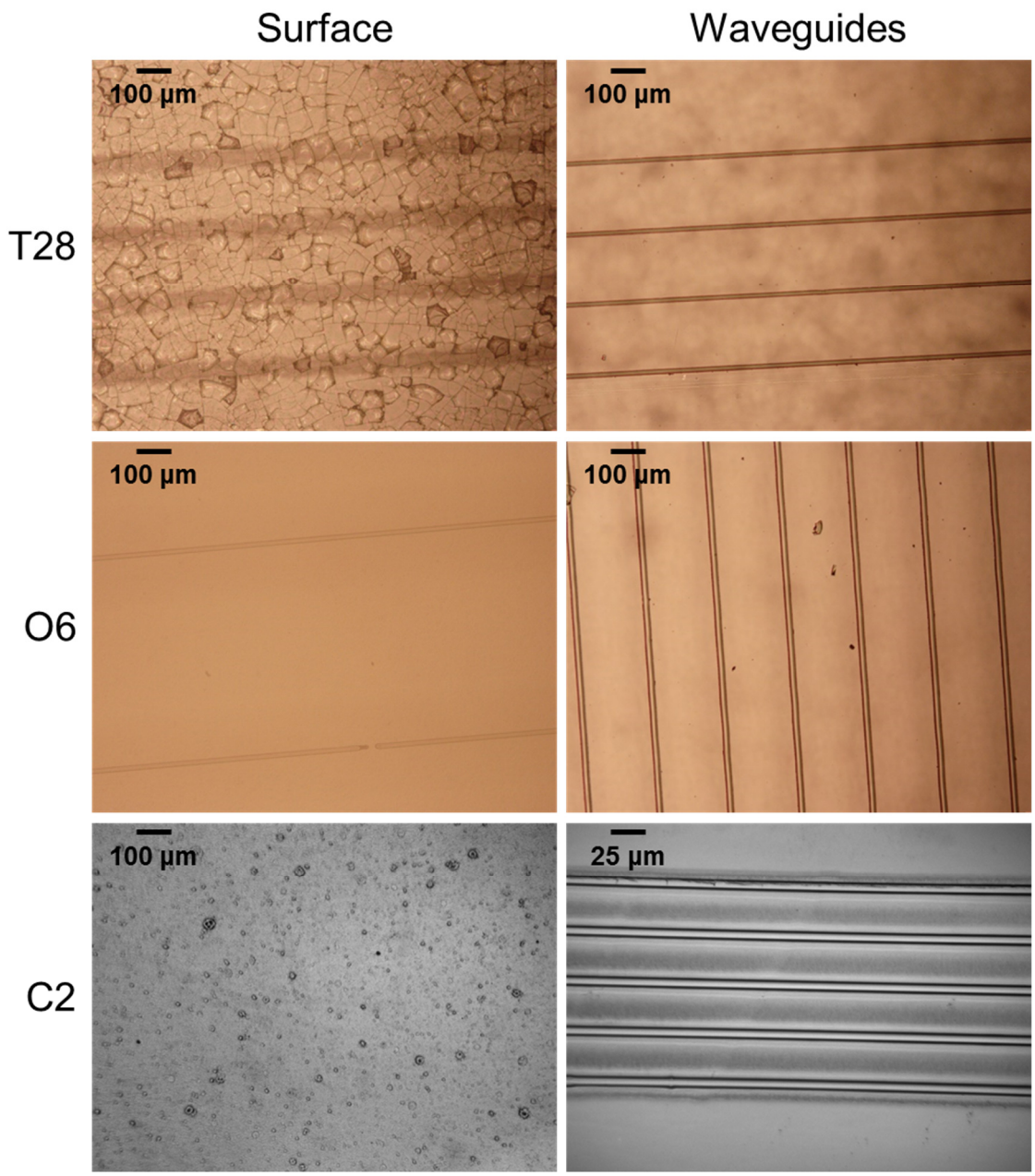

Figure 5-11: Microscope images of samples T28, O6 and C2 with focus on the sample surface and deposited waveguides

Additional checks were also performed on the surface of the samples showing various unexpected features. T28 was discovered to have small cracks on the surface forming flakes which were believed to be an outcome of too high temperature of the in-situ heating during the erbium implantation stage [13]. The same surface defect was not observed on either sample C2 nor O6. However, in case of the first one, the surface was not completely smooth and relatively large particles of the TZN target material deposited on the surface rather than implanted into the glass were visible. A similar phenomena was observed in the polymer thin films reported in Chapter 4 leading to a belief that the ULPI process still

needed further optimisation to ensure fabrication of smoother doped films as reported in [14].

To confirm the visual observations made with the microscope, SEM was employed to further investigate the two samples – T28 and O6 as presented in Figure 5-12. The first sample was chosen to inspect the nature of the cracks leading to a number of additional features being spotted. In addition to micron-sized particles of the target glass seen in Figure 5-12 b), a number of larger pieces were noticed with size comparable or larger to that of the waveguides (Figure 5-12 a)). A much better implantation quality was observed on the surface of the sample O6 with very few pieces of the target glass deposited on top of the surface rather than implanted (Figure 5-12 d)).

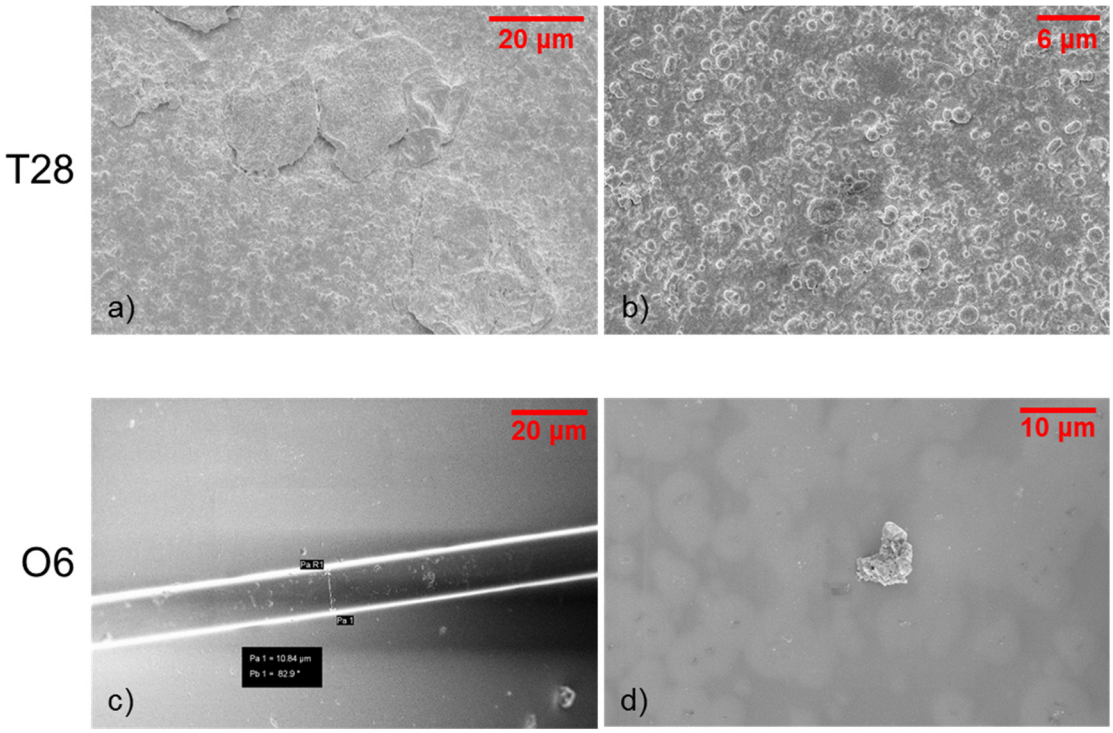

Figure 5-12: SEM images of samples T28 [a), b)] and O6 [c), d)]

5.4.2 Near-field Profile Measurements

In addition to visual inspection, near-field profiles were recorded as shown in Figure 5-13 a) and b). The most promising results were recorded using red HeNe laser sample on sample T28 where light modes under the strip as well as in the strip were recorded depending on the lensed fibre alignment. The structure was found to be highly multi-modal due to its size as the ridge was found to be 9 × 15 µm^2. This size was also confirmed through a profilometer measurement.

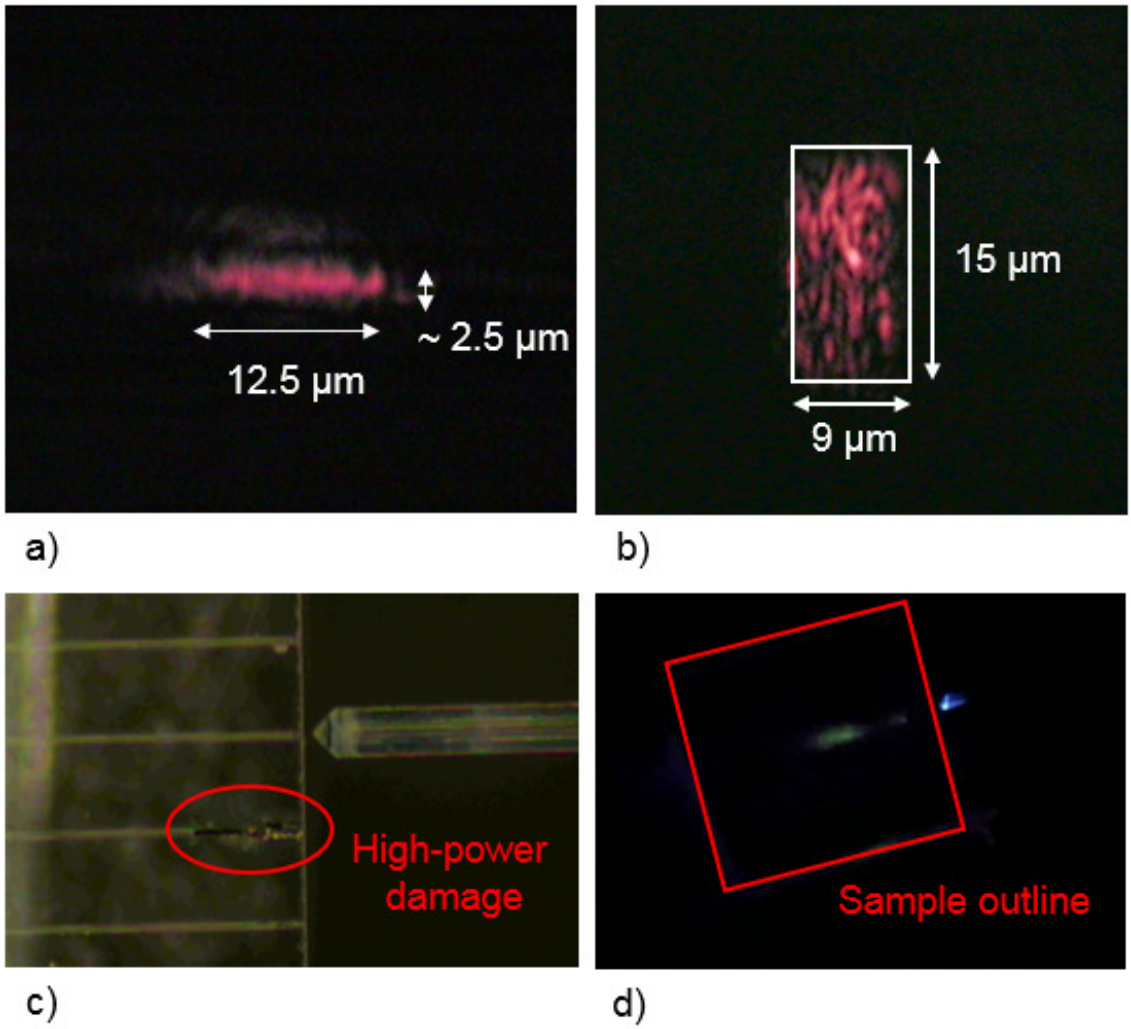

Figure 5-13: Sample T28 investigation: a) & b) near-field profiles, c) sample edge view highlighting high-power damage and d) green upconversion light

Furthermore, the sample was investigated for green light upconversion emission through 976 nm pumping as on the setup shown in Figure 5-14. The pump power was increased to find the maximum that could be delivered to the system before polymer was damaged (Figure 5-13 c)). It was found that less than 400 mW could be delivered before the polymer waveguide was destroyed. With this limit in mind, it was possible to observe a weak green upconversion light only in sample T28 as presented in Figure 5-13 d). Through this investigation a problem of poor quality waveguiding became apparent. A green light was expected to cover the entire length of the sample [15] while in this work only small traces were visible in a number of points along the sample.

5.4.3 ASE Measurements

Amplified spontaneous emission measurements were performed on the most promising ridges using the setup presented in Figure 5-14 without the tuneable laser turned on. The

intensity of the erbium emission spectrum was measured at the output and input of the sample under a 976 nm pump excitation.

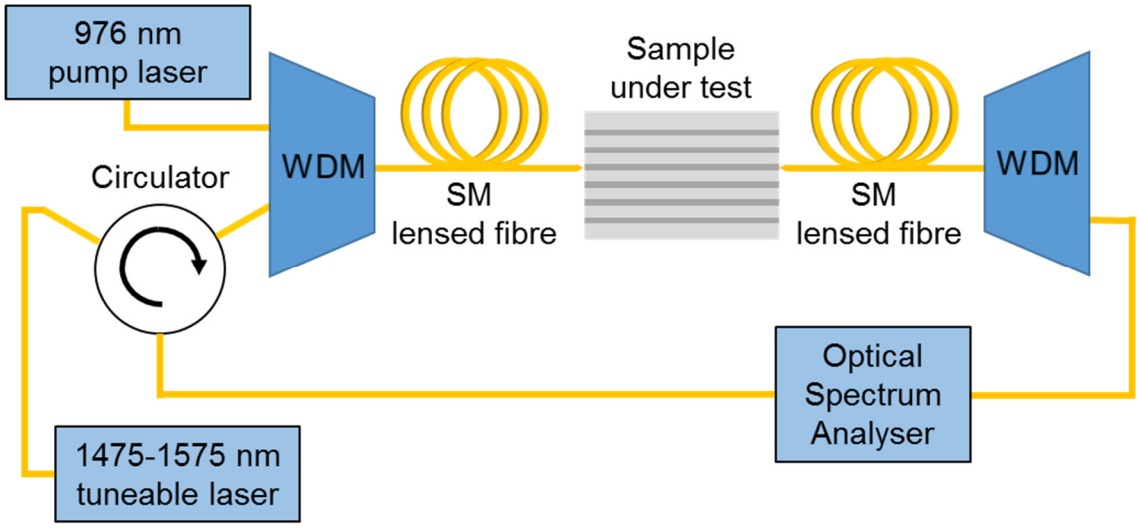

Figure 5-14: Amplifier characterisation setup

The results of the measurement are presented in Figure 5-15 for the two ridges with strongest signals on sample T28. The first observation was that the ASE power is very weak, under -80 dBm for all wavelengths. In theory, a signal stronger than -50 dBm was expected based on the high dopant concentration of 1.63×10^{21} cm^{-3} and the pump power of over 300 mW. This expectation was confirmed by an experimentally measured ASE peak of -51 dBm in a system with lower erbium concentration (1.1×10^{20} cm^{-3}) and pumped at much lower power of 180 mW [16]. Additionally, a difference of almost 8 dB between signal measured at the front and back of the sample indicated that the light is not guided well underneath the polymer strip and high losses were incurred along the sample.

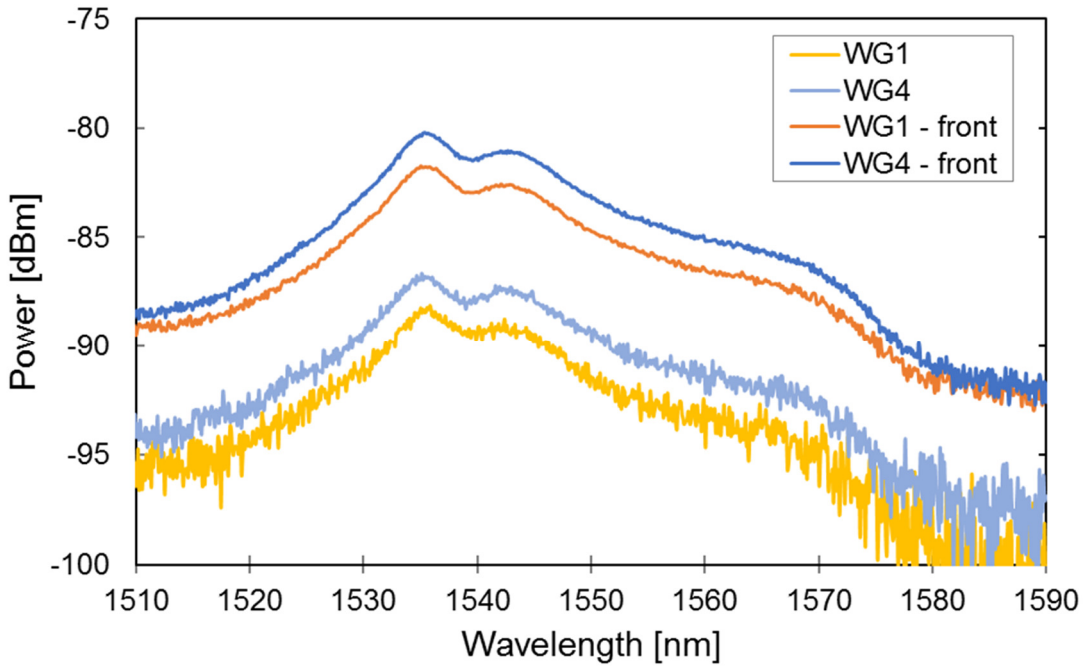

Figure 5-15: ASE emission from front and back of T28 sample

5.4.4 Surface Roughness

The final confirmation of the underlying problems with the hybrid glass-polymer system presented in this thesis was made through measuring the surface roughness of the fabricated samples. A height of a 3-mm-long section around the central part of samples T28 and C2 was measured using a profilometer. The obtained outline was then averaged over the entire length and the distance from this average for both samples is plotted in Figure 5-16. It was noticed that sample T28 has a larger variation and in some cases peaks over 1 μm higher than the average could be observed. The root mean square (RMS) value was calculated to be 193.3 nm and 95.8 nm for T28 and C2 respectively. This was a large value, particularly when compared with 46 nm experimentally measured on UV-photolithography-developed siloxane polymers [16].

The importance of low surface roughness is highlighted by the impact it has on the propagation loss in optical waveguides. This source of loss can be theoretically quantified using Gaussian statistics with the upper bound for a single mode planar structure shown in Equation (5.2) [17].

$$\alpha = 0.76 \frac{\sigma^2}{k_0 d^4 n_1} \tag{5.2}$$

where α is the scattering loss, σ is the surface roughness, k_0, d and n_1 are the free-space wavenumber, planar layer thickness and refractive index respectively. The quadratic relationship between the scattering loss and the surface roughness stresses the importance of smooth waveguide boundaries for low-loss transmission.

This formula is a useful tool to estimate the maximum potential loss and emphasise its dependence on the surface roughness. It needs to be used carefully, due to the number of the underlying assumptions. The single mode assumption allowing usage of this equation is not true for T28 (sample too thick), but in case of C2 the upper bound on the slab waveguide can be estimated to be 82 dB/cm. Even though this number shows that the scattering loss can be expected to be very high for a surface with this roughness, in practice this number should be much lower due to presence of the polymer ridge that reduces the refractive index contrast.

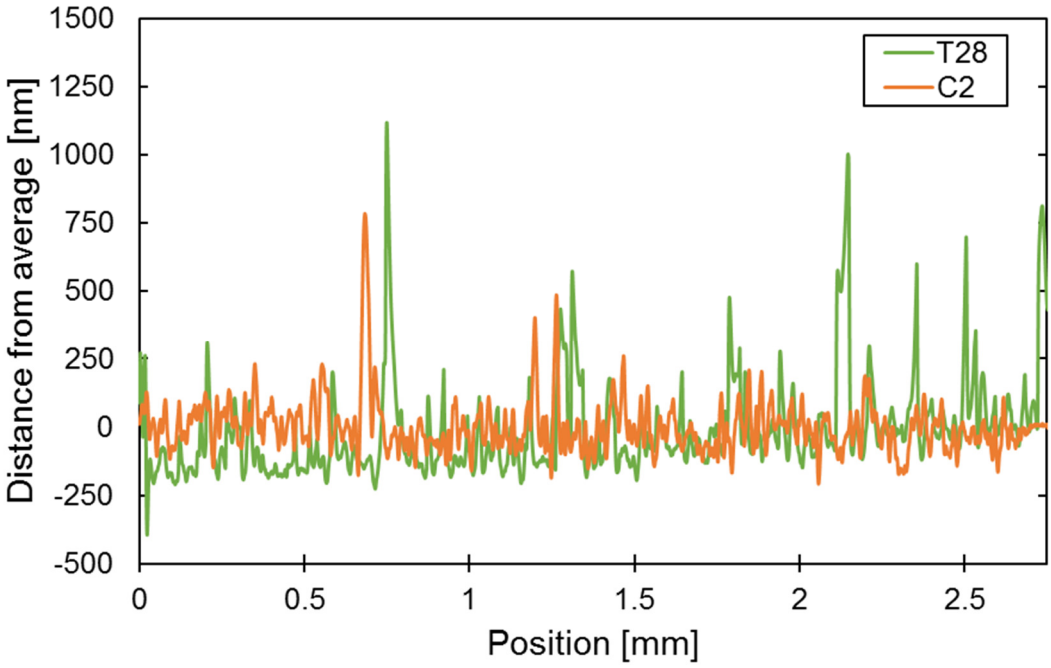

Figure 5-16: Surface roughness measurements for samples T28 and C2 showing large deviation

5.5 Conclusions

The combination of the ULPI fabrication in silica glass and siloxane materials to create hybrid waveguide structures has a potential to achieve high-gain erbium-doped optical amplifiers. In this chapter, the performance of such EDWAs via simulation studies based on the parameters of the fabricated Er-doped glass layers is investigated. Two common

waveguide configurations: the channel and strip-loaded geometry are compared in terms of their performance. Simulation results on a 1-cm-long channel EDWA provide optimisation guidelines for the co-doping of Er and Yb as a function of the background waveguide loss and upconversion coefficient. The study has shown that variation in the background loss has a minimal impact on the preferential erbium-to-ytterbium ratio, while change in the upconversion factor results in a great shift in this optimum.

The investigated scenarios reveal that, when pumped at 200 mW, a 1-cm-long device can produce a gain of 4.2 dB even when worst case scenario for upconversion (10×10^{-23} m^3s^{-1}) is accounted for. In the more realistic case, when the upconversion factor is scaled linearly with erbium concentration, the optimal Er:Yb ratio of approximately 1:1 yields a gain of 7.7 dB/cm in a hybrid channel waveguide. This result indicates that an optimised system with a fixed dopant concentration of 1.63×10^{21} cm^{-3} has potential of delivering high gain even when operated at moderate pumping powers.

Strip-loaded waveguide is an alternative hybrid geometry which has the benefit of a single step ridge deposition fabrication. It is shown that under the same single mode assumptions as for channel structure a similar internal gain figure of 7.4 dB is theoretically possible. This is achieved by adjusting the Er:Yb ratio to 1:2 where the new maximum is found for the given operating conditions.

The polymer waveguide lithography process is adjusted for a small glass sample deposition required for fabrication of hybrid strip-loaded structures. This is then used to prepare three samples for the hybrid EDWA studies. The experimental analysis via microscope (including SEM), ASE measurements and surface profiling has revealed that the fabricated structures do not perform in accordance to the simulation studies. It is believed that a combination of rough surface (RMS in range of 95.8-193.3 nm) and larger than required polymer waveguides have been the main causes behind this disappointing outcome. However, the latter reason is believed to be only a secondary problem as high-gain (6.6 dB/cm) multimode erbium-doped amplifiers have been demonstrated in the past [18]. Therefore, to fully benefit from the high erbium concentration provided though the ULPI, further optimisation of the process parameters is required to reduce the surface roughness while maintaining favourable properties measured in thin films.

Despite the fact that the hybrid EDWAs have not been successfully realised, the optimisation approach proposed in this chapter has a lot of potential to improve performance of alternative designs based on other systems, particularly ones with all the parameters, including the key upconversion factor, well-established through experimental

studies. The presented optimisation based on polymer and ULPI technologies is still valid and, with the high surface roughness eliminated, can be employed in future as recently shown in similar, non-optimised, hybrid structures [19].

5.6 References

[1] K. Yan *et al.*, "Emission properties of erbium-doped Ge-Ga-Se glasses, thin films and waveguides for laser amplifiers," *Opt. Mater. Express*, vol. 4, no. 3, p. 464, 2014.

[2] S. Suntsov, C. E. Rüter, and D. Kip, "Er:Ti:$LiNbO_3$ ridge waveguide optical amplifiers by optical grade dicing and three-side Er and Ti in-diffusion," *Appl. Phys. B Lasers Opt.*, vol. 123, no. 4, pp. 1–7, 2017.

[3] G. C. Righini and M. Ferrari, "Photoluminescence of rare-earth-doped glasses," *Riv. del Nuovo Cim.*, vol. 28, no. 12, pp. 1–53, 2005.

[4] D. E. McCumber, "Einstein relations connecting broadband emission and absorption spectra," *Phys. Rev.*, vol. 136, no. 4A, pp. 16–19, 1964.

[5] R. S. Quimby, W. J. Miniscalco, and B. Thompson, "Clustering in erbium-doped silica glass fibers analyzed using 980 nm excited-state absorption," *J. Appl. Phys.*, vol. 76, no. 8, pp. 4472–4478, 1994.

[6] Y. Benmadani, A. Kermaoui, M. Chalal, W. Khemici, A. Kellou, and F. Pellé, "Erbium doped tellurite glasses with improved thermal properties as promising candidates for laser action and amplification," *Opt. Mater. (Amst).*, vol. 35, no. 12, pp. 2234–2240, 2013.

[7] I. Jlassi, H. Elhouichet, M. Ferid, R. Chtourou, and M. Oueslati, "Study of photoluminescence quenching in Er3+-doped tellurite glasses," *Opt. Mater. (Amst).*, vol. 32, no. 7, pp. 743–747, 2010.

[8] J. D. B. Bradley, L. Agazzi, D. Geskus, F. Ay, K. Worhoff, and M. Pollnau, "Gain bandwidth of 80 nm and 2 dB/cm peak gain in $Al_2O_3:Er^{3+}$ optical amplifiers on silicon," *J. Opt. Soc. Am. B*, vol. 27, no. 2, pp. 187–196, 2010.

[9] A. Z. Subramanian, G. S. Murugan, M. N. Zervas, and J. S. Wilkinson, "Spectroscopy, Modeling, and Performance of Erbium-Doped Ta_2O_5 Waveguide Amplifiers," *J. Light. Technol.*, vol. 30, no. 10, pp. 1455–1462, 2012.

[10] H. Yamauchi, G. S. Murugan, and Y. Ohishi, "Optical properties of Er 3+ and Tm

3+ ions in a tellurite glass," *J. Appl. Phys.*, vol. 97, no. 4, 2005.

[11] J. A. Vallés, M. A. Rebolledo, and J. Cortés, "Full characterization of packaged Er-Yb-codoped phosphate glass waveguides," *IEEE J. Quantum Electron.*, vol. 42, no. 2, pp. 152–159, 2006.

[12] F. Wang *et al.*, "Er^{3+}/Yb^{3+}-codoped phosphate glass for short-length high-gain fiber lasers and amplifiers," *Appl. Opt.*, vol. 54, no. 5, pp. 1198–1205, Feb. 2015.

[13] J. Chandrappan, V. Khetan, M. Ward, M. Murray, and G. Jose, "Devitrification of ultrafast laser plasma produced metastable glass layer," *Scr. Mater.*, vol. 131, pp. 37–41, 2017.

[14] J. Chandrappan *et al.*, "Target dependent femtosecond laser plasma implantation dynamics in enabling silica for high density erbium doping," *Sci. Rep.*, vol. 5, 2015.

[15] K. Yan, K. Vu, and S. Madden, "Internal gain in Er-doped As2S3 chalcogenide planar waveguides," *Opt. Lett.*, vol. 40, no. 5, pp. 796–799, 2015.

[16] A. Laliotis, E. M. Yeatman, and S. J. Al-Bader, "Modeling signal and ASE evolution in erbium-doped amplifiers with the method of lines," *J. Light. Technol.*, vol. 24, no. 3, pp. 1589–1600, 2006.

[17] F. P. Payne and J. P. R. Lacey, "A theoretical analysis of scattering loss from planar optical waveguides," *Opt. Quantum Electron.*, vol. 26, no. 10, pp. 977–986, 1994.

[18] G. F. R. Chen, X. Zhao, Y. Sun, C. He, M. C. Tan, and D. T. H. Tan, "Low Loss Nanostructured Polymers for Chip-scale Waveguide Amplifiers," *Sci. Rep.*, vol. 7, no. 1, pp. 1–8, 2017.

[19] Y. Yi, H. Wang, M. Jiang, X. Wang, F. Wang, and D. Zhang, "Multilayer Hybrid Waveguide Amplifier for Three-Dimension Photonic Integrated Circuit," *IEEE Photonics Technol. Lett.*, vol. 27, no. 22, pp. 2411–2413, 2015.

6 ERBIUM-DOPED POLYMER WAVEGUIDES

Work on the design, fabrication and characterisation of hybrid structures was presented in the previous chapter. Even though these polymer-glass devices are compatible with the polymer platform, the erbium is confined in the glass and an organic waveguide is added on top. However, as seen in the state-of-the-art review in Chapter 2, direct doping of polymers has resulted in the highest reported internal gain in EDWAs to date.

In this chapter, purely polymer-based systems are presented using the fabrication technologies and processing steps introduced in Chapter 4. Based on the Er-doped thin film characterisation of the ULPI as well as nanoparticle dispersion obtained samples, the latter technique is selected for NP-doped waveguide implementation in this thesis.

The fabrication of Er-doped polymer waveguides is discussed highlighting changes from the original protocol for an undoped material. The additional steps of membrane filtering and ultrasonication are investigated to assess their impact on NP dispersion uniformity. The fabricated waveguides are then visually inspected and characterised using the methodology presented in the previous chapter in addition to transmission measurements across the erbium emission spectrum.

The measurement results are then used to extract additional parameters for simulation studies of the NP-doped polymer amplifiers. The emission and absorption cross sections are estimated using the McCumber theorem leading to a good match between the analytical model and measurements in terms of their spectral shapes. The main loss contributors and the Er-concentration are derived for a full EDWA simulation based on cross section results combined with a Rayleigh scattering model.

Furthermore, the EGC NP-doped polymer EDWAs are modelled using the rate-equations model introduced in Chapter 3 and employed in Chapter 5. The parameters are adjusted with the fabricated material properties showing a good match with the experimental values. The leading cause of poor performance is determined and a potential device performance with reduced scattering losses is presented and compared with alternative state-of-the-art NP-doped polymer systems.

6.1 Device Fabrication

The erbium-doped waveguides presented in this chapter were prepared by combining the results of the thin-film analysis and the optimised polymer-only fabrication process discussed in Chapter 4. The protocol was adjusted to account for additional processing

steps such as ultrasonication and filtering of the doped core material as summarised in Figure 6-1.

Several wafers were prepared with the available material of various NP concentrations. In every case the wafer fabrication process was preceded by a material preparation that was not required in the case of the pure WG-2020 core polymer. The additional steps after the core material and the nanoparticles were mixed together included magnetic stirring and ultrasonication. These processes were employed in order to ensure a more uniform dopant distribution as well as to reduce particle agglomeration in the solution.

The remaining steps in the process followed the optimised wafer scale protocol for all-polymer systems with an additional optional step of membrane filtering. This addition to the process was an outcome of the Er-doped thin film characterisation performed in Chapter 4 with the most promising syringe membrane size of 200 nm used during the wafer-scale core material deposition before the spin-coating step. All the wafers prepared using this procedure included this additional fabrication step except for the lowest concentration of 0.05 wt.% used as a reference for the higher concentration devices.

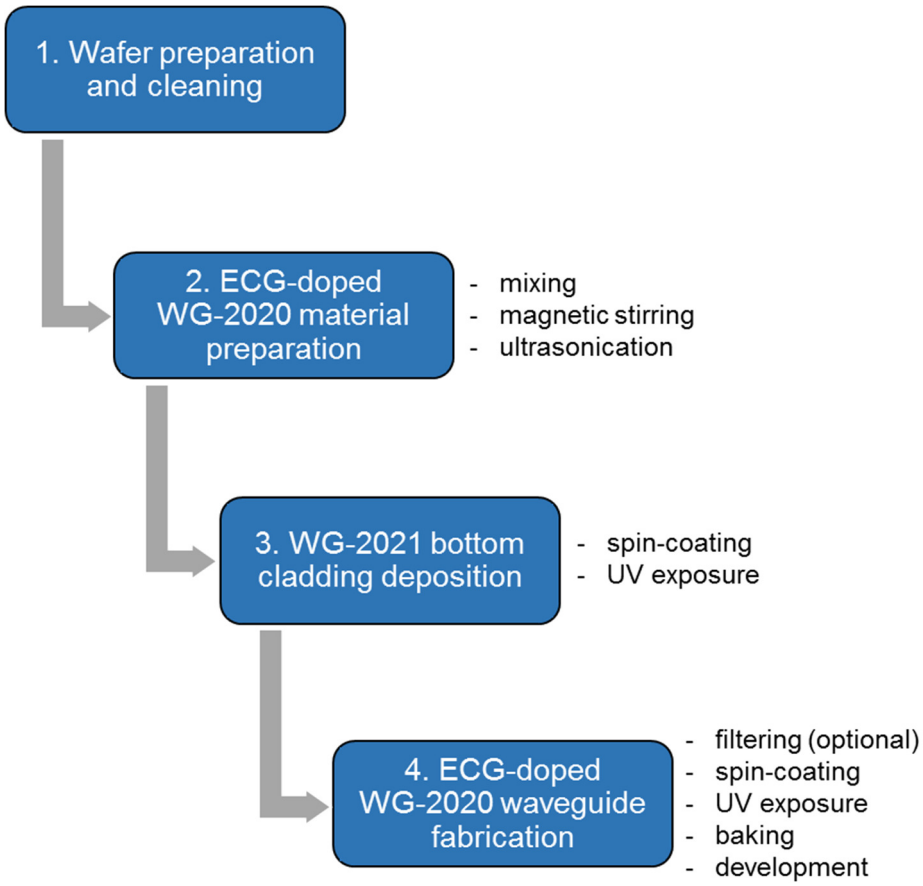

Figure 6-1: Fabrication process flow for EGC-doped polymer wafers

Based on the optimised fabrication procedure, four wafers were fabricated for further investigation. Two of them were used as references. The first was prepared using an undoped WG-2020 core material while the second had a low NP concentration of 0.05 wt.% and waveguides were produced without the additional filtering step. The remaining two wafers were prepared using higher concentrations of 5.1 wt.% and 9.8 wt.%.

6.2 Device Characterisation

In this section the fabricated EGC-doped polymer waveguides are characterised, and the results discussed. The prepared wafers were visually inspected and the highest quality sections diced into smaller samples for further investigation. Near-field profile observations were used to assess the waveguiding potential and the most promising components were selected to measure the transmission across the 1475-1575 nm wavelength range of interest.

6.2.1 Visual Inspection

The fabricated wafers were inspected visually with a microscope to assess the quality of the waveguides as well as to identify any potential issues arising during the fabrication process. The images of the waveguides post fabrication as well as the central section of the wafer are summarised in Figure 6-2. The undoped polymer wafer was prepared as a reference with good quality waveguide sections visible.

Initially, the lowest concentration of 0.05 wt.% nanoparticles was used to investigate the outcome of the process without the additional filtering step. After the spin-coating step large NP agglomerations were visible on the surface with sizes greater than those of the designed waveguides. After UV photolithography and development, even waveguides that were not completely damaged by the largest particles had very rough surfaces. This was demonstrated through a highly granular and often interrupted waveguide surface.

As a result of these observations, wafers were prepared with the additional filtering step to remove the largest nanoparticle agglomerations from the mix. Much higher concentrations of 5.1 and 9.8 wt.% (shown in Figure 6-2) were chosen based on the available material mixes. These two concentrations also highlighted an important phenomenon occurring during the fabrication process: despite the additional filtering step, agglomerations larger than the membrane size formed on the wafer after the initial

deposition. This led to a yellowing of the wafer surface as well as visible damage to the obtained waveguides.

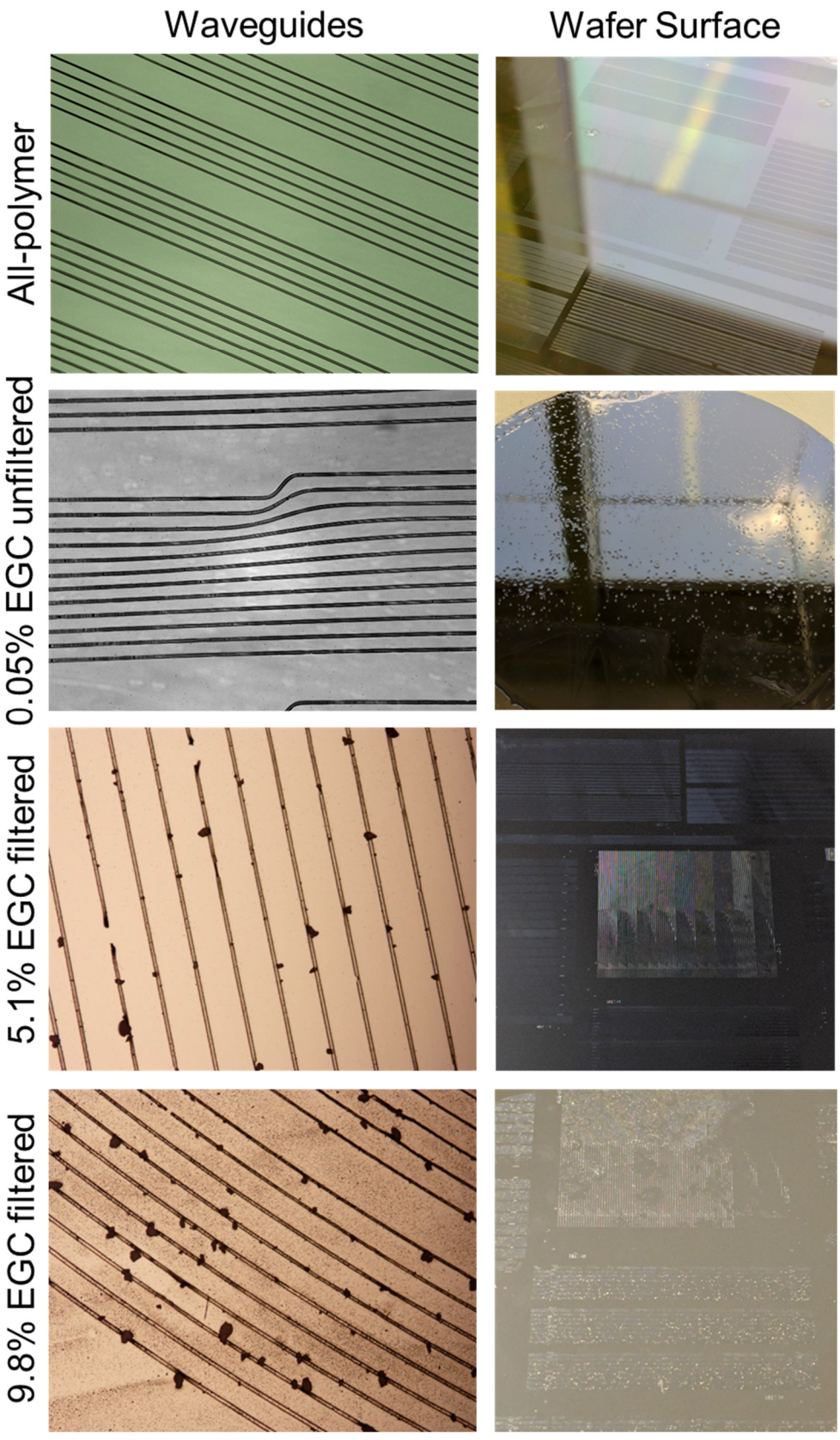

Figure 6-2: Waveguide and wafer surface for EGC-doped polymers at various concentrations

The visible particle agglomeration prompted further investigation into the cause of the quality deterioration of the deposited material since the same outcome was not visible in the previously fabricated thin films using the same material as reported in Chapter 4. The analysis of the differences in the fabrication protocol led to a notion that the rotation speed during the spin-coating step was the biggest change between the two processes. In order to test this theory, the remainder of the material was used to prepare smaller 30 × 20 mm^2 samples using an identical process except for the spinning speed which varied from 1000 to 5000 rpm.

The prepared samples were then measured using a profilometer to check for any differences in the surface roughness. The RMS results obtained across the 6-mm-section taken in the middle of the samples showed an increase in the surface roughness as presented in Figure 6-3. A smooth surface with RMS under 100 nm was measured at 1000 rpm used for thin film fabrication in Chapter 4. However, for the waveguide fabrication on a wafer scale in this chapter, a much higher speed of 4000 rpm resulted in a rougher surface with RMS of almost 7000 nm as indicated in this measurement. This result confirmed that the quality degradation problem observed during the wafer fabrication process was most likely an outcome of the increased rotation speed during the spin-coating process.

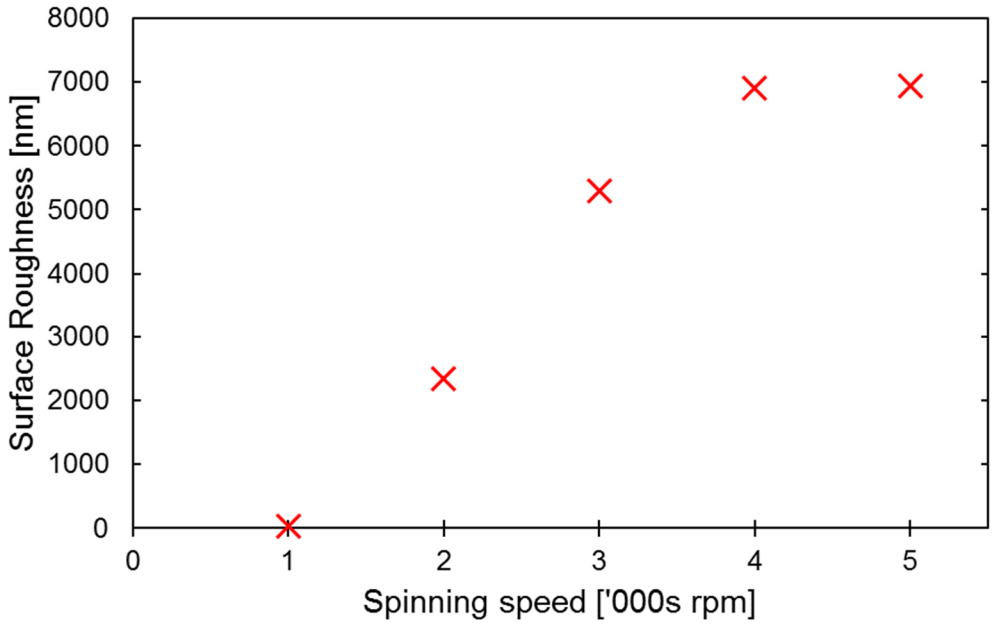

Figure 6-3: Surface roughness variation over spin-coating speed of NP-doped polymer based on 30 × 20 mm^2 samples

6.2.2 Near-field Profile Measurements

The visual inspection of the fabricated waveguides was followed by dicing of the wafers into smaller sections to identify best quality waveguides for further testing. Straight sections were investigated via red-light illumination used in the previous chapter to find candidates with the strongest output.

The near-field profiles and images of the waveguide facets made from the 5.1 wt.% EGC material were recorded with examples shown in Figure 6-4. As a result of this testing, it was observed that waveguides with larger cross-sections (approximately 9 × 5 μm^2 as confirmed with a profilometer measurement) possessed clearer output profiles. However, due to the relatively large size of these features in combination with the lack of the top cladding, a multimodal behaviour was observed as shown in Figure 6-4.

Even though the large size was not desirable due to reducing the potential device efficiency, similar sized devices without the top cladding have been reported with a low internal gain [1][2]. Furthermore, the lack of visible particle agglomerations on a set of waveguides of this size was believed to allow for transmission measurements and to provide useful information in terms of losses due to additional scattering from the dispersed particles inside of the waveguide.

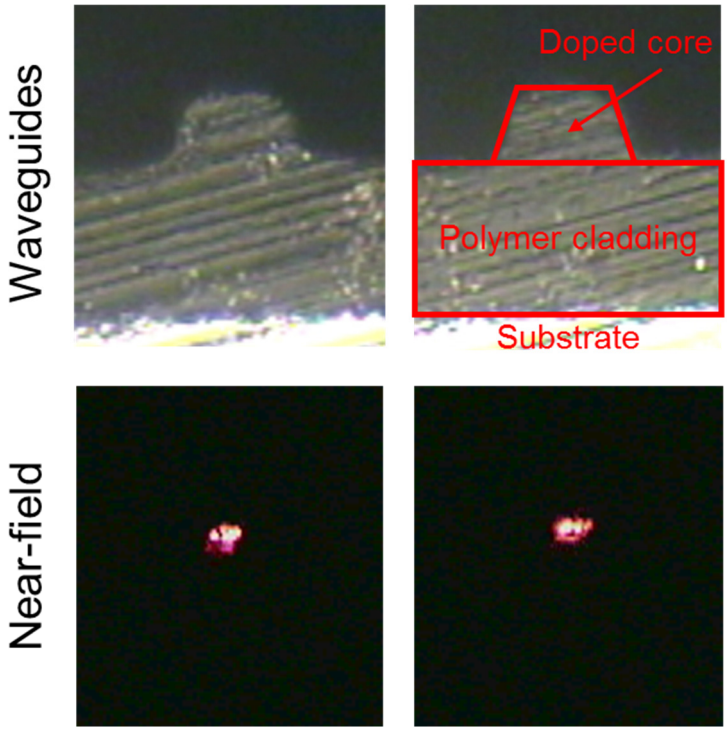

Figure 6-4: Waveguide facet pictures after dicing and near-field images under red-light illumination of the most promising waveguides

6.2.3 Gain/Loss Measurements

The NP-doped polymer waveguides were investigated using the experimental setup shown in Figure 6-5. Their loss performance in the 1475-1575 nm wavelength range was measured using a tuneable laser (HP 8168E) and optical spectrum analyser (Yokogawa AQ6370D) with the pump laser turned off during measurement. The same measurement was repeated with the pump laser turned on as well as without the sample for a back-to-back (B2B) reference.

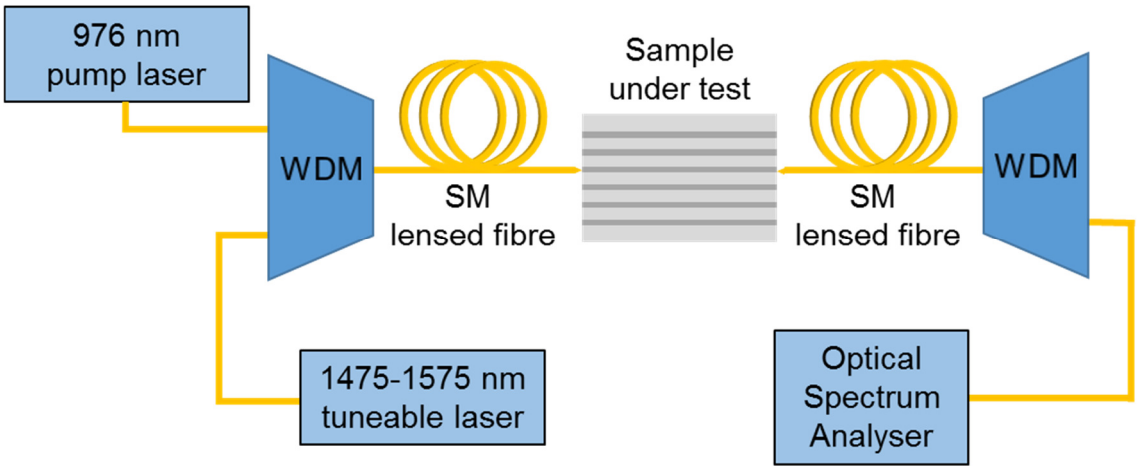

Figure 6-5: Er-doped waveguide transmission characterisation setup

As a result of the measurements across the sample, a highly promising 1.4-cm-long waveguide was found and fully characterised. The insertion loss was calculated through measurements with and without the sample as plotted in Figure 6-6 a). The obtained spectrum indicated that the signal across the entire measurement range experienced much higher loss than expected based on the used polymer material investigated in Chapter 4. Furthermore, the observed shape was similar to a typical erbium absorption band [3]–[5] with some minor differences. The absorption peak at 1533 nm matched well the value expected for Er; however, the secondary peak occurring below 1500 nm was larger than anticipated relative to the maximum.

Another outcome of the measurements was a calculation of the signal enhancement along the sample under approximately 300 mW pumping as shown in Figure 6-6 b). The relative difference resulting from pumping was only up to 2 dB which was lower than 7.6 dB reported in a similar polymer amplifier attempt [6].

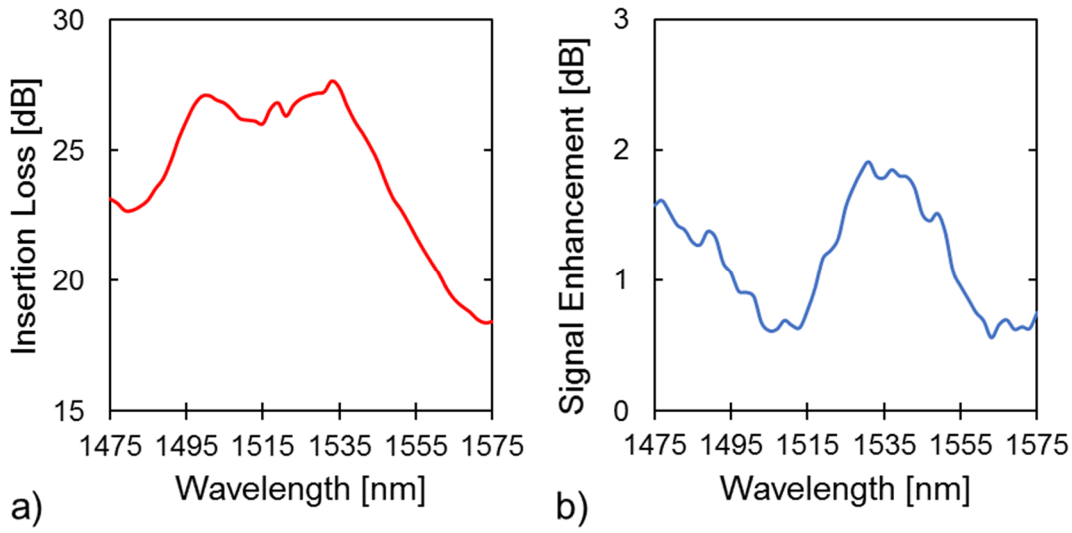

Figure 6-6: The results of a) insertion loss measurement and b) signal enhancement as a result of pumping

The poor transmission results combined with visual inspection results prompted a further analysis into the underlying causes of this behaviour. In order to gain a better understanding of the high losses and low relative gain, modelling of the various loss sources was performed and then combined with the full amplifier model as reported in the next section.

6.3 Device Loss Analysis

The obtained insertion loss of a 1.4 cm long NP-doped polymer waveguide across the erbium emission region was too high to form efficient waveguide amplifiers. As a result, the underlying loss components were identified, and their magnitude was estimated in order to better understand the limitations in the observed device performance. Three main loss components could be recognised: propagation and coupling loss due light propagation in the polymer waveguide (polymer-only), scattering (Rayleigh) loss due to the presence of the NPs in the polymer core material, and erbium absorption loss due to the presence of the Er ions.

6.3.1 Loss Component Breakdown

The initial loss component breakdown was performed in three stages to estimate the contribution of various components as shown in Figure 6-7. These results were obtained through a combination of additional experimental measurements as well as theoretical

modelling, as described below. The final outcome was then compared to a simulated EDWA system to check the assumptions made in the process.

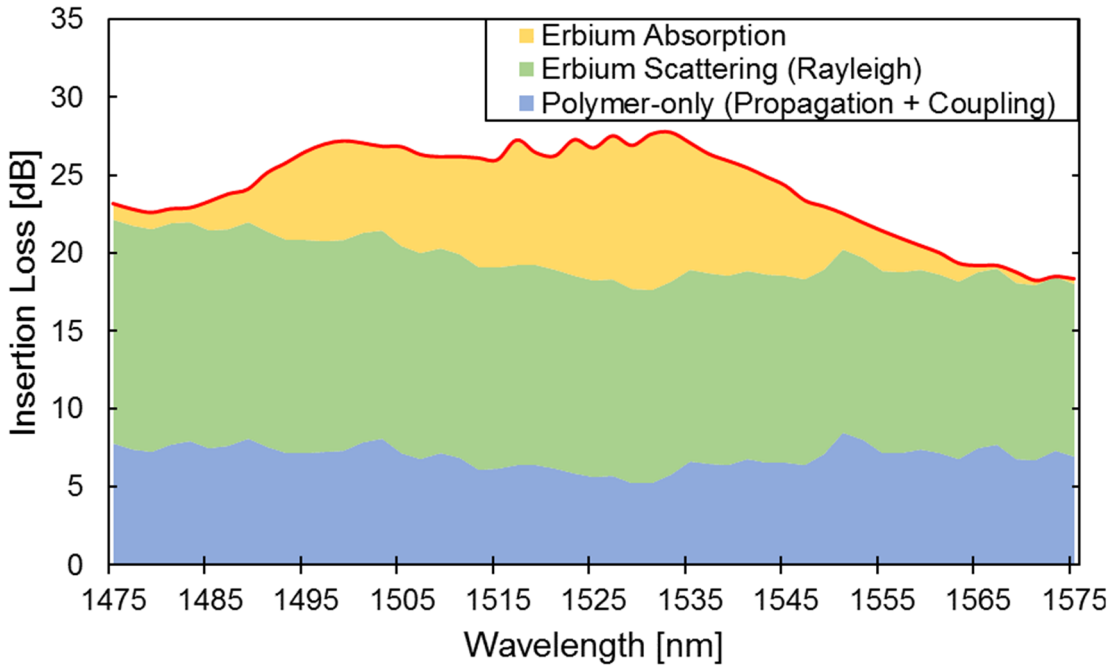

Figure 6-7: Insertion loss (red line) of a 1.4-cm-long NP-doped waveguide and estimated loss components

Firstly, the polymer-only loss was estimated using a non-doped polymer waveguide of the same dimensions and length. The wafer was prepared following an identical fabrication procedure, with WG-2020 material as a core, and then diced into equally sized samples. The values obtained this way were used to represent the underlying waveguide propagation loss as well as the coupling loss in and out of the device.

In order to distinguish between the remaining two signal attenuation sources an assumption regarding the erbium absorption at the highest recorded wavelength had to be made. The fact that very low Er-induced absorption losses are expected at 1575 nm [4] meant that the remaining loss at this wavelength could be assigned to NP-induced scattering in the waveguide.

The scattering loss is calculated using a Rayleigh model [7] with the scattering coefficient and the resulting loss estimated using equations 3.14 and 3.15 introduced in Chapter 3, respectively. The analysis reveals a scattering loss between 11 dB and 14 dB for the wavelength range studied. The lowest value is assigned to the difference between the polymer and total losses. Then based on this, the loss value is fitted into the model to

arrive at the highest scattering value of 14 dB at 1475 nm as expected from the wavelength dependence of the Rayleigh loss.

In order to obtain a more detailed picture of the dispersed nanoparticles, further investigation using the Rayleigh scattering model was performed as shown in Figure 6-8. The ceria (EGC) and phosphate NPs were investigated at various concentrations to provide a better understanding of the impact of particle size and type on scattering. The second material was added as a reference to the EGC used in this work and a phosphate glass was chosen as it was previously investigated as a material for polymer dispersion [8]. The key difference between the two materials lay in their refractive indices where the typical range for erbium-doped ceria is 2.0-2.2 [9], [10] compared to 1.5-1.6 for rare-earth-doped phosphate [11]–[13].

As a result of much smaller refractive index contrast between the spherical nanoparticles and the polymer host, the acceptable particle size for a given scattering loss level was much higher for the phosphate glass. In order to keep the NP-induced scattering arising from a 10% doped mix at a reasonable 1 dB/cm level the theoretical dopant radius limit for EGC was 14 nm compared to 74 nm in the case of the P_2O_2:Er. Furthermore, in both cases increasing the concentration of the dispersed dopant in the mix resulted in a higher Rayleigh loss. The important assumptions in this model were that the particles had a very narrow size distribution and were homogenously dissolved which might not always be the case in practice.

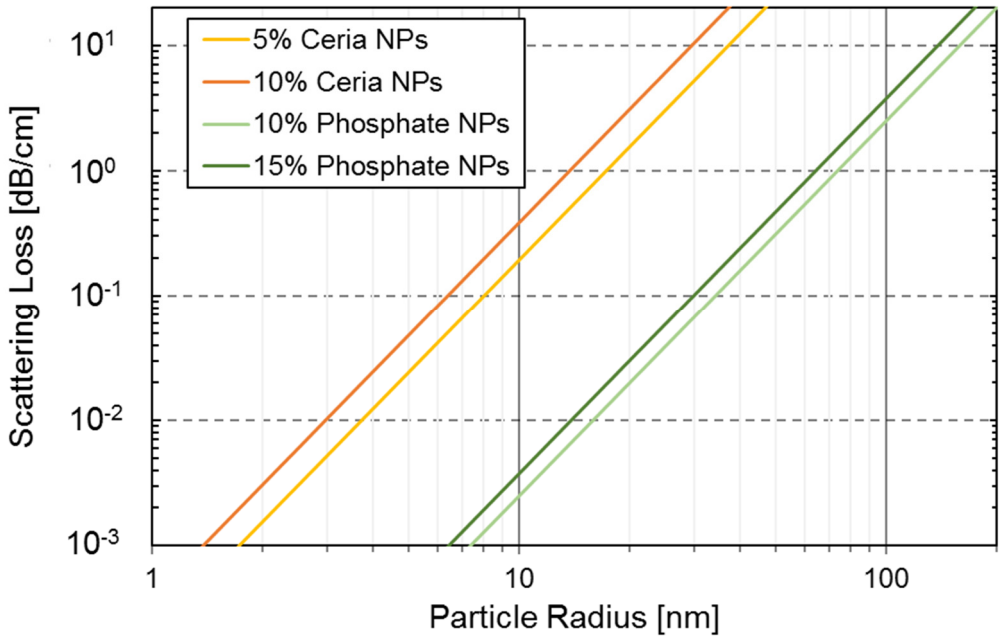

Figure 6-8: Dependence of the scattering loss at 1550 nm on the NP radius for ceria and phosphate mixed with polymer

The above model for ceria nanoparticles was used in order to approximate the size of the NPs in the waveguide. For a 5.1% concentration of EGC, the particle radius required to match the estimated loss of 11.9 dB (8.5 dB/cm) at 1550 nm was 36 nm. This estimate indicated that there was particle agglomeration taking place in the doped polymer as the pre-mixing particle size was in the range of 7 to 10 nm as shown in Chapter 4. In practice, however, the resulting particle size was likely to be even higher as the 200-nm-membrane filtering process was expected to remove the largest ceria clusters, thus reducing the actual NP concentration. Therefore, based on the scattering loss estimate, the lower limit to the ceria cluster radius was predicted to be 36 nm, but was expected to be larger than this value.

The remaining loss in the source breakdown presented in Figure 6-7 was assigned to erbium absorption. This was verified in the following section by comparing it to a predicted absorption spectrum obtained through the previously introduced McCumber theorem.

6.3.2 Parameter Extraction

In order to validate the above transmission loss analysis, the procedure proposed by Miniscalco [14] was employed to derive the Er absorption cross section from the thin film photoluminescence in the same way as for the EDTS samples in Chapter 5. This procedure enabled not only the comparison between the experimental and theoretical erbium absorption spectra but also estimation of the Erbium concentration inside the waveguide.

The measured emission spectrum of the Er-doped thin film presented in Chapter 4 was used to calculate the emission cross section of the material as shown in Figure 6-9 a). The corresponding absorption cross section was then derived using the Füchbauer-Ladenburg method. The expected shape of the absorption spectrum was measured [15], but no quantified cross section results for erbium-doped ceria in the 1500-1600 nm range were found to compare with the values predicted in this work.

Finally, the Er absorption loss predicted through the McCumber theorem (red line) and the loss analysis of the experimental results (yellow line) were compared as presented in Figure 6-9 b). Relatively good agreement was obtained between the two methods with a high correlation factor of 0.8. The two spectral response shapes exhibited peak absorbance around 1531 nm and a smaller secondary peak below 1500 nm. The good match between the two results not only validated the above loss component analysis, but

also allowed for an estimation of the erbium concentration. The absorbance matching through the least mean square error method led to a dopant ion valuation at approximately 1.5×10^{20} cm^{-3}. This result was an order of magnitude lower than the value reported in the EDTS glass layer in the previous chapter but was believed to have the potential for the provision of the internal gain. In order to assess the suitability and perspectives of this doping approach, the cross section and concentration parameters derived here were used for a more detailed amplifier study presented in the next section.

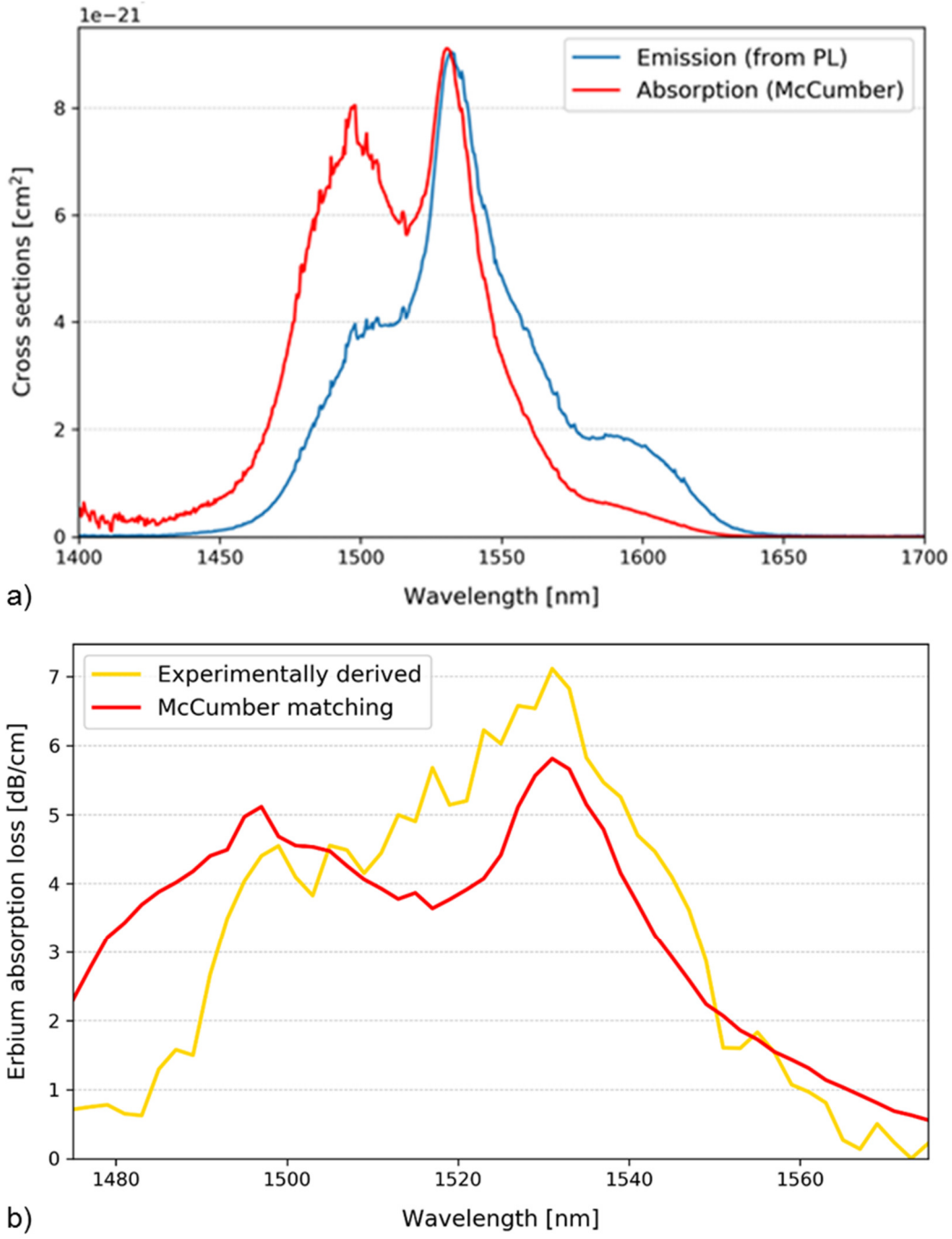

Figure 6-9: Er-absorption analysis: a) expected absorption cross section based on the McCumber theorem and b) matching with the measured absorption

6.3.3 Model Variation

As a result of the above loss analysis, it was concluded that the fabricated NP-doped polymer waveguides suffer from a very large scattering loss due to particle clustering in the polymer matrix. Even in the case of the best obtained features with no visible ceria agglomerations the losses were estimated to be in the range of 11 to 14 dB. However, the analysis process also predicted that the Er concentration in the waveguide would be approximately 1.5×10^{20} cm^{-3}.

The rate equations model put forward in Chapter 3 was then used to further investigate an EDWA relying on extracted parameters. The results shown in Figure 6-10 are based on the measured 1.4-cm-long Er-doped waveguide that had a rectangular cross-section of 9×5 μm^2.

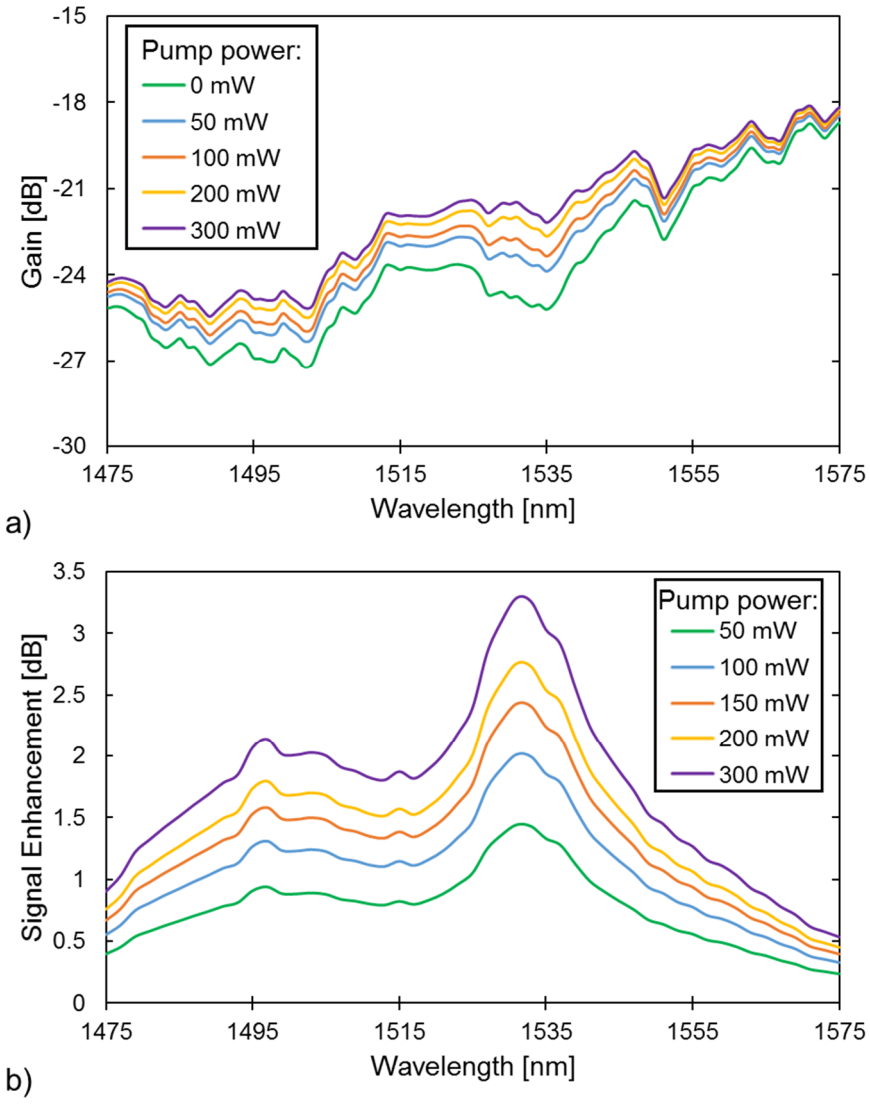

Figure 6-10: NP-doped waveguide simulations showing a) gain and b) signal enhancement for various pump powers

Most of the key parameters such as the lifetime, absorption/emission cross sections and background loss were derived experimentally, except for the upconversion factor that was unknown. Even though the erbium concentration was estimated to be 1.5×10^{20} cm^{-3}, which was an order of magnitude lower than obtained through ULPI, there was no ytterbium in the mix. Furthermore, the great interest in the upconversion efficiency of ceria nanopowders [15]–[17] indicated that a very high value of 10×10^{-23} m^3s^{-1} should be used in this case.

The simulation results confirmed the very high losses exceeding 25 dB that were measured in the waveguide (Figure 6-10 a)) as well as the poor response to the pump power (Figure 6-10 b)). The simulation results showed that a combination of high upconversion and scattering losses prevent signal enhancement from reaching 3.5 dB even at the relatively high pump power of 300 mW. The predicted low internal gain confirmed that high scattering losses were detrimental to the device operation as they not only reduced the magnitude of the signal but also diminished the pump power absorption.

The measured signal enhancement was then compared with the simulations to check if a good agreement was obtained, as presented in Figure 6-11. The resultant plots had a correlation factor of 0.62 and a poor match was obtained at lower wavelengths of the investigated range. A possible explanation for discrepancies in shape between the two plots was the fact that the measured signal was very weak and, therefore, prone to noise.

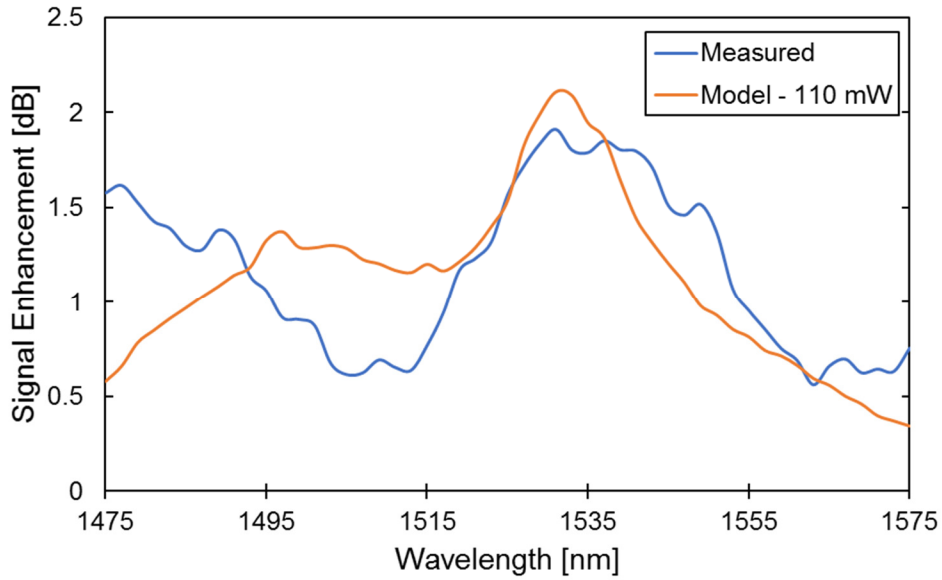

Figure 6-11: Signal enhancement spectrum matching of experimental measurements and model predictions

In order to match the magnitudes across the investigated range, RMSE minimisation was performed on the simulation results. This approach led to a pump power at the waveguide input estimate of 110 mW. Even though approximately 300 mW were launched in the experiment, when the component losses on the input side of the setup and the coupling loss in the waveguide were accounted for, a similar value was expected.

6.4 Waveguide Potential Validation

The results of experiments and simulations both indicated that the poor performance of the investigated device made it unsuitable for signal amplification. The main reason was apportioned to the very high scattering losses arising from poor dopant particle dispersion. To validate the potential of this approach and, in particular, the utilisation of the EGC NPs employed in this work, additional simulations were run. Throughout this study, the impact of scattering loss as well as other waveguide properties were investigated.

6.4.1 Scattering Loss

The high scattering loss estimated in the previous section prevented the waveguide from performing the desired operation. In order to investigate the potential to form an EDWA using this approach three scenarios, based on the extracted parameters, were explored as shown in Figure 6-12.

In the first case, a 1-cm-long device was assumed to have a background loss of 11.6 dB/cm corresponding to previously estimated NP scattering (9.3 dB/cm) and polymer loss (2.3 dB/cm). The combined impact resulted in a consistent loss with erbium absorption further contributing to signal power reduction. The high losses also meant that even at pump power of 300 mW only minimal signal enhancement was possible at wavelengths above 1560 nm (signal above the dashed line).

The second scenario, shown in Figure 6-12 b), assumed that the scattering loss due to the EGC particles was reduced to 0.3 dB/cm achievable in similar NP-doped systems [18]. Even in this case 300 mW were required in order to overcome the Er absorption losses at the peak wavelength of 1534 nm. Better performance was observed at longer wavelengths where small relative gain of up to 0.5 dB/cm was possible. This result highlighted that even though signal enhancement was achieved, an internal gain was not possible in a large, multi-mode waveguide fabricated using the materials used in this work.

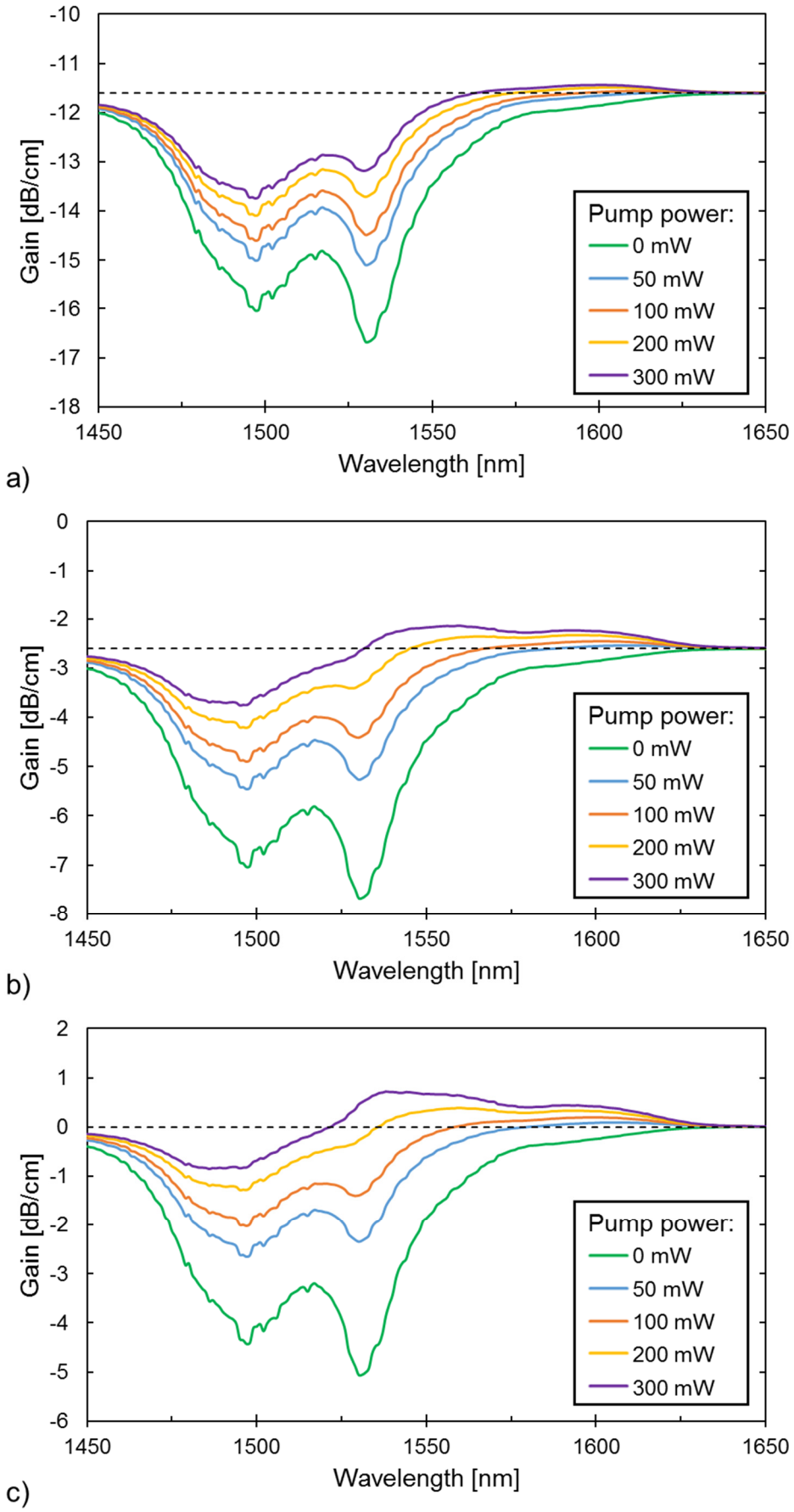

Figure 6-12: NP-dispersed EDWA simulations with background loss set to a) 11.6 dB/cm, b) 2.6 dB/cm and c) 0 dB/cm

In the final scenario, plotted in Figure 6-12 c), an ideal case of a lossless device was considered to check the possible gain magnitude and the amplification spectrum. An internal gain of 0.8 dB/cm peaking at 1538 nm indicated an important design issue. As a result of the device's large cross-section area (45 μm^2), higher pump powers were required to provide population inversion of the large number of Er ions. This effect was additionally compounded by the upconversion process, further reducing the number of erbium ions available for the stimulated emission on the radiative $^4I_{13/2}$ level.

A further check of the effect of high background loss was performed by comparing the expected reduction in the device's gain with the simulations as shown in Figure 6-13. This plot was obtained by comparing the magnitude of the signal at 1534 nm in the three scenarios considered above. While a background loss of 2.6 or 11.6 dB/cm would have indicated expected reduction in the gain magnitude to match these values, a larger drop was calculated in practice. An additional 0.5 dB and 2 dB difference was found, respectively. This indicated that, as a result of the high scattering loss, not only the signal itself but also the pump power was reduced along the device. This in turn led to a lower population inversion and thus further decreased the potential gain.

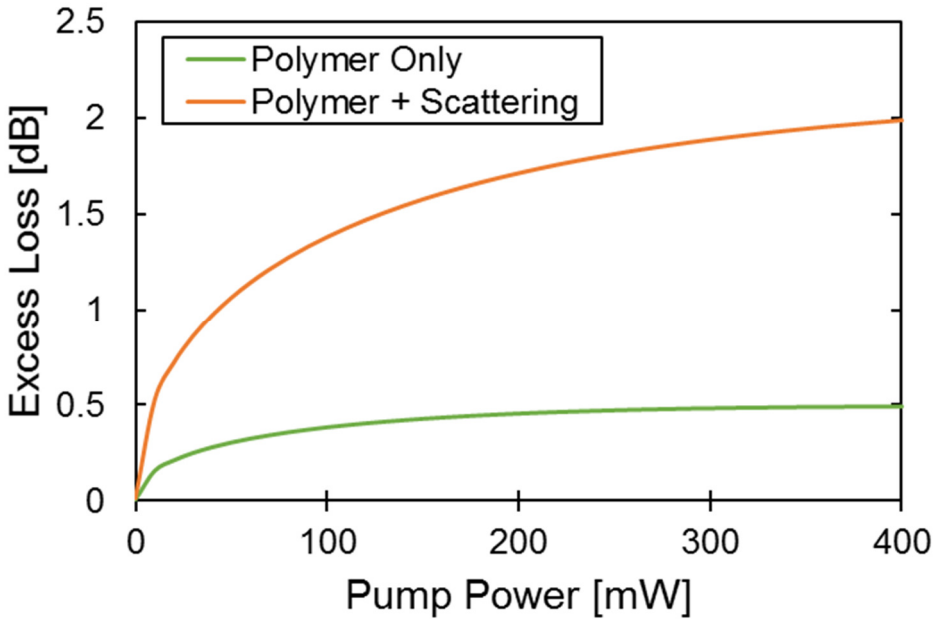

Figure 6-13: Excess reduction in the device gain due to scattering

6.4.2 Solubility Limit

The simulations in the previous section confirmed that the combination of high scattering losses and large waveguide dimensions prevented the efficient operation of the device. Based on the available mask for photolithography, the minimum waveguide size of 3 μm

was simulated to further investigate the potential performance of the EGC-doped polymer.

Simulations of a single mode 3 × 3 μm^2 waveguide were run to examine the impact of reducing the device dimensions as well as increasing the erbium concentration from 5 to 10 wt.% as shown in Figure 6-14. Two key conclusions were drawn based on the result of decreasing the device size: much lower pump power requirements for the population inversion and more efficient utilisation of the erbium ions. This was particularly visible in the case of lower dopant concentration where Er ions contributed to signal power increase across almost the entire investigated wavelength range.

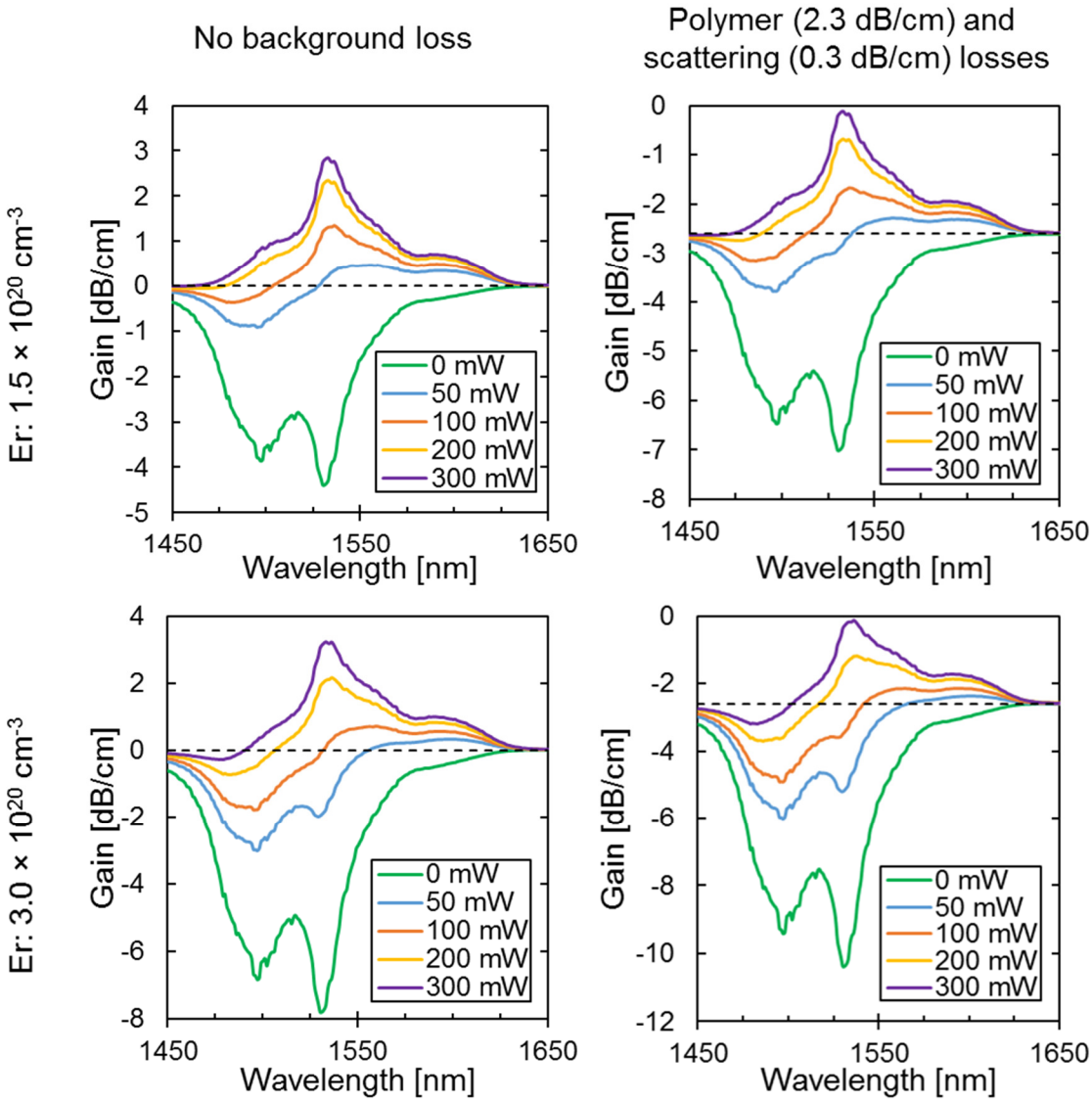

Figure 6-14: EGC-doped polymer gain potential based on a 3 × 3 μm^2 channel waveguide with 5 and 10 wt.% NP concentration

However, even with this improvement in efficiency signal enhancement was not strong enough to generate a net internal gain in the case of the device with parameters as listed in Table 6-1. At the peak emission wavelength, the net loss was reduced to approximately 0.1 dB/cm for both erbium concentrations of 1.5 and 3.0×10^{20} cm^{-3}. This indicated that at the lower concentration, net internal gain was not possible in a system that combined a relatively high upconversion factor and background loss. In the case of the higher dopant concentration, internal gain was possible at the higher pump power of 320 mW. This meant that the system was capable of overcoming background losses but was power inefficient as it required unsustainable pumping levels to do so. A potential solution in this case is to further reduce the device dimensions in order to increase pump density while maintaining or reducing the absolute value.

Table 6-1: Key simulation parameters used for NP-doped polymer studies

Parameter	Sym.	Value used	Reference
Er concentration	N_{Er}	$1.5/3.0 \times 10^{26}$ m^{-3}	
Er lifetime	τ_{Er}	5.6 ms	
Er absorption (1533)	σ_{12}	8.8×10^{-25} m^2	
Er emission (1533)	σ_{21}	9.0×10^{-25} m^2	
Er absorption (976)	σ_{13}	4.5×10^{-25} m^2	
Upconversion coefficient	C_{up}	1×10^{-22} m^3s^{-1}	[8],[19]
Erbium cross-relaxation	C_{cr}	0.7×10^{-22} m^3s^{-1}	[8],[19]
Overlap factors	Γ_s,Γ_p	0.76, 0.80	
Active region area	A	9 μm^2	
Background loss	l_s,l_p,l_j	2.6 dB/cm	

6.4.3 Discussion

In this section the potential of combining the available EGC nanoparticles with siloxane polymer is examined. Experimental measurements allowed for the estimation of important amplifier parameters such as Er lifetime, emission and absorption cross sections, background loss and dopant concentration. Based on these values, EDWA simulations were run showing the difficulty of achieving practical levels of internal gain with the undertaken approach. In order to better understand the underlying problems, a comparison with two recently reported nanocomposite systems was performed as shown in Table 6-2.

The two systems were selected as they emphasise the key design factors required for successful NP-doped polymer systems. In case of the phosphate glass particles [8], a purely theoretical study was performed exploring impact of particle size and NP concentration on the device performance. A more vital comparison is made with NaYF4/NaLuF4-doped PMMA [20] as it also offers insight into the fabrication of this type of composite materials. This work employed core-shell structures, which were based on a two-step preparation. Initially NPs were oleic-acid coated and copolymerised with methyl methacrylate and only after that a covalent-linking nanocomposite was synthesised. The benefit of the increased fabrication complexity was demonstrated by very good optical properties such as long erbium lifetime and high measured internal gain. This in turn indicates relatively low excess scattering losses and uniform particle distribution without clustering despite the relatively high Er/Yb concentration used.

Table 6-2: Simulation parameters comparison between this work and best reported values

Parameter	**EGC + siloxane (this work)**	**P_2O_2: Er/Yb + PMMA** [8]	**$NaYF_4$/$NaLuF_4$: Er/Yb + PMMA** [20]
Er concentration	1.5×10^{26} m^{-3}	1.0×10^{26} m^{-3}	2.8×10^{26} m^{-3}
Yb concentration	-	5.0×10^{26} m^{-3}	28×10^{26} m^{-3}
Er lifetime	5.6 ms	10.0 ms	12.0 ms
Yb lifetime	-	2.0 ms	1.86 ms
Er absorption (1533)	8.8×10^{-25} m^2	6.6×10^{-25} m^2	9.5×10^{-24} m^2
Er emission (1533)	9.0×10^{-25} m^2	9.0×10^{-25} m^2	2.7×10^{-24} m^2
Er/Yb absorption (976)	4.5×10^{-25} m^2	$2.58/2.5 \times 10^{-25}$ m^2	$2.36/100 \times 10^{-25}$ m^2
Upconversion coefficient	1×10^{-22} m^3s^{-1}	1×10^{-22} m^3s^{-1}	0.41×10^{-22} m^3s^{-1}
Er cross-relaxation	0.7×10^{-22} m^3s^{-1}	0.7×10^{-22} m^3s^{-1}	3.4×10^{-22} m^3s^{-1}
Overlap factors	0.76, 0.80	-	0.848, 0.87
Active region area	9 μm^2	-	26 μm^2 (ridge)
Pump power	300 mW	1 mW/μm^2	400 mW
NP size	12 nm	10-100 nm	-
Background loss	2.6 dB/cm	-	-
Internal gain	-0.1 dB/cm	up to 12 dB/cm	11.6 dB/cm

The first key observation was that both approaches reported in the literature took advantage of ytterbium co-doping. This addition not only allowed for more efficient pump absorption but also reduced the upconversion effect. This was expected based on studies performed in previous chapters on the ULPI fabricated and optimised samples, but it was not possible to take advantage of this in this case due to the lack of material availability.

In terms of absorption and emission cross sections the estimated values for EGC were very similar to those of phosphate glass NPs indicating a comparable potential in this regard. Much higher erbium peak emission/absorption cross sections of $2.7/9.5 \times 10^{-24}$ m^2 were reported for the core-shell $NaYF_4$ particles. An even higher pump absorption of 1.0×10^{-23} m^2 was provided by the ytterbium ions, making it almost two orders of magnitude better than the estimate for the ceria particles used in this work. Furthermore, the alternative approaches both had an erbium lifetime which was almost twice as long, i.e. 10 and 12 ms for P_2O_2 and $NaYF_4$ nanocrystals, respectively. While this difference did not fully explain the performance difference, it was an important factor in reducing the ceria nanoparticle performance.

A minimal difference was found among the three approaches in terms of their upconversion factors. While the same, relatively high values were used in this work and in the case of the P_2O_2 NPs, as explained in the previous sections, the core-shell structures relied on fitting the experimental results to estimate the upconversion factor as 0.41×10^{-22} m^3s^{-1}. This value was less than half of that used in this work, further explaining the reason behind the performance difference. It must be emphasised that the value used for ceria was a conservative estimate based on the reports of relatively high visible light upconversion [15]. However, an even higher value of 3.2×10^{-22} m^3s^{-1} has been previously reported in the past for certain cyclic polymer complexes [21].

Finally, an important distinction was noticed concerning the properties of the nanoparticles themselves. In both of the above literature reports, a small refractive index contrast below 0.1 was achieved between the dopants and polymer core. This in turn allowed for a relaxed limit on the particle size as seen by the 100 nm used in the case of phosphate glass NPs. For ceria used in this work the contrast was almost 0.5, resulting in a much lower requirement of approximately 12 nm for the particle size in order to keep the NP scattering loss at a low level of 0.3 dB/cm.

6.5 Conclusions

The dispersion of EGC nanoparticles in the siloxane polymer was investigated as a potential means for the formation of EDWAs. In this chapter, the fabrication process was explained showing the difficulty of obtaining high quality waveguides even with the introduction of additional processing steps such as membrane filtration and ultrasonication. Numerous fabrication attempts with various NP concentrations resulted in limited success and a low yield. After a number of visual inspection and transmission tests, the best performing waveguide section was selected for more detailed analysis.

The loss measurements across the erbium emission spectrum allowed for the estimation of major loss components, namely polymer propagation and coupling, Er absorption and NP scattering. The examination of the relative contributions of these factors led to the conclusion that a 9.3 dB/cm scattering loss due to NP clustering prevented the desired operation of the device. The results of this investigation were confirmed through good agreement between the measured erbium behaviour and theoretical predictions based on the Er-doped thin film properties. The measured scattering loss was not a fundamental limit and could be improved through ensuring a more uniform NP distribution in the polymer host. This could be achieved by, for example, employing an additional material in the mix designed to separate the dopant particles from one another via formation of core-shell structures.

Further simulations study based on extracted material properties assessed the potential of a channel waveguide with the estimated Er concentration of 1.5×10^{20} cm^{-3} assuming the scattering losses were reduced to 0.3 dB/cm. The obtained results show that while the performance greatly improved, a pump power of 320 mW was required for device transparency. This was caused by a low efficiency arising from the high upconversion observed in ceria as well as due to the lack of ytterbium in the dopant mix.

Finally, the system used in this thesis was compared with two state-of-the-art approaches to combine a polymer host with inorganic particles. Both phosphate glass and $NaYF_4$ nanocrystals demonstrated their capability to generate some of the highest reported internal gains in EDWAs, although only $NaYF_4$ was confirmed experimentally. The key difference between these reported materials and the ceria used in this work come from the addition of ytterbium in the dopant composition. The effect of co-doping is explored in detail in previous chapters based on the ULPI but was not possible with the NPs due to the lack of material availability. Furthermore, higher absorption and emission cross

sections as well as longer Er lifetime also contributed to the difference in performance. The last important distinction is that the EGC NPs have much higher refractive index contrast with the polymer host resulting in a strict particle radius limit of 12 nm needed to keep scattering loss at a reasonable 0.3 dB/cm required for practical devices.

6.6 References

[1] M. Ono, Y. Kondo, J. Kageyama, and N. Sugimoto, "Fabrication of ultra-compact Er-doped waveguide amplifier based on bismuthate glass," *J. Ceram. Soc. Japan*, vol. 116, no. 10, pp. 1134–1138, 2008.

[2] S. Suntsov, C. E. Rüter, and D. Kip, "Er:Ti:$LiNbO_3$ ridge waveguide optical amplifiers by optical grade dicing and three-side Er and Ti in-diffusion," *Appl. Phys. B Lasers Opt.*, vol. 123, no. 4, pp. 1–7, 2017.

[3] K. Yan, K. Vu, and S. Madden, "Internal gain in Er-doped As_2S_3 chalcogenide planar waveguides," *Opt. Lett.*, vol. 40, no. 5, pp. 796–799, 2015.

[4] Y. Benmadani, A. Kermaoui, M. Chalal, W. Khemici, A. Kellou, and F. Pellé, "Erbium doped tellurite glasses with improved thermal properties as promising candidates for laser action and amplification," *Opt. Mater. (Amst).*, vol. 35, no. 12, pp. 2234–2240, 2013.

[5] S. A. Vázquez-Córdova *et al.*, "High optical gain in erbium-doped potassium double tungstate channel waveguide amplifiers," *Opt. Express*, vol. 26, no. 5, pp. 6260–6266, 2018.

[6] T. Wang *et al.*, "Optical waveguide amplifiers based on $NaYF_4$: Er^{3+}, Yb^{3+} NPs-PMMA covalent-linking nanocomposites," *Opt. Mater. Express*, vol. 5, no. 3, p. 469, 2015.

[7] W. Blanc and B. Dussardier, "Formation and applications of nanoparticles in silica optical fibers," *J. Opt.*, pp. 1–13, 2015.

[8] S. Ghatrehsamani and G. E. Town, "Optical Gain in Polymer Composite Materials With P_2O_2:Er^{3+}/Yb^{3+} Codoped Nanoparticles," *IEEE J. Quantum Electron.*, vol. 53, no. 2, pp. 2–6, 2017.

[9] I. Porosnicu, D. Avram, B. Cojocaru, M. Florea, and C. Tiseanu, "Up-conversion luminescence of Er(Yb)-CeO_2: Status and new results," *J. Alloys Compd.*, vol. 711, pp. 627–636, 2017.

[10] M. Mogensen, N. M. Sammers, and G. A. Tompsett, "Physical, chemical and electrochemical properties of pure and doped ceria," *Solid State Ionics*, vol. 129, no. 1–4, pp. 63–94, Apr. 2000.

[11] D. Milanese, D. Janner, E. Ceci-Ginistrelli, N. Boetti, D. Pugliese, and J. Lousteau, "Highly Doped Phosphate Glass Fibers for Compact Lasers and Amplifiers: A Review," *Appl. Sci.*, vol. 7, no. 12, p. 1295, 2017.

[12] Schott, "IOG-1 Phosphate Laser Glass for Ion Exchange Applications," Mainz, Germany, 2013.

[13] M. A. Martínez Gámez, M. A. H. Vallejo, A. V. Kiryanov, L. Licea-Jiménez, J. L. M. Lucio, and S. A. Pérez-García, "Fluorescence properties of Yb^{3+}-Er^{3+} co-doped phosphate glasses containing silver nanoparticles," *Methods Appl. Fluoresc.*, vol. 6, no. 2, 2018.

[14] W. J. Miniscalco and R. S. Quimby, "General procedure for the analysis of Er^{3+} cross sections," *Opt. Lett.*, vol. 16, no. 4, pp. 258–260, 1991.

[15] V. Singh, M. Rathaiah, V. Venkatramu, M. Haase, and S. H. Kim, "Intense up-conversion luminescence in Er^{3+}/Yb^{3+} co-doped CeO_2 powders," *Spectrochim. Acta - Part A Mol. Biomol. Spectrosc.*, vol. 122, pp. 704–710, 2014.

[16] N. Shehata, I. Kandas, E. Samir, K. Meehan, and M. Aldacher, "Parametric study of up-conversion efficiency in Er-doped ceria nanoparticles under 780 nm excitation," *J. Lumin.*, vol. 176, pp. 372–380, 2016.

[17] M. Jamshidijam, P. Thangaraj, A. Akbari-Fakhrabadi, M. A. Niño Galeano, J. Usuba, and M. R. Viswanathan, "Influence of rare earth (RE=Nd, Y, Pr and Er) doping on the microstructural and optical properties of ceria nanostructures," *Ceram. Int.*, vol. 43, no. 6, pp. 5216–5222, 2017.

[18] G. F. R. Chen, X. Zhao, Y. Sun, C. He, M. C. Tan, and D. T. H. Tan, "Low Loss Nanostructured Polymers for Chip-scale Waveguide Amplifiers," *Sci. Rep.*, vol. 7, no. 1, pp. 1–8, 2017.

[19] A. Shooshtari, T. Touam, S. I. Najafi, S. Safavi-Naeni, and H. Hatami-Hanza, "Yb^{3+}-sensitized Er^{3+}-doped waveguide amplifiers: a theoretical approach," *Opt. Quantum Electron.*, vol. 30, pp. 249–264, 1998.

[20] M. Zhang *et al.*, "High-gain polymer optical waveguide amplifiers based on core-shell $NaYF_4$/$NaLuF_4$: Yb^{3+}, Er^{3+} NPs-PMMA covalent-linking nanocomposites,"

Sci. Rep., vol. 6, no. November, pp. 1–8, 2016.

[21] L. H. Slooff *et al.*, "Rare-earth doped polymers for planar optical amplifiers," *J. Appl. Phys.*, vol. 91, no. 7, pp. 3955–3980, 2002.

7 Conclusions and Future Work

This thesis presented a comprehensive review of the current progress in the field of the EDWAs. Particular focus was placed on the recent achievements in the area of polymer-based systems where the highest gain per unit length in practically sized devices have been reported to date. Furthermore, a theoretical study using a rate-equations model was performed to determine the key requirements for high gain amplifiers. As a result of this study, a novel methodology of optimising the ratio of the Er:Yb co-dopant ions that took into account the device structure as well as the upconversion factor was developed.

A feasibility study on the fabrication of polymer platform compatible amplifiers was performed by investigating a number of potential approaches. Ultrafast laser plasma implantation and nanoparticle dispersion into a polymer host have been selected for implementation. The first approach was chosen due to the potential for extremely high RE-dopant concentration of 1.63×10^{21} cm^{-3} demonstrated in silica glass. It was investigated for both hybrid glass-polymer systems as well as, for the first time, direct implantation into a siloxane material. The comprehensive investigation into the optical properties of the obtained thin films allowed for the selection of ULPI-fabricated hybrid devices and NP-dispersed polymer waveguides for further analysis.

The process of depositing polymer waveguides on erbium-doped tellurite modified silica to form strip-loaded waveguides was developed. Despite the early promising results of the optimised recipe, this approach was shown to have high sensitivity to feature size as well as being prone to surface scattering. Throughout this study a number of parameters was extracted from the fabricated samples allowing for a detailed analysis of the potential and competitiveness of the strip-loaded geometry with the standard channel waveguide geometry. In case of a system with 200 mW pump power, the gain difference between the two geometries was only 0.3 dB/cm after Er:Yb ratio optimisation performed for both designs.

An alternative approach of dispersing erbium-gadolinium ceria particles in a siloxane polymer host was explored. The problem of particle insolubility was addressed with an extended fabrication procedure incorporating ultrasonication, magnetic stirring and membrane filtering. The combination of these additional steps was shown to improve the quality of the prepared thin films in terms of their photoluminescence intensity and the Er metastable lifetime. Based on these results, a number of samples was prepared and investigated in terms of a waveguide amplifier potential. Visual inspection combined with transmission measurements on the samples showed poor performance. A detailed analysis of the waveguides and use of an appropriate model confirmed that high scattering loss of

approximately 9.3 dB/cm is the main factor preventing desirable operation. Further theoretical investigation led to the conclusion that the specific ceria NPs used in this work were not the optimal material choice due to the lack of ytterbium co-doping and high refractive index contrast with the polymer host. Suggestions were provided on how to improve the results and achieve the desirable outcome by for example, employing core-shell structures or employing Er-doped phosphate glass NPs, which have a very similar refractive index value.

7.1 Conclusions

Polymer-based erbium-doped waveguide amplifiers are a promising candidate for addressing the increasing demand for compact active components that can be integrated in practical systems. This is emphasised by the recent increase in the number of successful demonstrations of polymer-based systems with the internal gain figure reaching approximately 10 dB/cm [1]–[3].

In this thesis, the key parameters of the erbium doping were investigated in terms of the factors limiting the performance of this type of amplifiers. Based on these, supplemented with the waveguide design parameters, a detailed rate-equations-based model was prepared. An optimisation of the reported ULPI fabricated thin films with dopant concentration of 1.63×10^{27} m^{-3} showed that a 2×2 μm^2 channel waveguide was capable of delivering a gain of 9.6 dB/cm when pumped at a moderate power of 200 mW. This result was predicted based on a combination of measured parameters reported on the erbium-doped tellurite modified silica [4] combined with upconversion factor values that were linearly scaled with the Er concentration in the range of 1.63-16.3 $\times 10^{26}$ m^{-3} and 0.4-4 $\times 10^{-23}$ m^3s^{-1}, respectively.

A number of observations was made in the process regarding the impact of various design aspects on the final performance. In an amplifier that contains only erbium dopant ions, the optimum concentration depended on the available pump power. In case of a 200 mW limit, there was no benefit of increasing the concentration beyond 6.9×10^{26} m^{-3} in the investigated system as after that point any additional erbium ions contributed more to the reabsorption rather than the stimulated emission leading to a reduction in the achievable gain. The benefit of introducing ytterbium, which operates as a sensitizer, to the mix is highlighted by the fact that the predicted gain increased from 5.9 dB/cm to 9.6 dB/cm with no design changes other than concentration adjustments. Under the same constraint

of the maximum achievable concentration, by introducing 7.3×10^{26} m^{-3} Yb, the Er concentration could also be increased to 9.0×10^{26} m^{-3} leading to a higher overall gain.

The scalability of this approach was also examined by establishing the maximum gain for 3- and 5-cm-long amplifiers. The material properties were assumed to remain the same, the upconversion factor was scaled linearly with erbium concentration as in case of 1-cm-long devices, background loss was constant at 1 dB/cm and coupling losses ignored (internal gain). In case of an erbium-only system under a 200 mW power constraint, a gain of 14.0 and 18.5 dB was possible when dopant concentration was set to 5.3 and 4.5×10^{26} m^{-3} for the 3- and 5-cm-long device, respectively. This could be further improved by Yb sensitisation to 23.0 and 27.2 dB with Er:Yb ratios of 6.1:10.2 and 4.5:11.8. A 9 dB highlights the benefit of co-doping Er with Yb. Furthermore, it was observed in this work was that the relative concentration of ytterbium to erbium increases with both the length of the device and its cross-section area.

The simulation studies were based the ultrafast laser plasma implantation technology that was then experimentally investigated for the silica host and, for the first time, polymer substrates. The obtained thin films were characterised in terms of their optical properties. In case of a glass substrate, the EDTS layer was measured to have a lifetime up to 12.1 ms with an emission FWHM of 18.9 nm. This was obtained from a melt-quenched target glass with 1.95 wt.% of Er and Yb with 1:2 ratio. The direct implantation into a Dow Corning WG-2020 siloxane polymer has proven more challenging due to the damage to the material resulting from the process. The ULPI process parameters were adjusted by lowering the substrate temperature to 100 °C (from 700-750 °C) and reducing the procedure time to 1 hour (from 4-8 h) in order to fabricate more promising samples as summarised and compared with the alternative methods in Table 7-1. The measured Er lifetime of up to 4.2 ms and FWHM of 39.0 nm looked promising, however a direct comparison of the PL emission revealed a twelvefold drop in the intensity despite a concentration reduction by a factor of only 4. Additionally, a further analysis exposed a non-uniform distribution and a surface damage arising in the process.

An alternative method of dispersing nanoparticles directly in a polymer matrix before the fabrication via traditional polymer techniques was investigated. Available ceria NPs were investigated and compared with the ULPI created samples. The EGC-doped thin films were prepared at a variety of concentrations ranging from 0.05 to 12.5 wt.%. As a result of a comparison study, an increase in the PL intensity with dopant concentration was observed, while FWHM and Er lifetime stayed approximately constant around 31 nm and

5.7 ms, respectively. Even when an additional filtering step was introduced, the emission intensity did not increase linearly with the concentration as expected, indicating that ion quenching due to the NP clustering was occurring.

Table 7-1: Key physical properties of the best sample for a given approach to EDWA formation used in this thesis

Parameter	EDTS (T28)	ULPI polymer (F3)	EGC polymer (5.1 wt.%)
FWHM [nm]	18.9	39.0	27.0
Lifetime [ms]	12.1	4.2	5.7
Peak emission wavelength [nm]	1534	1533	1533
Target material concentration [wt.%]	1.95	0.5	5.1
Estimated concentration [$\times 10^{26}$ m^{-3}]	16.3	4.4	1.5

In order to take advantage of the ULPI fabrication method, a hybrid design was proposed to combine the highly-doped EDTS layer with the siloxane polymer material. A strip loaded geometry was chosen as it allows a straightforward integration with the polymer platform. Simulation studies also showed a comparable performance with the standard channel waveguide configuration. The integration of EDTS planar layers can be achieved through implantation before polymer features are added on top to avoid the damage from the ULPI process.

An adjusted model accounting for the asymmetry due to the EDTS layer contact with the silica glass was prepared for a polymer-surrounded channel waveguide. The simulations studies revealed that, when pumped at 200 mW, a 1-cm-long hybrid channel device with yielded a gain of 7.7 dB. In this case, the upconversion factor was scaled linearly with the erbium concentration leading to the optimal Er:Yb ratio of approximately 1:1. The alternative strip-loaded hybrid geometry was compared with the channel waveguide using the same dopant parameters. It was shown that, under the same single mode assumptions as for the channel structure, a similar internal gain figure of 7.4 dB could be achieved. This was attained by optimising the Er:Yb ratio to 1:2. The main reason behind the requirement for a higher ytterbium content was due to a larger effective active area of 8.96 μm^2 under the polymer ridge compared with 3.6 μm^2 for the channel geometry.

The polymer waveguide fabrication process was optimised for a 2×3 cm^2 glass substrate compatible with the ULPI setup. The experimental analysis via the scanning electron

microscopy, ASE measurements and surface profiling revealed that the fabricated structures did not perform as the simulation studies predicted. The poor performance was attributed to the combination of rough surface (with RMS values in range of 95.8-193.3 nm) and larger than predicted polymer waveguides.

The second approach to fabricate the EDWAs investigated in this thesis was dispersion of the nanoparticles in the siloxane polymer. A fabrication process with additional membrane filtering and ultrasonication steps based on available erbium-gadolinium ceria NPs was proposed in order to reduce the particle agglomeration. Despite a low yield, a number of readings were obtained for the performance analysis. The loss measurements across the erbium emission spectrum of 1475-1575 nm allowed for estimation of the major loss components, namely polymer propagation and coupling, Er absorption and NP scattering. The examination of the relative contributions of these factors led to a conclusion that a high scattering loss of 9.3 dB/cm due to NP clustering prevented the desired operation of the device.

Further simulation study based on the extracted material properties estimated the Er concentration to be approximately 1.5×10^{20} cm^{-3}. However, an extended analysis assuming a more practical scattering loss of 0.3 dB/cm [5] revealed that a pump power of 320 mW was required for a device transparency. This was caused by a low efficiency arising from the high upconversion factor observed in ceria as well as lack of ytterbium in the dopant mix.

A comparison of the approaches proposed in this thesis with state-of-the-art approaches to EDWAs was used to supplement the feasibility study. The key difference between the most successful attempts and the ceria used in this work came from the addition of the ytterbium in the dopant composition. The resultant higher pump light absorption cross-section as well as a longer metastable lifetime and a reduced upconversion factor explained the performance difference. The last important conclusion was that the EGC NPs employed in this work had much higher refractive index contrast with the polymer host resulting in a strict particle radius limit of 12 nm needed to keep the scattering loss at a 0.3 dB/cm achieved in best reported amplifiers.

The proposed Er:Yb optimisation approach has a lot of potential to maximise performance of the approaches studied in this thesis as well as alternative designs based on other material systems, particularly ones with all the parameters, including the key upconversion factor, well-established through experimental studies. Similar, non-optimised, hybrid structures have been recently shown [6] suggesting a combination of

polymer and ULPI technologies can be employed and the composition optimised using the proposed methodology, once the high surface roughness is eliminated.

7.2 Future Work

This thesis presented work on design, optimisation, fabrication and characterisation of the erbium-doped waveguides compatible with the polymer platform. There is room for improvement on the performed work in a number of aspects.

7.2.1 Experimental Confirmation of the ULPI Upconversion Factor

The proposed methodology for erbium-ytterbium ratio optimisation offers a guideline for performance improvement for EDWAs independently of the underlying implementation technology. While the underlying model has been tested and compared with other theoretical work [7]–[9] as well as experimental results [10], it could not be verified on the ULPI samples. The poor quality of the waveguides prepared for the strip-loaded approach resulted in a need for the parameter extraction from thin films using well-established procedures. However, the results obtained in this way were missing a key component of upconversion factor that needs to be experimentally confirmed on either the proposed hybrid approach or in a standard stand-alone glass system. Therefore, next step towards the model completeness is to determine the upconversion factor experimentally through measurements on a waveguide with known erbium properties followed by a model fitting. To achieve this, a fabrication process resulting in a low-loss EDWA device in either channel or strip-loaded geometry is required.

Another useful study related to the upconversion coefficient is to employ ULPI in order to implant Er ions into the aluminium oxide platform. Erbium upconversion in Al_2O_3 has been extensively studied in the past, including the impact of the fabrication process on the green light emission. This study could be extended by doping a sample with a similar waveguide design using ULPI and then compare the upconversion results with existing devices obtained with alternative fabrication methods.

7.2.2 Alternative Fabrication Method of Hybrid Waveguides

The feasibility study on combining the siloxane polymer with the ULPI carried out in this thesis highlighted the difficulty of combining the two technologies. Even a better-established process of implanting into the silica glass to form an EDTS layer has yielded a surface roughness of up to 194 nm for the 2.5-μm-thick sample. The hybrid strip-loaded

structure with a target 3×3 μm^2 ridge is only predicted to work well with a lower surface scattering. For this design to work well, more work is required on reduction of the surface roughness arising from the implantation process. An alternative approach is to combine much thinner Er-doped planar layers with a polymer ridge fabricated using a different method, such as electron-beam lithography, that allows the creation of much smaller features than UV photolithography which was used in this work.

7.2.3 Core-Shell Structures

The second fabrication approach selected in this thesis used the direct dispersion of the ceria NPs in the polymer matrix. Even though the additional membrane filtering step removed the largest particle agglomerations from the mix, the resultant waveguides had losses that were too high for a practical operation. The success of using core-shell structures with an intermediate polymer, such as polyhedral oligometric silsesquioxane (POSS) [11], highlights the need of additional fabrication steps. All of the most recently reported high-gain polymer EDWAs discussed in Chapter 2 have employed this technique. This trend indicates that uniform dopant distribution can be achieved with a range of different NP types and could be applied to the ceria material used.

7.2.4 Ytterbium/Cerium co-doping of ECG NPs

The lack of ytterbium co-doping was also identified as one of key performance-limiting factors for the EGC NPs employed in this work. In order to maximise the potential of this material, not only the Yb can be added according to the optimum found with the proposed model, but also the fraction of cerium should be reduced. Ce ions introduce an additional energy transfer path in the system that has been reported to reduce the upconversion process as shown in Figure 7-1. However, an optimal inclusion factor of 2 % has been reported with an increase beyond this value shown to reduce the overall 1550 nm emission strength [12].

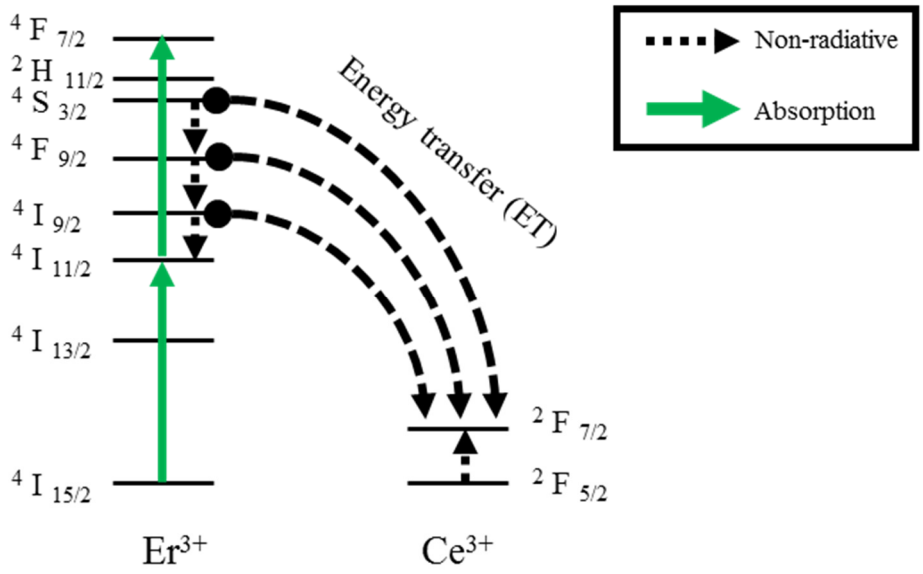

Figure 7-1: Additional energy transfer paths introduced by co-doping erbium with cerium

7.2.5 Modelling of the Dopant Lifetime Change with Concentration

The methodology of optimising the Er:Yb ratio is useful for systems where the total concentration is limited by the dopant solubility. Linear scaling of the upconversion factor with erbium concentration allows for an accurate representation of a trend empirically reported in alumina [13]. A further potential enhancement of this optimisation procedure can be an inclusion of the effect of ion ratio on the metastable lifetimes of both Er and Yb. Although this parameter is strongly dependent on the host material as discussed in Chapter 2, it has also been reported to vary with the dopant concentration in the same host [14]. Therefore, a number of ULPI-fabricated samples with varying Er:Yb ratios can be used to experimentally derive the lifetime relationship for both codopants.

7.2.6 Optical Resonator

Finally, the focus in this work was to design, fabricate and characterise the feasibility of these devices to act as optical amplifiers, but as mentioned before, they can also be used as a basis for laser sources. As discussed in Chapter 2, a number of erbium-doped waveguide lasers have been founded on a further development of the amplifiers [15]. An addition of an optical feedback in the system to the EDWA acting as the active region is required to create a signal generating device.

This has not yet been successfully achieved for polymer-based systems, but worked in some of the more mature EDWA approaches. Early attempts that reported the C-band

lasing of Er-doped phosphate glass, employed external optical cavities such as end-deposited mirrors [16] or butt-coupled fibre Bragg gratings (FBG) [17]. These methods have allowed to take advantage of either straightforward fabrication processes or readily available reflection components. However, these solutions suffered from the inherent problems with misalignment and, more importantly, system integration difficulty due to the laser signal leaving the chip.

Several methods have been used to design on-chip resonators for Er-doped systems as presented in Figure 7-2. The end mirrors can be replaced with distributed Bragg reflectors (DBR) on both ends of the device [18] or into the centre of the waveguide to form a distributed feedback laser (DFB) [19]. Another approach to create a feedback structure in a single processing step is to integrate ring resonators as demonstrated in aluminium oxide integrated system [20]. All three of the above approaches to form an on-chip cavity can be potentially realised on the polymer platform as the underlying components have already been demonstrated for other applications [21], [22].

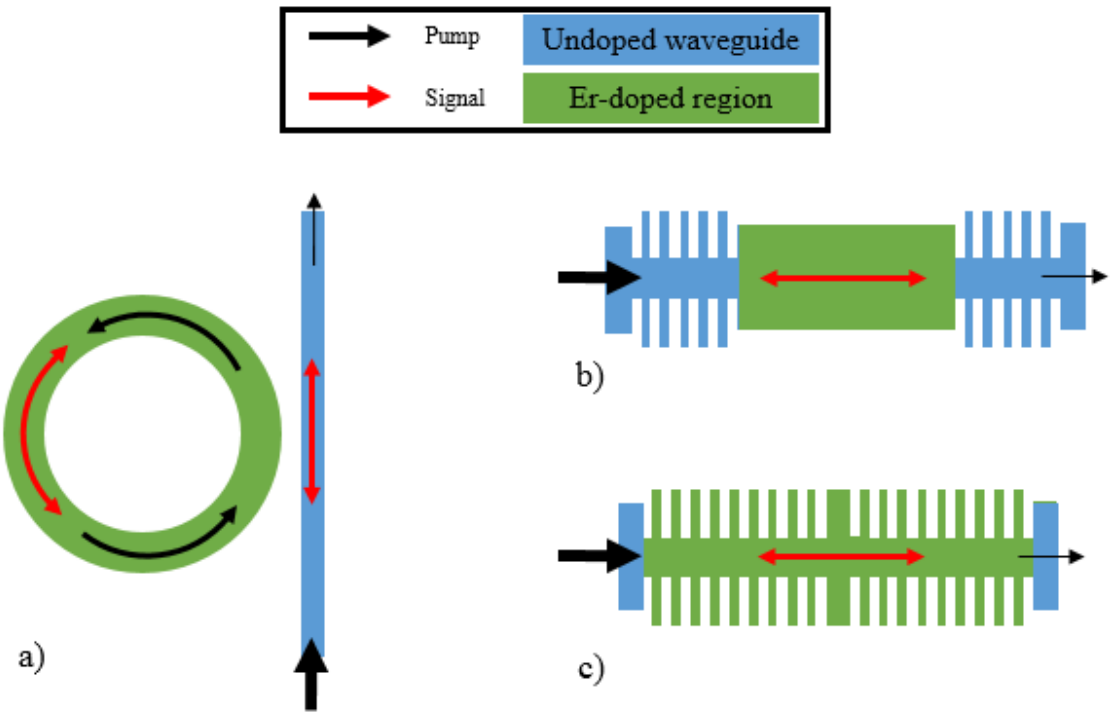

Figure 7-2: Potential integrated optical feedback structures: a) microring resonator, b) DBR and c) DFB

7.3 References

[1] M. Zhang *et al.*, "High-gain polymer optical waveguide amplifiers based on core-shell $NaYF_4$/$NaLuF_4$: Yb^{3+}, Er^{3+} NPs-PMMA covalent-linking nanocomposites,"

Sci. Rep., vol. 6, no. November, pp. 1–8, 2016.

[2] T. Wang *et al.*, "Optical waveguide amplifiers based on $NaYF_4$: Er^{3+}, Yb^{3+} NPs-PMMA covalent-linking nanocomposites," *Opt. Mater. Express*, vol. 5, no. 3, p. 469, 2015.

[3] P. Zhao *et al.*, "Optical Amplification at 1525 nm in $BaYF_5$: 20% Yb^{3+} , 2% Er^{3+} Nanocrystals Doped SU-8 Polymer Waveguide," *J. Nanomater.*, vol. 2014, pp. 1–6, 2014.

[4] J. Chandrappan *et al.*, "Doping silica beyond limits with laser plasma for active photonic materials," *Opt. Mater. Express*, vol. 5, no. 12, p. 2849, 2015.

[5] G. F. R. Chen, X. Zhao, Y. Sun, C. He, M. C. Tan, and D. T. H. Tan, "Low Loss Nanostructured Polymers for Chip-scale Waveguide Amplifiers," *Sci. Rep.*, vol. 7, no. 1, pp. 1–8, 2017.

[6] Y. Yi, H. Wang, M. Jiang, X. Wang, F. Wang, and D. Zhang, "Multilayer Hybrid Waveguide Amplifier for Three-Dimension Photonic Integrated Circuit," *IEEE Photonics Technol. Lett.*, vol. 27, no. 22, pp. 2411–2413, 2015.

[7] S. Ghatrehsamani and G. E. Town, "Optical Gain in Polymer Composite Materials With P_2O_2:Er^{3+}/Yb^{3+} Codoped Nanoparticles," *IEEE J. Quantum Electron.*, vol. 53, no. 2, pp. 2–6, 2017.

[8] N. Lou, G. Liang, J. Hao, R. Gu, and Q. Li, "Improved gain characteristics by forward- backward pumped configuration in erbium-ytterbium–doped phosphate glass waveguide amplifier," *Opt. Eng.*, vol. 46, no. 4, 2007.

[9] A. Shooshtari, T. Touam, S. I. Najafi, S. Safavi-Naeni, and H. Hatami-Hanza, "Yb^{3+}-sensitized Er^{3+}-doped waveguide amplifiers: a theoretical approach," *Opt. Quantum Electron.*, vol. 30, pp. 249–264, 1998.

[10] A. Z. Subramanian, G. S. Murugan, M. N. Zervas, and J. S. Wilkinson, "Spectroscopy, Modeling, and Performance of Erbium-Doped Ta_2O_5 Waveguide Amplifiers," *J. Light. Technol.*, vol. 30, no. 10, pp. 1455–1462, 2012.

[11] E. Ayandele, B. Sarkar, and P. Alexandridis, "Polyhedral Oligomeric Silsesquioxane (POSS)-Containing Polymer Nanocomposites," *Nanomaterials*, vol. 2, no. 4, pp. 445–475, Dec. 2012.

[12] X. Zhai *et al.*, "Enhancement of 1.53 μm emission band in $NaYF_4$:Er^{3+},Yb^{3+},Ce^{3+} nanocrystals for polymer-based optical waveguide amplifiers," *Opt. Mater.*

Express, vol. 3, no. 2, p. 270, Feb. 2013.

[13] L. Agazzi, K. Wörhoff, M. Pollnau, K. Worhoff, and M. Pollnau, "Energy-Transfer-Upconversion Models, Their Applicability and Breakdown in the Presence of Spectroscopically Distinct Ion Classes: A Case Study in Amorphous $Al_2O_3:Er^{3+}$," *J. Phys. Chem.*, vol. 117, no. 13, pp. 6759–6776, 2013.

[14] J. Chandrappan *et al.*, "Target dependent femtosecond laser plasma implantation dynamics in enabling silica for high density erbium doping," *Sci. Rep.*, vol. 5, 2015.

[15] C. Grivas, "Optically pumped planar waveguide lasers: Part II: Gain media, laser systems, and applications," *Prog. Quantum Electron.*, vol. 45–46, pp. 3–160, 2016.

[16] W. Liu, S. N. Houde-walter, D. L. Veasey, and A. P. Peskin, "Design and optimization of a diode-pumped fiber-coupled Yb : Er glass waveguide laser," vol. 39, no. 33, pp. 6165–6173, 2000.

[17] R. Osellame *et al.*, "Waveguide Lasers in the C-Band Fabricated by Laser Inscription With a Compact Femtosecond Oscillator," vol. 12, no. 2, pp. 277–285, 2006.

[18] M. Belt and D. J. Blumenthal, "Erbium-doped waveguide DBR and DFB laser arrays integrated within an ultra-low-loss Si_3N_4 platform," *Opt. Express*, vol. 22, no. 9, pp. 10655–10660, 2014.

[19] Purnawirman *et al.*, "Ultra-narrow-linewidth $Al_2O_3:Er^{3+}$ lasers with a wavelength-insensitive waveguide design on a wafer-scale silicon nitride platform," *Opt. Express*, vol. 25, no. 12, p. 13705, 2017.

[20] N. Li *et al.*, "Monolithically integrated erbium-doped tunable laser on a CMOS-compatible silicon photonics platform," *Opt. Express*, vol. 26, no. 13, 2018.

[21] T. Park, J. Shin, G. Huang, W. Chu, and M. Oh, "Tunable channel drop filters consisting of a tilted Bragg grating and a mode sorting polymer waveguide," *Opt. Express*, vol. 24, no. 6, p. 5709, 2016.

[22] C. Zhang, S. L. Chen, T. Ling, and L. J. Guo, "Review of imprinted polymer microrings as ultrasound detectors: Design, fabrication, and characterization," *IEEE Sens. J.*, vol. 15, no. 6, pp. 3241–3248, 2015.

APPENDIX

UV Photolithography Mask Design

The UV photolithography mask shown in Figure A- was designed specifically for this project. As described in Chapter 3, the design accounted for the ULPI sample size (2 x 3 cm^2) and enabled single mode operation under a wide range of dopant concentrations.

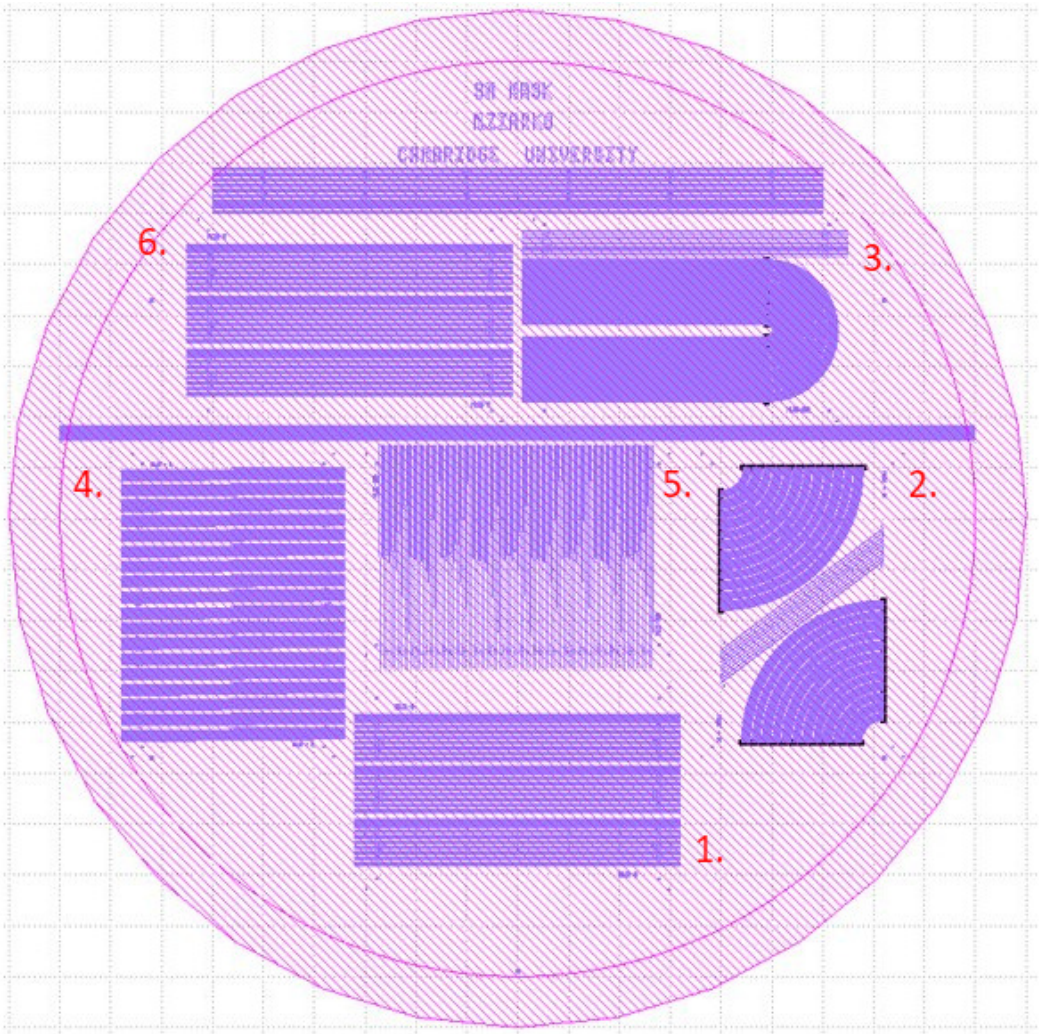

Figure A-1: Mask design with the key sections marked

ULPI-compatible sections:

1 & 6. 3-cm-long straight waveguides with feature width varied in rang of 3-20 µm;

2. 90° bends with varied bending radius (2.2-14 mm) and width (3-10 µm);

3. 180° bends (U-turns) with varied radius (0.5-7 mm) and width (3-10 µm);

4. S-bends with 150 µm y-offset over a range of lengths between 0.25 and 20 mm;

5. Y-splitters with branching angle varied between 0.3° and 53°;